TECHNISCHE UNIVERSITÄT MÜNCHEN

Lehrstuhl für Messsystem- und Sensortechnik

Fiber-Optical Sensing for Telecommunication Satellites

Dipl.-Ing. Univ. Philipp Putzer

Vollständiger Abdruck der von der Fakultät für Elektrotechnik und Informationstechnik der Technischen Universität München zur Erlangung des akademischen Grades eines

Doktor-Ingenieurs

genehmigten Dissertation.

Vorsitzender: Prof. Dr.-Ing. Gerhard Rigoll

Prüfer der Dissertation:

1. Prof. Dr.-Ing. habil. Dr. h.c. Alexander W. Koch
2. Prof. Felix Jose Salazar Bloise, Ph.D.

Die Dissertation wurde am 28.02.2017 bei der Technischen Universität München eingereicht und durch die Fakultät für Elektrotechnik und Informationstechnik am 25.01.2018 angenommen.

Abstract

The presented thesis focuses on the development of a fiber-optical measurement system using fiber Bragg grating sensors for temperature measurements. The interrogation technique is based on a tunable laser concept, more precisely on a modulated-grating Y-branch laser diode. The interrogation system is designed for space applications, enabling the use of fiber-optical sensing on board telecommunication satellites. Current implementations for temperature measurements suffer from high weight of the sensor harness, an excessive degree of inflexibility for later changes and high assembly and integration costs. These drawbacks can be improved or even avoided by using fiber-optical sensing. By integrating the fiber-optical sensors directly into satellite panels, smart panels can be constructed which allow an integrated measurement of temperatures at dedicated positions.

The extreme conditions in space environment for the target application such as large temperature differences and high radiation loads due to cosmic radiation, required detailed analysis on system level for temperature and radiation. Especially due to the cosmic radiation a radiation simulation of the entire measurement system is carried out. The simulation results form the baseline of the subcomponent radiation test series, carried out in this thesis. The presented test results are completely new and focus on the fiber-optic and opto-electronic components used in the interrogation system.

A particular focus is placed on radiation effects for optical fibers and fiber Bragg gratings. From the respective literature it is already known that optical fibers suffer from darkening effects [1] due to radiation whereas FBGs suffer from high radiation induced Bragg wavelength shifts [2]. An optical fiber based on a pure silica core was chosen for this thesis and was tested according to the target application. The grating writing technique (written by ultra-violet laser of femto-second infrared laser) influences on the radiation induced wavelength shift is investigated in more detail. Finally a combination of optical fiber and FBG writing technique is presented to achieve the target measurement accuracy of $\pm 1°C$ over the full lifetime of 15 years in orbit.

A detailed description of the developed hardware with special focus on low noise current sources is presented in this thesis. The performance, limited due to the low number of available radiation hard components for space applications, was exhausted as much as possible. In addition strategies to minimize the measurement errors caused by birefringence effects are presented, the implementation of the most suitable strategy is discussed.

The thesis concludes with a detailed performance evaluation of the developed interrogation system. Thermal test results of FBG sensors using the developed interrogator illustrate that the performance goal of measurement accuracy of ± 1 °C is achieved.

Zusammenfassung

Das in dieser Arbeit entwickelte faser-optische Messsystem ist für den Einsatz in Weltraummissionen konzipiert. Das System soll den Zugang der faser-optischen Messtechnik für Raumfahrtanwendungen, speziell für Telekommunikationssatelliten, ermöglichen. Momentane Implementierungen der Temperaturüberwachung und Regelung leiden unter hohem Gewicht der Kabelbäume, große Inflexibilität für spätere Änderungen und hohen Herstellungs- und Assemblierungskosten. Diese Nachteile können vermieden werden, wenn faseroptische Sensorik zum Einsatz kommt. Durch Integration der Sensoren direkt in die Satellitenpaneele können intelligente Paneele hergestellt werden, welche bereits vorintegrierte Messstellen vermessen können.

Aufgrund der extremen Umgebungsbedingungen für Systeme im Weltraum, wie z.B. große Temperaturdifferenzen und hohe Strahlenbelastungen durch kosmische Strahlung, wird eine detaillierte Analyse der oben genannten Effekte durchgeführt. Speziell für die Strahlenbelastung wird eine Simulation des Gesamtsystems ausgeführt. Die Ergebnisse der Simulation sind das Grundgerüst der Bestrahlungstests für die elektro-optischen und optischen Komponenten, welche im Rahmen dieser Arbeit ausgeführt werden. Die Messergebnisse zu den verbauten Komponenten sind neu und bisher in dieser Form nicht verfügbar.

Zusätzlich wird der Einfluss von Strahlungseffekten in optischen Glasfasern sowie in Faser Bragg Gittern untersucht. Aus der Fachliteratur ist bekannt, dass optische Fasern unter Verdunkelungseffekten durch ionisierende Strahlung leiden [1], wohingegen FBGs eine strahlungsinduzierte Verschiebung der Bragg-Wellenlänge aufweisen [2]. In dieser Arbeit wird eine optische Glasfaser mit einem puren Quarzglaskern ausgewählt, getestet und für die Zielanwendung verifiziert. Der Einfluss der verwendeten Einschreibetechnik für die FBG Sensoren (geschrieben mit ultra-violett Laser oder femto-Sekunden infra-rot Laser) und die verursachte Verschiebung der Bragg-Wellenlänge durch Strahlung wird genauer untersucht. Schlussendlich wird eine Kombination aus optischer Glasfaser und Einschreibetechnik präsentiert, welche die geforderte Messgenauigkeit von ± 1 °C über die Lebensdauer von 15 Jahren erreicht.

Eine detaillierte Beschreibung der entwickelten Hardware mit speziellem Fokus auf die entwickelten Stromquellen mit geringem Rauschen ist ebenfalls enthalten. Die Performance, limitiert durch die geringe Verfügbarkeit von raumfahrtqualifizierten Bauteilen, wurde soweit wie möglich ausgereizt. Zusätzlich werden in der Arbeit Strategien präsentiert, um den Messfehler durch Doppelbrechungseffekte der FBG-Sensoren zu minimieren, wobei die Implementierung der vielversprechendsten Strategie genauer aufgezeigt wird.

Die Arbeit schließt mit einer detaillierten Evaluation der erreichten Performance des entwickelten Messsystems ab. Thermaltests von FBG Sensoren, gemessen mit dem entwickelten Messsystem, zeigen das Erreichen der geforderten Messgenauigkeit von ± 1 °C.

Contents

Page

Contents **4**

1 Satellite Based Fiber-Optical Interrogation **7**
1.1 MG-Y based Fiber-Optical Interrogator Module 7
1.2 Outline 7

2 Fiber-Optical Temperature Measurement in Space **10**
2.1 Motivation 10
2.1.1 Drawback of the Current State-of-the-Art Implementation 12
2.1.2 Benefit of the HSB System 14
2.2 Environmental Conditions 14
2.2.1 Orbit Constellation 14
2.2.2 Cosmic Radiation 16
2.2.3 Temperature 33
2.2.4 Shock and Vibration 36
2.3 Hybrid-Sensor-Bus (HSB) Project 38

3 Scanning Laser Based Fiber-Optical Interrogator Module **42**
3.1 Scanning Laser Technologies 42
3.1.1 Semiconductor Tunable Laser 43
3.1.2 Fiber Based Tunable Laser 44
3.1.3 External Cavity Tunable Laser 45
3.2 MG-Y Laser Technology 46
3.2.1 Wavelength Tuning 47
3.2.2 Laser Temperature Dependency 51
3.2.3 Monitoring the Output Wavelength 52
3.3 MG-Y Laser Calibration Procedure 54
3.3.1 Calibration Process Description 55
3.3.2 Calibration Setup 56
3.3.3 Nonlinear Tuning Property 56
3.3.4 Wavelength's Phase Current Dependency 59
3.3.5 Look-Up Table Generation 60
3.3.6 Master Look-Up-Table Generation and Validation 64
3.4 Fiber Bragg Grating Technology 66
3.4.1 FBG Measurement Principle 67
3.4.2 Theoretical Description 69
3.4.3 Model Verification 73
3.4.4 Polarization Effects in FBGs 75

3.4.5 Depolarization Techniques . . . 81
3.4.6 FBG Type Differentiation . . . 87
3.4.7 Fabrication of FBGs . . . 88
3.4.8 Bragg Wavelength Peak Determination . . . 93
3.4.9 Radiation Effects in Optical Fibers and FBG Sensors . . . 101

4 Fiber-Optical Interrogator Design 105
4.1 Requirements . . . 105
4.1.1 Interrogator Module Requirements . . . 106
4.1.2 Fiber-Optical Sensor Requirements . . . 109
4.2 Radiation Analysis . . . 111
4.2.1 Radiation Shielding Approach . . . 112
4.2.2 Detector Location and Modeling . . . 112
4.2.3 Analysis Results . . . 112
4.3 Design Trade-Offs . . . 114
4.3.1 Scanning Laser Trade-Off . . . 115
4.3.2 Polarization Scrambling Technique Selection . . . 116
4.3.3 FBG Writing Technique Selection . . . 117
4.3.4 Peak Find Algorithm Selection . . . 118
4.3.5 Trade-Off Summary . . . 123
4.4 Fiber-Optical Interrogation Module Design . . . 124
4.4.1 Querying Multiple Parallel FBG channels . . . 125
4.4.2 Redundancy Concept . . . 125
4.4.3 Fiber-Optical Sensor Multiplexer . . . 126
4.4.4 Wavelength Referencing System . . . 127

5 Fiber-Optical Interrogator Development 128
5.1 Hardware Architecture . . . 128
5.1.1 Laser Transmitter . . . 128
5.1.2 Receiver . . . 144
5.1.3 Controller Module . . . 149
5.1.4 Optical Front-End . . . 150
5.2 Software Architecture . . . 152
5.2.1 FPGA Requirements . . . 152
5.2.2 Interrogation Cycle . . . 153
5.2.3 FBG Peak Detection . . . 153

6 Fiber-Optical Interrogator Test and Verification 155
6.1 Functional Tests . . . 155
6.1.1 FBG Measurements . . . 155
6.1.2 FBG Thermal Test Results . . . 156
6.1.3 Polarization Induced Measurement Error . . . 161
6.2 Environmental Tests . . . 163
6.2.1 InGaAs Photodetector Displacement Damage Test . . . 164
6.2.2 Fiber-Bragg Grating Total Dose Test . . . 164
6.2.3 Single-Mode Optical Fiber Total Dose Test . . . 167
6.2.4 MG-Y Laser Diode Radiation Test . . . 167
6.3 Measurement Results and Evaluation . . . 170
6.3.1 InGaAs Photodiode Radiation Test Results . . . 171

6.3.2 Fiber-Bragg Grating Radiation Test Results . . . 173
6.3.3 Pure Silica Core Fiber Gamma Radiation Test Results . . . 176
6.3.4 MG-Y Laser Diode . . . 177

7 Summary, Conclusion and Outlook 186
7.1 Assessments . . . 186
7.2 Further Applications and Outlook . . . 189
7.2.1 Qualification of the HSB System . . . 189
7.2.2 Enhancement of Technology Readiness Level . . . 190
7.2.3 In-Orbit Verification Onboard Heinrich-Hertz Satellite . . . 191
7.2.4 Embedding Fiber-Optical Sensors in Spacecraft Panels . . . 192

A Appendix 194
A.1 Acknowledgment . . . 194
A.2 Own Publications . . . 194
A.3 Supervised Student Theses . . . 195

List of Figures 197

List of Tables 207

Acronyms and Abbreviations 209

Bibliography 212

Chapter 1

Satellite Based Fiber-Optical Interrogation

1.1 MG-Y based Fiber-Optical Interrogator Module

The measurement system developed in this work shall replace the electrical, point-to-point wired temperature sensors of telecommunication satellites by fiber-optical based sensors. Due to the increased complexity of such satellite systems and the need for higher number of sensors in future with existing weight limitations, a fiber based solution would be the optimum choice. A more detailed discussion about the advantages of fiber-optical solutions for the target application can be found in section 2.1.

The interrogation technique of the developed measurement system is based on a modulated-grating Y-branch (MGY-) laser diode [3] which can be tuned in wavelength from 1528 nm to 1568 nm [4]. A special calibration procedure is elaborated to allow a wavelength tuning with a spacing of 10 pm. The calibration data of the laser diode is stored in a look-up table which entries are used to control three control currents of the laser diode. A detailed literature inquiry followed by a design trade-off was carried out to find the most promising laser type (described in detail in section 3.1) which fits to the space application limited by the extreme environment. For the MG-Y laser diode a in-deep characterization was carried out to identify the performance aspects and technical limitations.

Due to the fact that the used laser diode emits highly polarized light and that the FBG sensors show wavelength errors due to birefringence of the fiber, special mitigation techniques are discussed.

1.2 Outline

In section 1.1 a brief introduction to the developed fiber optical interrogation module (FIM) is given, a more detailed discussion about the motivation can be found in section 2.1. A short flowchart illustrating the different sections and the main task carried out in these sections is illustrated by figure 1.1.

In section 2.1 the target area for which the interrogator shall be used is presented. The application focus lies in this work in temperature measurements inside a geostationary

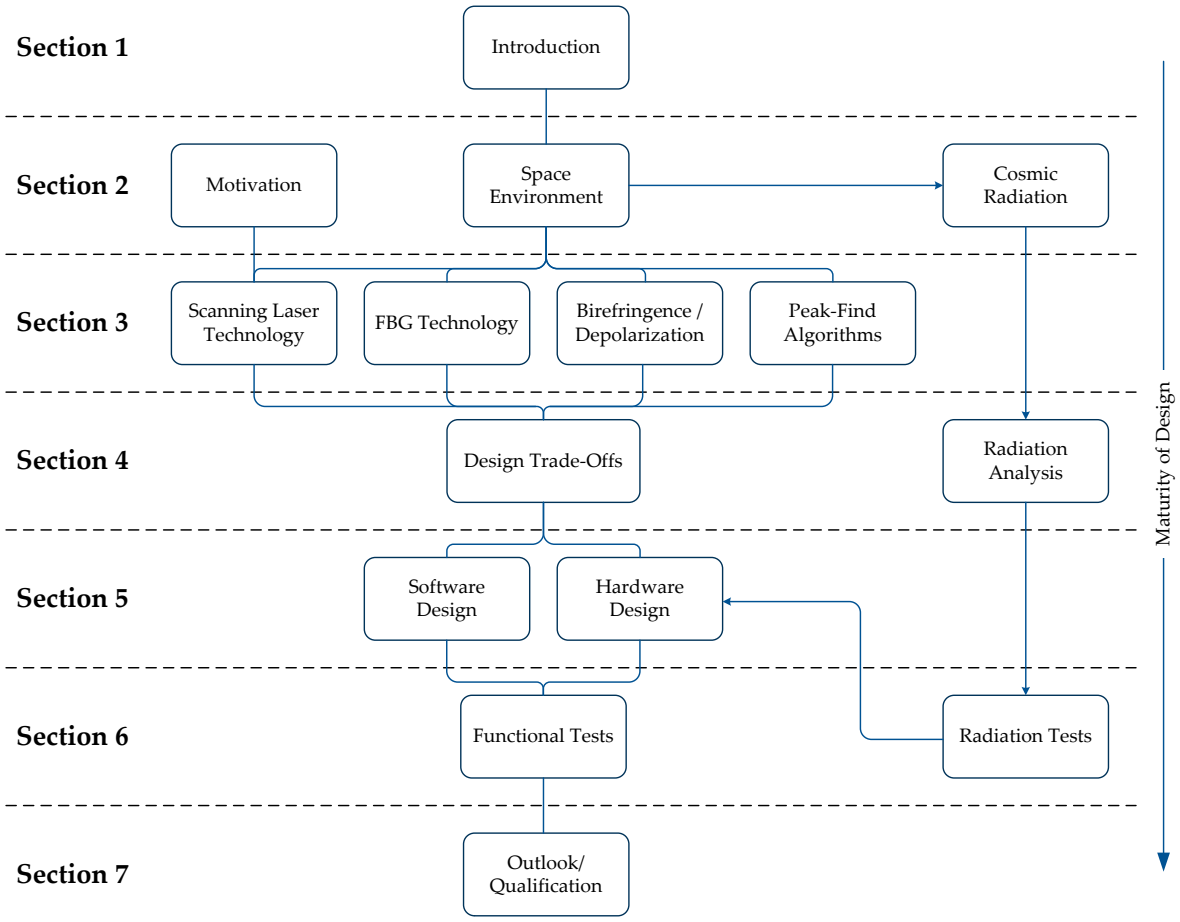

Figure 1.1: *Graphical illustration of the content of the different sections in this work, for details refer to text.*

telecommunication satellite. The drawback of current state-of-the art implementations are addressed and solutions how fiber-optical sensing can improve the current situation are presented. Because the FIM shall be used in space applications, a detailed introduction to satellite orbit constellations and space environment is given in section 2.2. The most challenge area for the developed system is the cosmic radiation to which the satellite and the equipment inside is exposed. Detailed investigation of radiation effects, their sources and shielding possibilities are presented in section 2.2.2.

The theoretical emphasis of the work is presented in chapter 3, including the different possible scanning laser techniques (see section 3.1). Special focus is given to the functional performance, usage and calibration of a MG-Y tunable laser diode (see section 3.2). In addition the fiber Bragg grating (FBG) technology (see section 3.4), and the birefringence effects arising from the usage of a highly polarized light source (see section 3.4.4) are described herein. As last point different peak find algorithms are presented in section 3.4.8 which are necessary to detect the peak wavelength of the FBG in the reflected spectra.

Based on the technical solutions found in chapter 3, a detailed trade-off is carried out to find the most promising candidate architecture for the later implementation. The summary of the trade-off can be found in section 4.3.5. In addition, a detailed set of requirements for the developed fiber-optical interrogator is elaborated, given in section

4.1. For the full system a radiation analysis based on the mechanical model and the orbit parameters is carried out in section 4.2. The results of this analysis are used for component selection and radiation test definition in section 6.2.

The design of the hardware (see section 5.1) and software (see section 5.2) are both given in chapter 5. The hardware development focuses on five low-noise current driver circuits for controlling the laser's output wavelength. Circuit simulations and noise measurements of the final driver circuits are given in section 5.1.1. In addition a temperature controller circuit was designed allowing a tight control of the laser crystal's temperature to ensure wavelength stability.

In chapter 6 the radiation test results of the single components and the functional test results of the complete interrogator module are given. For the radiation test results in section 6.2 special attention is paid to performance impacts due to radiation for the photodetectors (see section 6.3.1), the MG-Y laser diode (see section 6.3.4) and the Fiber Bragg gratings (see section 6.3.2). Resulting design changes due to performance degradation are taken into account in the final design presented in section 5.1. Thermal cycling test results of FBG sensors are presented in section 6.1.2 proving the functional and performance requirements of the developed system.

The presented work closes with section 7, summarizing the achieved goals of this work and giving a short outlook to further activities. Further activities such as the full qualification of the entire system are described short in section 7.2.1 whereas a future implementation, combining fiber-optical sensing and optical data communication, is given in section 7.2.4. Last but not least the flight opportunity of the entire HSB system (see also section 2.3 with the developed fiber-optical interrogator module as flight demonstrator onbord the German telecommunication satellite Heinrich Hertz (H2-Sat) is given in section 7.2.3.

Chapter 2

Fiber-Optical Temperature Measurement in Space

2.1 Motivation

State-of-the-Art satellite sensing systems for housekeeping measurements have complex harness with a high mass impact and are cumbersome in terms of satellite integration [5]. A picture of the satellite harness [6] of Galileo IOV spacecraft is given in figure 2.1 where more than 50% of the cables are used for low bandwidth housekeeping data acquisition. In a telecommunication satellite most of the housekeeping sensors are simple temperature sensors (NTC temperature sensors for low precision and PT100/PT1000 temperature sensors for high precision), which are queried with moderate speeds (< 1 Hz). Flexibility and adaptability of the harness for different missions or later changes in the overall satellite design is not possible. The problems are mainly due to the point-to-point wiring of the used sensors.

Figure 2.1: *Picture of a satellite harness [6]*

The use of sensor buses will result in a flexible system that saves mass and volume and can easily be adapted to different missions or satellite buses. The interrogator unit will have the capability to query multiple channels to enable the highest flexibility of the data acquisition system. The number of sensors does not influence the hardware design of the sensor interrogator as long as the maximum number of sensors per channels is not exceeded. Through a modular setup of the sensing unit, additional modules can be plugged-in to reach the required number of sensors. The combination of the electrical

Inter-IC (I^2C) sensor bus with fiber optic sensing (FOS) allows a further reduction of harness complexity. In figure 2.2 on the left side a state-of-the-art implementation is given where each single sensor is connected to a central interrogator module. For temperature sensors within a telecommunication satellite with 1000 temperature sensors an average wire count of 2.6 wires are assumed according to satellite manufacturer (OHB System Bremen [7]). A modern and new design to overcome these problems is shown on the right side of figure 2.2. Each sensor is connected in a bus-like manner to a central interrogation system where each sensor can be queried by its individual address. The same structure can be implemented for electrical and fiber-optical sensors, where in the latter case the addressing is done by different wavelengths of the single sensors [5].

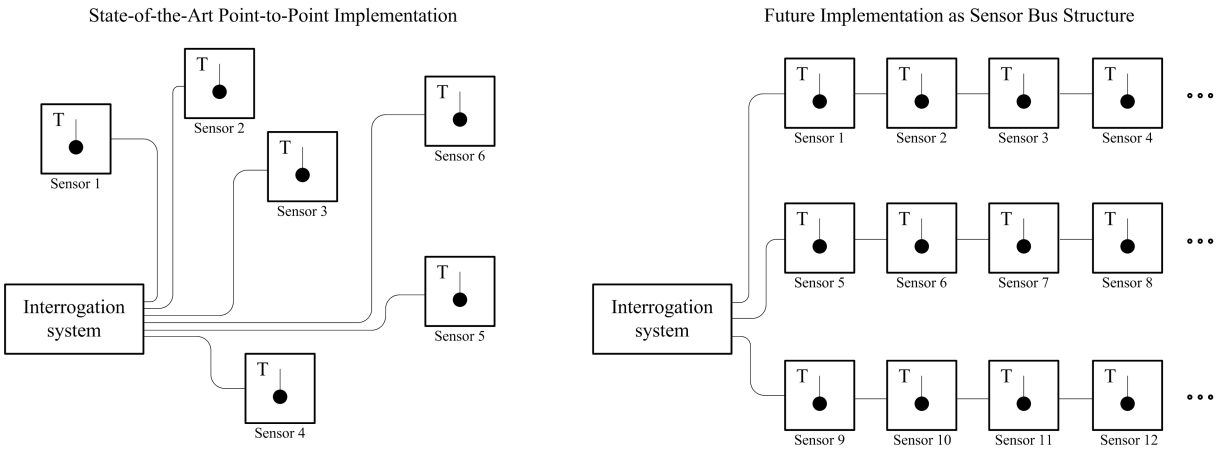

Figure 2.2: *Left: Current "State-of-the-art" sensor implementation for telecommunication satellites of the SGEO series [7] where all sensors are connected point-to-point to a central interrogation unit. Right: Future implementation as a sensor bus structure: The sensors can be electrical or fiber-optical.*

Multiple temperature sensors can be implemented in optical fibers and connected to the fiber-optical interrogator module. The number of sensors is only limited by the maximum reserved wavelength bandwidth of the fiber Bragg grating (see section 3.4.2). The sensor fiber itself is very light and does not influences the mass of the satellite. Another major advantage of optical fibers is the possibility to place the fiber and the sensor inside a satellite panel, as illustrated in figure 2.3. this would decrease the assembly effort in later design stages.

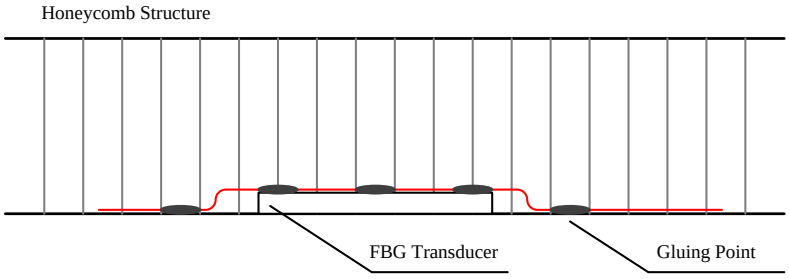

Figure 2.3: *Sketch of an integrated fiber-optical transducer inside a satellite panel.*

2.1.1 Drawback of the Current State-of-the-Art Implementation

In State-of-the-Art (SOA) satellites lots of temperature and other slowly varying signals for housekeeping have to be measured. In modern satellites the number of sensors can reach up to 1000 sensors including redundant sensors and sensors for ground testing which cannot be removed before flight [7]. This high number of sensors increases the harness complexity and weight. In addition the effort for late design changes is very high and costly.

The next paragraphs summarize thematically the drawbacks of the current architecture:

Mass Effect. In a standard telecommunication satellite a temperature measurement point is not measured by only one sensor but with up to four sensors. This is due to the redundancy and reliability requirements. Two sensors are queried sequentially by the main unit. If a sensor fails or shows non-normal values, the redundant unit is switched on and it queries the same measurement point with the two redundant sensors. So, a three-out-of-four weighting is done, for which four sensors are necessary. Assuming a median wire count per sensor of 2.6 wires/sensors, this results in 10.4 wires per sensor position [7]. Depending on the satellite platform, more than 100 such temperature measurement points are foreseen. In addition sensors for ground testing during AIT processes are implemented. Some of them cannot be removed after testing and will fly as dummy mass into orbit.

AIT Effort. The high number of sensors and the related increase in wire count makes the harness integration more complex and increases the assembly effort. Because the harness is the first element which is integrated in a satellite and it is the latest part which is designed (after the electronic boxes are designed/defined), later changes are nearly impossible. Adding a new sensor or changing the sensors position comes along with the partly or complete disassembly of the harness. Also the sensors for ground testing must be assembled and integrated. This adds additional work which is only necessary for testing and not for the operation of the satellite in space.

Low Flexibility. Adding additional sensors is nearly impossible due to the strict harness design and the point-to-point wiring topology. This low flexibility has a negative impact on the satellite design. The flexibility can easily be improved by adding intelligent sensor to the electrical sensor bus. The configuration inside the sensor system presented here is based on configuration lists. Therefore adding sensors or changing conversion factors is very easy and increases the flexibility.

Cost. The major cost driver is the integration effort of the sensor harness in the satellite. For more complex spacecrafts such as satellite science missions the harness and the optical path of the instruments must avoid collisions to work properly. Each time the instrument changes, the harness design must be adopted which increases the costs. In addition the hardware cost are important, arising from the costs of sensors, cable and connectors. Saving sensor wires has a direct impact on cable and connector costs.

Assembly. According to the SGEO reference architecture [7], a sensor harness comprising 340 electrical sensors is assumed. Assuming 50 (25 main plus 25 redundant) sensors at each satellite side-panel this results in a wire count of: 4 panels * 2.6 wires/sensor * 50 sensors/panel = 520 wires and crimp contacts (2.6 wires are the average for a sensor and 4 panels are assumed to be equipped with electronic subsystems). Each wire must be pinned manually in different connectors. If a 37 pin D-SUB connector type has been selected 14 connectors must be used. By using fiber-optical sensors, the sensors could be embedded e.g. in the satellite panels (resulting in a smart panel). Therefore the assembly of single sensors is not applicable. The costs for such smart panel are higher than for a standard panel but they are compensated by reduced assembly costs. In addition due to sensor multiplexing technology for fiber-optical sensing only one fiber is necessary to read out multiple sensors. For the design example here it is assumed that up to 12 optical sensors can be implemented in a single fiber, resulting in 28 fiber-optical sensor strings.

Integration. In sum 520 cables are necessary for standard point-to-point wiring of the sensors for the illustration example SGEO. For a smart panel 28 fibers for fiber-optical sensing are necessary, resulting in a reduction of wire count by more than 90% in comparison to the classical electrical system. Considering the electrical bus topology with a sensor distance of 0.8 m and four wires for the bus itself, a length of (4 wires) * (0.8 m length)*(320 sensors) = 1024 m results. This results in a reduction of the overall length by 50% compared to the SGEO architecture where a mean wire length of 4m is given by the manufacturer. Smaller wire length will reduce the integration effort additionally. The effective integration effort when using sensor bus configurations is assumed to be reduced by a factor of 50%, resulting from the length reduction of 50% and total wire count reduction when fiber-optical sensing is implemented.

EMI/EMC Problems. Because of the nature of electromagnetic radiation, electrical wires are sensitive to EMI effects. This effects is present in both directions: The wires can be sensitive to EMI as for example analog signal lines, or they can be the source of EMI as for example Space-Wire cables. Implementing the necessary wire shielding increases the harness mass additionally.

2.1.2 Benefit of the HSB System

In the first place the HSB system reduces effort and thereby the overall costs during AIT. Compared to standard point-to-point wiring of sensors, the sensor bus will only take approximately 25% of integration time due to the bus like topology and shorter wire lengths. Due to its simple structure, only small number of sensor lines (e.g. one electrical and one optical per panel) are required to equip the panels with temperature sensors. In addition interfaces are reduced and “plug-and-play” manufacturing of satellites can be promoted. First estimations have been performed using data from OHB System AG. The total mass for the sensor system on board the SGEO telecommunication satellite is more than 25 kg [7]. The mass reduction gained by the HSB system has been identified to be approximately 12 kg, which would significantly reduce the overall sensor system mass by a factor of two. The free mass can be allocated to the payload which makes the overall satellite more cost effective.

An additional benefit of the HSB system is the possibility of out-sourcing of the housekeeping functionalities from the satellite management unit (SMU). The SMU will only be triggered by the HSB system if one of the sensor's values lies out of range. So most of the processing power of the SMU is available for higher priority and high speed tasks such as orbit control.

2.2 Environmental Conditions

2.2.1 Orbit Constellation

In this section the definition of a satellite orbit is presented, as well as the defining parameters and types of different orbits to be distinguished [8]. A satellite orbit is in general a circular path around Earth at a certain height, on which the satellite is moving. By placing the satellite with correct initial velocity and direction vector, it keeps the orbit. For some orbits correction maneuvers are necessary, especially for lower Earth orbits due to the presence of remaining atmospheric particles, slowing down the satellite. If the satellite's velocity decreases, the Earth's gravitational field acts on the satellite, pulling it versus atmosphere where it will be destroyed due to the high generated heat by friction.

In figure 2.4, a typical orbit is shown. There are three interesting parameter which describe the orbit. The *Apogee* altitude is the maximum distance between Earth's surface and satellite orbit whereas the *Perigee* altitude is the minimum distance between orbit and surface. The orbit itself is inclined for a certain angle with respect to the Earth's equator (red line in the figure). For a complete circular orbit, the height of the satellite orbit and the inclination are sufficient for orbit description. In this case, the Apogee and the Perigee have the same value.

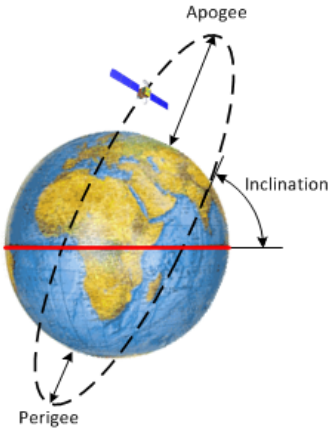

Figure 2.4: *Description of a satellite orbit with Apogee (point of maximum distance), Perigee (point of minimum distance) and inclination with respect to equator.*

The different satellite orbits can be classified into four groups, depending on the distance to Earth and on its shape. The different orbits are summarized in table 2.1. Each orbit configuration has special parameters, depending on the final usage of the satellite. The low Earth orbit (LEO) is used for manned spaceflight (ISS), weather satellites, science missions and military intelligence. The height is quite low and the round-trip time is in the order of some hours. The medium Earth orbit (MEO) has a much increased

height and round-trip time. This orbit is mostly used for navigation satellites such as Galileo, GPS and Glonass. The highly elliptical orbit (HEO) is a special orbit with a high discrepancy in Apogee and Perigee values. The last orbit type is the geostationary orbit (GEO) which has a very large distance to Earth. Satellites following this orbit have a round trip time of 23h 56m and 4.1s and are geosynchronous with the Earth rotation. This means that a satellite in this orbit is always pointing to the same point on Earth's surface. This makes this orbit very attractive for telecommunication satellites but also for new generation of weather satellites. [8], [9]

Parameter	**LEO**	**MEO**	**HEO**	**GEO**
Height [km]	200-1500	6000-12000	-	35786
Apogee [km]	-	-	33000	-
Perigee [km]	-	-	350	-
Inclination [°]	98	55	18	0
Round-Trip Time [h]	1.5-5	5-12	12	24
Usage	ISS, weather satellites	navigation	transfer orbit, science	meteorology, communication
Rad. simulation				
Height [km]	800	20000	33000/350	35786
Inclination [°]	98	55	18	0

Table 2.1: *Summary of satellite orbits with height values, possible inclination and orbit usage. LEO Low Earth Orbit, MEO Medium Earth Orbit, HEO Highly Elliptical Orbit, GEO Geostationary Orbit [8].*

In figure 2.5 the different orbits are illustrated, the difference in distance between the different orbits can clearly be seen. Also the high elliptical orbit (HEO) is shown.

2.2.2 Cosmic Radiation

In this section a detailed explanation of the source of the cosmic radiation is given. Radiation effects are rarely concerned for the development of ground based equipment (excluding devices inside fusion reactors or special medical equipment). When developing equipment for space application, radiation load has a high impact to the overall system design, affecting cost due to the necessary usage of special and highly reliable integrated circuits (IC), and mass due to the required shielding materials.

In addition, equipment which is flying in orbit must be divided into two groups. The first group comprises equipment for small satellites with limited mission duration (< 1 year), In-Orbit-Verification (IOV) equipment in which small parts can be made out of commercial non-radiation hard components and Cube-Sats launched mostly by universities. Basically this group includes equipment with moderate money budget where it is not possible or also not necessary to use highly reliable and costly components. The second group includes equipment flying on satellites which play a major role in defense, Earth observation, weather prediction, telecommunication and science. Basically these satellites and missions are included in the programs of the European (ESA), American (NASA)

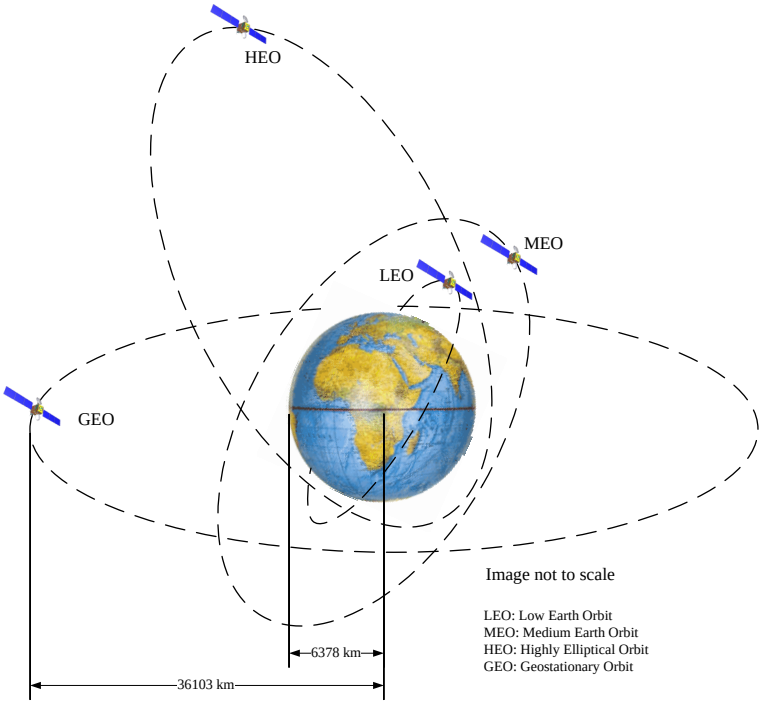

Figure 2.5: *Illustration of different satellite orbits around Earth according data obtained from [8] and [9].*

and Japanese (JAXA) space agencies. In such missions the radiation load is usually much higher than for equipment in the first group [10], the mission life time can be in the range of several years or decades and a mission loss would have a very high impact [11]. Such missions are not limited to orbits around earth, thinking on missions to Mars, Jupiter, or missions to comets such the in 2003 launched Rosetta mission.

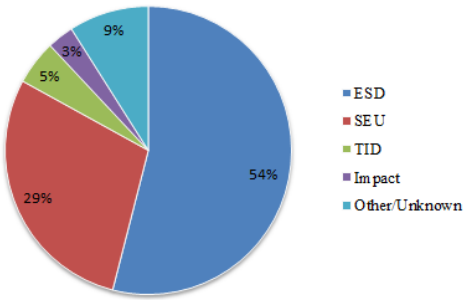

Figure 2.6: *Failures and mission losses due to different error mechanisms such as electrostatic discharge (ESD), single event upsets (SEU), total ionizing dose (TID) and other unknown error mechanisms [12].*

In figure 2.6, a diagram explaining the different error causes which yield to equipment failure or complete mission loss is presented. The failures caused by radiation effects are given by the TID (5%)and SEU (29%) values which have in sum a contribution of 34% to the presented data [12]. Hence a high amount of failures is caused by radiation effects and consequent malfunction of integrated components. Most of the failures could be avoided by carefully selection of components and detailed radiation analysis. For this in the next

sections a detailed introduction to cosmic radiation is given.

In section 2.2 the different orbit constellations have been introduced. The orbit of a satellite highly influences the radiation load seen by the equipment inside the spacecraft. The radiation load of different orbits is also introduced as well as the Earth's radiation belts holding tapered protons and electrons. Two basic radiation effects are introduced affecting both the performance of electronic and optical components but in different ways. At the end the energy spectra and depth dose curves of different orbits are presented.

Earth's Radiation Belts

The main source of charged particles in the atmosphere is the sun, emitting mainly solar electrons with energies in the range from 0.1 MeV up to 7 MeV and solar protons with energies between 0.1 MeV up to 400 MeV. These charged particles interact with the Earth's magnetic field which results to the trapped particle belts [10]. These belts were first discovered by the NASA mission *Explorer-1* and are named after the astrophysicist James Van Allen who developed the scientific measurement instrument on board the satellite [13, 14]. Two radiation belts surrounding the Earth are observed, the inner belt and the outer belt. A sectional view of the Van-Allen-Belts is given in 2.7 for the inner belt (left) and the outer belt (right) respectively.

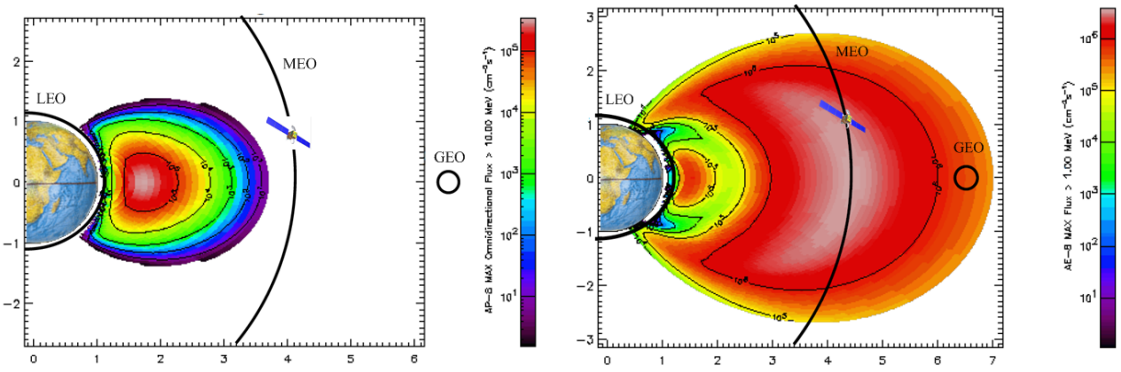

Figure 2.7: *Left: Proton flux forming the inner radiation belt. Right: Electron flux contributing to the inner radiation belt and forming the outer belt [15].*

The inner belt has an extension of approximately 2.5 Earth radii (with respect to the Earth's middle point, Earth radius is 6378 km) and consists out of protons with energies up to 600MeV and electrons up to several MeV. LEO and MEO satellites usually transverse this belt, depending on the altitude of the orbit. The peak intensities are found in the equatorial regions at 2000-3000 km altitude and are different for protons and electrons, as can be seen by figure 2.7. The inner belt has a lower limit of about 1000 km, but near the poles the magnetic field lines are oriented vertical to the Earth's surface resulting in lower altitudes of the inner belt at the pole areas. In the polar region charged particles can penetrate the atmosphere at lower altitudes causing the auroras, also known as *Aurora Borealis* or *Aurora Australis* occurring on the North or South pole respectively. The negative side action of this amazing natural spectacle is the heavily increased radiation load for satellites in a polar orbit. [10]
The outer radiation belt is formed by electrons and soft protons 0.1 MeV up to 5 MeV and has an extension of about 10 Earth radii, depending on the solar activity. MEO and

GEO satellites transverse the outer belt, for GEO electrons are the main contribution of radiation effects. The peak intensity is again found in the equatorial region at altitudes of 1000-20000 km. Near the poles the belt is shaped due to the magnetic field lines, resulting in an increased radiation load in this region. [10]
The Van-Allen-Belts are the reason for different radiation levels seen in various orbits. The total dose can vary from 0.1 krad (Si) per year in LEO up to 1 Mrad (Si) per year at the inner point of the proton belt [10].

Next, a short overview of particles is given which are forming the radiation environment for satellites [16]:

- Trapped solar and galactic electrons: The energies of this particles are in the range from 100 keV up to 7 MeV, forming the outer belt's main radiation. Such particles can be shielded by several mm of aluminum. But shielding with high-Z materials leads to secondary radiation effects like the generation of γ radiation due to Bremsstrahlung [17].

- Trapped solar and galactic protons: The emitted protons from the sun have energies in the range between 1 MeV and 200 MeV, but during solar flares the they reach also energies up to 400 MeV and more. The protons are trapped in the inner radiation belt and are the main contribution to radiation to satellites in low Earth orbits. In general protons have a larger penetration depth (see also figure 2.16), so they can reach components behind several mm of aluminum. Protons have a contribution to ionizing effects due the charged nature of the particles and can cause single event effects (SEE) due to undesired charge impact by hitting electrical components.

- Galactic cosmic rays: This particles are made of highest energy heavy ions and high energetic γ ray pulses. Such particles are generated by supernova explosions and particles accelerated in the near of black holes. This kind of particles causes severe effects in any exposed material, fortunately their flux and density is low. The main effect of this particle are SEEs, causing permanent damage of components [18].

- Gamma radiation and solar UV: The solar spectrum and deep space radiation results in a radiation background in the range from 3 eV upwards for UV and for γ-rays in the range from 124 eV up to 12.4 keV. This particle radiation effects materials such as glass and polymers [19]. Wire isolation materials, thermal painting, optical coatings, optical fibers and isolation foil materials will degrade.

South Atlantic Anomaly (SAA)

The Earth's magnetic field is not a perfect dipole. Anomalies and asymmetries are occurring at certain positions. These asymmetries arise on the one hand from a tilt of 11° between Earth's rotational axis and magnetic dipole axis and on the other hand from a displacement of the geomagnetic axis from the geographical axis by 500 km towards the North Pacific. Because the magnetic field is different on the two sides of Earth, also the Van-Allen belts are different. The inner proton belt dips low above the South Atlantic due to a locally minimized magnetic field, creating a localized increased particle flux. This asymmetry is known as the South Atlantic Anomaly, SAA. This is a high radiation area for LEO satellites, and can be avoided by choosing orbits with inclination lower than 45°.

In figure 2.8, a simulation of a satellite in LEO with an altitude of 500 km is illustrated. On the left side the proton particle flux is given, whereas on the right side the electron particle flux in given. The SAA can be seen in both figures, for the electrons flux on the right also the increase electron radiation near the poles can be observed. [10]

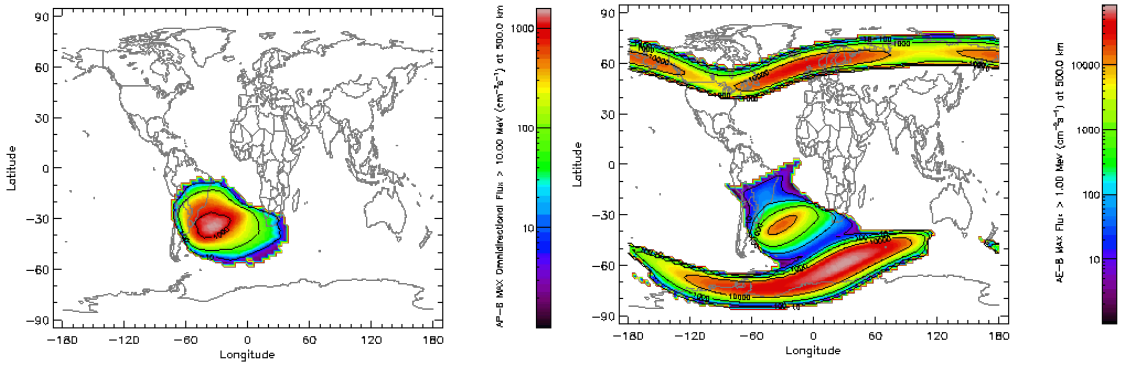

Figure 2.8: *Left: Increased proton flux above the South Atlantic. Right: Increased electron flux above South Atlantic and South- and North-Pole [15].*

Types of Cosmic Radiation and Their Effects

In this section the different types of radiation in a satellite orbit are presented and their impact in performance of different components inside the satellite are discussed. The radiation effects can be distinguished by the effect onto the target material and are divided into two groups.

The displacement damage effects are mainly caused by non-charged particles by damaging the crystal lattice structure due to their high energy. Particle radiation from neutrons, protons and ions causes this damage effect. In addition to the displacement damage the impact of protons and ions causes also ionization effects. This effects counts to the first group, see also figure 2.9 on top left. [20], [11], [21]

The ionization effects count to the second group, illustrated in 2.9 on top right [20]. These effects can be accumulated effects or single event effects causing latch-up of electrical components. The particles involved are charged particles such as protons, electrons and ions but also gamma rays. The impact of protons and ions cause in addition also displacement damage effects. A diagram showing the separation of the effects caused by non-charged and charged particles respectively is given within figure 2.9.

In table 2.2, the resulting radiation effect for different types of particles is shown. Charged particles cause ionization effects in a direct way, but also neutrons can cause these effects in an indirect way by producing secondary fission products in the target material. Also gamma rays show the same effect. This is very important for ground testing, because a 'cheap' Co_{60} source [22] can be used to emulate ionizing effects on component level. Particles with a certain mass (few orders higher than the mass of electrons) cause displacement damage in the lattice structure. The effect can also be observed for electrons and gamma rays, but by applying small shielding thicknesses as it is for example the case for electrical components, the effect can be avoided. [10]

As seen in the previous section the different particles in orbit can cause displacement damage or ionization effects. Depending on the target material and its functionality the component can be susceptible to DD effects, TID effects or both. Table 2.3 summarizes

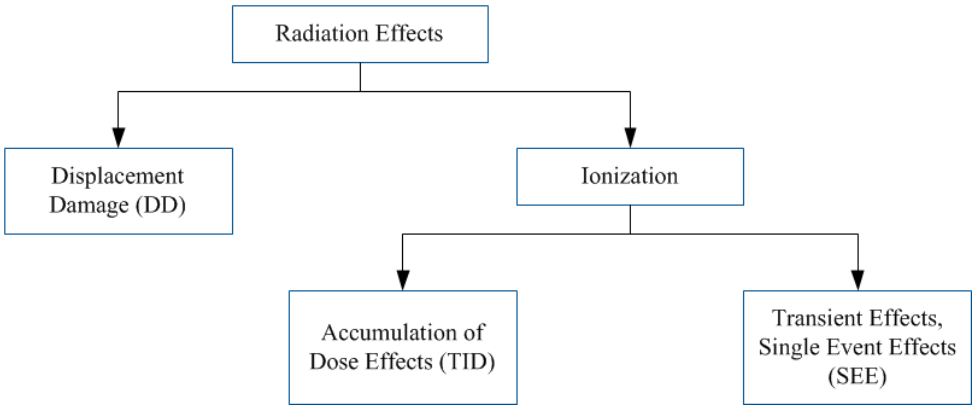

Figure 2.9: *Radiation effects distinguished by the involved particles where displacement damage effects and ionization effects are caused by non-charged or charged particles, respectively. Diagram derived from data in [20].*

Type of Radiation	**Ionization Effect**	**Displacement Damage**
Gamma, γ	indirect	seldom
Electron, e^-	direct	seldom
Neutron, n^0	indirect	yes
Proton, p^+	direct	yes
Heavy Ions	direct	yes

Table 2.2: *Ionization and displacement damage effects for different particles [10].*

the sensitivity effects for different components and technologies. This table is important for selecting the correct ground testing method for a certain component. For a laser diode for example the effect of displacement damage (TNID) is more important than the ionization effect which has a minor contribution.

Total Ionizing Dose (TID) For materials in which in general the electrons occupy most of the atomic volume, a small amount of energy is transferred to an electron by an incoming particle. In a semiconductor material, an electron is raised from the valence band to the conduction band. Therefore ionizing generates an electron-hole pair (EHP) which is able to travel through the device and or be deposited at certain locations in the device causing changes in performance [11]. The generation of an EHP is illustrated in figure 2.10. When an EHP is generated by a photon, the minimum energy must be larger or equal to the bandgap energy of the target material. If the target material is instead hit by a high energy particle, as it is the case during space missions, the determination of the minimum energy is not as easy as for photons. The high energy particle generates a shower of secondary electrons with different energies and a mean path length which overlaps at several lattice positions. The table within figure 2.10 indicates the minimum energy of a particle to generate an EHP caused by a high energy particle. [11]

The total ionizing dose (TID) is defined as the amount of radiation (energy) absorbed by the device with respect to the target material which absorbs the radiation [23].

$$D = \frac{\Delta E}{\Delta m} = \frac{\Delta E}{\rho \cdot A \cdot \Delta x} \tag{2.1}$$

Component	Technology	Effect
Integrated Circuits	Power MOS	TID, SEGR, SEB
	CMOS	TID, SEE
	Bipolar	TNID, SEU, SET, TID
	BiCMOS	TID, TNID, SEE
	SOI	TID, SEL (no SEL)
Optoelectronic	MEMS	TID
	CCD	TNID,TID,SEE
	CMOS APS	TNID, TID, SEE
	Photodiodes	TNID, TID, SET
	LEDs	TNID
	Lasers	TNID
	Opto-Coupler	TNID, SET
	InSb, (In)GaAs, HgCdTe, GaAlAs	TNID
Solar Cells	Cover Glass/Bounding	TID
	Cell	TNID
Non-optical Material	Crystal Oscillator	TID
	Polymers	TID (radiolysis)
Optical Materials	Silica Glass	TID
	Alkali Halides	TID, TNID

Table 2.3: *Overview of damage effects for integrated circuits and opto-electronic devices according [20].*

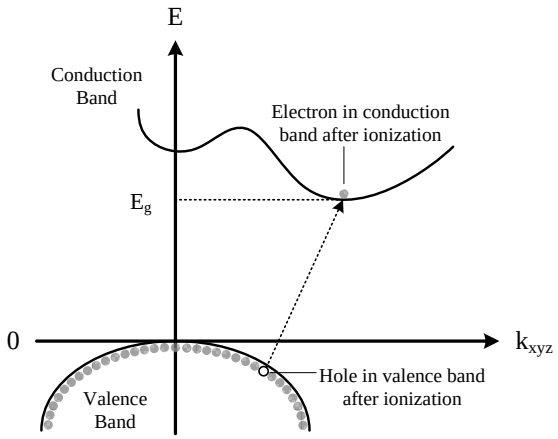

Material	Bandgap Energy E_G(eV)	Electron-Hole-Pair Threshold Energy
Si	1.12	3.6
InP	1.35	4.5
GaAs	1.43	4.7
SiC	2.86	8.5
SiO_2	9.1	18

Figure 2.10: *Left: Conduction and valence band of a semiconductor with up-lifting of an electron from the valence band into the conductive band due to radiation. Right: Bandgap energy and necessary threshold energy for EHP generation for different semiconductor materials [11].*

where ΔE is the mean energy imparted by ionizing radiation, Δm is the unit mass, ρ is the density of the material, A is the area of the target material and Δx is the thickness.

The dose (D) is measured either in rad (radiation absorbed dose) or in Gray (Gy) which is the correct SI unit derived from J/kg. (1 Gy = 100 rad = 1 J/kg). As mentioned before, the dose depends on the target material. For common materials the conversion factor is given to: 1 rad (Si) = 0.58 rad (SiO_2) = 0.94 rad (GaAs) [21].

TID has its origin mainly in γ-radiation or Bremsstrahlung from electrons and ions stopped in the material. TID can lead to charging of isolation materials (polymers and ceramic) and also of metal-oxide structures in electronic devices. For optical materials the TID effects play the major role. Due to the generation of EHPs in the optical material so called *Color-centers* (also called 'Farbzentren' from the German word Farbe/Color) are generated. These color centers are responsible for the increase in attenuation during radiation exposure of optical materials such as lenses and optical fibers.

In space missions TID effects are caused by electrons for missions in GEO due to the outer radiation belt but also by protons for missions in lower orbits (LEO, MEO) due to the transit of the inner radiation belt. The impact of protons has two effects, first the proton deposit charge in the target material (total dose effect) and in the second stage the proton causes damage on the lattice structure of the target material (displacement damage).

Bremsstrahlung The so called Bremsstrahlung is an electromagnetic radiation which is generated by decelerating a charged particle when deflected by an atomic nucleus or a shielding structure. The traveling particle loses kinetic energy, which is converted into a photon satisfying the law of energy conservation. The generation of Bremsstrahlung for particles with energies lower than a few MeV is negligible, but becomes very important if the ion/particle reaches energies higher than 600 MeV/Z (rule of thumb, Z denotes the atomic nuclei charge number).
Stopping of electrons is mainly done by the generation secondary X-ray or gamma radiation. The energy loss due to Bremsstrahlung generation is given to [23]:

$$I_{Brems-rad} \sim \frac{z^2 \cdot e^4 \cdot Z^2}{(4\pi\epsilon_0)^2 \cdot m_{Par}^2} \cdot \frac{1}{r^4} \tag{2.2}$$

where z is the atomic number of the particle, Z is the atomic number of the target (shielding) material, e is the elementary charge, ϵ_0 is the dielectric constant, m_{Par} is the mass of the incident particle and r is the radius of the first and lowest energy shell of the hydrogen atom.

The ratio in masses between a proton and an electron is nearly 2000:1, therefore the generated Bremsstrahlung for an electron is by a factor of 10^6 higher. In addition, the amount of generated radiation depends on the used shielding material. If electrons will be shielded with high-Z materials a very high amount of Bremsstrahlung will be generated. A higher dose by the shielding material would be the effect. The generation of Bremsstrahlung σ_{Br} is proportional to the ratio of the atomic number of the target (shielding) material (Z) and the mass of the incident particle m_{Par}:

$$\sigma_{Br} \sim \frac{Z^2}{m_{Par}^2} \tag{2.3}$$

It can be seen that the efficiency of generating Bremsstrahlug is higher for particles with small mass such as electrons incident on high-Z shielding materials. [23], [21]

Displacement Damage (DD/TNID) In contrast to the previous presented ionizing effects, displacement damages are referred to crystal damages introduced by high energy non-charged particles. Due to the high energy of the incident particles, the atoms in the crystal structure are displaced, creating lattice vacancies and interstitial atoms. This is illustrated in figure 2.11 on the left hand side [11].

For particles with low energy simply Frenkel pairs (vacancy and interstitial atoms) are produced. The generation of Frenkel pairs is a normal process which takes place in most of crystal types under room temperature conditions, the generation of vacancy atoms and the fill-up of interstitial atom positions are balanced. When the target material is hit by a high energy particle (>1 keV), also Frenkel pairs are generated but also create cascaded regions where many displaced atoms are located [24]. The energy imparted by the incident particle to the displacement atom in excess of that required to displace it from the lattice structure goes into kinetic energy. Frequently the displaced atom has sufficient energy to generated a cascaded damage structure as shown in figure 2.11 on the right [24].

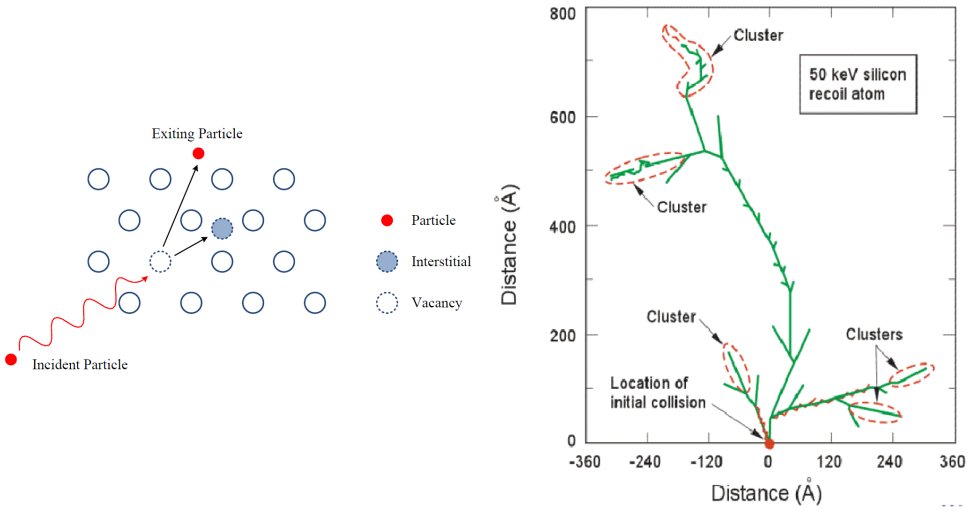

Figure 2.11: *Left: Generation of a single Frenkel pair (vacant and interstitial lattice element) by an incident high energy particle. Right: Monte Carlo simulation of a cascaded damage structure in silicon (Si) [24].*

The necessary threshold energy which is the minimum energy that must be absorbed by the lattice atom to be removed from the initial position is related to the crystal binding energy. The energy is correlated with the inverse of the lattice spacing of the crystal. As higher the threshold energy is, as more resistant to displacement damage the material is. In table 2.4 are some displacement threshold energies for several semiconductor material given. [11]

As discussed before, the displacement damage effects have the origin in the impact of non-charged particles. The idea is now to summarize these non-ionizing processes and to assume that a displacement damage dose (as it is also the case for the total ionizing dose, TID) is deposited in the material. The idea behind the NIEL (non-ionizing energy loss) hypothesis is to test the target material with only few different particle energies and interpolate the damage effect to the full spectrum. So any particle fluence can be reduced to an equivalent 1 MeV or 10 MeV particle fluence which produces the same bulk damage [25]. For component testing neutrons are often used due to the lower price for test facilities and testing time. To calculate the necessary neutrons to see the same damage,

Material	Displacement Energy Threshold [eV]
InAs	7.4
InP	7.8
GaAs	9.5
Si	12.9
Ge	14.5
GaN	19.5
4H-SiC	21.3

Table 2.4: *Displacement threshold energy for different semiconductor materials [11].*

this simple formula applies [26]:

$$G = \frac{\text{NIEL(10MeVn)}}{\text{NIEL(TargetMeVx)}} \tag{2.4}$$

where *NIEL(10MeVn)* is the energy loss for a 10MeV neutron used in the test facility and *NIEL(Target MeVx)* is the energy loss for the expected particle and energy. The number of test particles must be simply multiplied by this factor. The NIEL values for common materials are given in figure 2.12, on top for Si and on bottom for GaAs as target material, respectively. [27]

In figure 2.12 it can also be seen that the non-ionizing displacement damage reaches the highest values for protons with low energy. As lower the energy of the protons is as more time for interactions with the crystal lattice structure they have. Fortunately most of the low energy protons are shielded by the metallic housing and also by plastic materials containing a high amount of hydrogen both acting as low-Z shielding materials. For silicon it can be seen in addition that neutrons or protons with energies higher than approximately 10MeV result in the same NIEL value.

Linear Energy Transfer (LET) While charged particles are traveling through materia they lose their energy by impacts with the valence and core electrons of the atomic shells of the target (shielding) material. The deposited energy of the traveling protons, electrons or heavy ions is a function of the kinetic energy. The energy (E) lost per distance (dx) is called Linear Energy Transfer or LET. The LET follows the Bethe-Bloch formula [28]:

$$LET = -\frac{1}{\rho_{Target}} \cdot \left.\frac{dE}{dx}\right|_{Loss} \tag{2.5}$$

$$LET = 2\pi \cdot N_A \cdot r_e^2 \cdot m_e \cdot c^2 \cdot \frac{Z_{Tar} \cdot Z_{Par}^2}{A \cdot \beta^2} \cdot \left[\ln\left(\frac{2m_e \cdot \gamma^2 \cdot v^2 \cdot W_{max}}{I^2}\right)\right] - 2\beta^2 - \delta - 2\frac{C}{Z_{Tar}} \tag{2.6}$$

Where r_e is the radius of electrons, m_e is the electron mass in eV, N_A is the Avogadro constant, I is mean activation/ionization potential of the target atom, A is the atomic mass number of the target atom, Z_{Tar} is the charge number of the target nucleus, Z_{Par} is the charge number of the impacting heavy ion, proton or electron, $\beta = v/c$, $\gamma = 1/\sqrt{1-\beta^2}$, ρ is the density correction factor, C is the atomic shell correction factor, W_{max} is the

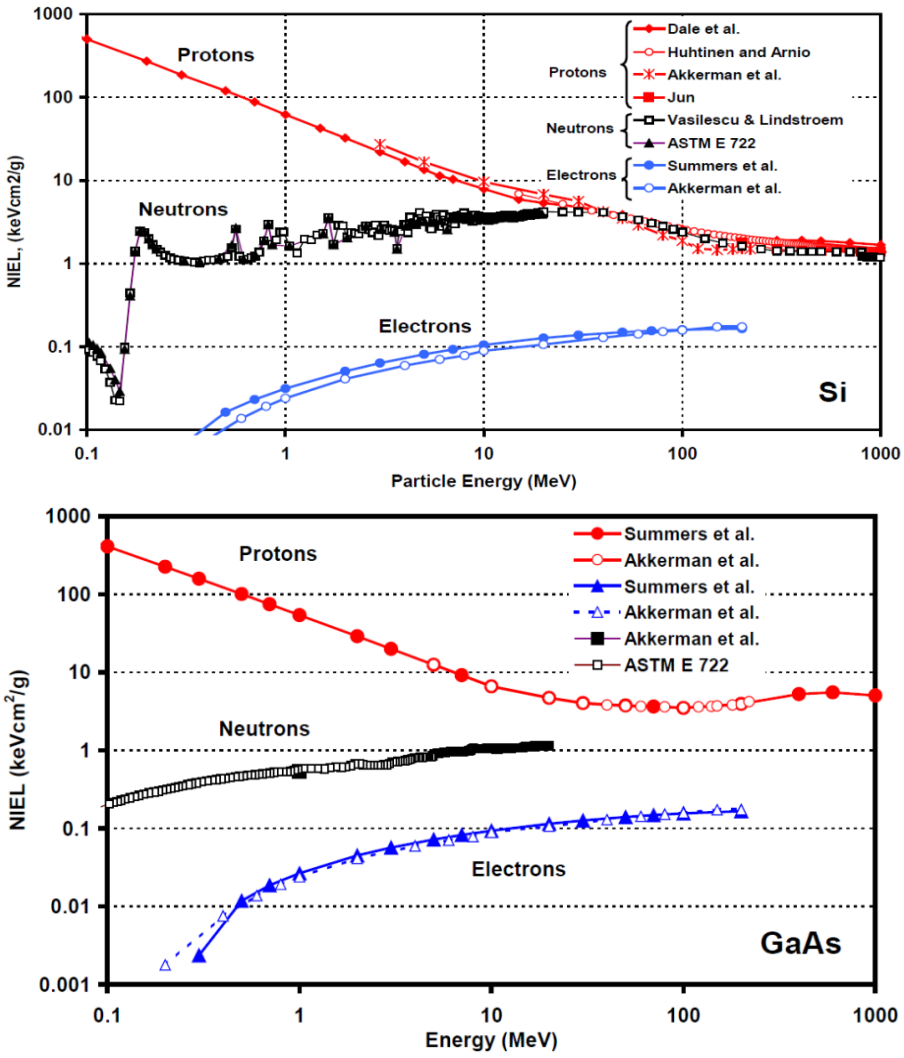

Figure 2.12: *Top: NIEL energy loss for protons, neutrons and electrons for Si as target material, bottom: NIEL energy values for GaAs as target material. [27]*

maximum energy transfer per single interaction, $W_{max} \approx 2m_e c^2 \beta\gamma$ for $M \gg m_e$. Details concerning equation 2.6 can be found in [28].

The most important information are summarized below:

- The linear energy transfer (LET) (energy loss) is proportional to the square of the atomic charge of the particle Z_{Par}.
- Particles with higher atomic charge have a shorter range into the target material and are stopped earlier.
- The LET is nearly independent of the particle mass due to the fact that $Z/A = (^{12}C) \approx 0.5$ and for $Z/A = (^{208}Pb) \approx 0.4$, where A is the atomic mass number and Z is the atomic number of the target atom.

The LET spectra are simulated with the SPENVIS software taking into account the dedicated orbit parameters and satellite lifetime. In addition for all simulations in the next section an equivalent shielding thickness of 2 mm was used. The results are depicted in figure 2.13.

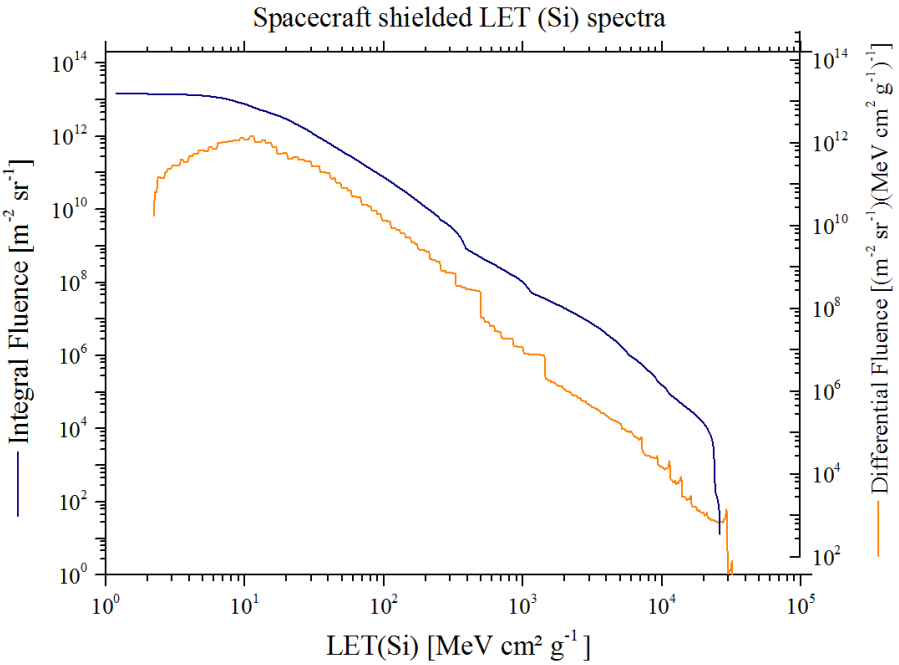

Figure 2.13: *LET diagram derived by simulation for a spacecraft shielding thickness of 2mm for a mission in the geostationary orbit. [15]*

Single Event Effects (SEE) Single-Event effects (SEE) are mainly caused by charged particles and are the major concern in active electronic devices. As the name implies, a single particle can result in a malfunction or complete destruction of a component. SEE are the result of a charge impact given by an incident particle to semiconductor structures which can cause additional charges in unwanted regions or additional unwanted current paths. A good example is a CMOS structure in which two FETs, one with positive polarity and the other with negative polarity, are implemented. In the nominal condition only one path is carrying current, but if a SEE occurs, both FETs are in its on-state, a high short circuit current which destroys the device is the consequence. [21], [11], [23].

SEE are divided in two groups, the first group indicates errors resulting in a complete failure of the part, so called *hard-errors*, the second group combines only temporary effects and errors, so called *soft-errors*. In addition the results of the SEE can be distinguished:

- Single Event Latchup (SEL): This error occurs when parasitic FETs or thyristors are triggered, generating a high current path from the supply voltage rail to ground. The component can be destroyed if this over-current condition is not detected immediately. By switching the device off and on (so called power cycling), the error can be cleared depending on the duration of the SEL event and the maximum current. In addition this effect is temperature dependent, devices are more sensitive to SEL at higher temperatures [29].

- Single Event Burnout (SEB): This is an non-reversible destructive effect which occurs in the drain-source path of power MOSFETs by triggering a parasitic NPN transistor.

- Single Event Gate Rupture (SEGR): This effect occurs also in power MOSFETs and destroys the gate oxide leading to malfunction of the component.

- Single Event Upset (SEU): This effect describes unwanted changes in memories and digital circuits by bit-flips. This effect is a non-destructive effect but can cause corrupt data, program crashes and functional interrupts. By adequate design of the digital electronic and by implementing triple modular redundancy (TMR) and voting mechanisms, SEUs can be detected and mitigated. SEU can also be seen in commercial components at sea level due to radioactive impurities leading to alpha radiation. [11]
- Single Event Transient (SET): This is a transient, normally non-destructive effect which can be seen at the output active electronic devices. By adequate low pass filtering, this effect can be reduced. The duration is in the order of pico-seconds given by the traveling time of the particle through the device and the internal recovery.

Energy Spectra

As shown in section 2.2.1 for different mission types dedicated orbits are preferred. Depending on the selected orbit and mission time the satellite and the components herein are exposed to different amount of radiation. This includes different energy spectra but also different particle types. If a satellite is mainly located in LEO, only the inner Van-Allen-Belt must be crossed, so mainly protons are liable for the radiation effects. On the other hand if the satellite is located in the GEO, most of the radiation is generated by trapped electrons in the outer Van-Allen-Belt [8] [23]. In figure 2.14, both Van-Allen-Belts and different satellite orbits are illustrated. The red areas indicate the maximum particle density of the radiation belts.

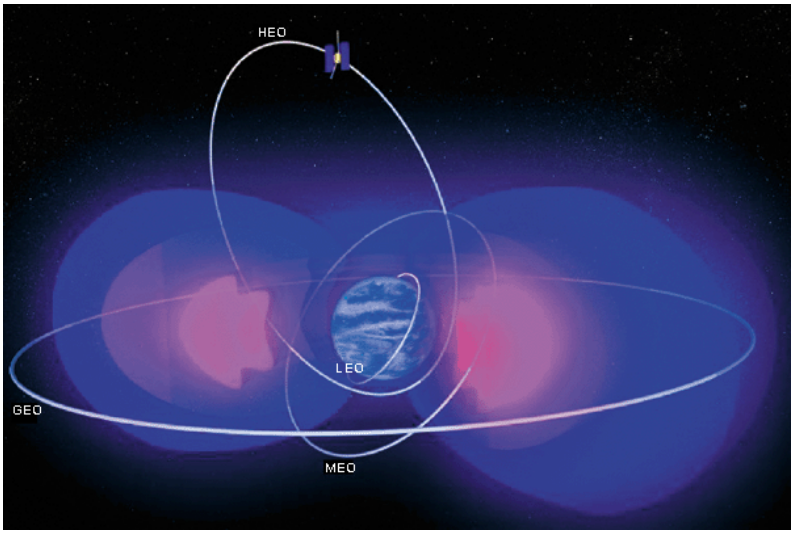

Figure 2.14: *Different orbit constellations crossing the Van-Allen-Belts (not to scale). (Illustration by B. Jones, P. Fuqua, J. Barrie, The Aerospace Corporation).*

The energy spectra for different mission scenarios, as indicated by table 2.1 are simulated by a free radiation simulation tool called SPENVIS [30]. By inserting the orbital parameters the differential flux for electrons and protons can be simulated. The results are given within figure 2.15 on the left side for protons and on the right side for electrons respectively.

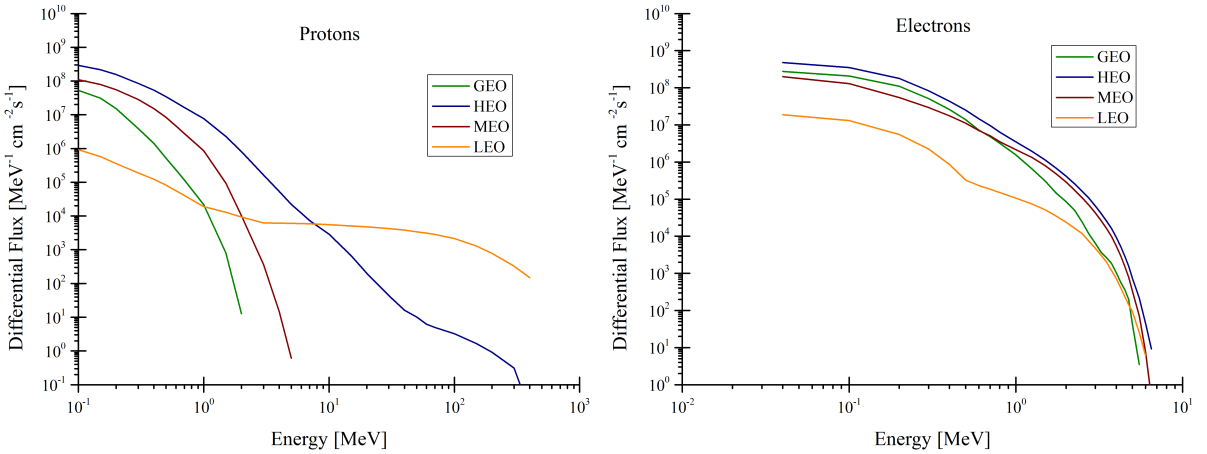

Figure 2.15: *Differential flux for protons (left) and electrons (right) for different satellite orbits [15].*

Proton Spectrum For the proton spectrum it can be seen that for a satellite in the LEO and HEO also high energetic protons are present. The differential flux can be further enhanced when the satellite transverses the South-Atlantic Anomaly (SAA) where additional high energetic protons are trapped [10]. The HEO orbit crosses also the inner radiation belt (refer to figure 2.14) and leads to an increase in differential proton flux. For the MEO and GEO orbit protons are from minor concern also because low energetic protons can be shielded easier than high energetic particles. This can be seen in the diagram in figure 2.16, showing the mean range of protons and electrons in aluminum.

Electron Spectrum The electron spectrum shows higher differential flux for satellites in the GEO, MEO and HEO orbit. As seen before, the outer radiation belt consists mostly out of trapped electrons and satellites orbiting Earth at far distances cross the outer belt. For the LEO the differential flux of electrons is orders of magnitudes lower than for high altitude orbits.

Cosmic Radiation Shielding

To protect the electronic and optical components against cosmic radiation, a shielding material surrounding the equipment with a certain thickness has to be implemented. Incident particles such as protons and heavy ions loose energy by collisions with the atoms within the shielding material, whereas electrons are stopped or slowed down by the generation of Bremsstrahlung (X-rays).

The range of protons and electrons in aluminum as function of their energy is given in figure 2.16. Here an example for a shielding thickness of 2 mm of aluminum is given. Protons and electrons with energies higher than 20 MeV or 1 MeV respectively can pass the shielding material. By taking into account the differential flux spectra given in figure 2.15 it can be estimated if the thickness is sufficient or if particles with high damage effect are still reaching the component.

From the engineering point of view, one of the most important information is the expected radiation behind a certain shielding thickness. These graphs can be simulated also with the SPENVIS software [30], resulting in the mission specific 10 MeV proton fluence and in the total ionizing dose (TID) respectively. The plots for different orbits are

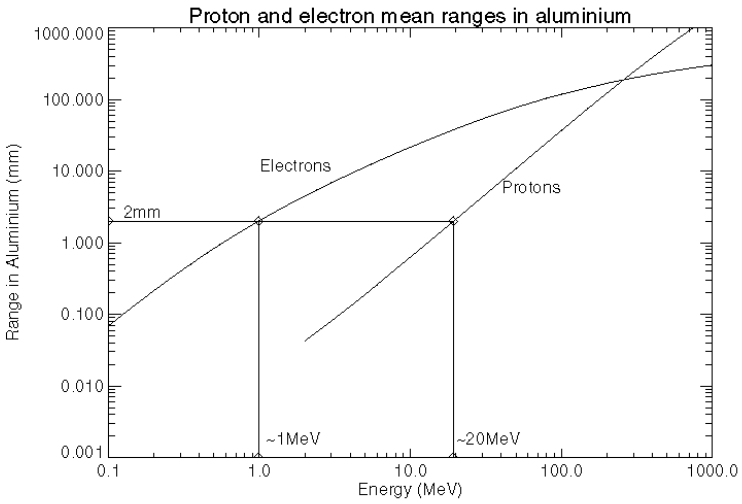

Figure 2.16: *Mean range of protons and electrons in aluminum according to [31].*

given in figure 2.17. As seen before the protons cause displacement damage in the crystal lattice structure in addition to ionizing effects. With the plot in figure 2.17 on the left the total number of 10 MeV protons behind the shielding can be calculated. Depending on this number the number of target elements for component testing is selected. According to the NIEL hypothesis and under the assumption that silicon (Si) is the target material an equivalent displacement damage effect will be seen independently if protons or neutrons are used for testing (see also figure 2.12). It can also be seen that for orbits crossing the inner radiation belt (HEO, MEO) the proton fluence increases dramatically with respect to satellites in GEO.

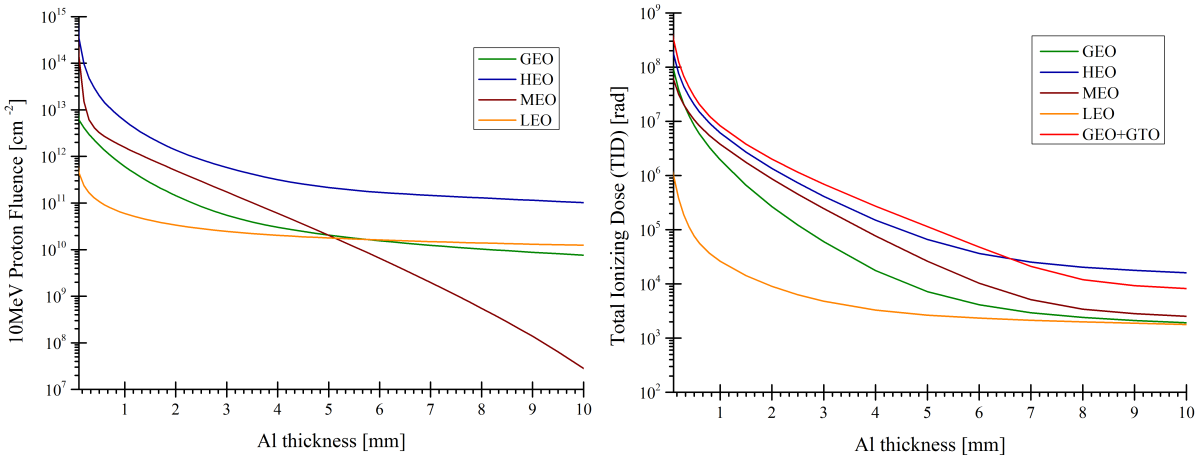

Figure 2.17: *Proton fluence (left) and total ionizing dose (TID, right) as function of aluminum shielding thickness for different orbits.*

On the right side of figure 2.17, the total ionizing dose as function for the shielding thickness for different orbits is given. In general the TID value is a good starting point for space component selection. Many manufacturers of space components offer devices with guaranteed operation up to 100 krad or 300 krad. This is one of the limitations when designing electronics for space applications, the shielding must be adjusted to meet the radiation requirements for the specific mission. As can be seen, the TID value is

quite low for satellites in LEO, but increases dramatically for the other orbits. A special case is plotted in figure 2.17 by the red curve. This curve shows the result for a GEO mission with a mission time of 15 years including the time for GEO transfer orbit (GTO). Bringing the satellite into the geostationary orbit by the use of the GTO, less powerful rockets can be used. The satellite itself is able to reach the GEO by an implemented, so called 'Apogee-motor' [8]. But for this the satellite transverses the inner radiation belt several times, resulting in a increase of ionizing effects due to the impact of trapped protons. So the overall dose is enhanced strongly as can be seen by the red curve.

Dose Depth Curve as Function of Atomic Number

The effectiveness of shielding material is heavily depending on the incident particle type and the atomic charge number (Z) of the shielding material. In figure 2.18 a simulation of the dose-depth characteristic is carried out with *SPENVIS* for aluminum with a charge number of 13 and for Tantalum with a charge number of 73 respectively. On the left of figure 2.18 the TID for incident protons as a function of shield mass thickness is shown whereas the TID for electrons is shown on the right.

It can be seen that for proton shielding a low-Z material is more effective than a high-Z material. The effectiveness increases with smaller atomic charge number (Z). So also materials containing lots of hydrogen bonds such as the printed circuit board have a contribution for shielding against protons. The effectiveness of the shielding against protons is proportional to $\frac{Z}{A}$, where Z is the charge number and A is the atomic mass number.
For electrons the opposite behavior is observed as shown in figure 2.18 on the right. Here the high-Z element (Tantalum in the recent case here) is more effective than a lower-Z material. For electrons the effectiveness is proportional to $\frac{Z^2}{A}$, where Z is the charge number and A is the atomic mass number. [23]

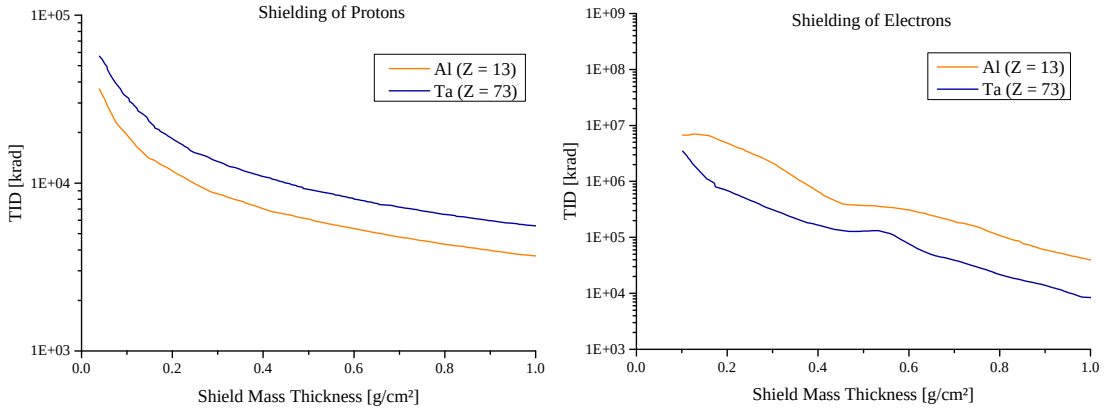

Figure 2.18: *Left: Dose-depth curve for proton shielding for Aluminum (low-Z) and Tantalum (high-Z) acting as shielding material. Right: Dose-depth curve for electron shielding for same materials. [15]*

Multi-Layer Shielding

As seen in section 2.2.2, the TID behind a shielding material strongly depends on the nature of the incident particles and the atomic charge number (Z) of the shielding material. Protons are stopped more efficient with low-Z materials such as Aluminum or

FR4 (PCB material) whereas electrons are stopped more efficiently with high-Z materials. So one could think about using a simple combination made out of low-Z material and high-Z material to implement a practicable radiation shielding. But considering the generation of Bremsstrahlung which efficiency is given to $\sigma_{Br} \sim Z^2/m^2_{Par}$ (see section 2.2.2) a high amount of Bremsstrahlung is generated when slowing down electrons within high-Z materials. So it is essential to implement another layer of low-Z behind the high-Z layer to avoid an enhancement of TID due to inappropriate shielding. In common cases the second shielding can be very small and is often given by the integrated chip (IC) housing itself. But it should be noted, that a detailed radiation analysis shall be carried out when multi-layer shielding structures are used to avoid a worsening of the shielding performance.

A common shielding structure based on a low-Z/high-Z/low-Z configuration is shown in figure 2.19. Within this picture also the stopping of protons and electrons is shown, it can be seen that protons are stopped in the first low-Z layer whereas electrons are slowed down in the high-Z layer by the generation of Bremsstrahlung. The generated Bremsstrahlung is shielded by another low-Z layer behind the high-Z layer. It is notable that for the efficiency of shielding the high-Z layer can be very small in the range of 50µm.

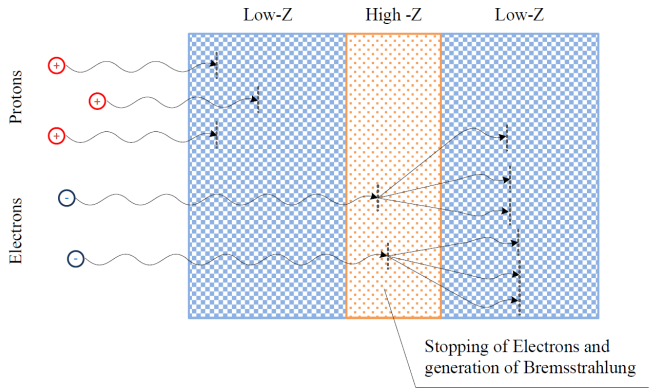

Figure 2.19: *Multi-layer shielding structure with Low-Z/High-Z/Low-Z configuration with illustrated stopping of incident particles.*

2.2.3 Temperature

Special consideration has to be given to temperature distribution within the satellite. Once the satellite is in orbit, thermal radiation is the only possible heat transport due to missing gravity causing absence of convection and missing atmosphere. The rate of heat flux from surface 1 to surface 2 follows the Stefan-Boltzmann law [32, 33]:

$$\dot{Q}_{1\to 2} = \frac{\delta Q}{\delta t} = \epsilon \cdot \sigma \cdot A \cdot (T_1 - T_2)^4 \tag{2.7}$$

where ϵ is the emissivity of the surface, σ is the Stefan-Boltzmann constant ($5.67 \cdot 10^{-8}\mathrm{W/m^2 \cdot K^4}$), A is the surface area and T_1 is the temperature of the surface 1 from which the heat is transported to surface 2 with temperature T_2. As can be seen the heat transport is directly proportional to the surface and emissivity, so for best radiated heat performance the emissivity should be high (>0.9) which is in general the case for most of black paintings.

For a space system design the thermal design inside the satellite and subsystem units is very important. For the entire satellite a complex thermal management system is implemented including loop-heat pipes (LHP), radiators, heaters and even highly specialized cooling compressors. More details to entire satellite thermal management can be found in [9]. Here at this point the interest is focused to the subsystem thermal design.

Concerning the herein designed interrogation system, a detailed analysis of the thermal management of each subsystem must be made. The system builds up mainly on electronic and opto-electronic components, for later ones only the active parts are interesting for thermal management. The process to get the thermal management system designed is as following:

- Taking into account the circuit drawings for each board, the components generating the most heat can be identified. This can be done by simple manual computation and analysis or for more complex circuit design with computer based SPICE simulation tools.
- In general the components acting as heat sources are: Linear voltage regulators, transistors in current sources, FPGAs, processors, diodes in power rails, switching regulators with included switch element, etc.
- By taking into consideration the simulation results, the amount of generated heat in Watts is known and can be allocated to the single circuit boards. It is very important in this stage that the generated heat is allocated to different areas of the PCB, even when the layout process is not started already, and not to a single point on the board.
- In the layout a lateral area, acting as heat sink of the PCB, shall be defined. This is normally the area closest to the mounting interface surface. Surface mounted components such as regulators or switching power controllers shall be located in this area. Transistors in metal housing configuration shall be directly screwed without intermediate PCB to the area with the most heat sinking capability.
- When defining the layer stack-up of the PCB, the heat transfer capability of the copper in the inner layer has to be considered. By increasing the number of layers and the thickness of the copper area the heat transport can be enhanced.
- With the final placement of the components and the power loss for each component is defined, a detailed thermal simulation shall be carried out. The simulation computes the heat distribution of the subsystem for minimum and maximum operational environmental temperatures. These results can be taken for optimization of the thermal concept. It is very important that for the simulation the conducted heat transport over convection is deactivated (outer space with no atmosphere and gravity) and the radiated emission is activated.

The temperatures for the herein designed interrogation system are given in table 2.5 [7]. The values are important for the definition of the environmental tests of the system, carried out in a later phase.

Req. No.	Requirement	Value
TMP1	Minimum operational temperature	-20°C
TMP2	Maximum operational temperature	+65°C

Req. No.	Requirement	Value
TMP3	Minimum start-up temperature	-35°C
TMP4	Maximum start-up temperature	+65°C
TMP5	Minimum non-operational temperature	-40°C
TMP6	Maximum non-operational temperature	+70°C

Table 2.5: *Temperature requirements for the interrogation system.*

2.2.4 Shock and Vibration

The shock and vibration loads during satellite launch are the hardest stringent conditions for the satellite and the subsystems. For ground based systems these loads are in general negligible but for space system they are of major concern. The source of such loads and how to deal with them are presented in the next paragraphs.

Quasi-Static Load In the case for so called quasi-static loads, the load is applied very slowly so that the structure deforms very slowly which makes the inertia force of components negligible. Such loads are caused by the constant acceleration of the launch vehicle mainly during the acceleration during first stage flight [8]. The constant acceleration for the stages of the Soyuz launch vehicle is depicted exemplary in figure 2.20 [34].

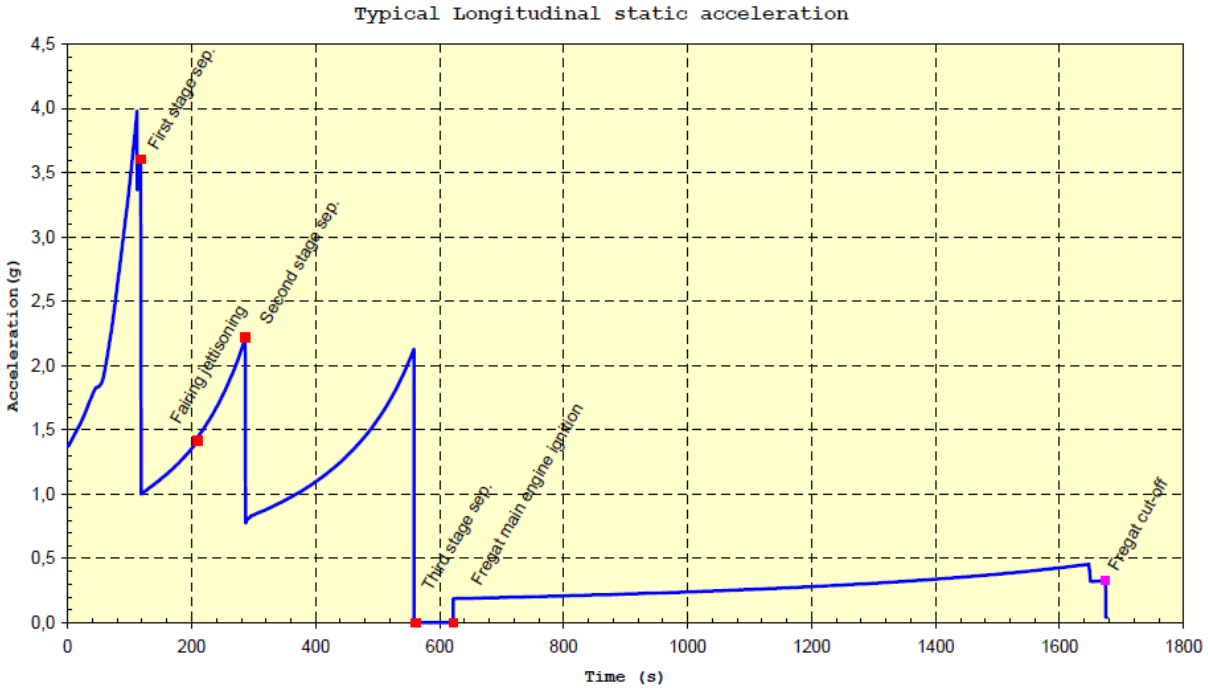

Figure 2.20: *Longitudinal static acceleration for the Soyuz launch vehicle taken from [34].*

For the HSB system, the quasi-static qualification load (including safety and qualification margin) is given to 20g for out-of-plane and in-plane load.

Sinusoidal and Random Vibration For a satellite and its subsystems not only static loads are applicable but also frequency dependent vibrations loads have to be considered.

The origin of sinusoidal vibrations arise from the powered flight of the launch vehicle (mainly the atmospheric flight), as well as during some of the transient phases. The duration of this loads is approximately six minutes in the case of the Soyuz launch vehicle [34]. For the HSB system a sinusoidal vibration qualification load like as shown in figure 2.21 on the left is applied. The sweep rate (rate of the frequency increased in a certain time interval) shall be 2oct/min for the qualification model and 4oct/min for the flight model [35].

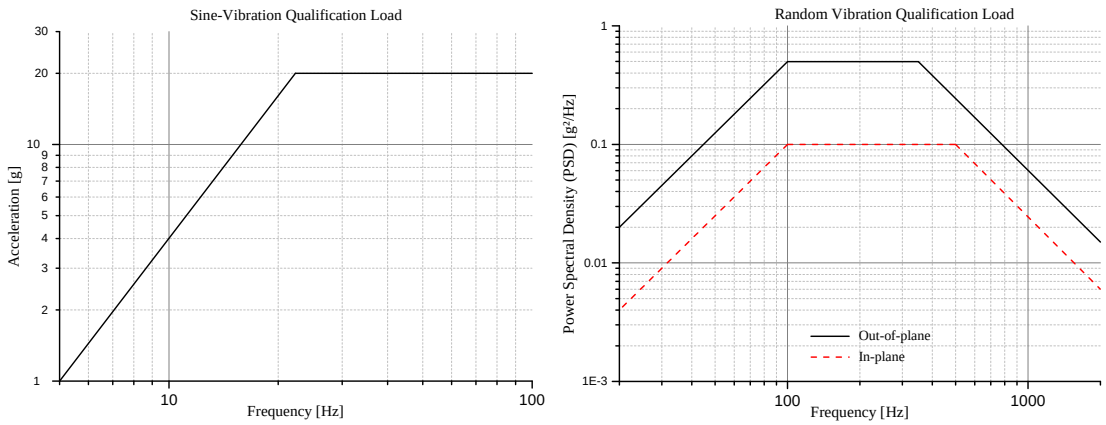

Figure 2.21: *Left: Sinusoidal vibration spectrum for the qualification load of the HSB system. Right: Random vibration qualification spectrum of the out-of-plane (straight black line) and in-plain (dashed red line) loads [36]*

Random vibrations at the spacecraft base are generated by the chemical propulsion system operation and by the adjacent structure's vibro-acoustic response. Maximum excitation levels are obtained during the first- stage flight. Acceleration power spectral density (PSD) and root mean square vibration levels (g_{rms}) used for the HSB system development are given in table 2.6. In figure 2.21 on the right the random vibration qualification load spectrum is illustrated [36].

Out-of-plane		**In-plane**	
f [Hz]	**Load**	**f [Hz]**	**Load**
20...100	+6 dB/oct	20...100	+6 dB/oct
100...350	0.5 g^2/Hz	100...500	0.1 g^2/Hz
350...2000	-6 dB/oct	500...2000	-6 dB/oct
Total g_{rms}	16.9g	Total g_{rms}	9.0g

Table 2.6: *Random vibration loads for the out-of-plane and in-plane qualification loads of the HSB system [35].*

Shock The shock loads seen by the satellite arise primarily during stage separations, fairing jettisoning and actual spacecraft separation. Depending on the target orbit and launch vehicle multiple shocks events are present. For the HSB system the qualification shock test shall be carried out for all three axes (X, Y, and Z) for three different frequencies

each. The shock loads are the same for out-of-plane and in-plane shock test. For the final flight model no shock test will be carried out, the requirement is verified due to similarity of qualification model and final flight model. The shock loads for the HSB qualification testing are given in table 2.7. [35]

Frequency [Hz]	**Load [g]**
100	15
3000	2000
10000	2000

Table 2.7: *Shock qualification loads for the HSB system, values are the same for out-of-plane and in-plane loads [35].*

2.3 Hybrid-Sensor-Bus (HSB) Project

The aim of the, by OHB System developed, measurement system, called Hybrid Sensor Bus (HSB) is to overcome the drawbacks of current State-of-the-Art satellite sensing designs. As discussed before in section 2.1.1, current designs suffer from high inflexibility and high mass impact both increasing the satellite costs. For this a measurement system combining electrical sensing and fiber-optical sensing is developed. The development of the fiber-optical sensing module which operates in conjunction with the other modules of the HSB system is part of this PhD.-Thesis. Nevertheless, the other modules are necessary to operate the fiber-optical sensing module. In addition, the functional and electrical interface requirements of the herein developed system depend strongly on the overall design concept.

The overall block diagram of the HSB system is given in 2.22 [5]. The system consists out of four modules, the power supply unit (PSU), the HSB controller module (HCM), the interrogator controller module (ICM) and the analog front-end of the fiber-optical interrogator module (FIM-AFE). The HSB system uses the RS485 bus for internal module communication. The data transported over the bus are mainly measurement data which are queried by the HSB Controller Module (HCM) from other modules. The system uses a single master concept. The internal RS485 system bus foresees the usage of a fully redundant system, so each module can be doubled for use in a redundant, single point of failure free configuration.

The electrical and mechanical properties are summarized in table 2.8 [5]. The maximum power consumption is a worst case value which is expected to occur during warming up from a minimum storage temperature of -40°C and is primarily caused by the temperature controller of the laser diode. The target mission is planned to be in a geostationary satellite orbit, so a lifetime of 15 years and a high reliability number were the design goal. For the system design, a detailed radiation analysis was carried out, to identify the maximum radiation loads inside the HSB box. The simulation results derived in this work are summarized in section 4.2.3.

The characteristic properties of the modules are described in the next sections. For the

Parameter	Value
Mass	3.5 kg
Envelope Dimension	160 mm x 118 mm x 224 mm
Number of I²C sensor strings	4 strings with 25 sensors each
Number of fiber-optical sensors	2 strings with 10 to 12 FBGs
Measurement rate	1Hz nominal, 10Hz fast mode for single sensors
Resolution	±0.5°C
Operational Temperatures	-20°C to +65 °C
Lifetime	15 years
Radiation load	< 100 krad inside box over 15 years
Power Avg	16.7 W
Power Max	27 W

Table 2.8: *Electrical and mechanical specifications of the HSB system.*

fiber-optical interrogator module an own section (see section 4.4) is introduced because it is the main part of this PhD.-Thesis.

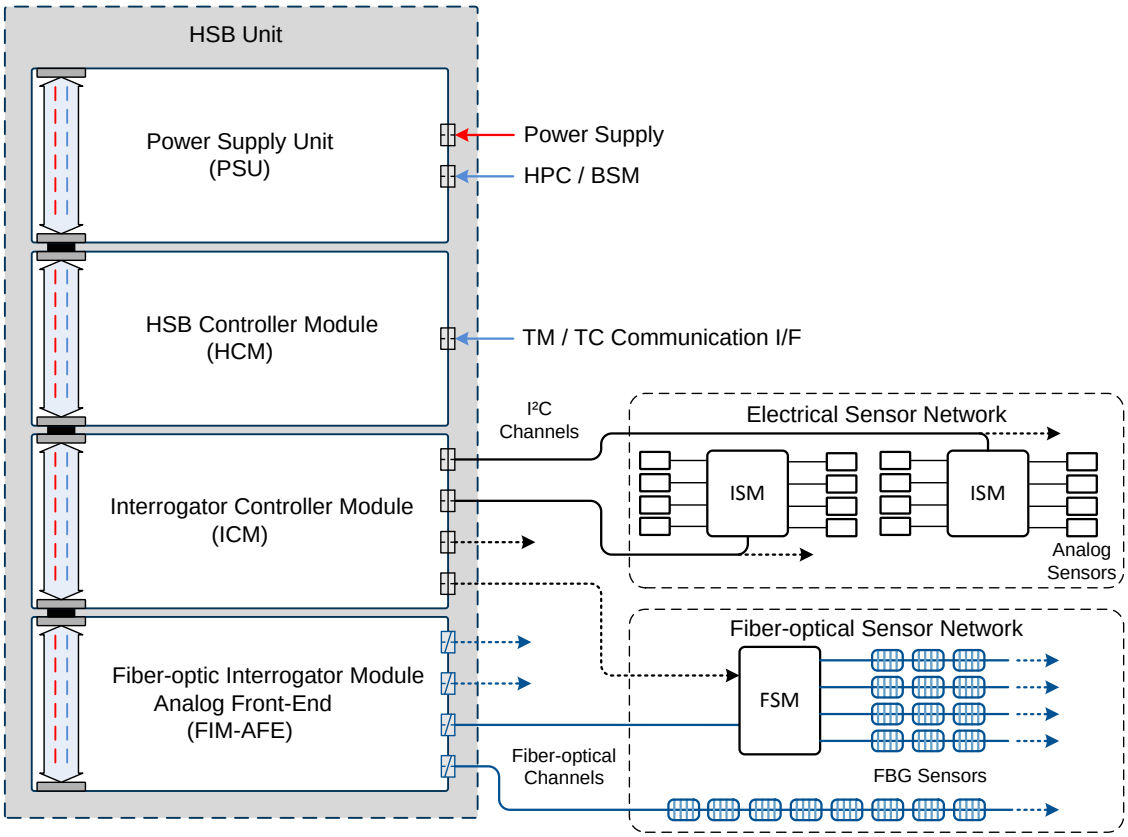

Figure 2.22: *Block and interface diagram of the Hybrid Sensor Bus system [5].*

A 3D model of the engineering model (EM) of the HSB system is shown in figure 2.23 [37]. The four different modules are stacked together and mechanically fixed by their mounting frames. To achieve a complete enclosure of the HSB box on the left and right module, side walls are mounted. In addition the left side wall acts also as mounting

interface of the DC/DC converter. Starting from the left hand side, the modules are accommodated as following: Power Supply Unit (PSU), HSB Controller Module (HCM), Interrogator Controller Module (ICM) and the Fiber-Optical Interrogator Analog Front-End Module (FIM-AFE).

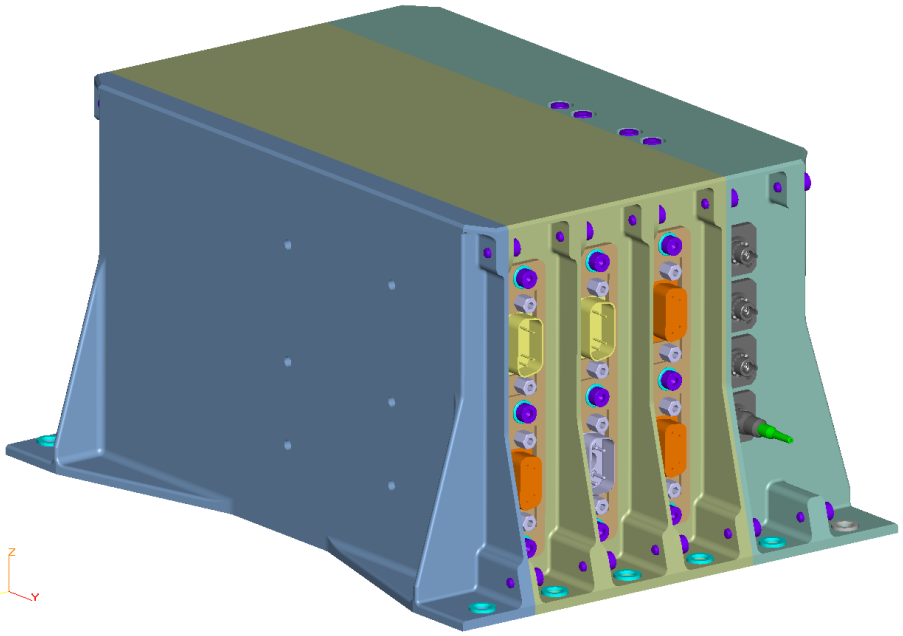

Figure 2.23: *3D model of the Engineering Model (EM) of the HSB system [37].*

Power Supply Unit (PSU) The PSU is responsible for the generation of the HSB internal 12V intermediate bus voltage from the satellite input power rail. Onboard the module the HSB input filters and primary DC/DC converter's output filters are implemented. The on/off commanding of the system is done over so called high-power commands (HPC) generated by the satellite bus. These signals are connected to the PSU module which internally generates steady-state signals from the pulsed HPC signals. The technical details for the PSU are as following [37]:

- Nominal input voltage: 50 V
- Generated secondary voltage: 12 V
- Maximum available power: 35 W
- HPC input voltage: 28 V (33 V max.)
- Open collector output for bi-level switch monitor (BSM) signals
- Internal temperature monitoring
- Housekeeping for secondary voltage and power
- Undervoltage lockout and over-temperature protection

HSB controller module (HCM) The HSB system contains an intelligent controller module for managing the data acquisition between modules and the data transfer to the satellite bus. In addition also some data averaging functionalities and alarm functions

for data being out of range are implemented. In this module, also the MIL-STD-1553 [38] decoding hardware is implemented, which interfaces with the satellite platform. The HCM controller is a powerful LEON3FT-based processor [39] using a real time operation system (RTEMS). The module generates all necessary power rails local onboard from the intermediate power rail generated by the PSU. More specific properties and functions are listed below:

- LEON3FT processor
- MRAM acting as boot loader storage
- MRAM for application software storage
- Gold / Silver Image for application software
- SRAM
- All memories are EDAC protected
- MIL-STD-1553B interface logic with external address selector
- Firmware upload possibility over MIL-STD-1553B

Interrogator Controller Module (ICM) The interrogator controller module is responsible for reading out the I²C sensor lines and controlling the analog frontend's ADCs and DACs to perform spectral measurements. All necessary power rails are generated onboard form the intermediate voltage. The core of the ICM is a space-proven, radiation tolerant and single event upset immune field programmable gate array (FPGA), which holds the state machine for controlling both types of interrogator, electrical and fiber-optical. For the electrical sensor bus, four I²C channels are implemented onboard the ICM. Each channel has a supply voltage rail of 5 V for powering external sensors. The power rail is protected inside the ICM against overcurrent events by a latch-up circuit. The sensor address and the dedicated commands to read out the sensor are stored in lists, which can be configured on ground as well as in orbit. In addition, the module also has an interface to the fiber-optical interrogator analog front-end board (FIM-AFE). In this way, both sensor busses, the I2C-bus on one side and the fiber-optical bus on the other side are controlled efficiently by a single FPGA. The laser diode is controlled in wavelength by the use of data stored into a look-up table (see section 4.4 for more details). So the logic used to control the fiber-optical interrogator module is sourced out to the ICM.

Fiber-Optical Interrogator Module (FIM) The focus of this work lies on the development of the fiber-optical interrogator modules. A more detailed description, taking also the results of different technology trade-offs into account, is given in section 4.4.

Chapter 3

Scanning Laser Based Fiber-Optical Interrogator Module

3.1 Scanning Laser Technologies

The fiber-optical interrogator developed in this work is based on a scanning laser which can tune its output wavelength in a certain range. Different laser systems are available which are operating according this method. Considering the functional requirements and the environmental conditions in space applications, a more detailed requirement specification for the system must be elaborated. Some requirements are focusing to the optical performance of the laser itself, and on the other hand some requirements arising from the environmental conditions in space for the target application, both having high impact to the system design.

In this section, the different requirements are gathered and summarized. First the different parameters are described and afterwards the numeric values for each requirement are given in tabular form.

- Operating wavelength λ_c: The central wavelength at which the laser shall operate. The telecommunication C-band located at 1550 nm is the desired operating wavelength band for the laser due to the availability of commercial components.
- Scanning range $\Delta\lambda$: Defines the range of stable operating wavelength of the laser. As higher the scanning range of the laser is, as more FBGs can be implemented in one fiber string.
- Operating mode: The laser shall operate in single mode to get feasible measurement results.
- Linewidth: The laser's linewidth must be magnitudes smaller than the FBG's spectral response to achieve the necessary resolution.
- SMSR: The side-mode suppression ratio indicates how strong the power of other eventual present laser modes is suppressed with respect to the main laser mode. If the SMSR is too small, multiple wavelengths are generated by the laser, which destroy the explicit correlation between output wavelength an measured spectral response.
- Output power: The output power of the laser shall have a significant level that multiple strings can be interrogated by the same laser in parallel.

- OSNR: The optical signal-to-noise ratio measures the ratio of signal power to noise power within a certain bandwidth (usually 0.1 nm).
- Output type: A fiber coupled laser is preferred due to the higher robustness and the omitted alignment.
- Scanning type: Indicates how the laser's wavelength is controlled. For space applications a setup without moving parts or highly sensitive components is required.
- Environmental: The setup must be very robust against environmental conditions like vibration, temperature and shock.
- Temperature range: The laser shall be able to work within a temperature range of -25°C to +65°C given by the system requirements. To maintain the laser crystal in the operational temperature range, a thermo-electric cooler might be necessary.
- Lifetime: The lifetime of the laser shall be as long as the lifetime of the satellite. In the case for a telecommunication satellite the lifetime would be 15 years.
- Mass: The mass impact shall be as small as possible due to high transportation cost and due to high vibration and shock loads for systems with higher masses.
- Volume: The volume of the laser inside the system is limited, so a smaller volume is preferred.
- Power consumption: Because power consumption is always a big concern in space projects, the necessary power for the laser diode shall be as low as possible. This point includes both, the laser power and the necessary power for temperature control of the laser.

In table 3.1 the requirements for the targeted laser system are summarized. The requirements consider on the one hand the functional requirements (LR1 to LR7) and on the other hand the environmental requirements arising from the application area (LR8 to LR14). These requirements have been derived at the beginning of the work from the HSB system requirements, see also section 4.1.

3.1.1 Semiconductor Tunable Laser

Due to the rapid development in the telecommunication area, different types of semiconductor laser diodes have been appearing on the market. Tunable lasers are used in telecommunication WDM systems for carrier signal generation. The single channels of the WDM systems are defined by the International Telecommunication Union (ITU) in [40] which are usually spaced by 50 GHz in optical frequency at a central wavelength of 1550 nm.

There are different types of semiconductor tunable lasers available [41]:

- GCSR: Grating-assisted co-directional Coupler with Sampled Reflector
- SSG-DBR: Super Structure Grating Distributed Bragg Reflector
- TTG: Sampled Grating Tunable Twin Guide

Req. No.	Parameter	Value
LR1	Central wavelength	1550 nm
LR2	Scanning range	40 nm
LR3	Operating mode	Single-mode
LR4	Linewidth	$<$ 10 MHz
LR5	SMSR	$>$ 25 dB
LR6	Output power	10 dBm
LR7	OSNR	$>$ 35 dB
LR8	Adjustment	no moving parts
LR9	Environment	robust against vibration
LR10	Temperature range	-25°C to +65°C
LR11	Lifetime	15 years
LR12	Mass	$<$ 20 g
LR13	Volume	$<$ 2x2x2 cm^3
LR14	Power consumption	$<$ 2 W

Table 3.1: *Derived requirements for the laser source for the developed fiber-optical interrogator.*

- MG-Y: Modulated Grating Y-branch Laser

For all of these laser types the wavelength can be adjusted with an external current. No moving parts are necessary, which allows a very compact and robust tunable laser design. By the absence of moving parts inside the laser, they can be distinguished from the ECDL lasers in section 3.1.3.

3.1.2 Fiber Based Tunable Laser

The combination of a broad-band amplifier gain medium and a very narrow band filter can be used to form a tunable laser. An erbium (Er^{3+}) doped fiber is often used as broad-band amplifier medium. But also a so called semiconductor optical amplifier (SOA) could be used. The bandwidth of the amplifier limits the tuning range of the laser [42]. So a higher bandwidth is desired. The Er-doped fiber is pumped with 980 nm laser light whose light is coupled into the fiber ring with a combination of a WDM and a coupler [43]. Such a setup is illustrated in figure 3.1. The Fabry-Pérot Filter (FPF) in the ring is used to select the desired lasing wavelength. By tuning the FPF's spectral range, the output wavelength of the system is changed. This can usually be done by applying a voltage to a piezo on which one of the mirrors of the FPF is mounted [44]. The finesse F of the FPF determines the linewidth of the output light. Thus a very narrow FPF is required to gain a narrow output linewidth.

By Zhong et al. [45] a 100 nm tunable fiber ring laser was demonstrated for which a driving voltage of less than 25V is necessary. The wavelength stability and the long term performance are limited by the used FPF. Due to thermal fluctuations or vibrations the spectral range of the FPF is changed, which in turn affects strongly the output wavelength. So, thermal control of the FPF and additional monitoring or feedback elements are necessary to fulfill the long term stability of such laser types. In addition, Er-doped fibers show a high attenuation due to radiation induced attenuation (RIA) which is presented in different papers [46], [47], [48] and [49]. When the attenuation inside the fiber

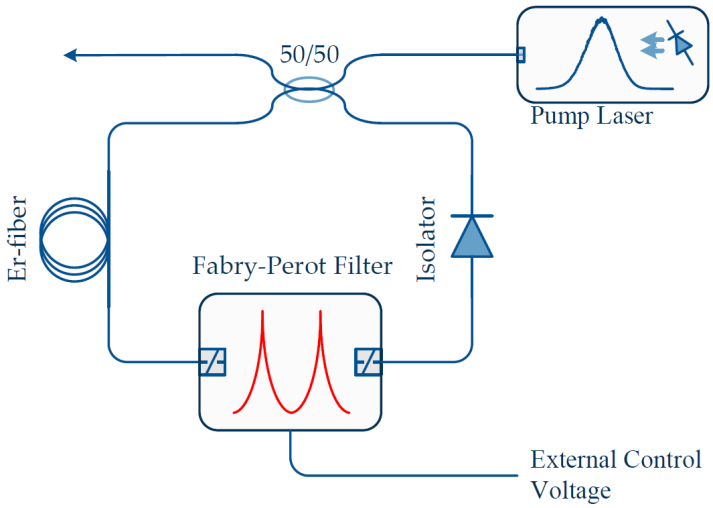

Figure 3.1: *Setup of a fiber based tunable laser with an Er-doped fiber as gain medium and a Fabry-Pérot filter (FPF) as wavelength selective device [43].*

increases, the output power of the laser system decreases, which leads to a smaller SNR of the interrogator system. This laser type might not be the best candidate for use in space applications. By using special radiation hard erbium doped fibers and a special treatment this problem can be reduced but it cannot completely mitigated.

3.1.3 External Cavity Tunable Laser

In an external cavity diode laser (ECDL) an external reflector is used to feed back a portion of the output light back into the laser cavity. This changes the phase and amplitude balance inside the cavity and as a result the laser wavelength varies. In addition the presence of an external cavity adds other advantage effects such as narrow linewidth of the output light in the kHz-region and a high side-mode suppression ratio (SMSR). Former designs had problems with the micro-mechanical mounting and manufacturing of the necessary gratings and tilting mirrors. Due to progress in MEMS technology area, ECDL lasers completely integrated into a chip have been demonstrated. Up to now these lasers are mainly discussed in literature. There future commercialization is still far away. To scan over a wavelength range of 40nm necessary voltages of 150V have been reported. [50], [42]

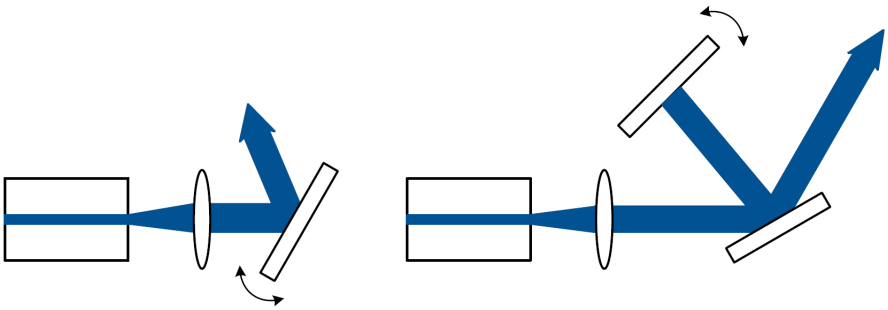

Figure 3.2: *Tunable external cavity diode laser (ECDL) in Littrow (left) and Littman-Metcalf (right) configuration.*

In figure 3.2 two possible tunable ECDL laser configurations are shown. The setup on the left side is called *Littrow-Configuration*, the setup on the right side is called *Littman/Metcalf Configuration* [51]. For both setups a rotating mirror is used to change the laser's output wavelength. These two configurations are the earliest presented ones. A full overview is presented by Liu et. al in [52]. To improve the linewidth and the single-mode operation of the laser a grating can be implemented. The grating acts as a wavelength filter and enhances the performance of the laser.

3.2 MG-Y Laser Technology

The fiber-optical interrogator designed within this work is based on the MG-Y laser technology, so a more detail insight to this special kind of laser shall be given here. The MG-Y laser is built up with two modulated grating reflectors (left and right) which are combined at one end. The overall laser shows a shape like the letter 'Y'. This is the origin of the name, modulated grating Y-shaped laser (MG-Y). [53], [54]. A schematic overview is given in figure 3.3.

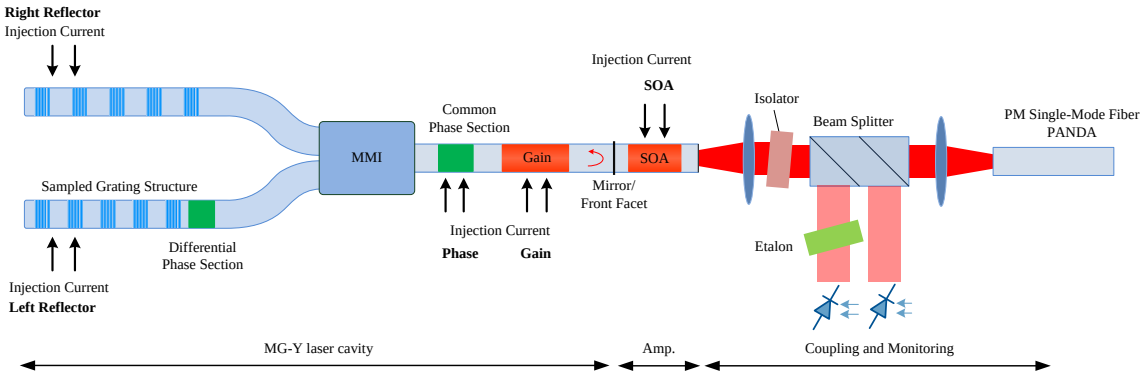

Figure 3.3: *Schematic of the MG-Y laser diode with Y-branch reflector structure, amplifier, monitor elements and coupling lens. MMI multi-mode interferometer, SOA semiconductor optical amplifier.*

The light in both reflectors (left and right reflector) is combined together in a Multi-Mode Interferometer (MMI) and subsequent amplified by the laser's gain section. A common phase section is used to align the resonator's longitudinal modes, yielding in a constructive or destructive interference. A minimum reflection of the cavity end facets is required to reduce interference effects between cavity modes and the sampled gratings reflection spectrum [55]. The power of the output light of the MG-Y structure is very small. For this an additional semiconductor optical amplifier (SOA) is placed next to the MG-Y structure. The output power of the laser is affected by the injected current into the SOA section. Followed by the SOA a monitor module within the same mechanical package is implemented. Inside the monitor module an optical isolator protects the laser section from unwanted back reflections arising from the etalon or from external disturbances. Behind the optical isolator, a small portion of the light is coupled out to an optical power monitor diode and to an etalon followed by a monitor diode. The etalon is made out of glass with a thickness of 1.5 mm (see section 3.2.3) and is used to determine the laser's output wavelength. Finally the light is coupled into a PM fiber which is connected to

subsequent measurement system. The PM fiber is not absolutely necessary but in the telecommunication area in which these types of lasers are used, the laser is followed by an electro-optical modulator for signal modulation. This modulator requires a definite polarization state. Also the used electro-optical polarization scrambler requires a PM fiber as input, see section 3.4.5. [53], [54], [3]

3.2.1 Wavelength Tuning

The laser's output wavelength is defined by the constructive overlapping of the reflector peaks from the left and right reflector. Each of the MG-Y laser's reflectors shows a comb-like reflection spectrum, whereby the reflectors have a slightly different peak spacing. The spectrum for the right reflector is given by the black line in figure 3.4, the spectrum for the left reflector by the red line respectively. At the wavelength at which the peaks from both reflector overlaps constructively, a single laser line appears at the output. Such an overlap is called *supermode*. The overlapping of different modes which form one strong mode is called additive Vernier effect [56]. At the output of the laser diode only the strongest mode is observable, the other modes are suppressed by more than 30 dB [4].

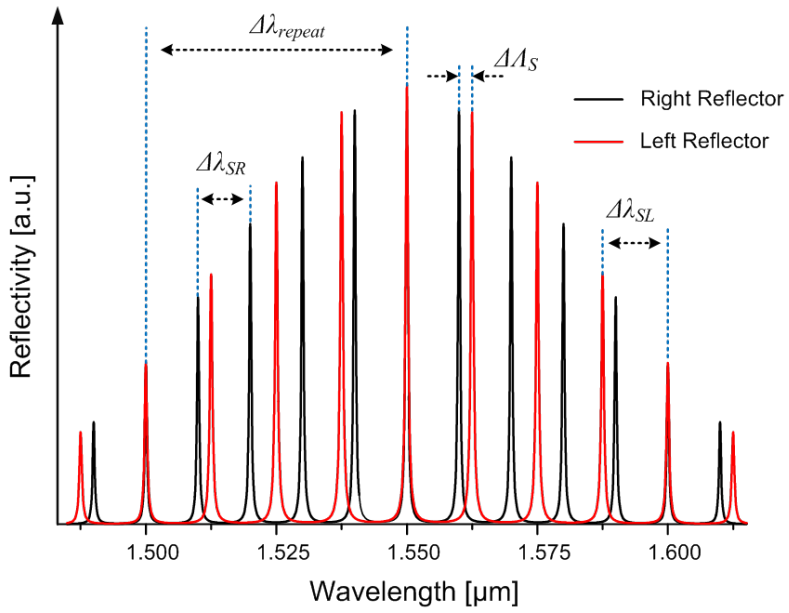

Figure 3.4: *Comb-like modes (theoretical model) of the left and right reflector with slightly different wavelength spacing. The different colors illustrate the different modes of each reflector (left, red and right, black). [56].*

When both reflectors are tuned against each other any output wavelength within a certain range is accessible. The range is limited by the repeating mode spacing $\Delta\lambda_{repeat}$. The repeating mode spacing is defined as the spacing where peaks of both reflectors start to overlap again [56]

$$\Delta\lambda_{repeat} = \frac{\Delta\lambda_{SL} \cdot \Delta\lambda_{SR}}{\Delta\lambda_{SL} - \Delta\lambda_{SR}}. \tag{3.1}$$

As discussed before, the modes of the two reflectors must be tuned to change the output wavelength. This can simply be done by injecting current into the left and right reflector

sections. Hereby the carrier concentration within the guiding layer of the section increases and the refractive index of the reflector section changes. By the injected current, the effective refractive index changes towards lower values and the reflector peaks are moving towards lower wavelengths. The change in reflector wavelength is proportional to the refractive index change. The refractive index change itself shows an exponential behavior as plotted in figure 3.5 [57].

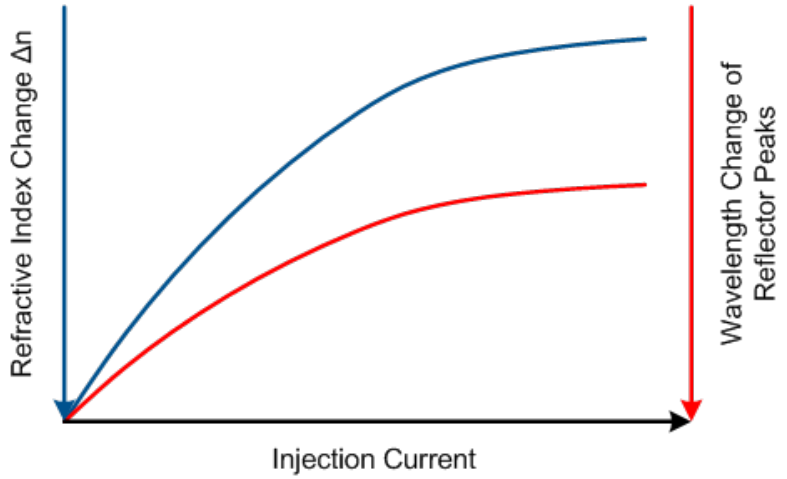

Figure 3.5: *Plot of the refractive index change as function of the injection current.*

For further discussions the current vector for the MG-Y laser is defined as

$$\vec{I}_{MGY} = \begin{pmatrix} I_R \\ I_L \\ I_{Ph} \end{pmatrix}. \tag{3.2}$$

When the two reflector currents I_R and I_L are perfectly set, the wavelength can be changed to lower values by applying the same amount of current to both reflectors. This is possible as long as a cavity mode hop occurs where the lasing wavelength jumps from one cavity mode to the next one.

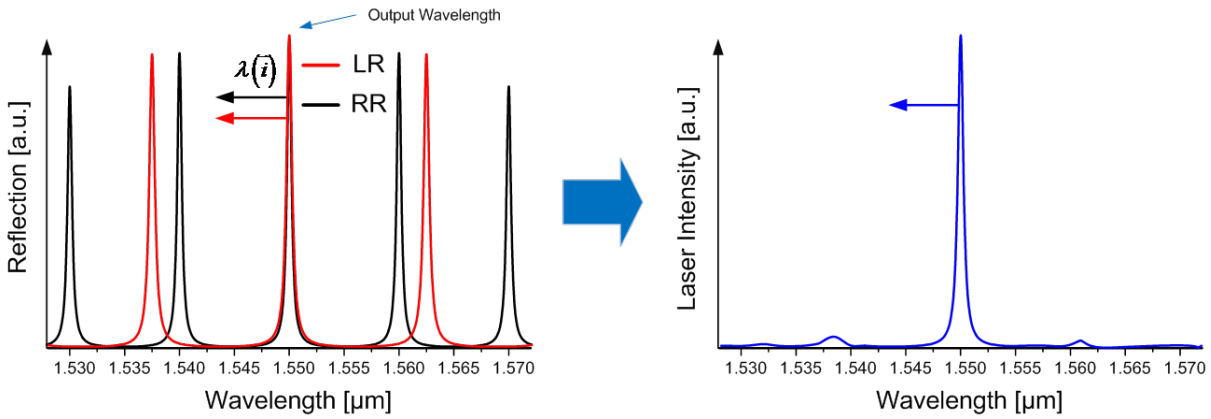

Figure 3.6: *Tuning principle of the MG-Y laser where the output wavelength is limited to the middle supermode.*

As can be seen in figure 3.5, the reflector refractive index saturates at a certain injection current. This limits the wavelength tuning within a so called *Wavelength Band* defined by a supermode [56]. To overcome the wavelength limitation, the supermode must be changed to the next adjacent one. This can be done by tuning just one injection current until the next two peaks of the reflector's overlap. This procedure is shown in figure 3.7. Here I_R is increased until the modes of both reflectors overlap at a wavelength of 1537.5 nm. The wavelength of the new supermode can now be tuned until the refractive index change saturates again and the next supermode must be selected.

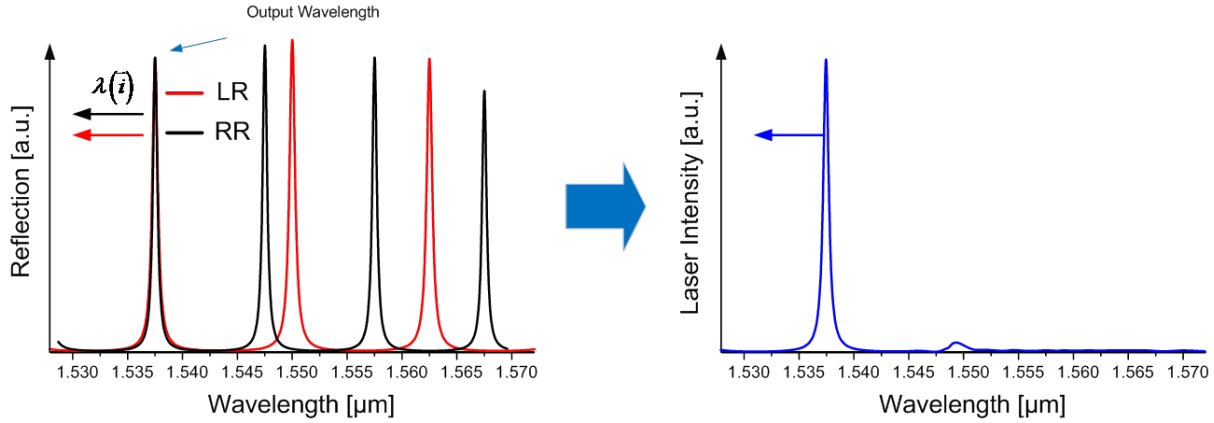

Figure 3.7: *Tuning principle of the MG-Y laser where the output wavelength is limited to the left supermode.*

By varying the MG-Y laser's currents I_R and I_L against each other at a constant phase current, a characteristic wavelength map of the laser can be obtained. In this map the wavelength values are mapped to specific colors whereas the x- and y- axes are defined by the left and right reflector respectively. A schematic illustration of the map is given in figure 3.8.

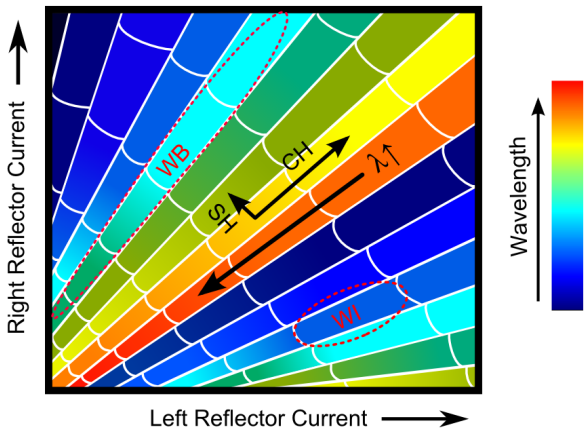

Figure 3.8: *Wavelength map of the MG-Y laser at constant phase current I_P. The wavelength is given by the color of the map as function of the two reflector currents I_R and I_L. WB wavelength band, SH supermode hop, CH cavity mode hop, WI wavelength island.*

The diagonal bands in the wavelength map are called wavelength bands (WB) corresponding to the wavelength tuning range of a supermode. Each wavelength band is

subdivided into the so called wavelength islands resulting from cavity mode hops. Single mode operation of the laser is guaranteed within these islands. On the boundaries of the islands, multimode operation can occur which is unwanted. Traveling along the diagonal wavelength band, hence increasing the reflector currents I_R and I_L, results in lower output wavelengths. So the laser's output wavelength in the same wavelength band is indirectly proportional to the reflector currents. To reach an adjacent wavelength band (movement in horizontal way in the wavelength map), a supermode hop is required by changing only one reflector current while keeping the other at the same value. The movement in diagonal direction induces less fluctuations in the laser structure due to linear increasing or decreasing reflector currents. Changing the wavelength band is done by escalated jumps in the current values of both reflectors, inducing thermal unbalances in the laser.

As discussed before, cavity mode hops occur when traveling along a wavelength band and passing different wavelength islands (WI). On the boundary of the wavelength islands, the laser emits multimode light which is highly unwanted. So a tuning mode must be found which reaches all possible wavelengths while the boundary of the islands are skipped. For this the phase current plays an important role. By injecting a current into the phase section of the laser, all wavelength islands are moved towards higher reflector currents. Basically all wavelength islands (WI) in figure 3.8 are shifted towards the top right corner of the map. By using at least two different phase currents, cavity mode hops can be avoided while tuning the laser's wavelength within a wavelength band. Hereby the wavelength islands from the phase current I_{P1} are overlapping with the cavity mode hop areas from wavelength islands given by the phase current I_{P2}.

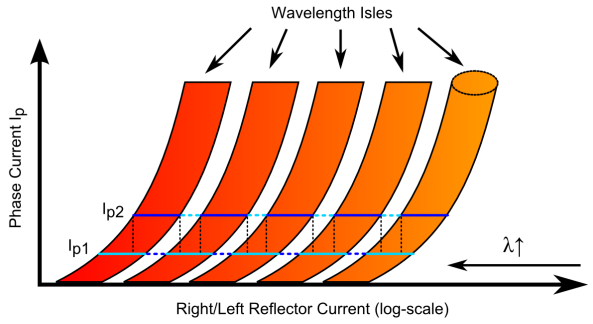

Figure 3.9: *Illustration of the effect of phase current injection to the MG-Y structure. The wavelength islands are illustrated as tubes which are moved in wavelength by changing the phase current.*

As can be seen in the schematic illustration in figure 3.9, the wavelength island are located at lower wavelengths λ for the phase current I_{P1} (cyan line) as for phase current I_{P2} (blue line). The reason of the island shift due to phase current lies in the resonator's optical path length. The path length of the resonator defines the spectral position λ_m of the cavity mode hops. The MG-Y laser's cavity can be seen as a Fabry-Pérot Etalon where the spectral positions λ_m of the laser's longitudinal modes are given as [3]

$$\lambda_m = \frac{2 \cdot L \cdot n_{\text{eff}}}{m} \tag{3.3}$$

where n_{eff} denotes the effective refractive index of the cavity, L is the lasers cavity length and m is the longitudinal mode number. By injecting a current into the phase section,

the cavity's effective refractive index n_{eff} is changed. This change affects also the optical path length and hereby the spectral position of the cavity modes [3, 53].

3.2.2 Laser Temperature Dependency

To identify the dependency of the MGY-laser's output wavelength from its temperature, a wavelength sensitivity analysis was carried out. For this dedicated current triplets have been identified for which the laser's output wavelength is located in the center of a wavelength island, ensuring stable operation for this analysis. Afterwards, the laser's temperature was varied in between +10°C to +50°C while monitoring the output wavelength by a wavemeter. As can be seen in figure 5.2, the laser crystal is mounted on a thermo-electric cooler to allow a tight temperature control which is necessary to ensure the stability of the laser's output wavelength. Changing the setpoint value of the temperature controller simply allowed this measurement.

The results of two fitted curves to the measurement data are given in figure 3.10. It can be seen, that the wavelength increases with temperature, so the dependency has a positive slope. It was also observed during the measurement that very large changes are present, especially for temperatures between +10°C and +20°C. The origin of this effect is assumed to lie in super mode hops inside the laser structure. A temperature sensitivity between 107 pm/°C and 113 pm/°C is determined.

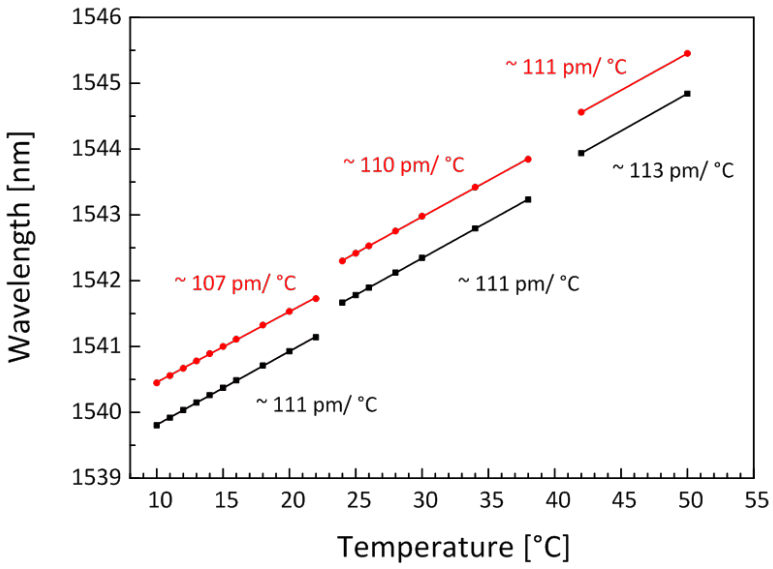

Figure 3.10: *Fitted curves to the measurement data of different stable wavelengths, minimum (red) and maximum (black) sensitivity is illustrated.*

3.2.3 Monitoring the Output Wavelength

For wavelength monitoring an etalon followed by a photodiode is implemented in the laser package (see figure 3.3) by the manufacturer of the laser diode [4]. An etalon has a transmissivity function showing repeating peaks with maximum reflections. The wavelength spacing between two adjacent peaks is defined as the free spectral range (FSR) and the linewidth of the peak is defined by the finesse (F) of the etalon [42, 58]. The

wavelength dependent transmission $T(\lambda)$ can be calculated by taking into account the ratio between the etalon signal ($U_Et(\lambda)$) and the reference signal ($U_Ref(\lambda)$) of the monitor diodes [57]. Taking the ratio of both signals is necessary to compensate for power fluctuations which occur during changing the wavelength bands which are seen also at the monitor outputs. Because the etalon works as a frequency discriminator, the fluctuation in output power would be seen misleadingly as fluctuation in wavelength. So it is ensured that a correlation of the etalon signal to the output wavelength is present even when the laser's output power is changed due to the injection current control vector $\vec{I}_{MGY}$

$$T(\lambda) = \frac{U_{Et}(\lambda)}{U_{Ref}(\lambda)}. \tag{3.4}$$

The transmission of an etalon as function of the wavelength is described by the Airy function [58] given by

$$T(f) = \frac{A}{1 + F \cdot \sin^2\left(\pi \cdot \frac{f - f_C}{FSR}\right)} + A_{Bias}. \tag{3.5}$$

where A is the amplitude factor (A=1 for an ideal etalon), A_{Bias} is a general offset parameter, f_c is a fit parameter determining the etalon's central frequency. The FSR is the spectral distance between two adjacent airy peaks. The finesse (F) depends on the reflectivity of the etalon's facets (R_{Et}) and can be defined by the ratio of the FSR and the full-width at half maximum (FWHM) value of an Airy peak. As higher the finesse, as sharper the Airy peaks. The FSR and the finesse are given by [58]

$$FSR = \frac{c}{2 \cdot d_{Et} \cdot n_{Et}} \text{ and} \tag{3.6}$$

$$F = \frac{\pi\sqrt{R}}{1 - R}. \tag{3.7}$$

where d_{Et} is the thickness of the etalon and n_{Et} is the refractive index of the material forming the etalon.

In figure 3.11 the previously discussed Airy fit on a set of measurement data is shown. The data was recorded with an initial calibrated MG-Y laser, which explains the outliers in the data represented by the red points. The outliers where traced back to the current noise of the laser drivers which was later on improved, see also section 5.1.1. The fitted parameters of the internal etalon of the MG-Y laser are summarized in table 3.2. By considering the etalon's transmission function, it is clear that the signal can be used for locking the laser to a certain wavelength. But it is also clear, that the etalon returns only a relative signal, so an additional absolute reference must be used (gas cell or athermal grating). The etalon in addition transforms frequency/wavelength fluctuations of the laser into intensity fluctuations. So, the etalon can be used to determine the laser's frequency noise in the optical domain.

3.3 MG-Y Laser Calibration Procedure

As stated before, the MG-Y laser is used for telecommunication applications in WDM systems for carrier signal generation. The telecommunication C-band located at 1550 nm

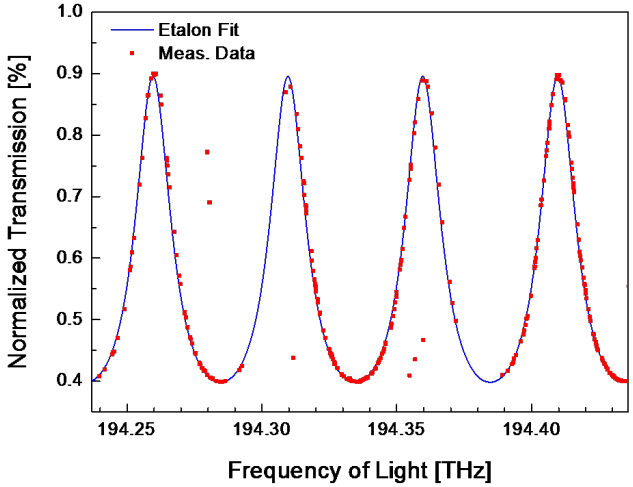

Figure 3.11: *Measured data from the MG-Y's internal etalon (red points) and Airy fit (blue line) to the measurement data resulting in the etalon transmission function.*

Parameter	**Fitted Value**
A	0.6301
A_{Bias}	0.2457
f_c	195.4086851283 THz
F	3.3962
FSR	49.99877 GHz
R_{Et}	≈ 0.4
$d_{\text{Et}} \cdot n_{\text{Et}}$	$\approx$ 3mm

Table 3.2: *Airy fit parameters for the MG-Y laser's internal etalon.*

is divided into 89 channels by the ITU standard [40] for which each channel is separated by 50 GHz in optical frequency. For the laser usage in telecommunication area, it must only be calibrated for 89 wavelengths. For the usage in an FBG measurement system where the wavelength spacing between adjacent wavelengths shall be smaller than 10 pm or 1.25 GHz thousands of calibrated wavelengths need to be available.

The specific calibration procedure determining the stable wavelength within the laser's operational area is presented within this section. At the end a Look-Up Table (LUT) containing stable wavelengths with their corresponding current vector (left reflector-, right reflector- and phase current) will be obtained. Based on this LUT, the MG-Y laser is controlled by the FPGA. More information about the hardware architecture of the designed system can be found in section 5.1.

3.3.1 Calibration Process Description

The principal procedure for calibrating the MG-Y laser is illustrated in the flowchart in figure 3.12. For the whole calibration process, the temperature of the laser is kept at 25°C. The SOA and laser currents are also kept at a constant value of 100 mA as it is the

nominal value given in the manufacturer's datasheet [4]. In fact only the three control currents (right reflector, left reflector and phase current) are changed during the process.

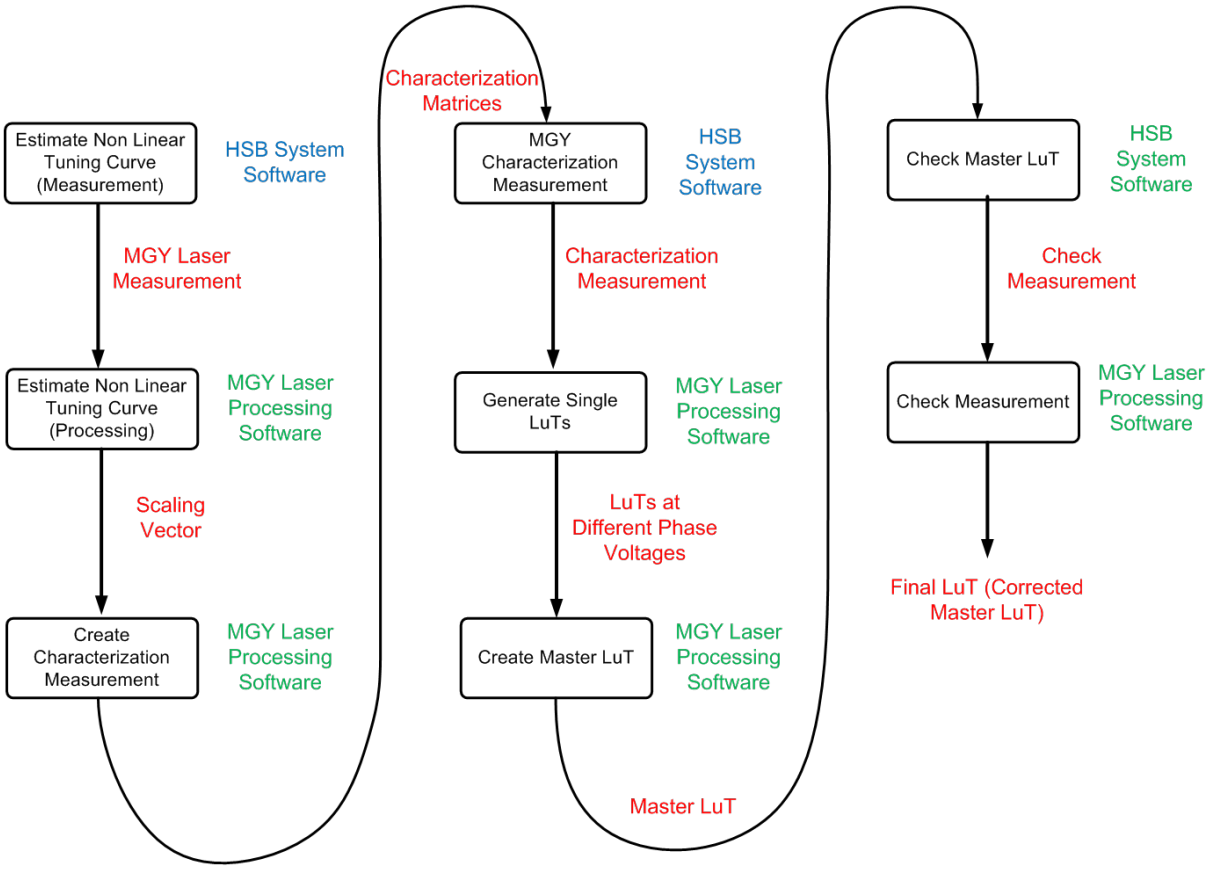

Figure 3.12: *Flowchart for MG-Y calibration procedure.*

In the first step, the MG-Y laser's non-linear wavelength tuning characteristic is identified, see section 3.3.3. This characteristic is necessary to generate a scaling vector by the processing software. This guarantees a uniform distribution of the laser's wavelength values with no gaps in-between during a wavelength scan. With this scaling vector three characterization matrices for different phase DAC voltages (0.72 V, 1.32 V, and 2.48 V)are generated. These values have been selected to cover the low-, the middle- and high reflector current range of the MG-Y laser.

To overcome hysteresis effects caused by the laser construction based on the Y-branch and the additive mode coupling, two different matrices are generated, one with a positive slope and one with a negative slope. Only wavelength values for which the direction of the movement of the current vector has no influence on wavelength are considered as correct values.

When the characterization matrices are generated a characterization measurement of the MG-Y laser is carried out. Different algorithms (see section 3.3.5 are applied to the measurement results to select MG-Y laser current vectors, where a stable laser operation is given. As result three LUTs are created, each for one phase current.

At the end, these three LUTs are combined to a master LUT which can be finally used by the laser system. At the end a stable and reliable LUT for MG-Y laser operation is available.

3.3.2 Calibration Setup

For the calibration of the MG-Y laser, a small setup is necessary consisting out of the FIM Controller Module (CM), holding the control logic, the Analog Front-End (AFE) board with implemented current drivers and MG-Y laser and a wavelength meter (HP86120B). The principal setup is given in figure 3.13. The wavelength meter is used to determine the actual wavelength and the Side-Mode-Suppression-Ratio (SMSR) with respect to the strongest laser line. The output power of the diode is measured by the internal monitoring photodiode and is send back to the measurement computer within the housekeeping data stream.

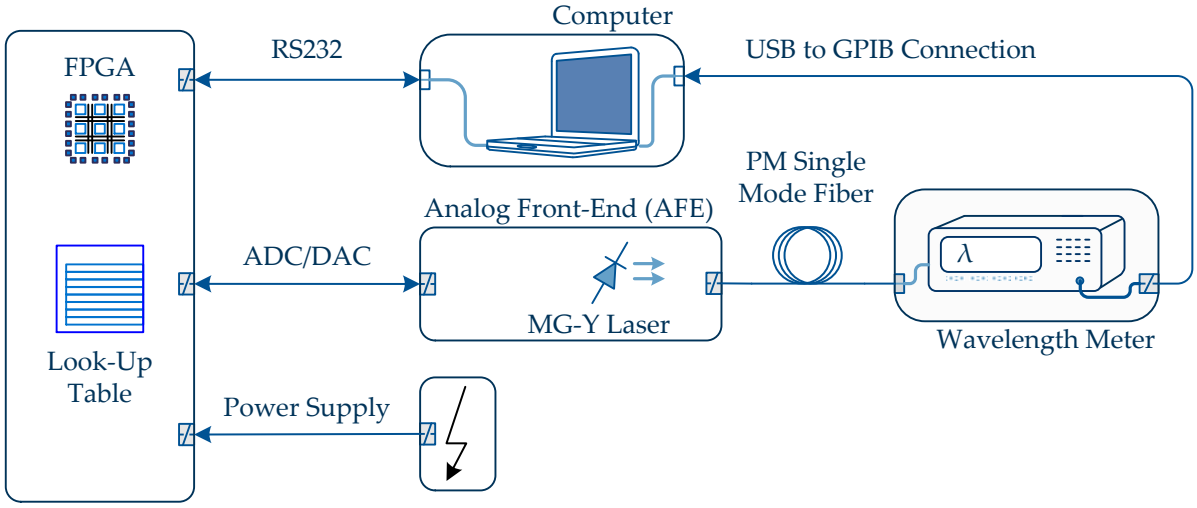

Figure 3.13: *Calibration setup for the MG-Y laser diode mounted onto the Analog Front-End broad (AFE).*

3.3.3 Nonlinear Tuning Property

The MG-Y laser has a non-linear wavelength tuning characteristic according to the phase, right- and left-reflector currents as can be seen in figure 3.5. By scanning the left- and right reflector currents against each other while holding the phase current at a constant value, the nonlinear wavelength tuning characteristic is determined. For this the DAC output voltages for the two currents are changed from 0 V to 2 V in 10 mV steps. For each doublet the laser's output wavelength is measured by the wavelength meter. This scanning process is given in figure 3.14 on the left side. On the right side a wavelength map, as it is used in the entire work to show the scanning mechanics and wavelength islands, is illustrated. The doublets are located in the beginning in the bottom left corner, moving to the top right corner.

The result of the measurement is shown in figure 3.15. The right- and left-reflector control DAC voltages ($U_R = U_L = U_{RL}$) are plotted on the x-axis whereas the laser's output wavelength is plotted on the y-axis. On the second x-axis also the converted current as it supplies the laser, is given. Due to the doublet generation according to figure 3.14 on the left, the DAC control values for both reflectors are equal.

To determine the mathematical function of the laser's output wavelength to the control current vector, a double exponential function is fitted to the data. Applying this fit, the

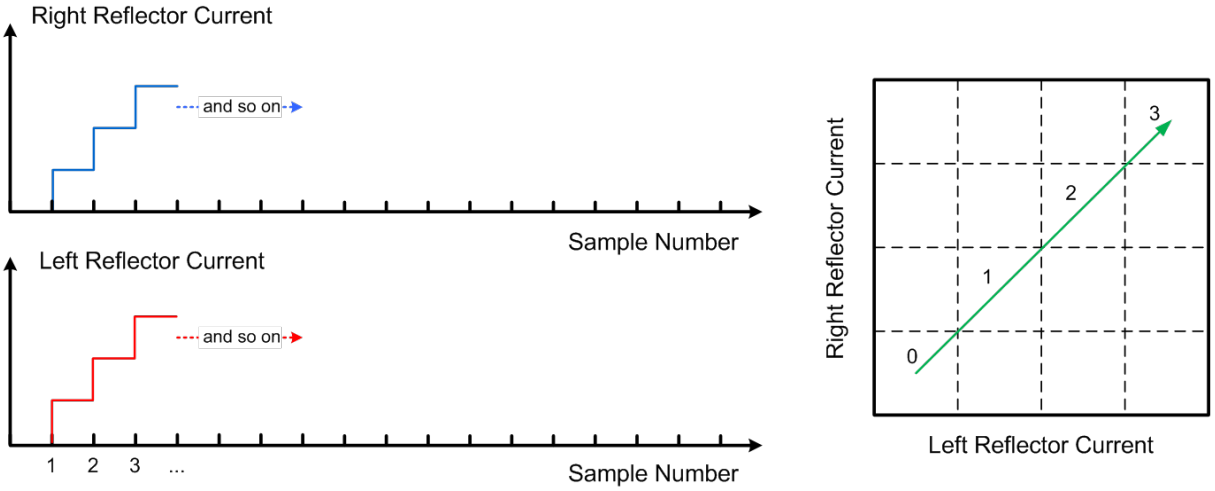

Figure 3.14: *Left: Principle of doublet generation for identifying the non-linear tuning behavior. Right: Right- and left reflector current map.*

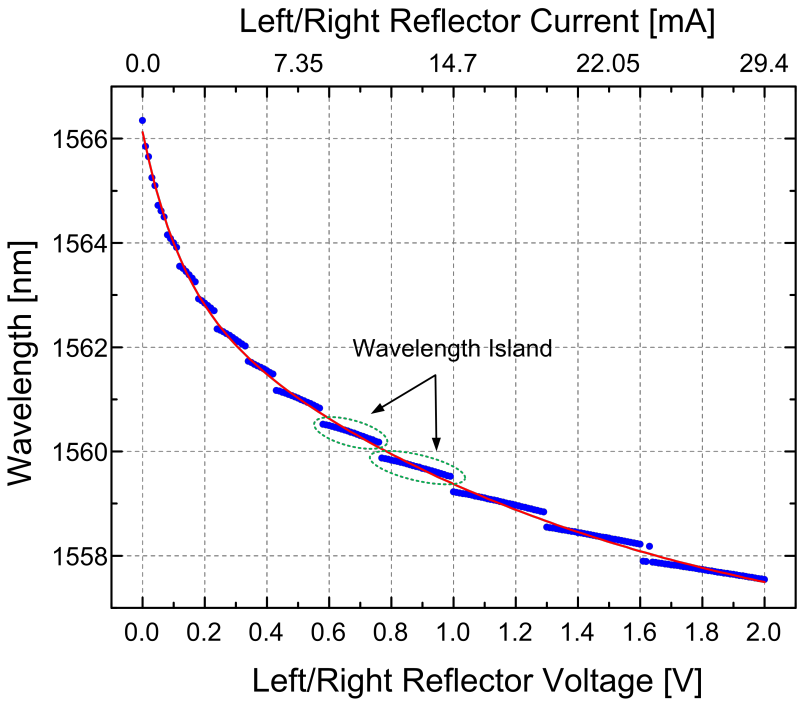

Figure 3.15: *Laser's output wavelength as function of the right- and left reflector control voltages, showing a strong nonlinear behavior.*

result illustrated within figure 3.15 are obtained, following the formula

$$\lambda_{NL} = 7.54\text{nm} \cdot e^{\frac{-U_{RL}[V]}{1.36V}} + 2.86\text{nm} \cdot e^{\frac{-U_{RL}[V]}{0.12V}} + 1555.77\text{nm}. \tag{3.8}$$

For the current controller design, the output wavelength as function of the laser input currents ($I_R = I_L = I_{RL}$) is necessary, so for the sake of completeness it is given here to

$$\lambda_{NL} = 7.54\text{nm} \cdot e^{\frac{-I_{RL}[mA]}{19.96}} + 2.86\text{nm} \cdot e^{\frac{-I_{RL}[mA]}{1.76}} + 1555.77\text{nm}. \tag{3.9}$$

Where λ_{NL} is the laser's output wavelength, U_{RL} is the DAC control voltage of the lasers right- and left-reflector current and I_{RL} is the current in milli-Amperes flowing into

the laser terminals.

As can be seen by the measurement result, the wavelength islands seems to be smaller for lower reflector values. In fact each wavelength island covers an equal wavelength range but due to the exponential wavelength tuning property of the laser, the wavelength is more sensitive towards lower reflector currents. As previously said, the step size was set to 10 mV. As consequence the sampling is coarser for low reflector currents which can be clearly seen in the wavelength map given by figure 3.16. Here the much smaller wavelength islands for lower control values are clearly visible.

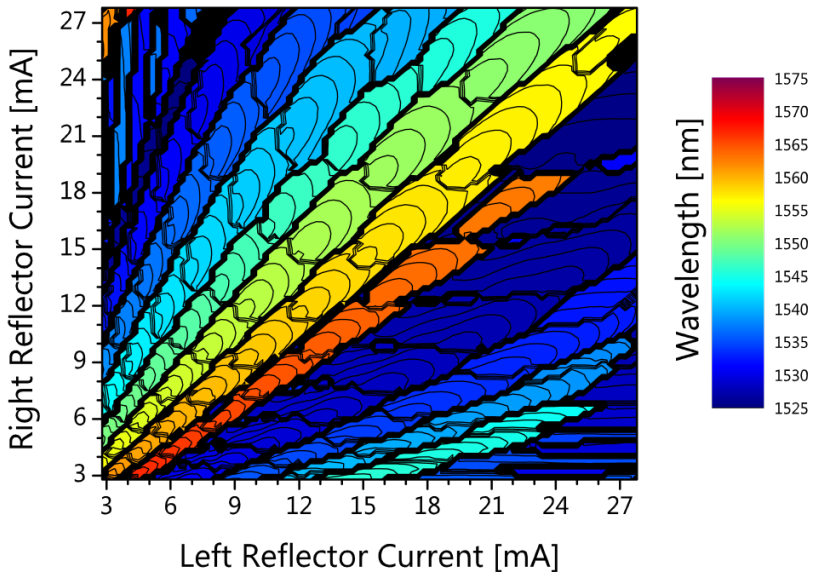

Figure 3.16: *Wavelength map with smaller wavelength islands for lower right- and left reflector control currents due to constant step size of 10 mV.*

To overcome the problem with the non-uniform wavelength islands, the right- and left-reflector have to be tuned finer (smaller step size) at lower currents and coarser towards higher currents to obtain an uniform sampling within the MGY laser's wavelength range. The double exponential fit, given by equation 3.8, is used as a scaling vector to obtain an enhanced reflector tuning vector. When the measurement is carried out with the enhanced vector, the wavelength map has a more uniform wavelength separation. This can be seen in the map given in figure 3.17 on the left. When the wavelength map is determined with the scaled current control vector a more uniform wavelength map is obtained which is an advantage for the following filter processes.

In figure 3.17 on the right side a measurement carried out with the uniform sampled vector (blue curve) and with the scaled vector (red curve) are shown. The red curve shows a clear linear trend in contrast to the blue curve. For the use of the laser within the measurement system a linear behavior is advantageous.

3.3.4 Wavelength's Phase Current Dependency

As seen in figure 3.8 a quasi-continuous tuning of the laser's wavelength is not possible due to cavity mode hops when just one fixed phase current is used. Such cavity mode hops can be avoided by using different phase currents whose exact values must be determined.

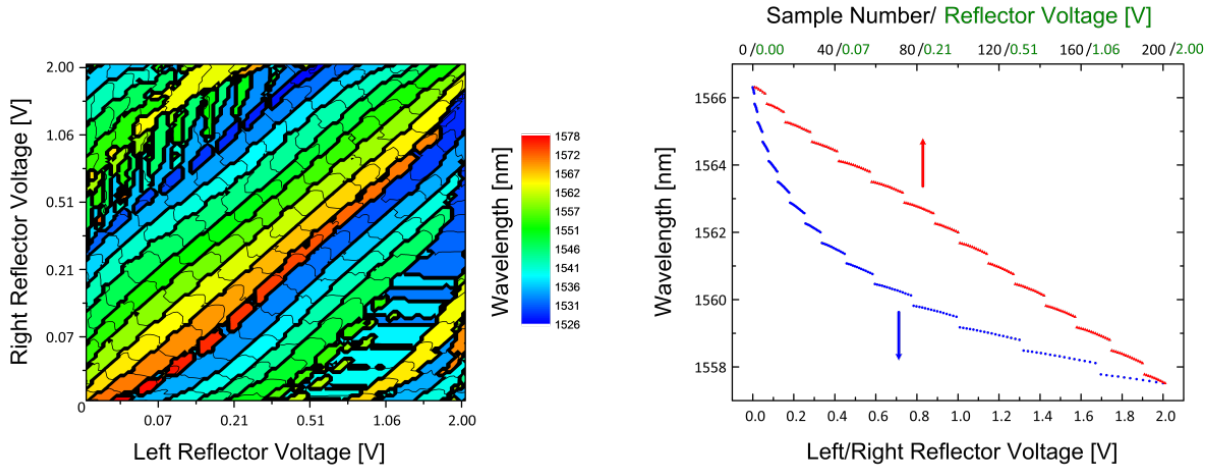

Figure 3.17: *Left: Laser's wavelength map obtained with the enhanced tuning vector eliminating smaller wavelength islands for lower reflector values. Right: Output wavelength as function of reflector values of uniform sampled measurement (blue curve) and scaled sampled measurement (red curve) respectively.*

The phase current behavior is determined by setting the right- and left-reflector currents in dependence to the phase control voltage and measuring the output wavelength. This procedure yields to a contour plot illustrated in figure 3.18. Wavelength differences of 100 pm are shown as contour lines, whereas the mode hop boundaries are indicated with thick black lines. As can be seen, the mode-hop boundaries and also the wavelength islands move towards higher reflector currents when the phase current is increased.

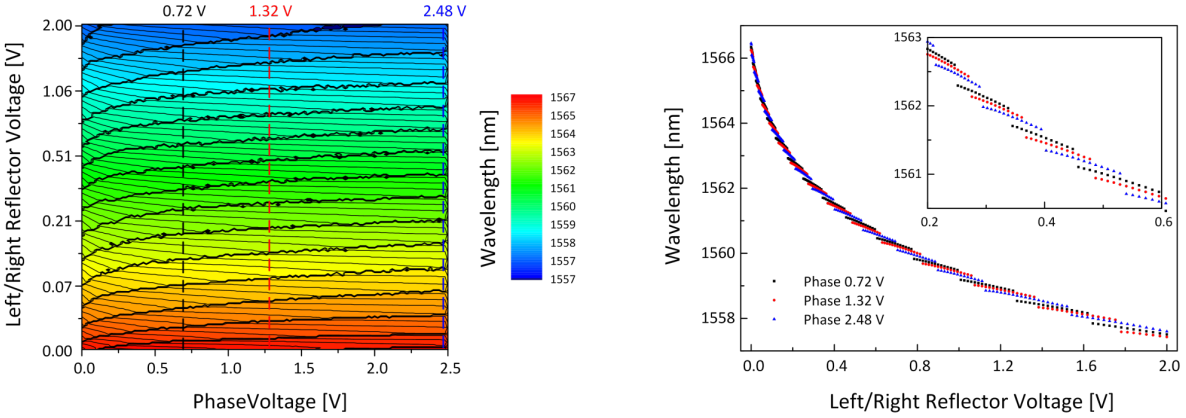

Figure 3.18: *Left: Contour plot of the laser's output wavelength as function of the phase control voltage. Right: Nonlinear tuning characteristic of the laser as function of the right- and left-reflector control voltage for the three different phase control signals.*

For the realization of a quasi-continuous wavelength tuning, the wavelength maps are measured at different phase currents. Hereby the wavelength islands shall cover the wavelength range of a cavity mode hop. This area is covered well for phase control voltages of 0.72 V, 1.32 V and 2.48 V as can be seen in figure 3.18 on the right side. It can also be seen that a quasi-continuous wavelength tuning through the laser's wavelength bands is possible with this three phase currents. Optionally, more than three phase currents are possible and would enhance the quality of the Look-Up Table (LUT) in terms of smaller wavelength spacing, however increasing also the LUT size.

3.3.5 Look-Up Table Generation

The aim of the calibration process is to obtain a LUT in which stable wavelengths and their corresponding current triplets are stored. How this LUT is generated is described in the next section.

At the beginning of the calibration for each of the three phase currents, a full characterization has been done, yielding to maps of wavelength, power, SMSR, etalon and reference signals. To overcome hysteresis effects, each measurement has been carried out three times, two times with the positive slope of the tuning vector and one time with the negative slope. This measurement data sets are fed to the processing software (red arrow) which flow is illustrated in figure 3.19. The generation program is divided into eight independent functions, after each step the LUT evolves in precision and stability. These functions are described in more detail in the next paragraphs.

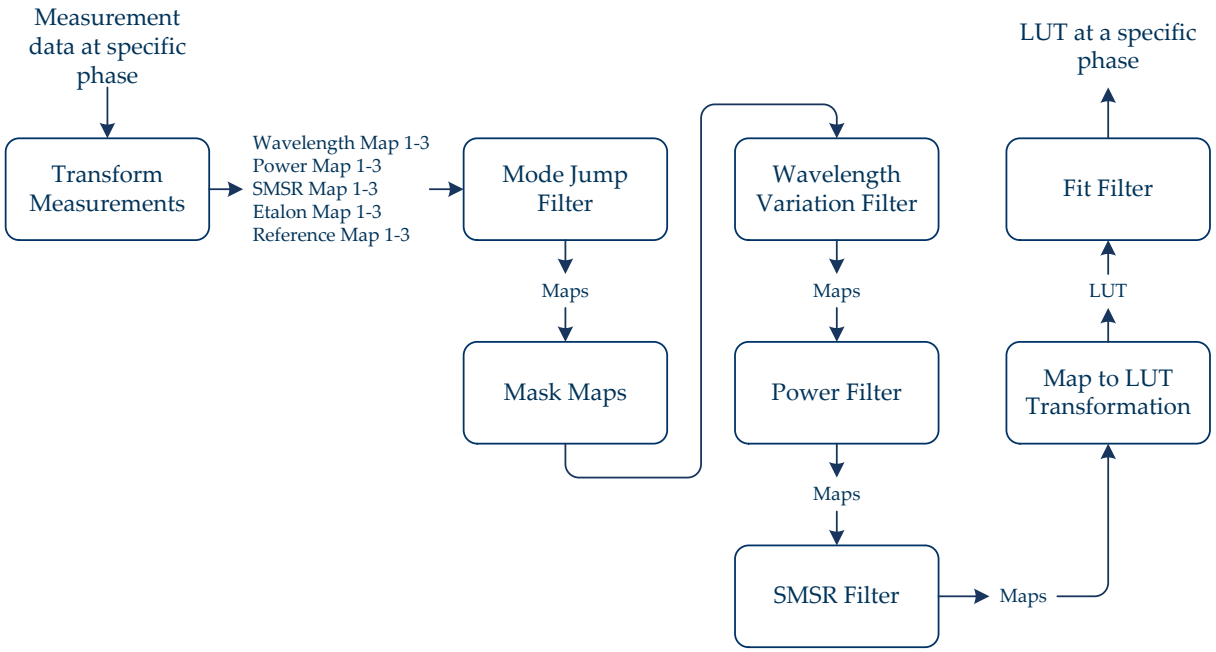

Figure 3.19: *Flowchart for LUT generation for a single phase current of the laser. The different functions are described in the next chapter.*

Mode-Jump Filter As it can be seen in the wavelength map of figure 3.17 on the left, the wavelengths are concentrated on island divided by a common border. The islands across a wavelength band (in diagonal direction from bottom left to top right) have nearly the same wavelength value. When a supermode hop occurs the wavelength band is changed, resulting in a high variation of the output wavelength. The wavelengths located at the border of the wavelength islands are not as stable as the wavelengths located in the middle of a wavelength island. For that a special filter has been designed to remove these points and their corresponding current triplets.

For this filter a kernel based algorithm is applied to the wavelength map. The kernel consists of nine pixels and has a quadratic shape. An illustration of the filter kernel is given in figure 3.20. The center pixel's wavelength is compared with its eight adjacent pixels by calculating the absolute wavelength difference. If a pixel is identified having a difference bigger than 100 pm, the center pixel is declared as unstable and is then

removed from the map. By applying the filter to all pixels of the map the border regions are deleted.

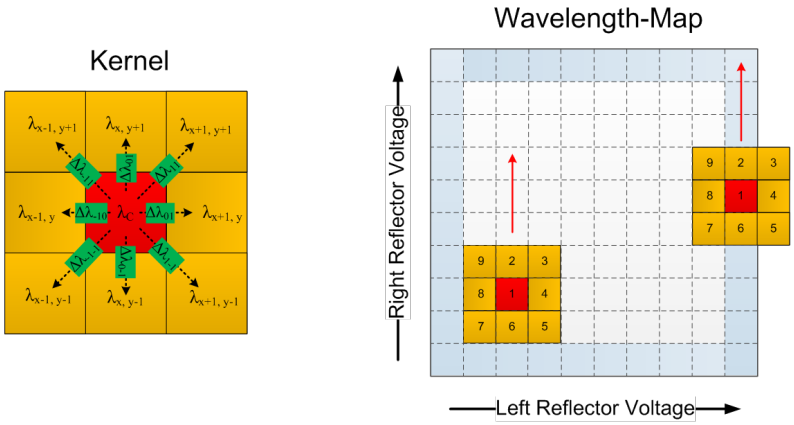

Figure 3.20: *Left: Filter kernel with eight adjacent pixels surrounding a center pixel. Right: Applying the mode-jump filter kernel to a wavelength, schematic view.*

The results when applying the mode jump filter can be seen in figure 3.21. On the left side the initial wavelength map is shown for which the mode jump filter kernel is applied, resulting in a wavelength map shown in the right of figure 3.21.

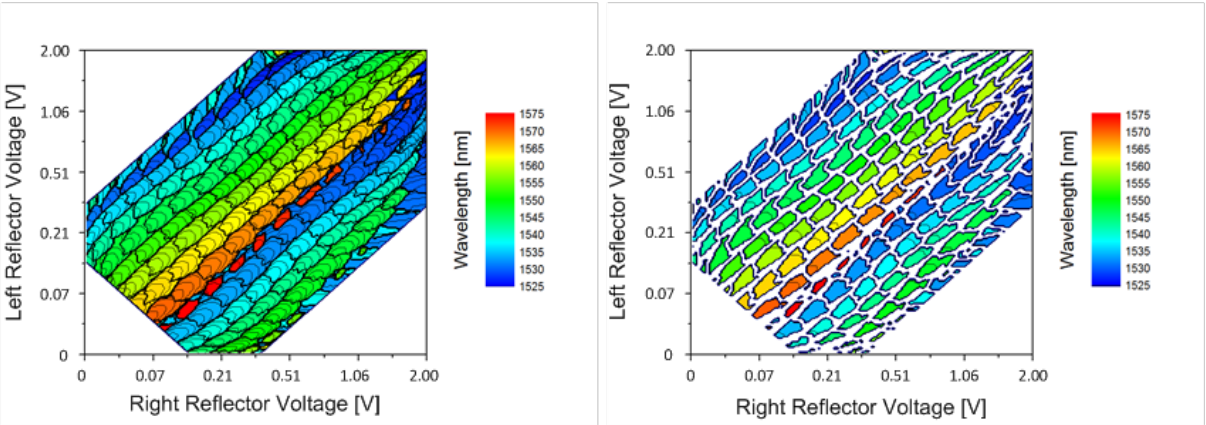

Figure 3.21: *Left: Initial wavelength map. Right: New wavelength map with removed unstable wavelengths on the border between wavelength islands.*

Masking Filter By investigation of the wavelength maps it is obvious that the same wavelength is generated by multiple combinations of the current vector. In fact, complete wavelength bands have repeating patterns which do not contribute to a stable and detailed LUT. If the laser currents are changed by a high amount the internal processes of the MG-Y structure is disturbed resulting in wavelength fluctuations. In addition the laser's temperature controller must be able to deal with such high fluctuations. For better stability strong current slopes shall be avoided. In order to delete repeating patterns in the wavelength map, a masking filter is applied to the map. This is illustrated in figure 3.22 by the red shadowed area in the left picture. In the right picture the repeating pattern is deleted resulting in a LUT which allows a more smooth tuning of the laser.

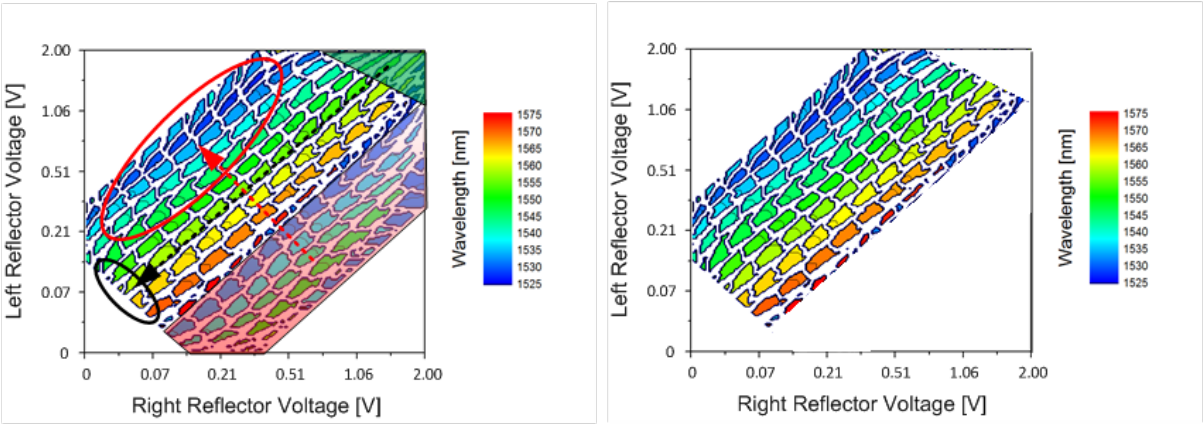

Figure 3.22: *Left: Wavelength map with repeating patterns (marked with red and black color). Right: Repeating patterns are removed.*

Wavelength Variation Filter This function is applied to the wavelength map to delete points which are identified to be affected by hysteresis effects. As mentioned before, the maps are measured with the positive and negative slope of the tuning vector. By comparing these maps, points with identical current triplets but with a wavelength difference higher than 10pm are declared as hysteresis affected and are deleted. The remaining points have almost no significant hysteresis.

Power and SMSR Threshold Filter As a last data consolidating step, the remaining wavelength maps are checked point by point for their power level and SMSR. Too low power and a poor SMSR will negatively affect the accuracy of the measurement system. Therefore points with power lower than 7.5 dBm and SMSR lower than 25 dB are deleted. In figure 3.23 the power (left side) and the SMSR (right side) measured by the wavelength meter are illustrated. In addition also the threshold levels are indicated by dashed lines.

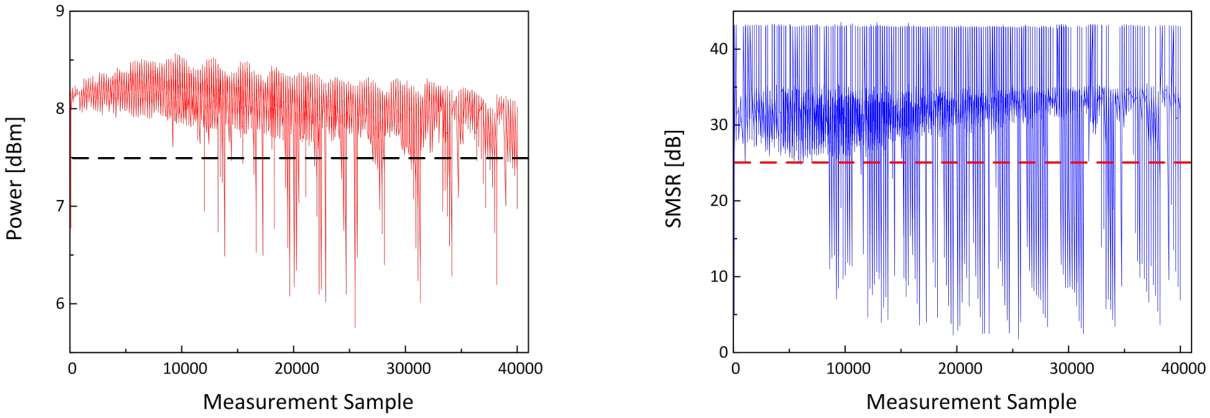

Figure 3.23: *Left: Lasers output power for different sample points with indicated threshold level of 7.5 dBm. Right: Side-Mode Suppression Ratio (SMSR) also with indicated threshold level of 25 dB.*

Wavelength Map to LUT Transformation After all fit filters have been applied to the measured wavelength maps, the transformation into a LUT for laser control holding

the current vector can be done. In addition also the etalon and reference photodiode values will be stored in the LUT for later laser stabilization. The wavelength values are sorted in ascending order. The control wavelength triplet as defined by equation 3.2 as well as the etalon and reference diode voltage are located within the same row of the corresponding MG-Y laser wavelength. An excerpt of the LUT for a phase voltage of 0.72 V is shown in table 3.3.

Wavelength [nm]	**RR[V]**	**LR[V]**	**PH[V]**	**Etalon[V]**	**Ref[V]**
1526.039	1.809494	0.493656	0.72	0.766602	1.77887
1526.072	1.780185	0.493656	0.72	0.508881	1.782227
1526.099	1.751494	0.493656	0.72	0.390472	1.782227
1526.463	1.723397	0.425902	0.72	0.488129	1.777191

Table 3.3: *Excerpt of a LUT for a constant phase value of 0.72V.*

After generating the LUT and caring out the first wavelength scan, results as given in figure 3.24 on the left are obtained. The laser's wavelength bands are indicated by the triangular like shape of the red and blue curve. The high fluctuations occurs because on the border region of two different wavelength bands the wavelength overlaps (see red marked area in figure 3.25 on the left). As mentioned before, such high amount of current change is not good for the system stability and has to be avoided. To overcome this problem, a polynomial curve is fitted onto each of the triangular like shaped wavelength bands. Afterwards each right- and left reflector value which differs for more than 200 mV from the fitted value is deleted. The same measurement is carried out with the fitted and cleaned LUT as can be seen in figure 3.24 on the right resulting in a more smooth tuning. Another option would be the interpolation between entries instead of deleting elements.

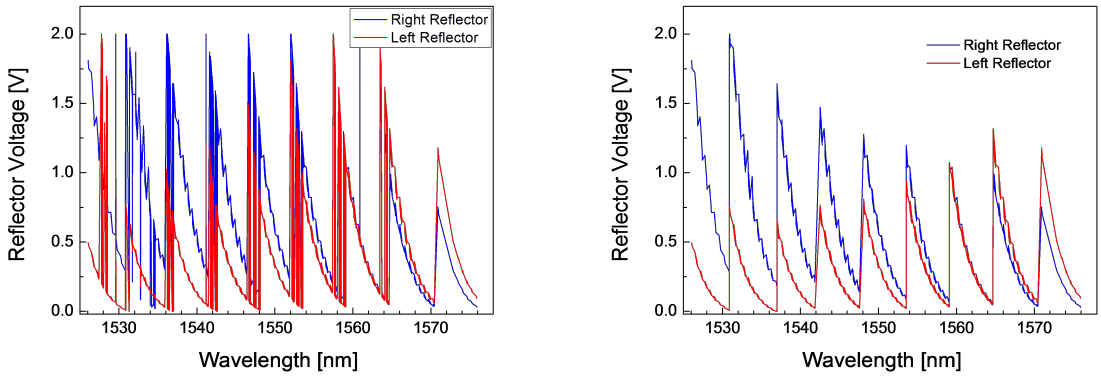

Figure 3.24: *Left: Spectral scan with high fluctuations in reflector values occur due to simple stacking of values. Right: Smooth LUT where values with a certain distance with respect to fitted values are deleted.*

In figure 3.25 on the left side the initial wavelength map corresponding to the non-smoothed LUT is given. The high fluctuations occur at the boundaries indicated by the red circle. The picture on the right shows the LUT where the high fluctuating areas are deleted.

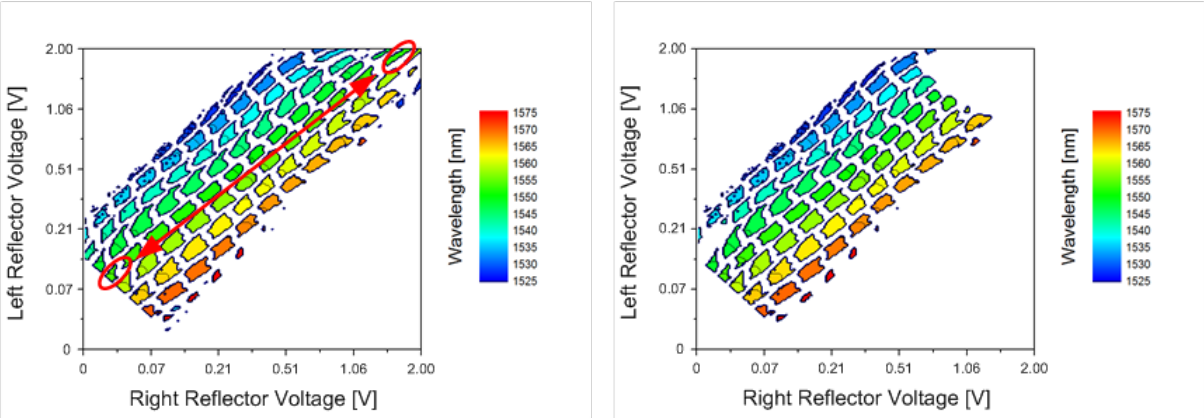

Figure 3.25: *Left: Wavelength map before smoothing. Right: Smooth wavelength map with deleted boundary points which cause high fluctuations in reflector values.*

3.3.6 Master Look-Up-Table Generation and Validation

In the previous section, the generation of a clean and smooth LUT for one phase current was described. For the calibration three different phase control voltages are used for which the resulting LUTs is linked together to a so called Maser LUT. After the linking process, an algorithm is applied to set a minimum wavelength spacing of 10 pm between adjacent wavelength values.

The wavelength spacing as function of the wavelength is shown in figure 3.26 on the left side. The lower wavelength areas between 1526 nm and 1531 nm as well as wavelengths higher than 1570 nm are covered not very well. The reason for the bad covering of the lower wavelength is found later in some noise issues within the used current driver. For the engineering model (EM) of the HSB system, the driver has been changed to a circuit as given in figure 5.3 with better noise performance. The poor coverage at higher wavelengths might result in operating the laser outside its nominal operation area, which is limited up to 1568 nm.

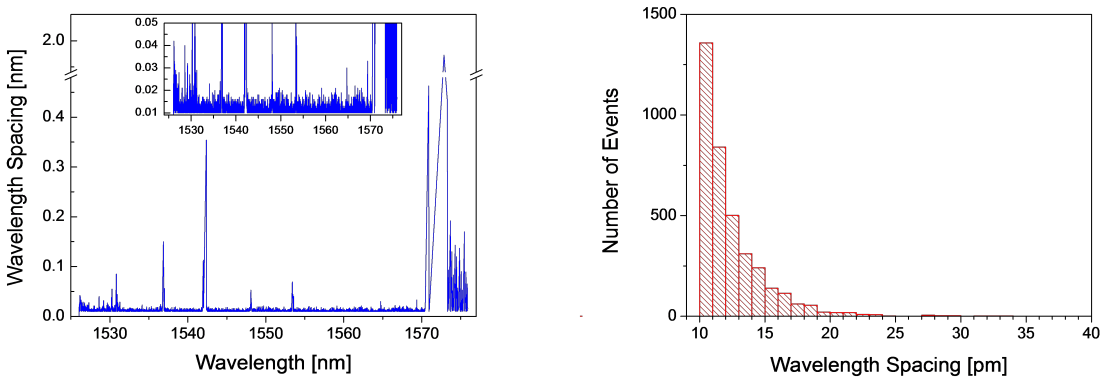

Figure 3.26: *Left: Wavelength spacing of the Master LUT as function of wavelength. Right: Histogram with regard to the wavelength spacing.*

The histogram of the wavelength spacing given in figure 3.26 on the right shows an exponential like distribution, whereby a spacing of 10 pm occurs most frequently.

3.4 Fiber Bragg Grating Technology

The next section introduces the fiber Bragg grating (FBG) technology in detail. Within this work these gratings are used as fiber optical sensors for temperature measurements. The gratings can be written directly into an optical fiber resulting in a very reliable, cost efficient and scalable senor technology. The Fiber Bragg Grating is one of the most popular fiber optical sensor, allowing the measurement of temperature or strain without electrical signals. Multiple FBGs can be implemented in series within the same optical fiber. With adequate multiplexing techniques each single sensor can be read out. The single FBG sensors can be separated from each other by a distance of more than 100 m, limited only by the attenuation of the used fiber.

In 1978 writing of permanent gratings in an optical fiber was firstly demonstrated by Hill et al. [59] at the Canadian Communication Centre (CRC). An intense Argon-ion laser beam ($488nm$) was launched into a germanium doped fiber for several minutes until an increasing of the reflected optical power was observed. By measuring the reflection of the written grating (over the entire 1 m long fiber) with a spectrometer, the formation of a very narrowband Bragg grating filter was confirmed. At this time the photosensitivity of germanium-doped fibers was not known and the results were quite surprising. The effect was further enhanced by understanding the two photon process at $488nm$ going to an single photon process with a wavelength at $244nm$ in the ultra-violet (UV) range which showed a higher efficiency in writing FBGs [60].

In the first years after the discovery of writing techniques, FBGs have been seen mostly as a scientific curiosity. Over time and also due to developments in the fiber-optic telecommunication area, FBGs became the basis for optical communication and sensor systems [61].

An FBG is formed by a periodically change in the fiber core's refractive index along the fiber axes. So no additional element is required, the FBG, acting as sensing element, can be written directly into the fiber core. The length of this refractive index variation is in the range of 10 mm. The length of the grating directly influences the maximum reflectivity given by (3.34). For standard FBGs written with UV laser light with reflectivities of approx. 30% grating lengths of 8 mm . . .10 mm are necessary [62].

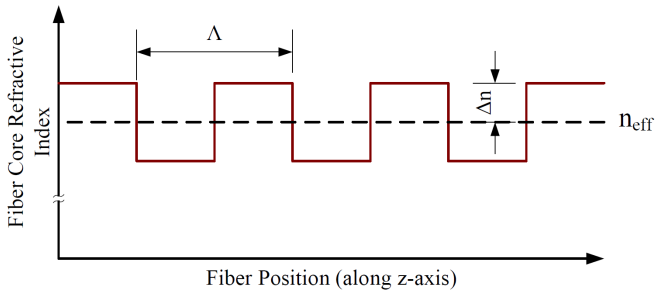

Figure 3.27: *Simplified refractive index of an FBG structure along the fiber position z.*

In figure 3.27 the refractive index along the grating position, written in the fiber's core, is illustrated. The mean value of the structure is defined as n_{eff} and the distance along the fiber axis between two refractive index discontinuities is defined as the grating pitch Λ. The wavelength which shows the highest reflection is determined by the so called Bragg condition [63]

$$\lambda_B \simeq 2 \cdot n_{eff} \cdot \Lambda \tag{3.10}$$

The same grating structure can furthermore be used for dielectric mirrors, optical band filters and in optical add/drop elements in the telecommunication area.

3.4.1 FBG Measurement Principle

In this section the measurement principle for FBG interrogation is presented. As discussed before in the section 3.4, the FBG has a strong reflection for light which fulfills the Bragg condition. When the grating is illuminated by a broadband light source, for example with by a superluminescent diode (SLD), only light for which the Bragg condition holds true is reflected back. The other non-coincided wavelengths can pass the grating without any loss. So, in the reflected spectrum a peak located at the Bragg wavelength λ_B appears. In the transmitted spectrum the difference between input spectrum and reflected spectrum is observed. This is illustrated in more detail in figure 3.28 in more detail.

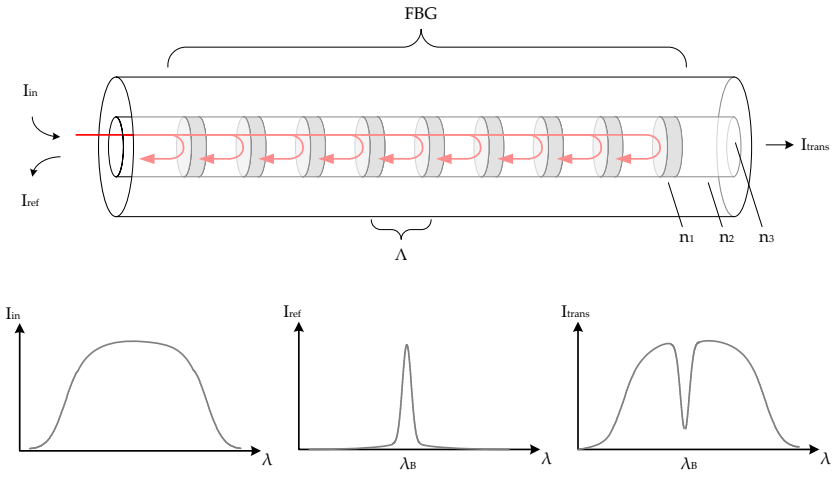

Figure 3.28: *Top: FBG structure with varying refractive index. Bottom-left: Input spectrum to the grating. Bottom-middle: Reflected spectrum at λ_B. Bottom-right: Transmitted spectrum with a dip located at λ_B due to the absence of the reflected light.*

The Bragg wavelength is a function of grating temperature and of mechanical strain applied on the grating. Hence, FBG measurements are in fact measurements of the wavelength at which the Bragg grating reflects light. The change in Bragg wavelength due thermal effects ($\lambda_B(T)$) arises from the thermal expansion of the fiber yielding to a change in the grating pitch and from the temperature dependent refractive index of the fiber $n_{eff} = f(T)$. The response of the wavelength to mechanical strain acting on the FBG sensor $\lambda_B(\epsilon)$ has the origin in the physical elongation of the sensor and the hereby changed grating pitch and in changes in the refractive index due to photo elastic effects ($n_{eff} = f(\epsilon)$). The shift of the Bragg wavelength due to temperature and strain can be expressed according to [64]

$$\Delta\lambda_B(T,\epsilon) = 2 \cdot n_{eff} \cdot \Lambda \left(\left\{ 1 - \left(\frac{{n_{eff}}^2}{2} \right) \left[P_{12} - \nu \left(P_{11} + P_{12} \right) \right] \right\} \varepsilon + \left[\alpha + \frac{\left(\frac{dn_{eff}}{dT} \right)}{n_{eff}} \right] \Delta T \right) \tag{3.11}$$

where ϵ is the applied strain to the grating, $P_{i,j}$ are the Pockels coefficients of the stress optic tensor of the glass, ν is the Poisson ration, α is the thermal expansion coefficient of the glass and ΔT is the temperature difference.

The thermal expansion coefficient of silica (α) is $0.55 \cdot 10^{-5} \frac{1}{K}$ whereas the thermo-optic coefficient $\frac{dn_{eff}}{dT}$ is $8.5 \cdot 10^{-5} \frac{1}{K}$. So the shift due refractive index change is approximately 15 times higher than due to thermal expansion [65, 66]. It can be seen that the shift in the Bragg wavelength due to temperature has its origin first in the change of refractive index due to temperature and secondly due to changes in the grating pitch. For silica glass (SiO_2), the strain affected term can be calculated to [64]

$$\left(\frac{{n_{eff}}^2}{2}\right)\left[P_{12} - \nu\left(P_{11} + P_{12}\right)\right] \approx 0.22 \tag{3.12}$$

Inserting the value from (3.12) and the parameters of (SiO_2) in (3.11) results in a strain sensitivity of a FBG without influence of temperature

$$\frac{\delta\lambda_B}{\delta\varepsilon} = 0.78 \cdot 10^{-6} \frac{\lambda_B}{\mu\varepsilon} \tag{3.13}$$

where λ_B is the Bragg wavelength of the grating and $\mu\epsilon$ is the strain in Microstrain $\frac{\mu m}{m}$. The same approach can be used to calculate the sensitivity of an FBG to temperature without the influence of strain to the grating, yielding

$$\frac{\delta\lambda_B}{\delta T} = 6.67 \cdot 10^{-6} \frac{\lambda_B}{K}. \tag{3.14}$$

Combining the results of (3.13) and (3.14), results in a simple function of Bragg wavelength shift due to temperature and strain

$$\Delta\lambda_B(\epsilon, T) = \frac{\delta\lambda_B}{\delta\varepsilon} \cdot \Delta\epsilon + \frac{\delta\lambda_B}{\delta T} \cdot \Delta T. \tag{3.15}$$

For the interrogation system presented within this work the operation wavelength is located in the telecommunication C-band with a central wavelength of 1550nm. Hence (3.15) can be numerically calculated to

$$\Delta\lambda_B(\epsilon, T) = 1.209 \frac{pm}{\mu\epsilon} \cdot \Delta\epsilon + 10.338 \frac{pm}{K} \cdot \Delta T, \tag{3.16}$$

where $\Delta\epsilon$ is strain in Microstrain and ΔT is the temperature difference in Kelvin.
Due to the by figure 3.29 illustrated capability of wavelength division multiplexing, an optical sensing bus system can be established. In the same fiber more gratings with different Bragg wavelengths λ_{B-i} can be written. The only limitation to the system is an adequate wavelength spacing of the different peaks also when the Bragg peak is shifted due to strain or temperature to their maximum values. Hence the peaks must never overlap to have an unambiguous correlation between peak wavelength and physical sensor number.

In figure 3.29 a sensor fiber containing four FBGs with different Bragg wavelengths is shown. The sensor fiber is illuminated with a broadband light source and the reflection and transmission spectra are illustrated. Light corresponding to the Bragg condition is reflected back and is seen as four independent peaks in the reflection spectrum. In the transmission spectrum in contrast this light is missing, seen as four dips in the transmission spectrum.

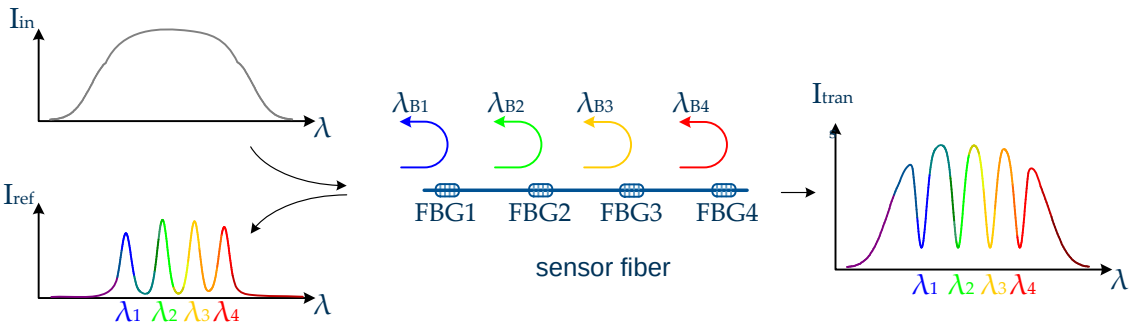

Figure 3.29: *A sensor fiber with four FBGs with different Bragg wavelength $\lambda_{B1} \ldots \lambda_{B4}$ is illuminated by a broadband light source. The single peaks appear in the reflected spectrum and are seen as dips in the transmitted spectrum respectively.*

3.4.2 Theoretical Description

In this section the solution of the coupled mode equation for describing the reflection of an Fiber Bragg grating is derived. Here at this point, the principal solving approach and the final equations for further modeling and simulating of FBG are in focus. [63, 67, 68].

The so called coupled-mode theory is used to gain information about the spectral dependencies of an FBG. The interesting information are the form of the reflection spectra, the maximum reflectivity, the full-width half maximum (FWHM) bandwidth as function of grating length, refractive index modulation and fringe visibility. For the solution of the coupled-mode equations, a simple uniform grating is considered, neglecting the birefringence in optical fibers and chirped or tilted gratings which results in apodized grating. The solution of such gratings is derived in [63].

For the next section a sinusoidal like shape of the induced refractive index change $\delta n_{eff}(z)$ across the fiber core is assumed. This assumption corresponds more to the real gratings than the simplified illustration given in figure 3.27.

$$\delta n_{eff}(z) = \overline{\delta n_{eff}} \left(1 + S \cdot \sin\left(\frac{2\pi}{\Lambda} \cdot z + \Phi(z)\right)\right), \tag{3.17}$$

where S is defined as the fringe visibility giving the modulation ratio for the average induced refractive index change spanning from zero (no modulation) to one (maximum modulation). The refractive index shape following this equation is given in figure 3.30 for an uniform grating with $\Phi(z) = 0$ (red line) and an raised sine apodized grating with $\Phi(z) \neq 0$ (blue line).

For the coupled mode theory two types of slow varying waves $A_m(z)$ and $B_m(z)$ of the m-th mode in the positive and negative direction respectively are assumed. Both waves are illustrated in figure 3.31 [69].

The coupled-mode theory describes the exchange of energy between the waves $A_m(z)$ and $B_m(z)$ in the optical fiber. In an ideal optical fiber these modes are orthogonal to each other and so no mode-coupling and energy transfer between the modes occurs. To calculate the transverse component of the electromagnetic field, a superposition of the m

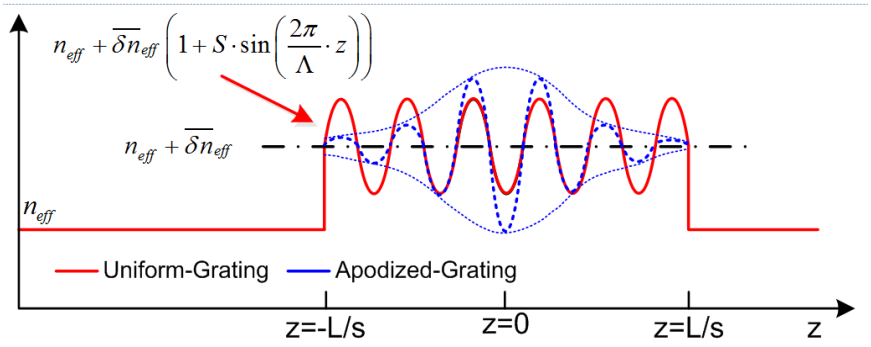

Figure 3.30: *Sinusoidal shaped refractive index change along the fiber for an uniform grating (red) and an apodized grating (blue).*

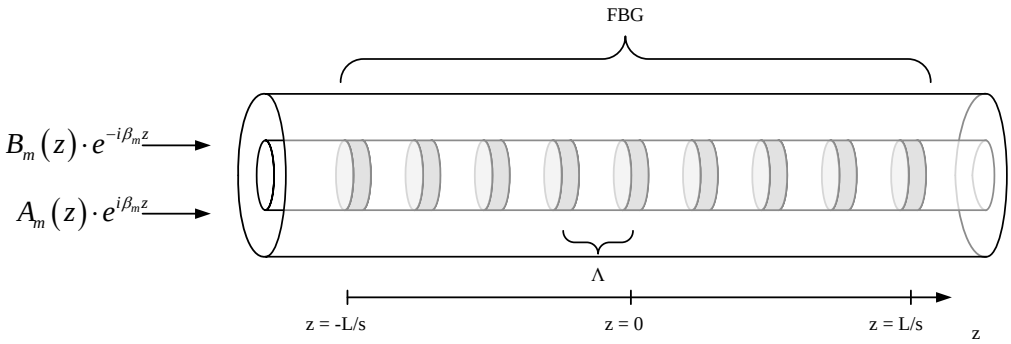

Figure 3.31: *Wave in transmission $A_m(z)$ and in reflection $B_m(z)$ of the m-th mode respectively.*

modes is done [63]

$$E^T(x,y,z,t) = \sum_m \left[A_m(z) \cdot e^{i\beta_m z} + B_m(z) \cdot e^{-i\beta_m z}\right] \cdot \mathrm{e}_m^{\mathrm{T}}(x,y) \cdot e^{-\omega t}, \tag{3.18}$$

where $A_m(z)$ and $B_m(z)$ are the amplitudes in positive and negative direction respectively, β_m is the propagation constant of the m-th mode and $\mathrm{e}_{\mathrm{m}}^{\mathrm{T}}$ indicates the distribution of the LP (linear polarized) modes.

Because all m modes are traveling within the same optical medium, the propagation constant β is given to [42]

$$\beta = \frac{2\pi \cdot n_{eff}}{\lambda_B} \tag{3.19}$$

In the presence of a dielectric perturbation, as it is the case for an optical grating, mode properties are changed which leads to a coupling between the modes and allows now an energy transfer between transmitted wave and reflected wave. The so caused perturbation leads to a variation of the amplitudes $A_m(z)$ and $B_m(z)$ as given in [63]

$$\frac{dA_m}{dz} = i\sum_q A_q\left(C_{qm}^T + C_{qm}^L\right) \cdot e^{i(\beta_q - \beta_m)\cdot z} + i\sum_q B_q\left(C_{qm}^T - C_{qm}^L\right) \cdot e^{-i(\beta_q + \beta_m)\cdot z} \tag{3.20}$$

$$\frac{dB_m}{dz} = -i\sum_q A_q \left(C_{qm}^T - C_{qm}^L\right)\cdot e^{i(\beta_q+\beta_m)\cdot z} - i\sum_q B_q \left(C_{qm}^T + C_{qm}^L\right)\cdot e^{-i(\beta_q-\beta_m)\cdot z} \tag{3.21}$$

Where C_{qm}^T and C_{qm}^L are the transversal and longitudinal coupling coefficients between the modes q and m respectively. For modes travelling in an optical fiber the longitudinal coupling coefficient can be neglected due to $C_{qm}^L \ll C_{qm}^T$. The transversal coupling coefficient between the modes q and m (C_{qm}^T) which are interesting here is given to [63, 70]

$$C_{qm}^T(z) = \frac{\omega}{4}\iint_\infty dx\,dy\,\Delta\varepsilon(x,y,z)\cdot\vec{e}_{qt}(x,y)\cdot\vec{e}_m^*(x,y) \tag{3.22}$$

Where $\vec{e}_m^*(x,y)$ is the conjugated complex LP mode and $\Delta\varepsilon$ is the perturbation of the electrical permittivity caused due to the induced refractive index change in the grating. This permittivity perturbation can be approximated to $\Delta\varepsilon \approx 2\cdot n_{eff}\cdot\delta n_{eff}$ as long $\delta n_{eff} \ll n_{eff}$ holds true. Taken into account the refractive index modulation δn_{eff} in (3.17) the electrical permittivity change yields to

$$\Delta\varepsilon\,(z) = 2\cdot n_{eff}\cdot\overline{\delta n_{eff}}\cdot\left(1+S\cdot\sin\left(\frac{2\pi}{\Lambda}\right)\right) \tag{3.23}$$

Taking into account that the perturbation of the electrical permittivity occurs only in the fibers core region, the transversal coupling coefficient in (3.22) simplifies to [63, 70]

$$C_{qm}^T\,(z) = \sigma_{qm}\,(z) + 2\kappa_{qm}\,(z)\sin\left[\frac{2\pi}{\Lambda}z + \phi\,(z)\right] \tag{3.24}$$

Where σ_{qm} is the so called "dc" period-averaged coupling coefficient and κ_{qm} is the "ac" coupling coefficient defined as

$$\sigma_{qm}(z) = \frac{\omega n_{CO}}{2}\cdot\overline{\delta n}_{CO}\iint_{core} dxdy\cdot\vec{e}_{qt}(x,y)\cdot\vec{e}_m^*(x,y), \tag{3.25}$$

$$\kappa_{qm}\,(z) = \frac{\omega n_{CO}}{4}\cdot\delta n_{ac}\iint_{core} dxdy\cdot\vec{e}_{qt}(x,y)\cdot\vec{e}_m^*(x,y), \tag{3.26}$$

where n_{CO} is the refractive index in the fiber core. The parameters $\overline{\delta n}_{CO}$ and δn_{ac} are the average (dc) and changing (ac) induced refractive index changes in the core. Assuming an FBG written in a single mode fiber, then the number of possible modes are reduced to the fundamental LP01 mode, traveling in positive z- and negative z- direction. Taking this into account, the variation of the amplitudes is then reduced to

$$\frac{dA(z)}{dz} = i\cdot A(z)\cdot C_{01-01}^T + i\cdot B(z)\cdot C_{01-01}^T\cdot e^{-2i\beta z} \tag{3.27}$$

$$\frac{dB(z)}{dz} = -i\cdot A(z)\cdot C_{01-01}^T\cdot e^{2i\beta z} - i\cdot B(z)\cdot C_{01-01}^T \tag{3.28}$$

Finally, the transmitted and reflected waves are coupled together by the coupling coefficient C_{01-01}^T. The resulting power reflection coefficient as function of wavelength $R(\lambda)$ of an uniform FBG is derived by using the synchronous approximation [70]

$$R\,(\lambda) = \frac{\kappa^2\sinh^2\left(\sqrt{\kappa^2-\sigma^2}\cdot L\right)}{\kappa^2\cosh^2\left(\sqrt{\kappa^2-\sigma^2}\cdot L\right)-\sigma^2} \tag{3.29}$$

The ac coupling coefficient κ (see also equation 3.26) is calculated to

$$\kappa = \frac{\pi}{\lambda} \cdot S \cdot \overline{\delta n}_{eff}, \tag{3.30}$$

where λ is the actual wavelength (in a simulation the control variable), S is the fringe visibility and $\overline{\delta n}_{eff}$ is the mean refractive index change in the fiber core of the grating. The dc coupling coefficient σ (see also equation 3.25) is given to

$$\sigma = 2\pi \cdot n_{eff} \cdot \left(\frac{1}{\lambda} - \frac{1}{\lambda_D}\right) + \frac{2\pi \cdot \overline{\delta n}_{eff}}{\lambda} \tag{3.31}$$

The parameter λ_D in equation 3.31 is the design wavelength at which the Bragg peak shall be located. λ_D equals in good approximation to the grating's Bragg wavelength λ_B because $\delta n_{eff} \ll n_{eff}$. If the small dc offset introduced by the induced refractive index change is neglected then $\lambda_D \approx \lambda_B$ holds true. The exact formula for the Bragg wavelength λ_B is derived to

$$\lambda_B = 2 \cdot (n_{eff} + \overline{\delta n}_{eff}) \cdot \Lambda \tag{3.32}$$

and can be simplified by taking into account the approximation $\delta n_{eff} \ll n_{eff}$ to the well known formula, given also at the beginning of this section [67]

$$\lambda_B \simeq 2 \cdot n_{eff} \cdot \Lambda \tag{3.33}$$

3.4.3 Model Verification

In this section the previously derived theoretical model of an FBG shall be verified by numerical simulation and comparison with measurement results from a real grating. The important parameters of the used gratings are known [71] so a detailed modeling is possible. The parameters are summarized in table 3.4. The used grating was a UV written grating provided by the company FBGS in Germany.

Parameter	**Description**	**Value**
λ_B	FBG's central wavelength	1533.131 nm
S	Fringe visibility	0.411
L	Grating length	8.26 mm
n_{eff}	Effective refractive index of fiber	1.43891
$\overline{\delta n}_{eff}$	Refractive index modulation	$8 \cdot 10^{-5}$
R_{max}	Maximum reflectivity	25.6 %
λ_{FWHM}	Full-width at half-maximum	0.0973nm
λ_{WZB}	Full-width between zeros	0.220nm

Table 3.4: *FBG parameters used for model verification [71].*

The comparison between the theoretical model derived from the coupled-mode theory and the measurement result is shown in figure 3.32. In the high reflection area of the FBG the values correlate very well, but in the side-lobes an error in reflectivity between 2-4 percent is present. Considering the measurement results, the peak has a higher side-lobe at the right side towards higher wavelengths than at the left side. This comes from

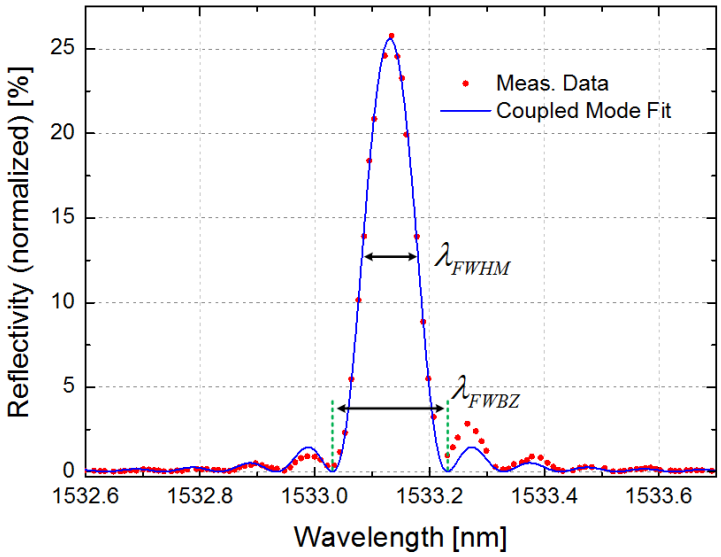

Figure 3.32: *Comparison of the reflected spectrum between the theoretical model (blue line) and the measurement result (red points).*

the apodization effect caused by small alignment errors during the writing process. The model does not consider apodized gratings due to $\Phi(z) = 0$ in equation (3.23).

Further parameter of interest is the maximum reflectivity as function of the grating length (L) and the refractive index change (δn_{eff}). By varying these parameters a custom made grating can be designed. For the maximum reflectivity the following formula applies [67]

$$R_{\max} = \tanh^2\left(\frac{\pi}{\lambda_B} \cdot S \cdot L \cdot \overline{\delta n}_{eff}\right) \tag{3.34}$$

where λ_B is the Bragg wavelength, S is the fringe visibility and $\overline{\delta n}_{eff}$ is the average refractive index change.

In figure 3.33 a simulation of the spectral response of a grating is illustrated. The length of the grating is varied between 1 mm and 15 mm. When the grating length is increased, the reflectivity of the grating increases too. In addition also the side-lobes next to the main reflection peak appear stronger for longer gratings. Such gratings are normally used in telecommunication applications in WDM systems for channel separation for which a high reflectivity is indispensable. For sensor applications such high reflective gratings are seldom used because of the high side-lobes causing measurement errors having the origin in inaccuracies of the peak detection if the side lobes are not recognized or modeled.

In figure 3.34 the simulated spectral response of the average induced refractive index change $\overline{\delta n}_{eff}$ in the range from $1 \cdot 10^{-5}$ to $8 \cdot 10^{-4}$ as control variable is shown. An increase in averaged refractive index change causes higher reflectivity but also higher side-lobes next to the main peak. Also the bandwidth of the grating (λ_{FWHM}) increases with higher values of $\overline{\delta n}_{eff}$. This parameter can be influenced at the writing process by increasing the irradiation time of the fiber to the writing laser beam or by the use of fibers with larger photo-sensitivity. The shape of the reflection spectra of the grating is also affected by higher values of $\overline{\delta n}_{eff}$. At a value of $3 \cdot 10^{-4}$ the reflection spectra is changed to a flat-top shape.

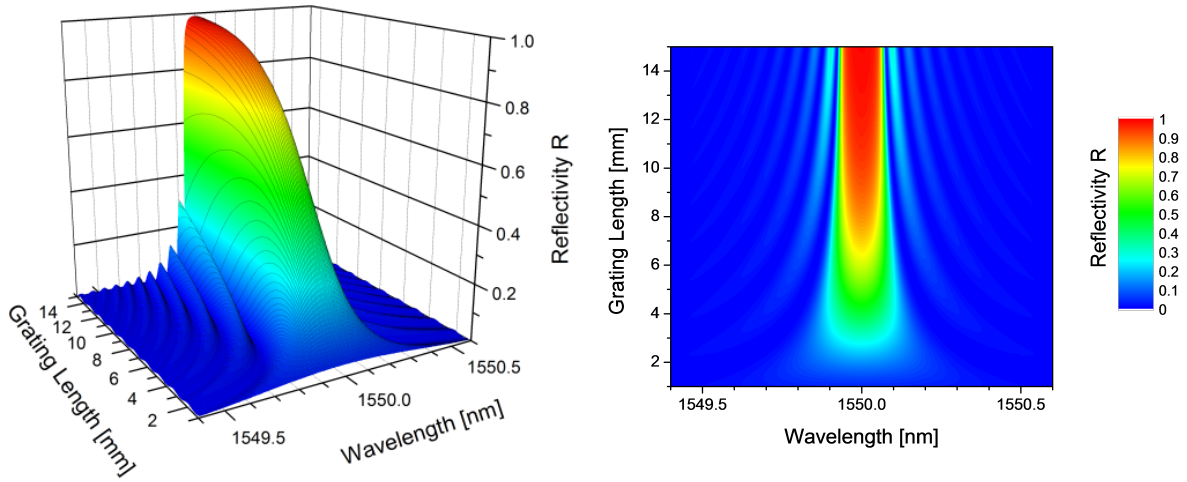

Figure 3.33: *Simulated spectral response of an FBG as function of the grating length (L). Simulation parameters: Grating visibility* $S = 1$*, averaged induced refractive index change* $\overline{\delta n}_{eff} = 0.0001$ *and effective index of refraction* $n_{eff} = 1.45$*.*

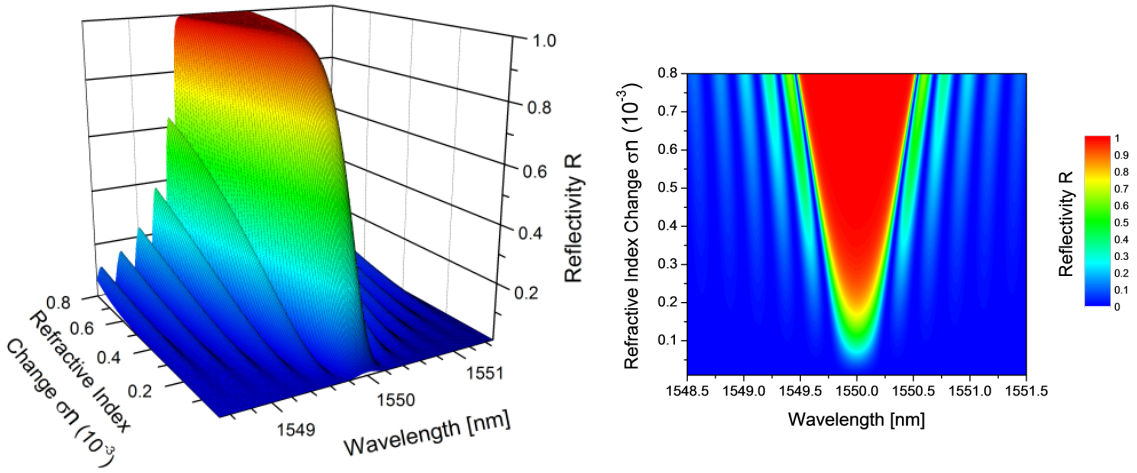

Figure 3.34: *Simulated spectral response of an FBG as function of the averaged induced refractive index change* ($\overline{\delta n}_{eff}$)*. Simulation parameters: Grating visibility* $S = 1$*, grating length* L *=5mm and effective index of refraction* $n_{eff} = 1.45$*.*

3.4.4 Polarization Effects in FBGs

In this section the effect of the birefringence of optical fibers and the herein written gratings is discussed. Because of the fact that the used semiconductor laser output is highly polarized, this effect has an important role within the interrogator system concerning the overall measurement error of the system.

First an introduction to the birefringence in optical fibers is given, including the physical origin of the effect. Afterwards the influence for FBGs written in this fibers is discussed. A mathematical model is presented which allows the calculation of the measurement error due to the birefringence effect. At the end of the section possible mitigation strategies to overcome this effect are presented at the end of the section.

Birefringence in Optical Fibers

In the general approaches it is assumed that the electrical permitivity is a simple scalar which relates the electrical field ($\vec{E}$) to the electrical displacement field ($\vec{D}$) [42]. To extend the theory to the birefringence this scalar must be seen as a 3×3 tensor of second rank with the nine elements. ϵ'_{nm} with $n, m = 1, 2, 3$. The tensor is symmetric for most dielectric materials [42] and so $\epsilon'_{nm} = \epsilon'_{mn}$ can be assumed. By simplifications this tensor can be diagonalized and its eigenvalues remain on the diagonal. All off-diagonal elements will be zero. So $\epsilon_{nm} = 0$ for all $n \neq m$ [42].

$$\boldsymbol{\epsilon} = \begin{pmatrix} \epsilon_{11} & 0 & 0 \\ 0 & \epsilon_{22} & 0 \\ 0 & 0 & \epsilon_{33} \end{pmatrix} \cdot \epsilon_0 \tag{3.35}$$

Now the electrical displacement field can be written as

$$\vec{D} = \boldsymbol{\epsilon}\vec{E} \tag{3.36}$$

The refractive index tensor is related to the electrical permittivity tensor by [42]

$$\boldsymbol{n} = \begin{pmatrix} n_{11} & 0 & 0 \\ 0 & n_{22} & 0 \\ 0 & 0 & n_{33} \end{pmatrix} = \sqrt{\boldsymbol{\epsilon}} = \begin{pmatrix} \sqrt{\epsilon_{11}} & 0 & 0 \\ 0 & \sqrt{\epsilon_{22}} & 0 \\ 0 & 0 & \sqrt{\epsilon_{33}} \end{pmatrix} \tag{3.37}$$

For further discussion the general solution for the wave equation is considered. Special attention is paid to the solution for the electrical field

$$\vec{E}(\vec{r}, \vec{t}) = \vec{E_0} \cdot \exp(-j(\vec{k} \cdot \vec{r} - \omega t - \varphi)) \tag{3.38}$$

$$\vec{H}(\vec{r}, \vec{t}) = \vec{H_0} \cdot \exp(-j(\vec{k} \cdot \vec{r} - \omega t - \varphi)) \tag{3.39}$$

For the propagation of an electromagnetic wave inside a fiber the following assumptions can be made

- The wave is linear polarized (LP1)
- The wave is seen as a transversal electromagnetic mode (TEM) without longitudinal component, hence $\vec{E_{0z}} = 0$ and the electrical field vector follows the form

$$\vec{E_0} = \begin{pmatrix} E_{0x} \\ E_{0y} \\ E_{0z} \end{pmatrix} = \begin{pmatrix} E_{0x} \\ E_{0y} \\ 0 \end{pmatrix} \tag{3.40}$$

- The wave propagates along the fiber in z-direction, so $k_x = 0, k_y = 0$ and the propagation vector results in

$$\vec{k} = \begin{pmatrix} k_x \\ k_y \\ k_z \end{pmatrix} = \begin{pmatrix} 0 \\ 0 \\ k_z \end{pmatrix} \tag{3.41}$$

- The propagation factors in z-direction are different for waves propagating in x- and y-direction, so in general $k_{zx} \neq k_{zy}$, due to $\epsilon_{11} \neq \epsilon_{22}$

By inserting these assumptions into the solution of the wave equation given by equation 3.38, the electrical field in x- and y-direction respectively is given to

$$\vec{E_x}(\vec{r},\vec{t}) = E_{0x} \cdot \exp(-j(k_{zx} \cdot r_z - \omega t - \varphi_x)) \cdot \vec{e_x} \tag{3.42}$$

$$\vec{E_y}(\vec{r},\vec{t}) = E_{0y} \cdot \exp(-j(k_{zy} \cdot r_z - \omega t - \varphi_y)) \cdot \vec{e_y} \tag{3.43}$$

The k-parameter are given due to the inverse dispersion relation to [42]

$$k_{zx} = \frac{1}{\omega\sqrt{\mu_0 \cdot \epsilon_{11}}} \quad \text{and} \quad k_{zy} = \frac{1}{\omega\sqrt{\mu_0 \cdot \epsilon_{22}}}. \tag{3.44}$$

(3.42) and (3.43) describe the electrical field in x- and y- direction. $\vec{E_x}$ and $\vec{E_y}$ have different amplitudes at the same time and position in the fiber due to the inherent birefringence of optical materials for which holds $k_{zx} \neq k_{zy}$.

Degree of Polarization

The polarization state of each light source can be described with the so called *Degree of Polarization (DOP)*, which indicates how strong light is polarized. The value for DOP lies in the range from zero to one, a value of one means that the wave is fully polarized whereas a value of zero indicates a completely depolarized wave.

A good starting point for the calculation of the DOP value are the so called Stokes parameter. The Stokes vector is a set of four real numbers (S_0, S_1, S_2, S_3). The parameter S_0 is directly proportional to the intensity and it is independent of the state of polarization. S_1 indicates the amount of light with horizontal or vertical polarization. S_2 gives the amount of light which is diagonal polarized (45° and 135° respectively). The fraction of the intensity with right or left circular polarization is determined by S_3. [42]

$$S_0 = |E_x|^2 + |E_y|^2 \tag{3.45}$$

$$S_1 = |E_x|^2 - |E_y|^2 \tag{3.46}$$

$$S_2 = 2\mathrm{Re}\{E_x^* E_y\} \tag{3.47}$$

$$S_3 = 2\mathrm{Im}\{E_x^* E_y\} \tag{3.48}$$

For easier calculations the vector is normalized by dividing each value by S_0, hence the values are unit-less and have a maximum amplitude of 1 [42].

$$\vec{S} = \begin{pmatrix} S_0 \\ S_1 \\ S_2 \\ S_3 \end{pmatrix} \quad \Rightarrow \quad \vec{S}_\mathrm{N} = \frac{1}{S_0}\begin{pmatrix} S_0 \\ S_1 \\ S_2 \\ S_3 \end{pmatrix} = \begin{pmatrix} 1 \\ S_{\mathrm{N}1} \\ S_{\mathrm{N}2} \\ S_{\mathrm{N}3} \end{pmatrix} \tag{3.49}$$

The stokes vector is independent from time and position because the electrical field vectors include all necessary information. The four parameters follow the relationship $S_0^2 = S_1^2 + S_2^2 + S_3^2$. This leads to the conclusion that only three instead of four parameters are necessary for DOP calculation. The DOP of a system, here labeled $\widetilde{\Pi}$, can be calculated according to [72]

$$\widetilde{\Pi} = \sqrt{\langle S_{\mathrm{N}1}\rangle^2 + \langle S_{\mathrm{N}2}\rangle^2 + \langle S_{\mathrm{N}3}\rangle^2} \qquad 0 \leq \widetilde{\Pi} \leq 1 \tag{3.50}$$

$$\langle S_{\mathrm{N}n}\rangle = \frac{1}{T}\int_0^T S_{\mathrm{N}n}(t)dt, \quad n = 1,2,3 \tag{3.51}$$

Birefringence Effects in Fiber-Bragg Gratings

In the previous presented formulas for the FBG reflectivity, see (3.29), no dependency to the direction of the electromagnetic wave is included. Up to now the relative refractive index change δn_{eff} was seen as uniform for x- and y- direction. The idea here in this work is to split up the reflection coefficient $R(\lambda)$ into two reflection coefficients, one for the x-polarized light and one for the y-polarized light [73]. For this, two new refractive indices are introduced, $n_{x,eff}$ and $n_{y,eff}$, respectively. The difference in refractive index is expressed by ζ

$$n_{x,\text{eff}} = n_{\text{eff}} - 0.5\zeta \tag{3.52}$$

$$n_{y,\text{eff}} = n_{\text{eff}} + 0.5\zeta \tag{3.53}$$

It is also assumed, that the refractive index shift $\overline{\delta n_{\text{neff}}}$, the fringe visibility S, the grating length L, the grating pitch Λ have the same value for both polarizations. The AC coupling coefficient κ, defined in the coupled-mode theory model (3.30) is not influenced by $n_{x,\text{eff}}$ nor by $n_{y,\text{eff}}$. Considering the DC coupling coefficient σ (3.31), a clear dependence to n_{eff} can be seen. So two new DC coupling coefficients σ_x and σ_y depending on $n_{x,eff}$ and $n_{y,eff}$ are introduced here

$$\sigma_x(\lambda) = 2\pi n_{x,\text{eff}} \left(\frac{1}{\lambda} - \frac{1}{\lambda_{x,\text{D}}}\right) + \frac{2\pi\overline{\delta n_{\text{eff}}}}{\lambda} \tag{3.54}$$

$$\sigma_y(\lambda) = 2\pi n_{y,\text{eff}} \left(\frac{1}{\lambda} - \frac{1}{\lambda_{y,\text{D}}}\right) + \frac{2\pi\overline{\delta n_{\text{eff}}}}{\lambda} \tag{3.55}$$

where $n_{x,\text{eff}}$ and $n_{y,\text{eff}}$ are the refractive indices in x- and y-direction respectively, $\overline{\delta n_{eff}}$ is the average refractive index change, $\lambda_{x,D}$ and $\lambda_{y,D}$ are the design Bragg wavelengths in x- and y-direction respectively. As can be seen by the parameters $\lambda_{x,D}$ and $\lambda_{y,D}$ the Bragg wavelength is also changed. This means that in the spectrum two peaks appear which are slightly shifted from each other, one for $\lambda_{x,D}$ and the other one for $\lambda_{y,D}$. When the grating is illuminated with completely depolarized light, the two overlapping FBG spectra would be seen as one peak arising from the summation of the two peaks. The two different Bragg wavelengths for each polarization direction follow the equations

$$\lambda_{x,\text{D}} = 2n_{x,\text{eff}} \cdot \Lambda \tag{3.56}$$

$$\lambda_{y,\text{D}} = 2n_{y,\text{eff}} \cdot \Lambda \tag{3.57}$$

Now the reflectivities $R_x(\lambda)$ and $R_y(\lambda)$ for polarization direction in $\vec{e_x}$ and $\vec{e_y}$ can be calculated

$$R_x(\lambda) = \frac{\kappa^2 \cdot \sinh^2(\sqrt{\kappa^2 - \sigma_x^2} \cdot L)}{\kappa^2 \cdot \cosh^2(\sqrt{\kappa^2 - \sigma_x^2} \cdot L) - \sigma_x^2} \tag{3.58}$$

$$R_y(\lambda) = \frac{\kappa^2 \cdot \sinh^2(\sqrt{\kappa^2 - \sigma_y^2} \cdot L)}{\kappa^2 \cdot \cosh^2(\sqrt{\kappa^2 - \sigma_y^2} \cdot L) - \sigma_y^2} \tag{3.59}$$

In figure 3.35 the reflections for a light wave in $\vec{e_y}$ direction and in $\vec{e_x}$ direction is given. As can be seen, the Bragg wavelength of the single reflection spectra are slightly shifted. The total reflection as it would be seen when a complete depolarized light source ($\widetilde{\Pi}$) would be used, is indicated with the blue line. This reflection spectra is simply determined by adding the red and green curve. For the plots it is additionally assumed that the reflected

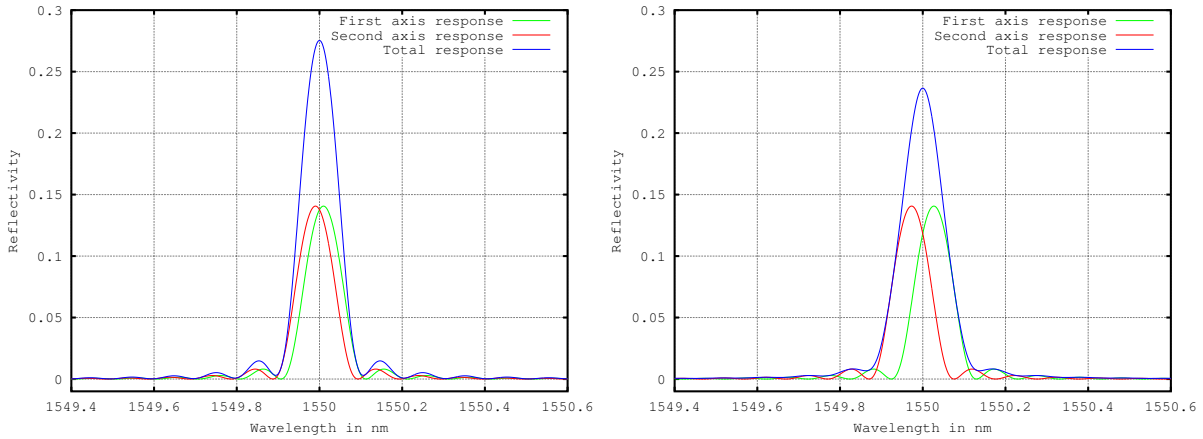

Figure 3.35: *Reflection spectra for both polarizations in $\vec{e_x}$ and $\vec{e_y}$ direction. The blue line indicates the total reflection by adding the red and green curve. For the calculation a birefringence of $1.8 \cdot 10^{-5}$ and of $5 \cdot 10^{-5}$ for the left and right fiber was used respectively.*

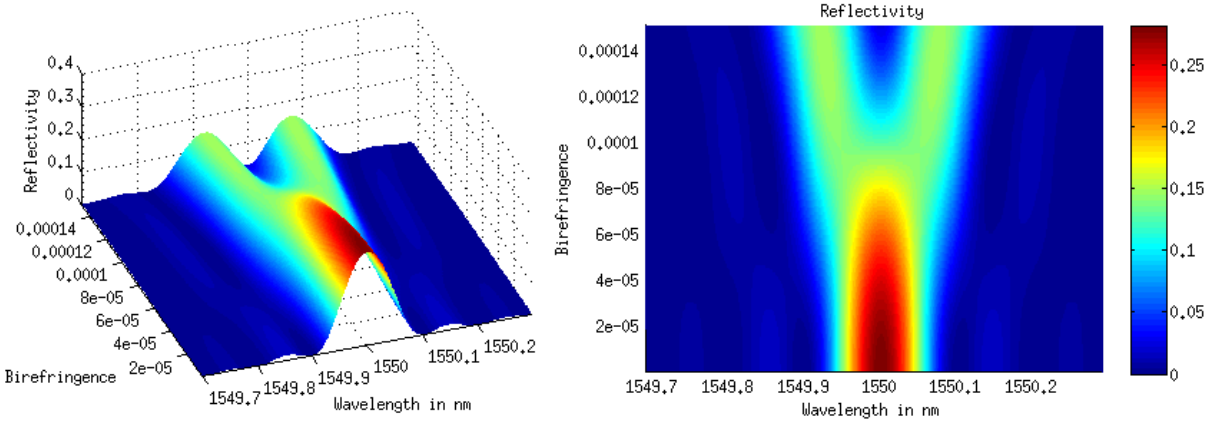

Figure 3.36: *FBG reflection spectra for an uniform lighted FBG for different values of birefringence. For extreme values the peak breaks up into two distinct peaks.*

power in each polarization state is the same. On the left hand side in figure 3.35 the simulated birefringence is $1.8 \cdot 10^{-5}$, on the figure on the right hand side it is $5 \cdot 10^{-5}$. In figure 3.36 the reflectivity of an FBG is plotted. By further increasing the birefringence, the peak becomes broader and the slope is decreased. For extreme values of birefringence the peak breaks up into two separated peaks. For even greater values, the two peaks are shifting further away from each other.

Until here it is assumed that the optical power is equal in x- and y-direction, hence $P_x = P_y$. Since this is not true in praxis, a formula must be found which includes the reflections for both Bragg wavelengths ($\lambda_{x,D}$ and $\lambda_{y,D}$) as function of a polarization depend power in x- and y- direction. The normalized power in the $\vec{e_x}$ direction is defined as ψ, the remaining portion of power $(1 - \psi)$ is then guided in the other polarization direction $\vec{e_y}$.

$$R_{\mathrm{b}}(\lambda) = \frac{P_x}{P_0} \cdot \frac{\kappa^2 \cdot \sinh^2\left(\sqrt{\kappa^2 - \hat{\sigma}_x^2} \cdot L\right)}{\kappa^2 \cdot \cosh^2\left(\sqrt{\kappa^2 - \sigma_x^2} \cdot L\right) - \sigma_x^2} + \frac{P_y}{P_0} \cdot \frac{\kappa^2 \cdot \sinh^2\left(\sqrt{\kappa^2 - \sigma_y^2} \cdot L\right)}{\kappa^2 \cdot \cosh^2\left(\sqrt{\kappa^2 - \sigma_y^2} \cdot L\right) - \sigma_y^2} \tag{3.60}$$

where the reflections for each Bragg wavelength are taken from (3.58) and (3.59). The power P_x and P_y can be calculated with the normalized Stokes vector $\vec{S_{\mathrm{N}}}$ to [42]

$$\frac{P_x}{P_0} = \psi = \frac{1 + S_{\mathrm{N1}}}{2} \tag{3.61}$$

$$\frac{P_y}{P_0} = 1 - \psi = \frac{S_{\mathrm{N2}}^2 + S_{\mathrm{N3}}^2}{2 \cdot (1 + S_{\mathrm{N1}})} \tag{3.62}$$

Since the measurement error induced by the birefringence, is simulated, a mathematical function $\lambda_{Error}(\psi, \zeta)$ can be fitted to the data in order to find an analytic solution. The desired fit-function is a polynomial with a degree of three which has pointed out to find a good and accurate solution. The fitted function is given to

$$\lambda_{\mathrm{Error}}(\psi, \zeta) = p_{00} + p_{01}\zeta + p_{11}\psi\zeta + p_{02}\zeta^2 + p_{12}\psi\zeta^2 \tag{3.63}$$

where λ_{Error} is the error in wavelength due to birefringence and power coupling, ψ is the normalized power in $\vec{e_x}$ direction and ζ is the difference in refractive index. The polynomial coefficients are summarized in table 3.5.

Coefficient	**Value**
p_{00}	0.3659 pm
p_{01}	511.5 nm
p_{11}	-1.023 µm
p_{02}	1.154 mm
p_{12}	-2.313 mm

Table 3.5: *Polynomial coefficients for the computation of the wavelength error induced by birefringence of the fiber.*

The last step is the determination of the DOP for a given maximum wavelength error λ_{Error} due to the birefringence of the fiber. Based on the required value of the DOP, the most suitable depolarization method will be selected.

If the birefringence value of the fiber ζ is known, the value of ψ can be calculated. By using the values $\pm$ 2.5 pm for the maximum allowed wavelength error and $4 \cdot 10^{-5}$ for ζ as birefringence value of the fiber, ψ can be computed to be within $0.46 \leq \psi \leq 0.54$, including some safety margin. By rearranging (3.61) the normalized Stokes vector component S_{N1} can be calculated to

$$S_{N1} = 2 \cdot \psi_{\max} - 1 = 2 \cdot 0.54 - 1 = 0.08 \tag{3.64}$$

The mean value of the Stokes vector components S_{N2} (diagonal polarized part of the light) and S_{N3} (circular polarized part of the light) are zero in the mean value because

both axes of the FBG are illuminated by nearly the same power. The conclusion of the section is that the used depolarization technique must be able to produce a DOP smaller than 0.08. So, a method for deriving the needed DOP for a certain wavelength allowed wavelength error as function of the birefringence of an optical fiber is presented.

3.4.5 Depolarization Techniques

In this section different techniques for depolarizing light are discussed. As given in section 3.4.4, an FBG measurement system, based on a highly polarized light source, shows a measurement error due to the birefringence effect of the used fiber. To overcome this effect, the light sent to the fiber shall have a degree of polarization (DOP) of a value lower than 8%. The presented methods herein are the Lyot depolarizer, the fiber ring depolarizer and an electro-optical polarization scrambler based on a $LiNbO_3$ bulk crystal. Not presented in this work are polarizers based on rotating waveplates due to moving parts and polarization switch based on the Faraday effect, because of the high emitted magnetic field. Both techniques are not usable for space applications due to limited performance.

Lyot Depolarizer

To explain the Lyot Depolarizer a short introduction to the coherence length of laser light is given. The coherence length of a light source (in normal case only laser sources have a notable coherence length) is the certain length within a fixed phase relation of the light wave exists [42]. Within this length, laser light from the same source can interfere. Normally, the coherence length of lasers for interference experiments is larger than the dimension of the experimental setup. So, the coherence length plays only minor role until it is large enough. For the Lyot depolarizer precisely the effect of coherence length is important.

The probability density function (PDF) of the laser's output spectrum is assumed to follow a Cauchy-Lorentz distribution [74]

$$S_{xx}(f, f_0, \xi) = \frac{1}{\pi\xi[1 + (\frac{f-f_0}{\xi})^2]} \tag{3.65}$$

where ξ is the lasers FWHM linewidth (for the used laser here 2.5 MHz, f_0 is the center frequency of the laser light (193.4 THz for light at 1550 nm). According to the Wiener–Khinchin theorem [42], which states that the power-spectral-density (PSD) of a wide-sense-stationary random process is the same as the Fourier transform of the corresponding autocorrelation function. So simply the inverse Fourier transform of the PSD must be calculated to get the autocorrelation function. [75, 76].

By solving the above given equation, the coherence function of a laser light with a Cauchy-Lorentz distributed PSD function is calculated to [76]

$$\gamma_c(\tau) = r_{xx}(\tau) = 1 \cdot \underbrace{e^{-2\pi\xi|\tau|}}_{(a)} \cdot \underbrace{e^{j2\pi f_0\tau}}_{(b)} = e^{2\pi(jf_0\tau - \xi|\tau|)} \tag{3.66}$$

where ξ is again the laser's FWHM linewidth, τ is the coherence time and f_0 is the central frequency. The exponential function (a) is the envelope of $\gamma_c(\tau)$ for which ξ indicates how quick the function decreases [74]. The second function (b) indicates an oscillating

exponential function with frequency f_0. The coherence length and coherence time are also determined by this function where the envelope of $\gamma_c(\tau)$ has dropped to $1/e$. For the used laser here and by inserting the values of ξ =2.5 MHz and f_0 = 193.4 THz in (3.66) the coherence function is given to

$$\gamma_c(\tau) = e^{j1.215\cdot10^{15}\frac{\text{rad}}{\text{s}}\tau - 1.570\cdot10^{7}\frac{\text{rad}}{\text{s}}|\tau|} \tag{3.67}$$

For later calculations of the Lyot Depolarizer, the envelope of the coherence function $\gamma_{\text{c,e}}(\tau)$ is necessary and is given here for a better overview

$$\gamma_{\text{c,e}}(\tau) = e^{-2\pi\xi|\tau|} = e^{-1.570\cdot10^{7}\frac{\text{rad}}{\text{s}}|\tau|} \tag{3.68}$$

The basic functionality of a Lyot depolarizer is that the incoming light is split into two orthogonal paths, one part is retarded and both parts are finally combined together. This concept works only for large retardation above the coherence of the laser light. For such a retardation above the coherence length, the phase shifts with respect to each other are nearly random and the waves lose their ability to interfere in the classic way. Due to the random phase shift, the emerging wave's polarization changes rapidly, so at a certain time the wave is fully polarized (DOP = 1) but in time average the polarization states balances itself out because each state has the same probability [77, 78, 79, 80]. This effect can also be seen as a spectral randomizing of the output states.

For fiber based Lyot depolarizers, two pieces of high birefringent fibers (PM fiber for example) with a defined length are spliced together with an angle of 45°. Due to this setup, the incoming light is fed also 45° towards the two axes of the PM fiber with different refractive indices. One half of the input light travels with the higher phase velocity, whereas the other half travels with a lower phase velocity and is therefore retarded. The length of the fiber depends on the magnitude of birefringence of the fiber and on the laser's coherence length. [78]

The Stokes vector components of the Lyot depolarizer are given according to [76]

$$\langle S_{\text{N1}}\rangle = \text{Re}\{\gamma_{\text{c}}(\tau)\} \tag{3.69}$$

$$\langle S_{\text{N2}}\rangle = 0 \tag{3.70}$$

$$\langle S_{\text{N3}}\rangle = \text{Im}\{\gamma_{\text{c}}(\tau)\} \tag{3.71}$$

$\langle S_{\text{N2}}\rangle$ is assumed to be zero due to the high polarization Extinction Ratio (PER) of 20dB of the used laser. The coherence function $\gamma_{\text{c}}(\tau)$ is derived by (3.67). Taking into account the formula for the DOP (3.50) the DOP of the Lyot depolarizer is simply given by the envelope of the coherence function $\gamma_{\text{c,e}}(\tau)$

$$\widetilde{\Pi}_{\text{Lyot}} = \sqrt{\langle S_{\text{N1}}\rangle^2 + \langle S_{\text{N2}}\rangle^2 + \langle S_{\text{N3}}\rangle^2} = |\gamma_{\text{c}}(\tau)| = \gamma_{\text{c,e}}(\tau) \tag{3.72}$$

Equation (3.68) can now be solved for $\tau(\gamma_{\text{c,e}})$ by taking into account the result from (3.72), yielding

$$\tau(\gamma_{\text{c,e}}) = \mp\frac{\ln(\gamma_{\text{c,e}})}{2\pi\xi} = \mp\frac{\ln(\widetilde{\Pi}_{\text{Lyot}})}{2\pi\xi} = \mp\frac{\ln(\widetilde{\Pi}_{\text{Lyot}})}{1.570\cdot10^{7}\frac{\text{rad}}{\text{s}}} \tag{3.73}$$

For a DOP of 0.08, the required shift in time is computed to $\tau(\gamma_{\text{c,e}})$ = 161ns. The necessary optical path length l_c resulting in this time shift is given by

$$l_c = c_0 \cdot \tau(\gamma_{\text{c,e}}) = 48m \tag{3.74}$$

So one path of the light must see a length difference of $l_c = 48\text{m}$ to result in a DOP of 0.08. By using a highly birefringent PM fiber with a birefringence of about $4 \cdot 10^{-4}$ the total fiber length must be greater or equal to

$$l_{\text{lyot1}} \geq \frac{48\,\text{m}}{4 \cdot 10^{-4}} = 120\,\text{km} \tag{3.75}$$

This result shows clearly that a Lyot depolarizer cannot be used for this laser due to the extreme long fiber length. The solution is not feasible due to the high cost, the non-negligibility of mass impact and the radiation induced attenuation to this long fiber. The Lyot depolarizer can be used for broad light sources like SLDs but not for narrow linewidth semiconductor lasers.

Fiber Ring Depolarizer

The idea of a fiber ring depolarizer was first presented by Lutz [81]. The setup uses only passive components and is well suitable to depolarize light from narrowband light sources in contrast to the Lyot depolarizer. The setup consists out of a 2x2 directional coupler (single mode or polarization maintaining) with a certain coupling ratio k. The coupling ratio is defined as the ratio of the output light between port (3) and port (4) when light is launched into port (1), see figure 3.37. One input and one output port of the coupler are connected or spliced together. For PM fibers forming this loop, the fast axes of the two fibers are oriented 90° with respect to each other. For unsymmetrical coupling ratios ($k \neq 0.5$) the output fiber with the highest output power is selected to form the fiber loop in order to maximize the power in the loop [82]. By Shen et al. [83] a setup was shown which works with standard single mode components, decreasing the setup costs dramatically.

The length of the fiber loop must be longer than the coherence length of the input laser light. The coherence length of the used laser follows the condition

$$l_{\text{c-Laser}} = \frac{c_0}{\pi \cdot \xi} \tag{3.76}$$

where c_0 is the speed of light in vacuum, and ξ is the FWHM linewidth of the laser, here 2.5 MHz. For the used laser in this work the coherence length is calculated to l_c= 38.2 m.

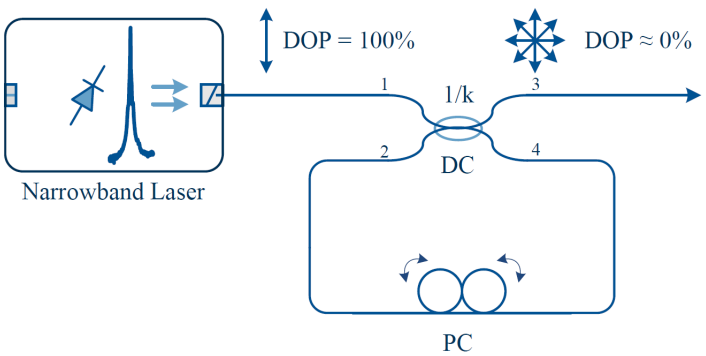

Figure 3.37: *Setup of a fiber ring depolarizer using a directional coupler (DC) with a certain coupling ratio k, for which one output is looped back to the input over a polarization controlling element (PC) [82].*

As discussed before the setup can be made out of polarization maintaining components [81] or by standard single mode components [83]. In the later case the fiber loop must contain a polarization controller to adjust the polarization. Here the first problem arises. Using nearly 40 m of fiber as calculated in equation 3.76, the polarization changes dramatically by moving the fiber or by other mechanical induced stress. So it is not possible to build a compact setup in which the polarization in the fiber loop is adjusted before splicing the loop together. For the presented setup in [81] the use of PM components is recommended. Here the movement of the fiber has no influence to the polarization because the PM fiber holds the polarization state of the light. In this setup the wavelength dependent coupling factor can cause problems. PM couplers have in general a smaller bandwidth as the single mode components, usually in the range of $\Delta\lambda = 20$nm. The laser used within this work has a bandwidth of $\Delta\lambda = 40$nm which is twice the allowed value. If the coupling ratio is changed, the DOP of the fiber ring depolarizer is also changed, so different wavelengths can have different DOPs.

In-Fiber Circular Polarizer

Another possible depolarizing technique is based on a so called chiral circular polarizer [84]. This setup uses special twisted fibers which are twisted while heated up inside an oven or by a high power laser beam. The helical structure defines, how the light is able to propagate inside the fiber. The polarizer is made out of two components, an input polarizer which polarizes the incoming light linearly followed by an circular polarizer. The light at the output of the component is nearly completely circular polarized according to the manufacturer [85]. So it can be assumed that in the output fiber the power in both fiber axes is the same and the FBG connected after the chiral circular polarizer sees identical amount of light from both fiber axes. [86, 87, 84, 88]

Performed experiments in this work have shown that the circular polarization is held also in a normal single mode fiber if the length after the polarizer is kept short (<1 m). In the herein presented system, the single FBG sensors are widely separated, lengths up to several 10 m are possible. The birefringence of the fiber affects the circular polarization because one direction is always traveling faster than the other orthogonal component. So after a few meters the circular polarization is destroyed and the problem of the polarization dependent spectral reflection remains. This fact was also demonstrated during performance tests for the chiral polarizer.

Electro-Optical Lithium-Niobate Polarization Modulator

The electro-optical $LiNbO_3$ polarization modulator is an active device which is used for polarization manipulation of laser light. The modulator is based on a waveguide structure implemented on a $LiNbO_3$ bulk crystal. $LiNbO_3$ is a widely used material in integrated optics because of its high refractive index of 2.3 and its electro-optical properties. The electro-optical property is described as a refractive index dependable to the applied electrical filed. For this basically two effects are responsible, the Pockels effect and the Kerr effect. Whereas the later effect is only important for high light intensities, which is not the case in this application here and can be neglected. [42]

For the tested polarization modulator a PM fiber is aligned with an angle of 45° with respect to the waveguide implemented onto a $LiNbO_3$ bulk crystal, see figure 3.38 [89]. Beside the waveguide two electrodes are implemented, the bottom electrode is grounded and the top electrode is fed to a signal generator. So, across the entire length of the

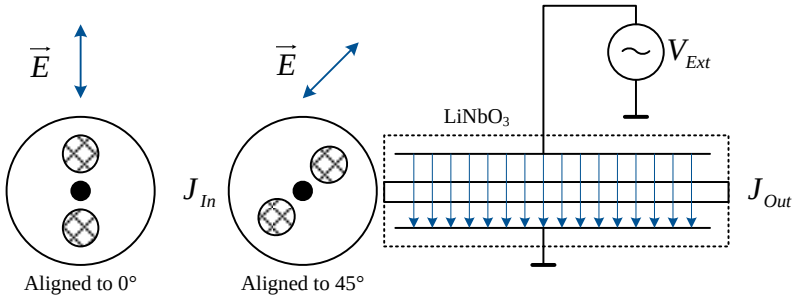

Figure 3.38: *Sketch of the setup of an electro-optical polarization modulator. A PM fiber is aligned with an angle of 45° to a* $LiNbO_3$ *waveguide on which a time varying electrical field is applied.*

crystal an electric field is present, depending on the applied external signal. The traveling light wave sees a phase shift φ which is directly proportional to the drive voltage V_{Ext} [42]

$$\varphi = \pi \cdot \frac{V_{Ext}}{V_\pi} \tag{3.77}$$

The normalized Stokes vector can be calculated from the Jones matrices given in [90] to

$$\vec{S}_{\mathrm{N}} = \begin{pmatrix} 1 \\ \cos(\varphi) \\ 0 \\ \sin(\varphi) \end{pmatrix} = \begin{pmatrix} 1 \\ \cos(\pi V_{\mathrm{RF}}/V_\pi) \\ 0 \\ \sin(\pi V_{\mathrm{Ext}}/V_\pi) \end{pmatrix} \tag{3.78}$$

To generate completely depolarized light, the mean value of the Stokes vector must be zero as it was mentioned before in (3.50). This can be achieved by varying φ from $0...2\pi$ at a constant velocity. So the sine and cosine function will have a mean value of zero. To fulfill this requirement, there are in principle three possible waveforms which can be applied to the modulator: Triangle, Sine/Cosine or Switching. The first two waveforms need a time varying function with a certain frequency. They are often used in amplifier systems in which the polarization state must be changed very fast to achieve a low DOP value.

For the developed system here, the measurement rate is moderate and lies in the range of some Hertz. So no high speed scrambling is necessary, which leads to a third, herein developed method, the so called *"Polarization Switching with Spectral Averaging"*. In this approach low scrambling speed and a synchronization between the measurement cycle and the polarization switching are required. Instead of depolarizing light, as it is done by the two previous presented methods, polarization switching toggles between two orthogonal states of polarization. In other words, the polarization is rotated by an angle of 90° between two measurements. So the light enters the sensor fiber with two subsequent polarization states orthogonal to each other. A birefringence in the fiber or mechanical rotation of the fiber transforms the polarization state but the two polarization states will still be orthogonal. In the FPGA both measurements must be combined by taking the average value of both measurements. As drawback, the measurement rate of this solution

is divided in half.

All three scrambling techniques (triangle, sine/cosine and switching/rectangular) based on the $LiNbO_3$ polarization scrambler showed good theoretical results. The signal amplitude and the scrambling frequency was higher for the methods with time varying signals applied to the modulator than for the switching waveform. The later method is easier to implement into the system developed in this work due to hardware limitations (supply voltage of $\pm$ 5 V. In figure 3.39 the simulation results of the DOP value carried out in this work function of the phase shift φ is plotted.

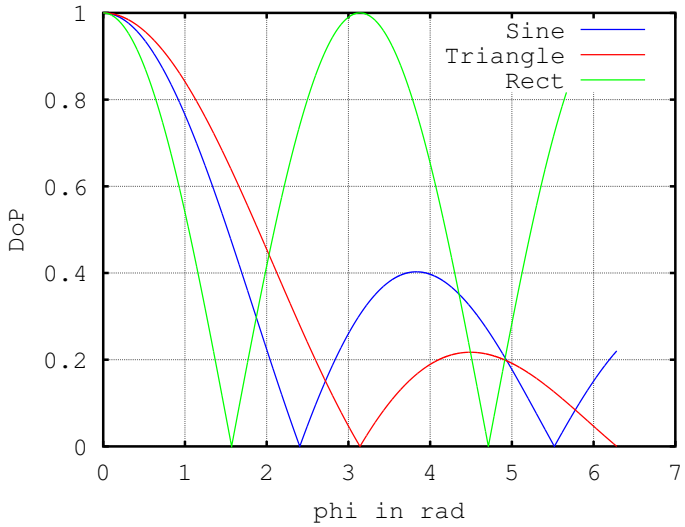

Figure 3.39: *Degree of Polarization (DOP) as function of the phase shift φ for the three presented scrambling methods.*

3.4.6 FBG Type Differentiation

FBG sensors are classified in three main groups depending on the necessary pulse energy during the writing process. The application area of the different types is distinguished by the allowed maximum operating temperature and the shape of the spectral response of the gratings. [91, 67, 68, 92]

- Type I gratings are formed in photo resistive fibers (Ge-doped or hydrogen H_2 loaded) at moderate intensities. The change in refractive index is caused due the local periodically variation of the light intensity of the writing laser beam. The reflection spectrum of the FBG is complementary to the transmission spectrum. So, there is no excessive loss in the cladding. Type I FBGs can be erased at relative low temperatures of approximately 200°C. The operation temperature range of this kind of FBGs is in the range from -40°C and +80°C [67]. The spectral width (λ_{FWHM}) lies in the range of 100pm. These gratings are widely used for sensing applications due to the moderate cost and good spectral performance [71]. The spectral response follows also strongly the coupled-mode model derived in section 3.4.2. [91, 67, 68, 92]

- Type II gratings are formed when high power pulsed lasers are used which damage the glass crystal locally. This results in a local change in refractive index along

the fiber. The necessary pulse power is given to approximately 30mJ. Such FBGs have a higher FWHM spectral width than type I FBGs and in general also a higher reflectivity [91]. The advantage of this type of fibers is the high maximum operating temperature of approximately 800°C. The FWHM spectral width lies in the range of 1nm. [91, 67, 68, 92]

- Type IIa/In gratings are a special form of type I gratings. In a static condition there is no difference in spectrum observable between type I gratings and type IIa gratings. The manufacturing process is different for type IIa gratings because the laser beam is not stopped after the initial grating appears. With continued exposure a second grating grows which exhibits a steady blue shift in the spectrum. The maximum operation temperature can be up to 500°C and is much higher than for type I gratings. Pure type IIa/In gratings are mostly of academic interest. [91, 67, 68, 92]

In addition to these three categories grating with combined properties have been presented. Mihailov et al. [93] has presented a grating written by a 800nm femto-second infrared (fs-IR) laser and a phase mask which combines the high spectral quality of type I gratings with the high operating temperature of type IIa gratings. The writing process by fs-IR laser pulses instead is a writing process which forms normally [67] type II gratings.

3.4.7 Fabrication of FBGs

As discussed before in section 3.4.2, the fabrication of an FBG is done by changing the refractive index δn_{eff} of the optical fiber core locally and periodically for a certain length L. The fiber type of interest is usually a single mode fiber in which only one transversal mode is present.

The writing process is usually done with UV laser light, due to the reaction of the UV light with photosensitive elements in the fiber core such as Germanium (Ge). This chemical process changes the refractive index δn_{eff} by a small factor, enough to induce a perturbation in the electrical permittivity $\Delta\epsilon$. The photosensitivity of the fiber core can be enhanced by implementing more Germanium (Ge) during the manufacturing process of the fiber [94]. The incident UV light forms a so called GeE' color center through photoionization of a GeO defect in the fiber core. These resulting color centers are responsible for changes in the UV absorption spectrum of the glass whereas the refractive index change δn_{eff} follows from the Kramers-Kronig relationship [94, 95]. The photo-induced refractive index change δn_{eff} is proportional to the Ge-dopant concentration. [67]

Another commonly used technique to increase the photosensitivity of a fiber is the so called hydrogen (H_2) loading under high pressure before the writing process. The high intense writing laser light causes the dissolved hydrogen to react in the glass with the Ge atoms, which results in a large permanent index change inside the fiber core [96, 97]. It has also been shown that the necessary laser intensity to write an FBG into the fiber is by the factor of seven lower in hydrogen loaded fibers than in unloaded fibers [98].

Amplitude Splitting Interferometer

In figure 3.40 a setup for writing FBGs in a fiber with an amplitude splitting interferometer is shown [92]. The writing laser beam with its wavelength λ_W is split up into

two beams with equal power. The wavelength of the laser light is usually located in the region in which the fiber is photosensitive, this is normally the case in the UV region. Both beams interfere with each other at the fiber's core location. The distance of the interference patterns with the maximum intensity (shown in blue bars) is the design grating pitch Λ and is given to [67]

$$\Lambda = \frac{\lambda_W}{2 \sin \alpha} \tag{3.79}$$

where λ_W is the wavelength of the writing laser beam and α is the angle between the horizontal axis of the fiber and the single beam. By changing the angle α the grating pitch Λ is affected and so the design Bragg wavelength can be written into the fiber.

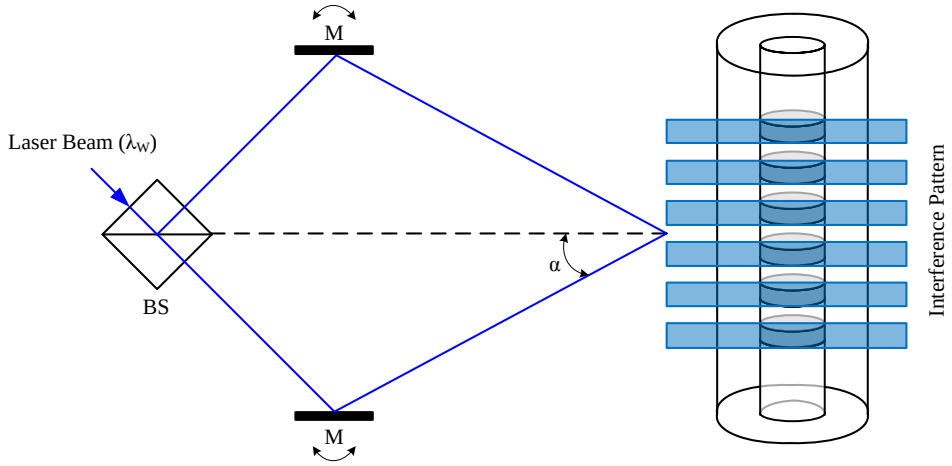

Figure 3.40: *Setup of the amplitude splitting interferometer for FBG writing, BS beamsplitter, M mirror. Drawing according description in [92].*

Phase-Mask Technique

A better method in terms of spectral quality of the grating is the phase-mask writing technique. A diffraction grating (phase mask) is implemented between laser light and optical fiber, which spatially modulates the writing beam and generates hereby the necessary interferogram. Special attention must be paid for the design of the phase mask, due to the fact that the interference pattern is generated between the -1. order and the +1. order. Hence, the power in these orders must be maximized, whereas the power in the 0. order ideally is suppressed. [99, 100]

The period of the FBG grating is directly a function of the of the phase mask's pitch [67]

$$\Lambda = \frac{\Lambda_P}{2} \tag{3.80}$$

where Λ_P is the pitch of the phase mask. A principal setup for the phase mask writing technique is illustrated in figure 3.41. The laser beams with the -1. order and +1. order create an interference pattern which is focused in the fiber core. The wavelength of the incident laser beam is located in the ultra-violet range (normally 244 nm generated by an Ar-Ion laser) for which the fiber shows a photosensitive behavior.

A tuning of the Bragg wavelength without changing the pitch period of the phase mask or the wavelength of the writing laser beam can be achieved by an angular orientation

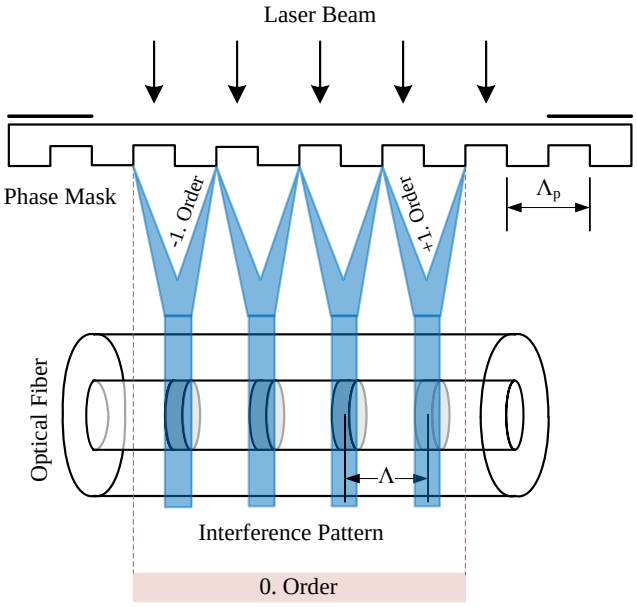

Figure 3.41: *Illustration of the FBG writing process using a phase mask and an UV writing laser. Drawing according description in [99, 100].*

between phase mask and fiber [100] or by the combination of the amplitude splitting interferometer and the phase mask. In the latter case the phase mask acts as beam splitter and as Bragg wavelength reference. Such a combination allows the inscription of widely tunable FBGs with a tuning range of more than 800 nm [91].

Femto-Second Infrared (fs-IR) Pulse Technique

Another technology for writing FBGs came up with the commercial availability of femto-second IR mode-locked laser. For this technique, pulse durations in the range of 100 fs and pulse peak energies up to 2 mJ are necessary [101]. The mostly used laser system is a Ti:Sapphire laser with a central wavelength of 800 nm [102, 93, 103, 104].

The focus of the fs-IR pulse reaches in the fiber core the glass transition temperature T_G and causes a refractive index change in the fiber due to induced dielectric breakdown. This results in localized melting and glass material compaction, hence the density and so also the electrical permittivity are changed. This comes to the same result as for UV written gratings, whereas for UV grating a photo-chemical reaction is responsible for the density change. [93, 98, 105, 106]

A setup for writing FBGs with fs-IR pulses point-by-point is illustrated in figure 3.42. The fs-IR pulses are focused into the fiber core with a microscope objective while the fiber is precisely moved along the fiber axis. The pulses and the focus position of the fiber must be exactly synchronized. The spectral and physical properties of such FBGs are similar to type II UV gratings [107]. The main challenge of this technique is the required sub-μm precision of the translation stage.

Other possibility is the use of a precise phase mask and the corresponding setup as presented in figure 3.41 with the only difference that a fs-IR laser source is used. With this solution the translation stage and the synchronization would be obvious. When the phase mask is used, special attention must be given to the broad optical spectrum of the fs-IR

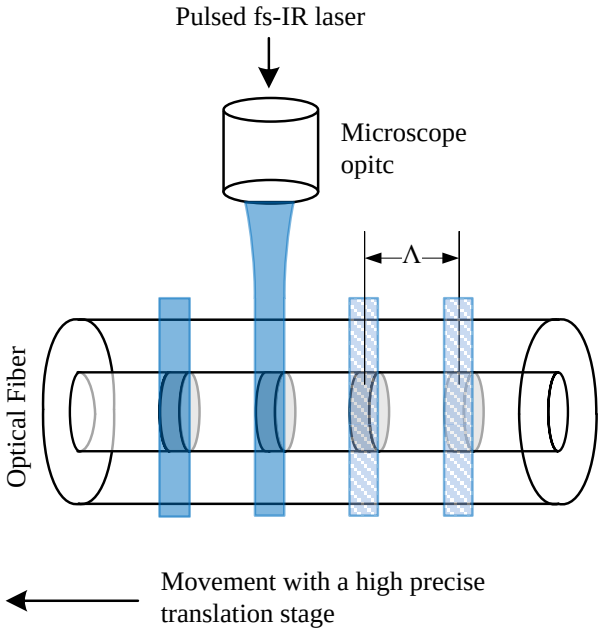

Figure 3.42: *Setup for writing FBGs with a femto-second infrared (fs-IR) pulsed laser and a high precision translation stage [102].*

pulses. When such a pulse passes through a phase mask, the pulse would be dispersed and its energy would be spread over a large area, resulting in lower peak intensity in the fiber. The pitch width of the grating must be readjusted to counteract the dispersive effect [108, 99]. It has also been shown that with the fs-IR technique it is possible to write both type-I and type-II FBGs into a fiber [101]. FBGs with a high refractive index change δn_{eff} of $1.9 \cdot 10^{-3}$ and a low polarization dependency can be produced with few light pulses [105]. It has been shown that with the fs-IR writing technology it is possible to form FBGs also in fluour (F)-doped, non Ge-doped and no hydrogen loaded fibers [2] or in standard telecommunication SMF28 fibers [105].

In literature various setups for writing FBGs with fs-IR laser pulses are discussed. They can be summarized into four groups:

- Pure amplitude splitting interferometry: The setup as illustrated in figure 3.40 is used. This setup is theoretically possible but without a phase mask the spectral quality of the grating is poor, hence it has no practical relevance.
- Pure phase mask technique: For this process a setup as it is given in figure 3.41 is used. The phase mask is irradiated by the femto-second laser pulses and the interference pattern generated by the phase mask changes due to the high intensity the refractive index in the fiber core. This technique is often used and given in the references hereafter [109, 110, 106, 98, 101, 93, 103, 111, 104, 112].
- Combination of phase mask technique with the amplitude splitting interferometry: By combining the amplitude splitting technique with the phase mask high quality gratings with adjustable Bragg wavelength can be written. The adjustment its done by changing the angle of the mirrors whereas the phase mask acts as beam splitter and wavelength reference. This technique is the most commonly used one and is also discussed in detail in the references herein [113, 105, 114, 115, 116, 117]

- Point-by-point-wise inscription: With this technique the grating structure is written into the fiber, as the name already says, point-by-point wise. The femto-second laser beam is concentrated into the fiber core with a microscope optic. The fiber core itself is brought into the correct position with a precise linear stage. The movement of the stage and the lasers pulse generation must be synchronized. In the following references this technique is presented in detail [118, 119, 102]

In figure 3.43 the spectral response of two FBG sensors written by UV laser light (black curve) and fs-IR laser pulses (right curve) are shown. The measurements were taken by the herein developed interrogator. The UV grating was made by the drawn tower grating technique [71]. The spectral quality is very good, only one small side lobe towards higher wavelengths can be observed. The parameters of this grating are summarized in table 3.4.

The fs-IR grating shown by the red curve in figure 3.43 is written by a 800nm mode-locked laser according the setup presented in figure 3.42. The grating structure is written point-by-point into the fiber with a high precision translation stage. The spectral quality is worser as for the UV written grating but for a type II grating very promising. Two side lobes can be seen on the spectral response, one smaller lobe towards lower wavelengths and one bigger lobe towards higher wavelengths. Despite of the high reflectivity of the fs-IR grating (about 90%), the side lobes were negligible small. The simulation in figure 3.33 shows that at higher reflections the side lobes increase dramatically. It was also observed in the measurement here that the fs-IR gratings do not exactly follow the coupled-mode theory model. This was also observed by other groups presented in [110, 105, 104]. Nevertheless, if high reflection values are needed which increases also the strength of the returned light signal, fs-IR written gratings are the agent of choice.

3.4.8 Bragg Wavelength Peak Determination

For a measurement sequence, carried out by the fiber-optical interrogator module, first the reflected spectra of the FBG has to be queried. As it is discussed in section 3.4.1 the information about strain or temperature lies in the spectral position of the Bragg wavelength λ_B. Hence, this wavelength must be determined by special algorithms as accurate as possible. The most suited algorithm is selected based onto its accuracy, robustness and implementation effort. To the later point a high relevance is given due to the planned implementation inside an FPGA with limited hardware resources.

Algorithm Description

As discussed in section 3.4.2 the best fit-function for a reflected FBG spectra is the coupled-mode equation itself. But considering the formula for the FBG's reflection (see equation 3.29) it becomes clear, that this functions cannot implemented in the target hardware platform due to missing floating point operations and limited hardware resources.

Due to this concern, different fitting algorithms have been considered in this work to find the most suited one. In total up to eight different types of peak find algorithms have been analyzed. They can be divided into two groups, the first group is based on mathematical formulas and equations whereas the second group is based on convolution kernels coming from the signal processing area [120]. For the first group, the formula based fitting functions, the following algorithms were analyzed:

- Maximum Search (MX)

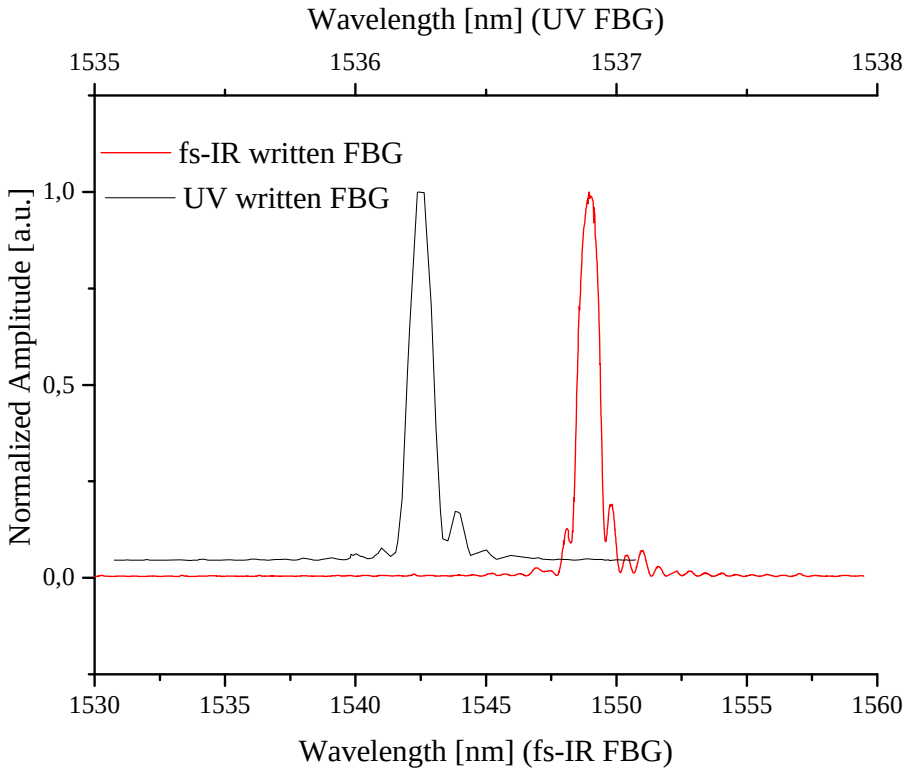

Figure 3.43: *UV written grating from type I (black) and fs-IR written grating (red) with a lower spectral quality due to higher side-lobes than the UV written grating. Note the different x-axes for both FBGs.*

- Centroid (CT)
- Parabolic Interpolation (PI)
- Gaussian Fit (GS)
- Trip-Hop (TH)

For the convolution based algorithms, the following kernels were analyzed:

- Linear Phase Operator (LP)
- Derivative of Gaussian (DoG)
- Derivative of a coupled-mode function (DoC)

The FBGs spectral response is generated by the coupled mode theory model and the different algorithms are applied to this spectrum afterwards. So the performance in terms of measurement error can be estimated for each type of algorithm. The different fits are discussed here in more detail.

Gaussian Fit: For this fit a Gaussian function following the equation [42]

$$I(\lambda) = A \cdot e^{-\frac{(\lambda-\lambda_{cG})^2}{2w^2}} + A_{Bias} \tag{3.81}$$

is fitted on the measurement data. Here the parameter A is the amplitude, A_{Bias} is the amplitude offset, and ω described the width of the Gaussian curve. The resulting Bragg

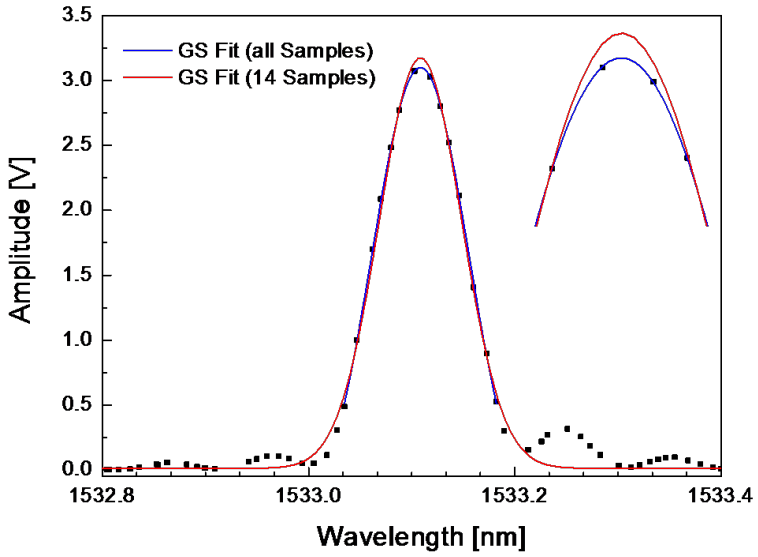

Figure 3.44: *Gaussian fit function applied to an FBG reflection spectrum, measured with the herein developed interrogator system, for all sample points (red line) and for the 14 strongest samples (blue line). A small deviation can be observed to a small fit error due to the FBGs spectral side-lobes.*

wavelength is described with the parameter $\lambda_c G$ which defines the center of the Gaussian curve. The fit has a high precision in the high reflective main peak region but the nonlinear least-square fitting method requires high amount of FPGA resources. Nevertheless, the high precision makes the Gaussian fit predestined for comparing the different fitting algorithms.

The determined Bragg wavelength depends also on the number of used samples. In figure 3.44 a fit by taking into account all measurement data (red line) and only the 14 strongest points (blue line) are illustrated. Both fits converge, but when all samples are taken into account, the Gaussian curve shows a worse approximation to the spectrum than for the 14 strongest points. Same results are presented also in [121]. The data in figure 3.44 were obtained by the developed fiber-optical interrogator system in this work.

Centroid (CT): The area below the FBG spectral response is approximated with n rectangles, each one defined by the amplitude of a sample point and the wavelength spacing between two sample points. Is the spectrum sampled with a non-uniform wavelength spacing, then the area under the i-th sample is defined to [122]

$$A_i = \frac{\lambda_{i+1} - \lambda_{i-1}}{2} \cdot I_i \tag{3.82}$$

where I_i is the amplitude of the i-th sample. For an uniform spaced spectrum as it is obtained for example from a spectrometer, the wavelength difference can be simplified to $\lambda_{i+1} - \lambda_{i-1} = \Delta\lambda_{eq}$. The central wavelength of λ_i can be obtained by graphical evaluation to:

$$\overline{\lambda_i} = \frac{\lambda_{i-1} + 2\lambda_i + \lambda_{i+1}}{4} \tag{3.83}$$

The final calculated centroid wavelength can be calculated to [122]

$$\lambda_{Centroid} = \frac{\sum_{i=1}^{n} \overline{\lambda_i} \cdot A_i}{\sum_{i=1}^{n} A_i} \tag{3.84}$$

by taking into account the area for each measurement sample set A_i from (3.82) and the i-th wavelength λ_i from (3.84). It shall be noted here, that the centroid algorithm is a suitable candidate also for type II gratings with a 'scrawly' spectral response. The principle of the centroid algorithm is illustrated by figure 3.45. For each measurement point a rectangular area is created (light blue boxes) with an area defined by (3.82), afterwards for each area the wavelength middle point is computed according (3.83). As last point the central wavelength is calculated by (3.84).

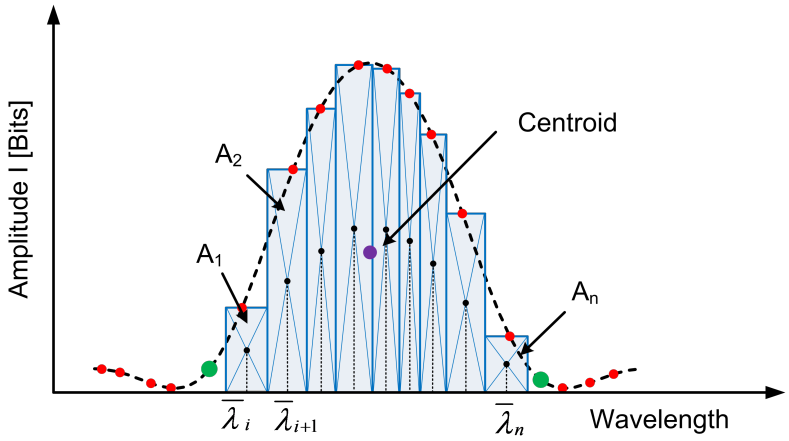

Figure 3.45: *Principle of the centroid fit function to an FBG reflection spectrum.*

Convolution based Peak Find Algorithms: The convolution based algorithms come originally from the digital signal processing area and are widely used for digital filtering and data manipulation [120]. The precision is quite high for uniform sampled gratings as it is the case for measurement date recorded by spectrometer based interrogators. In this algorithm, the data is convoluted by a specific kernel. Depending on the kernels' structure, an additional noise filtering (averaging) is applied on the input data. The idea behind the algorithm is to take the first derivative from the FBGs spectral response, which zero crossing is located exactly at the Bragg wavelength λ_B. A simulation result for a noise affected FBG spectral response (blue line) and the first derivative taken from the averaged signal (red line) is given in figure 3.46. The zero crossing of the first derivative gives λ_B. The intensities $I_{conv.}(i)$ for the first derivative are given to

$$I_{conv.}(i) = \sum_{m=-(M-1)/2}^{(M-1)/2} A_{FBG}(i) \cdot Kernel(i+m) \tag{3.85}$$

where $A_{FBG}(i)$ is the measured signal from the FBG and "Kernel" is the used convolution kernel. In this work three types of filter kernels are investigated:

- Linear Phase Kernel (LP): This type of kernel combined the classical moving average kernel with a derivation kernel for which no additional multiplication is necessary when the kernel is convoluted with the spectral response of the FBG. [122, 123].

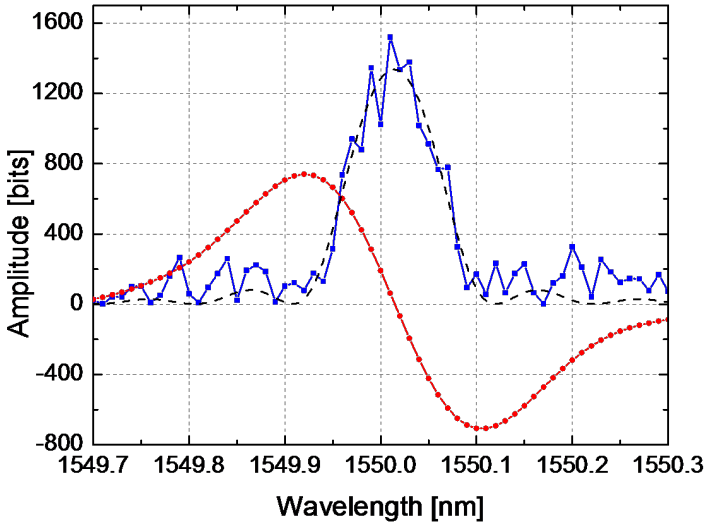

Figure 3.46: *FBG spectral response (blue line) with additional noise and the first derivative of the averaged signal (red line). The black dashed line indicates the ideal theoretical model derived by the coupled mode theory.*

- Derivative of Gaussian Filter (DoG): For signal with additional Gaussian noise this filter type showed in simulations (see section 4.3.4 the best performance. Here it is selected due to the similarity between the spectral response to the Gauss curve. The kernel size defines the cut-off frequency of the filter.
- Derivative of Coupled-Mode Filter (DoC): The FBG response follows the coupled mode function, so a special filter was designed which takes into account its specialties like side lobes. It is assumed that this filter shows a better behavior in terms of accuracy than the DoG based kernel.

The different filter kernels are illustrated in figure 3.47. For the linear phase kernel three different lengths (LP3, LP,5 and LP7), for the DoG two lengths (DoG5 and DoG7) were chosen. Table 3.6 list the filter coefficients and their corresponding transfer function $H(z)$. The amount of used FPGA hardware resources increases with filter type and filter length. The LP-kernels showed the lowest resource consumption and the highest computing speed. The DoC and DoG kernels need multiplicators due to the coefficients defining the shape and this increases the necessary hardware resources and decreases the computing speed. .

Trip Hop Algorithm: This peak find algorithm was developed in this work combining a high accuracy of the algorithm in terms of Bragg wavelength position and low required FPGA resources. In addition this filter type was also implemented in the control FPGA of the designed system. In figure 3.48 a sampled FBG spectrum is shown. Due to the wavelength tuning characteristics of the laser transmitter, the spectral response is sampled non-uniformly. The Trip-Hop algorithm requires three measurement samples for data processing. Hereby two adjacent samples S_1/S_3 have to be located on one edge of the FBG spectrum. As criterion for selection these sample points, the amplitude level shall be near to the half of the FBGs maximum intensity in the area where the FBG spectrum shows a linear gradient. A third sample point S_2 is located on the opposite edge on the right of the spectrum. Thereby the amplitude of S_2 lies between S_1 and S_3. In the next step, a line between $S1$ and $S3$ is interpolated and due to the almost linear slope between

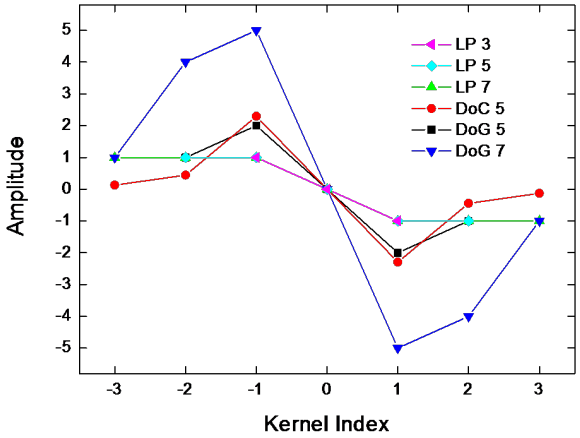

Figure 3.47: *Different filter kernels used for the convolution based algorithms. LP linear phase, DoG derivative of Gauss, DoC derivative of coupled mode fit.*

Type	**Coefficients**	**Transfer Function H(z)**
LP3	[1|0|-1]	$H_{LP3}(z) = z - z^{-2}$
LP5	[1|1|0|-1|-1]	$H_{LP5}(z) = z + z^{-1} - z^{-3} - z^{-4}$
LP7	[1|1|1|0|-1|-1|-1]	$H_{LP7}(z) = z + z^{-1} + z^{-2} - z^{-4} - z^{-5} - z^{-6}$
DoG5	[1|2|0|-2|-1]	$H_{DoG5}(z) = z + 2 \cdot z^{-1} - 2 \cdot z^{-3} - z^{-4}$
DoG7	[1|4|5|0|-5|-4|-1]	$H_{DoG7}(z) = z + 4 \cdot z^{-1} - 5 \cdot z^{-2} - 5 \cdot z^{-4} - 4 \cdot z^{-5} - z^{-6}$
DoC7	[0.13|0.45|2.29|0|-2.29|-0.45|-0.13]	

Table 3.6: *Filter kernels for the used convolution algorithms.*

these points, the inverse gradient can be given as

$$m_{13}^{-1} = \frac{x_3 - x_1}{y_3 - y_1} \tag{3.86}$$

To estimate the Bragg wavelength, a virtual sample S_4 located on the opposite edge with respect to S_2 is generated and has the same amplitude, hence $y_4 = y_2$. Thus $S4$ lies on the interpolated line between S_1 and S_3 and the wavelength for $S4$ is given as

$$x_4 = x_1 + (y_2 - y_1) \cdot m_{13}^{-1} \tag{3.87}$$

The Bragg wavelength $\lambda_B = x_5$ is then derived by calculating the mean value between x_2 and x_4

$$\lambda_B \approx x_5 = \frac{x_4 + x_2}{2} \tag{3.88}$$

This algorithm can be implemented in an FPGA by the usage of one divider, one adder, one subtractor and one multiplier, the division by the factor of two can be done by a simple numerical shift operation. So the resource usage of this algorithm is very small.

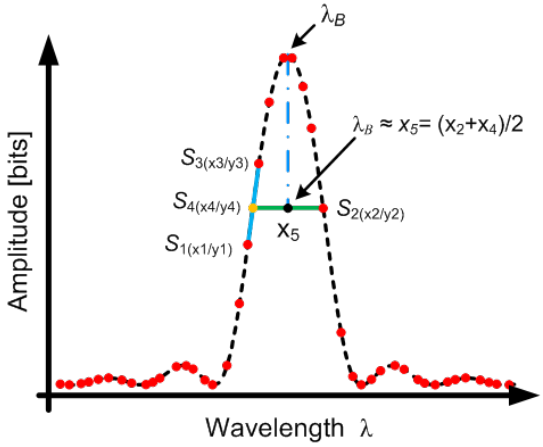

Figure 3.48: *Description of the Trip-Hop algorithm with the selected points S_1 , S_2 and S_3 on the slope of the spectrum and the calculated points S_4 and $x_5 \simeq \lambda_B$*

For the selection of the points S_1, S_2, S_3 a small decision logic must be implemented to increase the robustness. In the case that the FBG spectrum is represented only by a few samples, no sample triplet may be found. Hereby the Bragg wavelength is calculated using one sample on the left and another on the right edge of the FBGs spectral response.

Parabolic Interpolation: For this type of fit a mathematical function is fitted to the measurement results for which the vertex of the function determines the estimated Bragg wavelength

$$\lambda_B = \frac{\lambda_2^2 \cdot (y_3 - y_1) - \lambda_1^2 \cdot (y_3 - y_2) - \lambda_3^2 \cdot (y_2 - y_1)}{2 \cdot (\lambda_2 \cdot (y_3 - y_1) - \lambda_1 \cdot (y_3 - y_2) - \lambda_3 \cdot (y_2 - y_1))} \tag{3.89}$$

A polynomial fit to a set of measurement data is shown in figure 3.49. Such a function

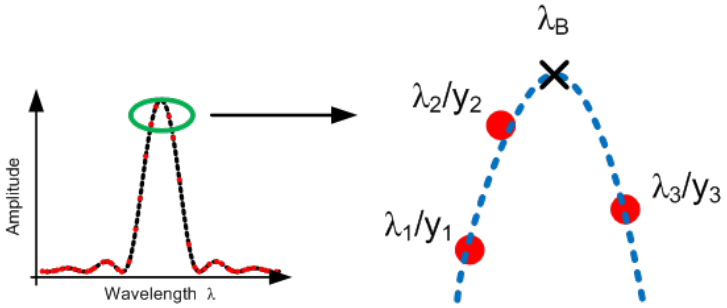

Figure 3.49: *Illustration of a polynomial fit on the FBG spectral response. The vertex of the function is the estimated Bragg wavelength λ_B.*

would work on a standard computer but the implementation in an FPGA would be a challenging task.

Simulation Environment

A numerical simulation tool was developed to estimate the peak find algorithms performances. A scheme of this simulation is shown in figure 3.50. At the beginning, the FBG spectral response for the design Bragg wavelength λ_B based on the coupled-mode model (see also section 3.4.2) is generated. The shape of the coupled mode function

depends on the input parameters such as grating length L, grating period Λ, induced average refractive index change $\overline{\delta n}_{\text{eff}}$, effective refractive index n_{eff} and the fringe visibility S of the FBG structure. In the second stage the generated spectrum is sampled non-uniformly to simulate the wavelength tuning characteristic of the used laser. Hereby, the spacing between consecutive wavelength values follows an exponential distribution. For noise analysis, intensity noise is added to the sampled FBG spectrum. The SNR of the FBG spectral response is defined as the ratio between the FBG's maximum reflectivity and the Gaussian noise variance. Intensity noise may occur due to power fluctuations from the laser, shot and thermal noise from the photodetector and jitter of the laser's output wavelength. To emulate the interrogator's detection unit, the FBG spectrum is sampled with a resolution of 12 bit allowing also to add different noise sources to the signal.

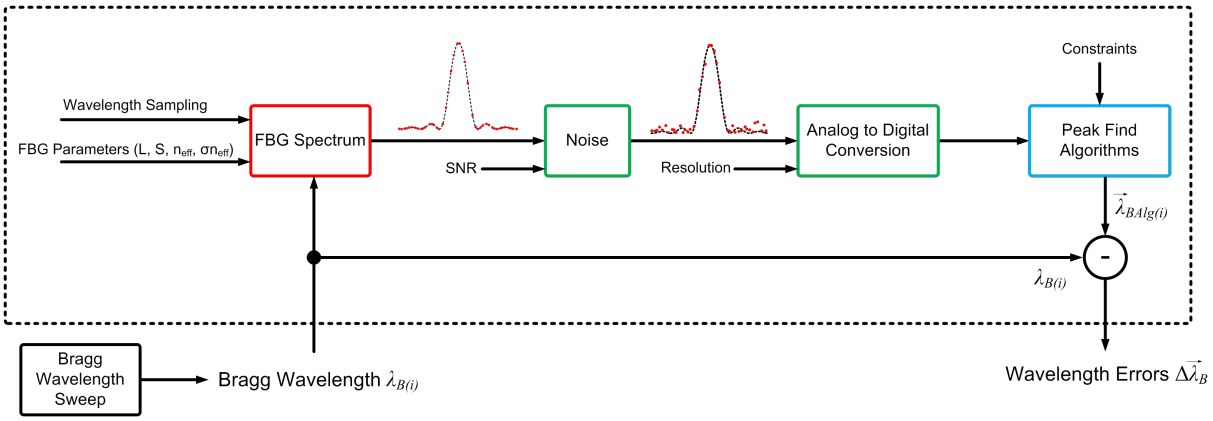

Figure 3.50: *Simulation tool for algorithm evaluation.*

Finally, all of the previously discussed peak find algorithms are applied to the generated FBG spectrum. Afterwards the center wavelength $\vec{\lambda}_{AlgB(i)}$ calculated by the algorithm is compared with the FBG's Bragg wavelength $\lambda_(B(i)$ for obtaining the algorithms error $\Delta\vec{\lambda_B}(i)$. During the simulation, the Bragg wavelength is swept from 1550nm to 1553nm in 1pm steps. Afterwards, the RMS and mean errors of the algorithms' Bragg deviations $\Delta\vec{\lambda_B}(i)$ are calculated. The simulation results are presented in section 4.3.4.

3.4.9 Radiation Effects in Optical Fibers and FBG Sensors

The measurement system developed in this work shall be able to cope with the environmental conditions in space applications. This takes also high radiation loads (ionizing and non-ionizing) into account. The developed sensing elements shall open also the possibility to mount the sensors outside of the satellite at which an extreme high total ionizing dose up to 25 Mrad or 250 kGy over a life time of 15 years [37] is expected, see also section 2.2.2. The high radiation load has its origin in a possible FBG sensor mounting position outside the satellite on the solar panels or radar reflection antennas. Here the shielding thickness of the surrounding material is quite low (approx. 0.5 mm aluminium equivalent [37]) resulting in this high values. The detailed TID value as function of the shielding thickness can be found in figure 2.17 on the right.

This high radiation load is seen as the most critical requirement for the FBG sensors in this work. For this reason, a detailed review of radiation effects in FBG sensors and

in optical fibers is given. The origin of the cosmic radiation is described in section 2.2.2 and a radiation analysis of the developed module is given in section 4.2.3.

Radiation Effects in Optical Fibers

Optical fibers have been widely used in space applications before, and many tests have been performed. Space flight qualification of optical fibers includes thermal and radiation tests, as well as mechanical tests like vibration and shock analysis. The highest impact on the fiber performance is the formation of color centers due to TID effects which increases the optical attenuation. The so called radiation-induced attenuation (RIA), given in dB/km, indicates the radiation dependent loss per unit length. Henschel et al [124] has shown that the Fluour-doped fibers from Draka and Fujikura have the lowest loss (Fujikura: 2dB/km and Draka: 10 dB/km after 10 Mrad(100 kGy). By Aikawa et al. [125] it has been shown that an F-doped fiber has a very good recovery characteristic after irradiation. There are material compositions known which degrade the radiation hardness of a fiber. Such materials are for example Phosphor (P), Nitrogen (N) and Germanium (Ge) whereby phosphor has the highest impact. A fiber containing phosphor will be immediately dark after the radiation test source is activated.

The information of figure 3.51 is taken from [1] and is illustrated here for highlighting the strong dependence of the induced loss to the fiber composition. As is can be seen, the Fluour doped fiber has the best performance under radiation whereas the Germanium doped fiber showed poor performance.

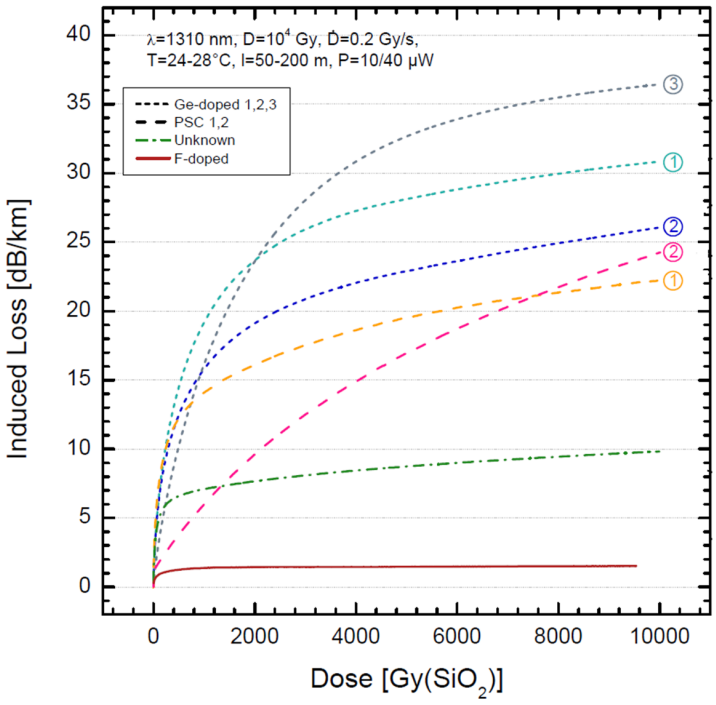

Figure 3.51: *Radiation induced loss of different fibers as function of TID, given in Gy, taken from [1].*

Other well-known radiation hardening of optical fibers is the hydrogen loading of the

fiber at high pressures and high temperatures. This is specially done for rare-earth doped fibers such as erbium amplifier fibers which are otherwise very sensitive to TID effects. The drawback of this solution is the potential diffusion of the hydrogen out of the fiber over long time scales. This can cause stability problems affecting the complete system. [126]

Radiation Effects in Fiber-Bragg Gratings

Because of the possible use of FBG sensors in nuclear facilities many studies and tests have been carried out to observe the Bragg wavelength shift (BWS) of FBGs during and after irradiation with γ-rays [127]. By Grobnic et al.[2], it has been shown that FBGs written by the fs-IR technology in F-doped fibers from Fujikura have the lowest BWS of only 3-7 pm after 10 Mrad (100 kGy). No influence in BWS due to radiation was observed, either if the fiber was H_2-loaded or not. The results were identical for type I and type II gratings. For such gratings, the only existing drawback is the random long-term drift of the Bragg wavelength which can be in the range of several pico-meters. It is assumed, that the Fluour inside the fiber still reacts with other present materials which causes a small change in the relative refractive index change n_{eff}.

The BWS in FBGs in standard fibers show a high impact to the H_2-loading before the writing process. For an unloaded standard single-mode telecommunication fiber (SMF28) a BWS of 10 pm after 100 kGy was observed, in contrast to 60 pm for the same hydrogen loaded fiber [2].

By Henschel et al. [128] it has been shown that also UV written FBGs can be resistant to radiation. In this experiment the fs-IR written FBGs have only a 10% - 20% smaller shift due to radiation. The highest impact to the BWS has again the hydrogen loading of the fiber before the writing process [128]. The pressure of the hydrogen loading has only small influence as has been shown by Henschel et al. [129]. It has herein also been shown, that the BWS is by a factor of two higher at temperatures around -50°C in contrast to 20°C. The BWS showed in the experiment a saturation behavior. So, after a certain dose the overall shift remains at a constant value. If the FBGs are written in a N-doped fiber, the BWS shows no saturation at doses even higher than 1 MGy [130]. Such gratings are not suitable for temperature monitoring in space applications but could be used as radiation sensors inside satellites.

Analysis of the BWS with different fiber coatings have been carried out by Gusarov et al. [131]. It has been shown herein, that the stripped fiber shows the lowest radiation sensitivity, whereas the ormocer coated fiber shows the highest shift. This might be due the radiation induced altering effect in the coating and thereby created mechanical stress between fiber core and coating. The best behavior against radiation shows the polyimide coating.

To sum up, it can be said that gratings written by UV laser light in H_2-loaded fibers show the highest shift in wavelength. The effective change in Bragg wavelength has its origin on one hand in the refractive index change due to radiolytic rupture of the OH and Ge-H bands inside the host material and on the other hand in a γ-induced compacting which changes the grating pitch Λ. Nonetheless, the H_2-loading before the writing process is indispensable to make the fiber photosensitive enough for an efficient writing of

the gratings by UV laser light.

By writing the gratings with an fs-IR laser light the photosensitivity of the fiber is not relevant due the extreme high pulse energy which damages the fiber core locally (type II grating). The fs-IR written gratings show a much better performance under radiation than the UV written and H_2-loaded type I gratings [128]. The maximum reported shift of 7pm results in a measurement error of $\approx 0.67°C$ by considering equation 3.16.

Chapter 4

Fiber-Optical Interrogator Design

4.1 Requirements

For space missions in general a large number of documentation and requirements have to be generated, checked and verified. The same holds true for the HSB system developed in this work. Specially the system related requirements have to be derived carefully from the satellite requirements before a hardware design can be established. For larger projects the data model is implemented in IBM - Rational DOORS ®^{TM} as it was the case in the HSB project [37].

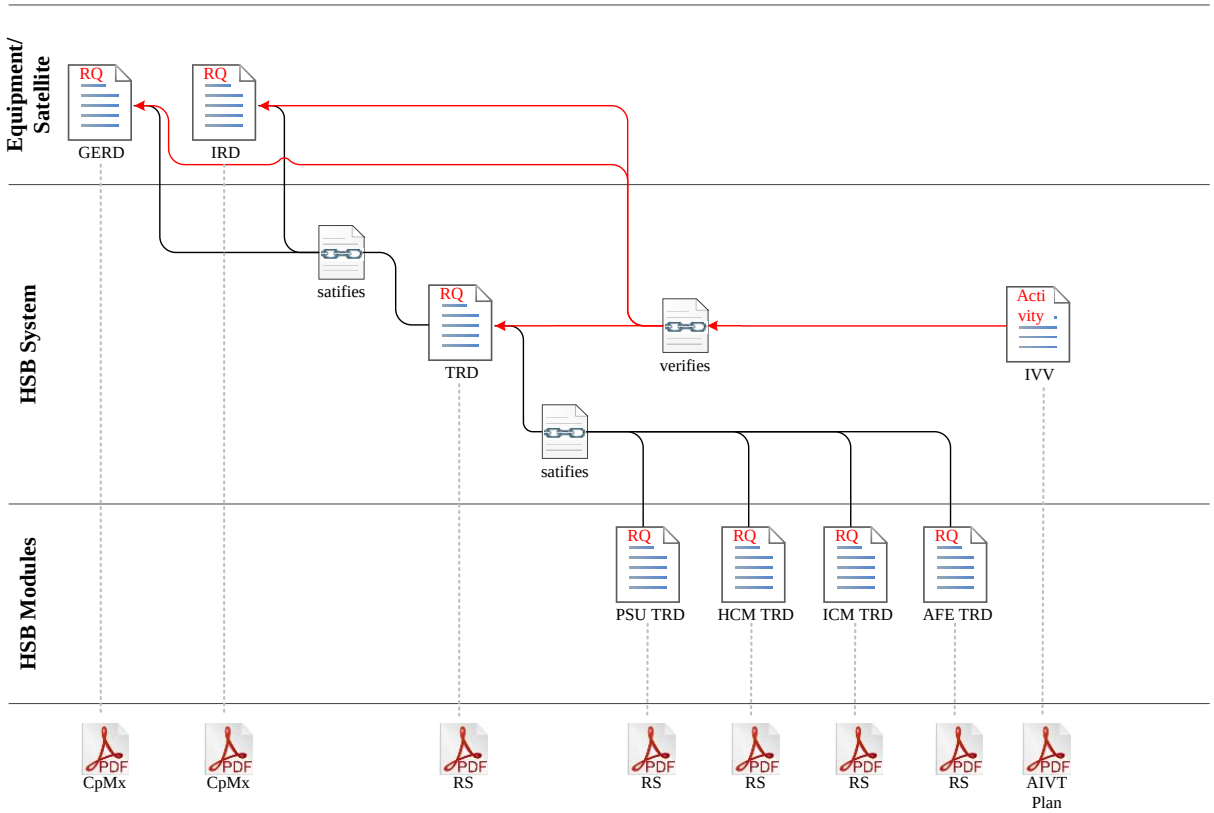

Figure 4.1: *HSB requirement data model implemented in IBM - Rational Doors.*

In figure 4.1 the requirement definition flow of the HSB system is illustrated. Starting with two requirement document sets from the satellite platform, namely the General Equipment Requirement Document (GERD) [35] and the Interface Requirement Docu-

ment (IRD) [36], the HSB Technical Requirement Document (TRD) is derived. This is done by considering the interface elements given by the IRD and taking only the relevant information out of the GERD dataset. For both requirement documents (GERD and IRD) compliance matrices are generated, illustrating the compliance to each single requirement of the satellite. In the HSB TRD all requirements are given which are defining the HSB system in terms of interface, performance, power consumption etc. On the same level as the TRD, the Independent Verification and Validation (IVV) module is located. In the IVV module all test activities are implemented and linked to the single requirements in the TRD, GERD and IRD. The output of the IVV module is a so called Assembly, Integration, Verification and Test Plan (AIVT plan). Finally, the TRD documents for the single modules of the HSB system are derived from the HSB system TRD. The procedure here is the same as for the satellite system requirements explained in the beginning.

4.1.1 Interrogator Module Requirements

In the very first stage of the HSB project a detailed requirement definition phase was carried out. This phase yielded to a detailed set of requirements of the fiber-optical interrogator which are given in table 4.1. Before the design of the interrogator module started, this set of requirements was derived and discussed with OHB if they will meet the target system requirements [5]. The laser requirements were presented in the previous chapter (see table 3.1) and are not repeated here again. By taking into account all of these requirements, the architecture presented in chapter 5.1 is derived.

Req. No.	Requirement
	General Requirement
FIM1	The interrogator shall have a measurement precision of ±0.5°C
FIM2	FIM shall evaluate measurement data and provide sensor responses as digitized values via the intermodule communication interface
FIM3	FIM shall include buffer memory that holds current measurement values of all sensors including time stamp to be polled by the HSB controller on demand
FIM4	The measurement rate of the fiber-optical interrogator shall be nominal 1 Hz.
FIM5	The Analog Front-End (AFE) shall include the electrical subsystems for controlling the laser diode, signal conditioning for the reflected light and temperature control of the laser
FIM6	The AFE shall include the electrical subsystem for signal conditioning of the reflected light
FIM7	The AFE shall include the electrical subsystem for temperature control and stabilization of the laser diode temperature
	MG-Y Laser Controlling Subsystem
FIM8	The voltage/current converter for the LD pin of the MG-Y laser shall have a settling time of 100 µs

Req. No.	Requirement
FIM9	The voltage/current converter for the SOA pin of the MG-Y laser shall have a settling time of 20 µs
FIM10	The nominal output current of the LD and SOA converter shall be 100 mA
FIM11	The settling time for controlling the phase, right and left reflector current shall be $\leq 5\mu s$
FIM12	For the phase input the maximal output current shall be 8 mA, for the right and left reflector input the maximal output current shall be 35 mA
FIM13	The etalon and reference photodiodes voltages after the transimpedance amplifier shall be monitored by the FIM controller. These signal shall be used for laser's wavelength referencing.
	Detection Unit Subsystem
FIM14	Each FBG sensor string shall be connected to an separate transimpedance amplifier onboard the AFE
FIM15	A multiplexer should be used to multiplex the signals for each string after the transimpedance amplifier
FIM16	The photodiodes shall be implemented direct on the AFE module
FIM17	The photodiode shall be able to detect light at 1550 nm with a minimum responsivity of 0.8 A/W
	Temperature Controller Subsystem
FIM18	The MG-Y laser diode shall be temperature controlled by the internal thermoelectric cooler (TEC)
FIM19	The nominal operating point of the lasers temperature shall be 10 kOhm (internal NTC resistor)
FIM20	The TEC shall be able to keep the MG-Y laser at 10 kOhm within the operational temperature range from -20°C to +65°C
FIM21	The temperature controller amplifier shall be able to source and sink a maximum current of 1 A.
FIM22	The voltage and current of the thermoelectric cooler shall be monitored as house-keeping values and shall be provided to the HSB system
	Analog/Digital and Digital/Analog Converter
FIM23	Onboard the AFE an ADC shall be implemented to measure analog house-keeping values and the reflections from the FBG sensor strings
FIM24	The ADC shall have a resolution of 12Bits or better
FIM25	The ADC shall have a sampling rate of > 500kS/s
FIM26	The ADC is controlled by the FIM-controller module (FIM-CM) over an SPI interface

Req. No.	Requirement
FIM27	For controlling the wavelength of the laser diode a DAC shall be used to control the voltage/current converters of the phase, left and right reflector inputs
FIM28	The settling time of the DAC shall be <10 µs
FIM29	The resolution shall be 12 Bits
FIM30	The maximum output shall not exceed 3.3 V
	Optical Front-End
FIM31	The optical front end shall be implemented inside the FIM module
FIM32	Only passive optical components shall be used for splitting and combining the light from the laser and from the FBG sensors
FIM33	Passive optical splitters instead of circulators shall be used
FIM34	The passive components and fibers used in the OFE shall be single mode (SM) and not polarization maintaining (PM)
FIM35	The operating wavelength of the component shall be 1550 nm ±40 nm
FIM36	The fiber-optical connectors to which the sensor networks will be connected shall be implemented in the front panel of the AFE module
FIM37	All fibers shall be spliced together according Telcordia norms. No connectors expect the connectors on the frontpanel shall be used

Table 4.1: *Derived requirements for the fiber-optical interrogator module (FIM) developed within this work.*

4.1.2 Fiber-Optical Sensor Requirements

The requirements for the fiber-optical sensor and transducer are given in table 4.2. As for the interrogation system requirements, also the following sensor requirements have been derived in a first stage of the work from the system requirements [5]. The table is divided into two sections, the first sections is related to the fiber-Bragg grating itself and its optical properties such as reflectivity, wavelength and spectral width. The second part of table 4.2 describes the physical properties of the transducer, a small mechanical package for the FBG sensor which is attached to the satellite structure. The transducer is necessary to decouple mechanical strain at sensor's position from temperature. See also equation 3.16 in section 3.4.1.

Req. No.	Requirement
	Optical Requirements of Fiber-Bragg Grating
FOS1	The FBGs central wavelength shall be located in the telecommunication C-band at 1550nm
FOS2	The grating shall be written with the fs-IR technology
FOS3	The grating length shall not exceed 8 mm in length

Req. No.	Requirement
FOS4	The reflectivity of the grating shall be higher than 30%
FOS5	The Full-Width-Half-Maximum (FWHM) bandwidth shall be in the range between 200 pm and 500 pm
FOS6	The polarization dependent loss (PDL) shall be lower than 0.1 dB
FOS7	The polarization dependent frequency shift (PDFS) shall be lower than 20 pm
FOS8	The side lobe suppression ratio (SLSR) shall be higher than 18 dB
	Physical Requirements of Transducer
FOS9	The fiber shall be glued to the FOS Transducer by a space qualified adhesive.
FOS10	The FOS Transducer shall be glued to the satellite structure by space qualified glue. (Same glue for all interfaces)
FOS11	The time constant for heat conduction shall be less than 10 s
FOS12	The minimum operational temperature of the FOS Transducer shall be -100°C
FOS13	The minimum operational temperature of the FOS Transducer shall be +100°C
FOS14	The FOS Transducer shall sustain the cosmic radiation of up to 25 Mrad, resulting in a Bragg wavelength shift of less than 10 pm
FOS15	The FOS Transducer (with glued fiber) shall sustain quasi static loads of 20g.
FOS16	The FOS Transducer (with glued fiber) shall sustain random vibration loads of 16.9g(rms)
FOS17	The FOS Transducer (with glues fiber) shall sustain shock loads of 2000 g
FOS18	The material of the FOS Transducer shall be metallic
FOS19	The mass of the FOS Transducer shall not exceed 5 g
FOS20	The FOS Transducer shall be designed in such way, that strain or mechanical stress to the FBG sensor does not change the Bragg wavelength more than 10 pm.
FOS21	The dimension of the FOS Transducer shall not exceed 15x30x5 mm^3

Table 4.2: *Requirements for the fiber-optical sensor used for temperature sensing onboard satellites.*

4.2 Radiation Analysis

For the full HSB system a radiation analysis was carried out after a first mechanical design was established. Starting from the mission definition, provided in general by the mission prime contractor, the environment according the radiation models is generated. This is shown in more detail in section 2.2.2.

There are in principal two steps to do to get accurate results. First a rough estimation of the expected total dose behind a certain thickness of shielding material is carried out. For doing this, a plot as shown in figure 2.17 on the right is generated. In the case here for the HSB system flying in geostationary orbit for 15 years, the red curve is applicable. The next step is to select a design goal for the maximum allowed TID value, in the case here a maximum TID of 100 krad including margin was selected. For such a TID value space qualified electronic components are still available. By taking into account the data from the red curve in figure 2.17 a shielding thickness of 5 mm of aluminum is necessary for this mission scenario.

With the selected thickness the mechanical design can be started and a more detailed radiation analysis can be carried out (see section 4.2.3). This analysis takes also the geometry inside the box into account and in addition the TID values at different points can be simulated.

4.2.1 Radiation Shielding Approach

An approach for shielding sensitive electronics or equipment against radiation is shown in figure 4.2. First the mission profile must be known or defined by taking into account orbit data, lifetime and launch date. Simulation results for different orbits with a life time have been simulated and are presented in figure 2.17 on the right [15]. The maximum allowable TID value shall also be defined at the beginning of the design phase (100 krad in the case of the HSB system). Mass limitations must be checked at beginning to do not violate mechanical requirements due to added mass for shielding. At last the interesting and sensitive points inside the equipment shall be defined for which the TID values shall be calculated.

When all parameters are available the simulation can be started. This can be done with the simulation software called *SPENVIS* or with *FASTRAD*, the latter one has a more user-friendly interface and allows the import of mechanical designs in 'step'-format. The software generates the expected TID levels computed by ray-tracing algorithms at before defined detector positions. These results are compared afterwards with the specified allowable dose in the first stage of the analysis. [15]

If the simulated TID value satisfies the allowed TID level, the analysis is finished successfully and no changes must be implemented in the design. If the simulations shows higher TID levels than expected, modifications must be made. These modifications strongly depend on the discrepancy between simulated and allowed values and can reach from small spot shielding on dedicated sensitive components to a complete modification of the mechanical design. After each modification or added shielding mass, the analysis must be restarted to check if the results are sufficient.

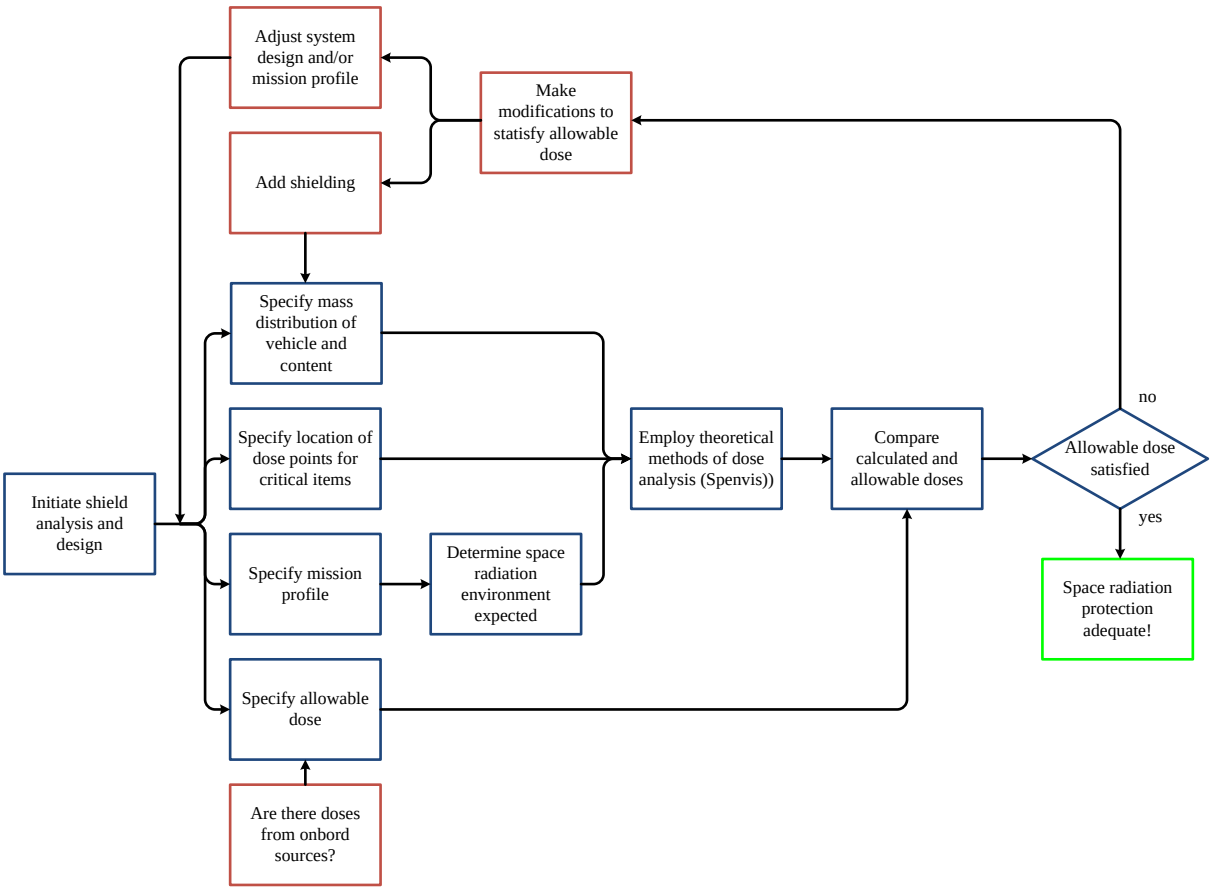

Figure 4.2: *Radiation shielding approach for space systems [8], [16].*

4.2.2 Detector Location and Modeling

To carry out a detailed radiation analysis, first a mechanical model of the system must be available. By using the software *FASTRAD* this model can be directly imported. The next step is the placement of the detectors for which the expected TID values shall be computed with ray-tracing algorithms. The 3D-model of the system is shown in figure 4.3 on the left side. On the right side the detector locations acting as the end points of the ray-tracing algorithm are shown [37].

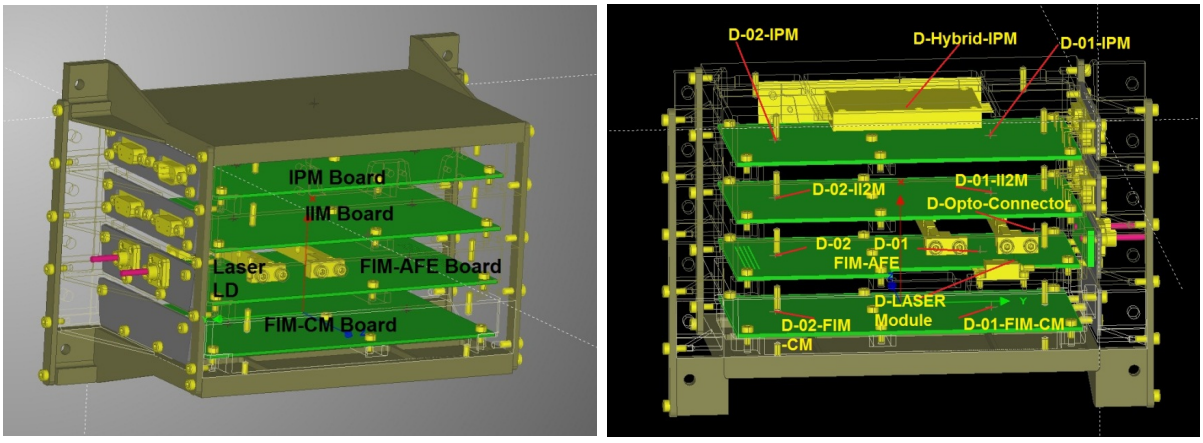

Figure 4.3: *Left: 3D model of the HSB unit used to carry out the radiation analysis. Right: Detector location for the ray-tracing computation [37].*

4.2.3 Analysis Results

The results of the radiation analysis are present in table 4.3 for the HSB system at the defined detector positions [37]. For the mission a radiation design margin (RDM) of 20% was defined [16], which is taken into account in the column on the right side. As can be seen the detectors placed at the outside of the HSB box sees a high amount of radiation (more than 10 Mrad) whereas the detectors inside stay all below 100 krad. The maximum TID will be seen on the FIM-CM board because its only shielded by one side wall. The MG-Y laser which is seen as a critical element has to cope with a TID of approximately 12.8 krad. The values in the first column are derived without additional shielding by the satellite bus (here a thickness of 0.5 mm aluminum is assumed). The SGEO platform is built with carbon-fiber reinforced plastic (CFRP) panels, resulting in a very low equivalent shielding thickness against TID [7, 35].

Detectors	**No H2Sat-bus shield**	**Shielded by H2Sat-bus**	**TID value with margin of 20%**
D-Z-Box outside	75.46 Mrad	8.36 Mrad	12.54 Mrad
D-Z-Box Top out	73.61 Mrad	8.43 Mrad	12.65 Mrad
D-Z-Box Down out	72.79 Mrad	7.66 Mrad	11.50 Mrad
D-01-IPM	25.87 krad	18.02 krad	27.03 krad
D-02-IPM	40.79 krad	26.07 krad	39.11 krad
D-Hybrid-IPM	1.95 krad	1.91 krad	2.87 krad
D-01-II2M	30.0 krad	19.9 krad	29.85 krad
D-02-II2M	17.3 krad	13.2 krad	19.8 krad
D-Opto-Con	17.42 krad	12.9 krad	19.36 krad
D-Laser-Module	10.67 krad	8.56 krad	12.84 krad
D-01-FIM-AFE	14.02 krad	11.1 krad	16.65 krad
D-02-FIM-AFE	14.51 krad	11.7 krad	17.55 krad
D-01-FIM-CM	63.83 krad	39.4 krad	59.1 krad
D-02-FIM-CM	24.27 krad	17.3 krad	25.95 krad

Table 4.3: *Analysis results for the HSB box for the different detector locations.*

To sum up, the radiation analysis has shown that the TID values inside the box is well below the previous assumed value of 100 krad including a margin of 20%. Nevertheless, the sensitive photonic and electro-optical elements must be tested in dedicated radiation test series, see also section 6.2.

4.3 Design Trade-Offs

Within the HSB project a detailed trade-off phase was included to find the best suited concept for the fiber-optical interrogator module. For this well established concepts on the commercial market are taken into account and are weighted against each other for their common and important parameters. The parameters are weighted with positive values (max +2) for better performance or lower risk and with negative values (max-2) for worse performance and high risk. In addition if a parameter is seen as absolute non-practical the entry is marked with NG for 'no-go', which leads to a complete exclusion of a concept.

Trade-Offs are carried out for the interrogation concept, the polarization mitigation concept, FBG writing concept and the FBG peak search algorithm.

4.3.1 Scanning Laser Trade-Off

In section 3.1 the different scanning laser technologies are discussed. In the section here the most suitable technology is selected. The selection takes also the harsh environment requirements, given by the usage of the system in space applications, into account. The rating of the three different technologies is summarized within table 4.4.

Parameter	**ECDL**	**Fiber-Laser**	**MG-Y laser**
Central Wavelength	0	0	0
Scanning range	0	+2	+1
Linewidth	+1	0	0
Wavelength Tuning	-1	0	+2
Environmental Conditions	-1	-2	+2
Mass	+2	-2	+2
Volume	+2	-1	+2
Power Cons.	+2	-2	+2
Robustness	0	-1	+2
Driving Voltage/Current	-2	0	+2
Linearity	+2	+1	-2
Long term stability	+1	-1	0
Σ	+6	-6	+13

Table 4.4: *Scanning laser trade-off table.*

The External Cavity Diode laser (ECDL) has a good performance considering the mass and power impact to the system [52]. Also the scanning range and the operating wavelength is rated neutral. The main disadvantage is the necessary tiltable mirror or grating, which makes the laser highly sensitive to environmental perturbations such as vibration or shock. This problem could be solved by using a fully integrated ECD-laser in which the mirror is moved by a MEMS structure. Such devices have been reported in scientific literature but they are currently not commercial available. In addition the driving voltage for the MEMS structures is quite high and lies in the range of 100 V [132, 52, 50].

The fiber ring laser in fact has a high maximum scanning range of nearly 100 nm [45]. The large scanning range is the only outstanding characteristic of this type of laser. The fiber-ring laser suffers from the high mass and power impact (pump laser and Er-doped fiber plus coupling elements) and from the high sensitivity of the internal Fabry-Pèrot filter to environmental noise and temperature. The long term stability is limited by the FPF, so a stabilization of this element is highly recommended. Also the radiation sensitivity of Er-doped fibers is very high, so a special treatment or shielding of the fiber is necessary.

The MG-Y semiconductor laser showed the best performance. The mass-, volume- and power impact is very small which is preferred for the planned system. The wavelength

adjustment is done by three electrical currents, so no moving elements are necessary. The only drawback of this solution is the high nonlinear and complex wavelength tuning procedure (see section 3.2.1). This can be compensated by a smart control algorithm to be implemented in the FPGA. The scanning range is smaller than for the fiber ring based solution and lies in the range of 40 nm [57].

4.3.2 Polarization Scrambling Technique Selection

In section 3.4.5 different methods are presented to decrease the degree of polarization (DOP) for the laser light to mitigate the measurement error induced by the birefringence of the fiber. A table summarizing the advantages and disadvantage of the presented methods is given in table 4.5.

Parameter	**Lyot**	**Circ.**	$LiNbO_3$ **Scrambler**	$LiNbO_3$ **Switch**	**In-Fiber Depol.**
Device Cost	-2	+2	-1	-1	0
Volume	-2	0	+1	+1	-1
Power/Attenuation	-2	+1	+1	+1	+1
Speed	+2	+1	+2	+2	+2
Env. conditions	-2	0	+1	+1	+2
Performance	-2	-2	+2	+2	+0
Circuit	/	/	-2	+2	/
Σ	-8	+2	+4	+8	+4

Table 4.5: *Trade-Off table summarizing the advantages and disadvantages of different polarization scrambling techniques.*

The classic Lyot depolarizer has the worst overall weighting due to the required long fiber caused by the high lasers coherence length, see section 3.4.5. This increases the volume of the depolarizer and also the attenuation inside the fiber. In addition the performance is also not comparable with the other methods.

The concept of the fiber ring depolarizer looks very promising, it contains only a passive directional coupler and a fiber loop with a length greater than the coherence length of the laser. The component cost is moderate but the required volume is higher because of the length of the fiber loop which must be packaged in the unit.

The chiral circular polarizer is a very simple device containing only two passive fiber-optical components. So the cost and the mass effect of this system are rated very good. But the depolarizer only generated circular polarized light at its output, so the polarization state is converted again in a linear state after a short distance (< 1m) in single mode fiber. So this concept cannot be used.

The best performance showed the $LiNbO_3$ based concepts either the scrambling approach or the switching approach. For the scrambling approach the necessary circuit complexity is rated poor because a special circuit for sine or triangle waveform is necessary. Nevertheless the available supply voltage in the system is not high enough for a sufficient

performance. For the switching approach with the same modulator, the requested voltage is lower and stays within the supply voltage of the system. With this approach an averaging of two measurements is necessary which reduces the systems bandwidth but decreases also the computational error induced by the peak find algorithms.

4.3.3 FBG Writing Technique Selection

In section 3.4.6 the different FBGs types are indicated whereas in section 3.4.7 the different fabrication methods of FBGs were presented. Based on this information and on the radiation test results in section 6.3.2, the most suitable FBG writing technique in the most promising fiber is selected. The selected FBG writing technique must fulfill the requirements regarding the high cosmic radiation (up to 25 Mrad) and high temperature measurement range (±100°C). The advantages and disadvantages of the different FBG writing techniques are summarized in table 4.6.

Parameter	**UV+H_2 Ge-fiber**	**UV no H_2 Ge-fiber.**	**fs-IR in F-fiber**	**fs-IR in PSC-fiber**
RIA fiber	-2	-2	+2	0
Spectral quality	+2	-2	+1	+1
Grating cost	+2	0	0	0
Fiber cost	+2	+2	+1	+1
BWS due to radiation	-2 (NG)	-2	+2	+2
Writing grating	+2	-2	+2	+2
FBG stability	+2	+2	-2(NG)	+2
Env. conditions	-2	-2	+2	+2
Σ	+4	-6	+8	+10

Table 4.6: *Trade-Off table summarizing the different FBG writing techniques, NG no-go.*

Gratings written by UV laser light in H_2 loaded or unloaded fibers suffer from high Bragg wavelength shift due to radiation. Nevertheless, the manufacturing costs of such gratings are very low which causes a positive rating. Unfortunately, the BWS is too high for such gratings to be used in space applications, reasonable this entry is marked as no-go (NG).

The fs-IR written gratings show a much better behavior in terms of radiation. In addition these types of gratings can be written in any fiber independent from H_2 loading or fiber composition. Fluour(F) doped core fibers have shown the lowest RIA, so this fiber type would be an attractive candidate. But in literature it has been shown by Henschel et al. [124] that gratings in F-doped core fibers are not stable over time, so this entry is marked as no-go (NG). The BWS due to radiation is not constant and can also reverse the direction of the shift over time. The origin might lie in the very reactive behavior of the Fluour molecules affecting the induced refractive index change δn_{eff}. Due to the high intense writing peak pulse power of the fs-IR writing technique, the gratings can also be written in a pure silica core fiber (PSC). This fiber has in fact a higher RIA but the gratings are stable over time and the BWS shift stays within the required boundary.

4.3.4 Peak Find Algorithm Selection

In this section simulation results regarding to the precision of peak find algorithms in dependence of the SNR of the spectral response of the FBGs and the impact of the wavelength sampling resolution of the FBG spectra are presented. Based on this results, the robustness of peak find algorithms are derived. Finally the most suitable candidates have been implemented into the FPGA and an evaluation with real hardware has been done. It has to be noted that the robustness and precision of the algorithms depend strongly on the boundary conditions and implementation structures. These conditions must be additionally implemented inside the control FPGA resulting in a higher consumption of resources. For SNR analysis a LuT containing discrete wavelengths from the used laser was taken for sampling the FBG spectrum. The wavelength spacing in the LUT shows an exponential like distribution with a minimum wavelength spacing of 10 pm and a standard deviation σ of 2.1 pm. The required measurement precision of 5 pm (see table 4.1) yields to a maximum RMS error of 1.66 pm according to 3σ of the Gaussian error distribution. This value is illustrated in the figures hereafter by the red dashed line. To test the different algorithms, the simulation environment presented in section 3.4.8 is used.

Performance Depending on Signal-to-Noise Ratio

The RMS wavelength errors of the peak find algorithms were estimated for SNR values from 5 dB to 30 dB. The simulation results of different peak find algorithms as function of the SNR of the reflected spectrum are given in figure 4.4 on the left. For the designed system a system-SNR greater than 30 dB is assumed. By using the developed calculator software shown in figure 5.15, SNR values of 80 dB are possible.

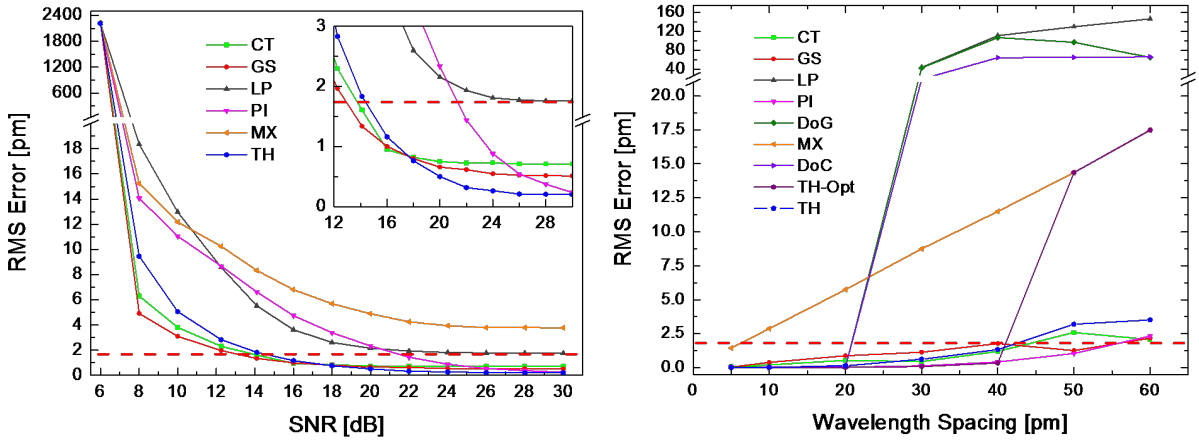

Figure 4.4: *Left: Simulation results of the different peak find algorithms as function of the SNR of the reflected spectrum. Right: Simulation result of the different peak find algorithms as function of the wavelength spacing in the reflected spectra. CT centroid, GS Gaussian fit, LP linear phase convolution kernel, PI polynomial interpolation, DoG derivative of Gaussian fit (convolution based), MX maximum search, DoC derivative of Coupled-Mode fit (convolution based), TH-Opt Trip-Hop algorithm optimized, TH Trip-Hop algorithm with no optimization. Adjacent simulated points are linearly connected.*

The linear phase operator (LP) shows a RMS error of 1.9 pm at an SNR of 30 dB. The LP is a digital filter and is designed for discrete uniform sampled data. But within the

measurement process the FBG spectrum is sampled non-uniformly, this leads to phase shifts within the Fourier space of the LP operator which further adds a tremendous error in the Bragg wavelength determination. So, care must be taken when interpreting the RMS error of the LP algorithm here.

The parabolic approximation (PI) is highly sensitive for low SNR values of the spectra but shows a small wavelength error of less than 0.5pm at SNRs greater than 30dB. The estimated error of the Trip Hop algorithm (TH), the centroid method (CT) and the Gaussian fit (GS) lie within the maximum RMS error of 1.66 pm for SNR values higher than 20 dB. The Gaussian interpolation method shows the best performance towards lower SNR. Nevertheless the Trip Hop algorithm shows the highest precision in Bragg wavelength determination at an SNR greater than 18 dB. The maximum algorithm (MX) never reached the error boundary of 1.66 pm for any SNR values. For FBG spectra with an SNR less than 8 dB all peak find algorithms starts to collapse.

Performance Depending on Wavelength Spacing

A further interesting aspect is the necessary wavelength spacing of adjacent sampling wavelengths. The measurement rate could be increased by using less wavelength values for sampling the FBG spectra. As result, the spacing of adjacent wavelengths grows. Simulation results regarding to the spacing of consecutive wavelength values and the wavelength error of the peak find algorithms are illustrated in figure 4.4 on the right.

The wavelength error of the maximum algorithm rises linear with a slope of 0.289 pm/pm(spacing). For a wavelength spacing less than 5 pm the maximum peak finder lies within the requirement in measurement precision. Convolution based algorithms (LP, DoG, DoC) show a precision better than 0.05 pm in Bragg wavelength determination until they collapse for a spacing of 20 pm. The convolution based algorithms fail when the number of samples which represent the FBG spectrum is less or equal the size of the convolution kernel.

The wavelength error with respect to FBG sampling wavelength spacing for two Trip Hop algorithms based on a slightly different logical program architecture is also depicted in figure 4.4 on the right. Thereby, the modified (TH-Opt) trip algorithm chooses the optimum measurement triplet. In general the modified algorithm shows a lower Bragg wavelength error compared to the simple Trip-Hop algorithm. For a wavelength spacing of 40 pm the optimized algorithm switches to the maximum peak find operator mode because no sample triplet can be found in the spectral response.

Performance Depending on Wavelength Variation

The lasers output wavelength shows an exponential distribution and is not uniform spaced over the spectrum. Due to this fact the robustness of the peak find algorithms regarding to a non-uniform sampled noise free FBG spectrum was obtained by varying the sigma (width) of the lasers wavelength distribution. Hereby the exponential distribution starts at a minimum spacing of 10 pm for consecutive wavelengths. The standard deviation of the wavelength distribution was varied from 1 pm to 9 pm. The simulation results concerning a non-uniform wavelength spacing and the resulting RMS error in Bragg wavelength estimation are shown in figure 4.5.

Convolution based peak find algorithms such as the linear phase algorithm (LP) and cross correlation algorithms (DoG, DoC) show a precision better than 0.02 pm for an uniform sampling of the FBG spectrum. Nevertheless the wavelength error estimated by these algorithms increases strongly if a non-equidistant sampling is present. The parabolic interpolation method is barely influenced by the non-uniform sampling, the wavelength error is less than 0.14 pm for all of the tested standard deviation values ($\sigma = 1pm...9pm$). The Trip Hop, Gaussian interpolation and centroid algorithm show a good robustness against non-uniform sampled FBG. However, the FBG spectral response is sampled rougher towards higher sigmas. This results in higher error in Bragg wavelength determination.

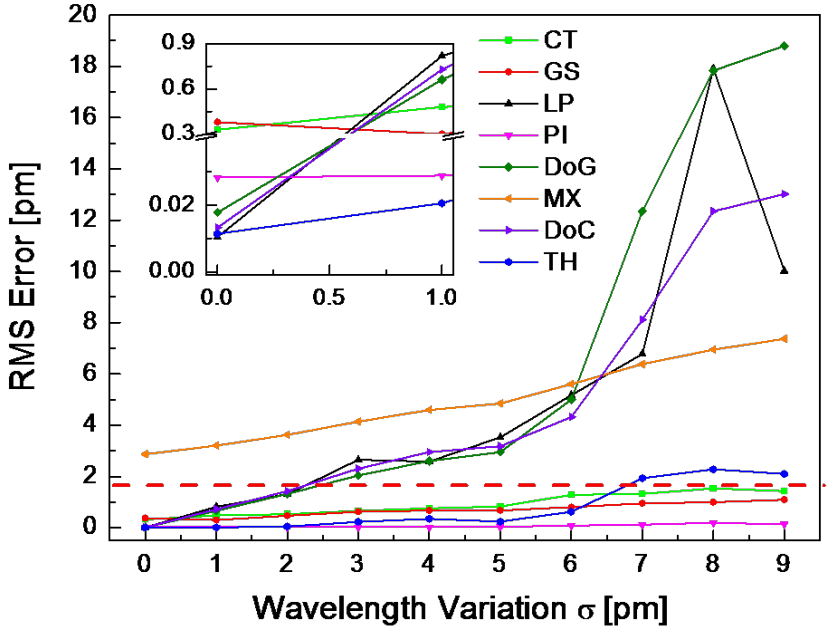

Figure 4.5: *Simulation result of the different peak find algorithms as function of the wavelength spacing in the reflected spectra. CT centroid, GS Gaussian fit, LP linear phase convolution kernel, PI polynomial interpolation, DoG derivative of Gaussian fit (convolution based), MX, maximum search, DoC derivative of Coupled-Mode fit (convolution based), TH Trip-Hop algorithm with no optimization.*

Performance Depending on Peak Shape

Depending on the amount of induced refractive index change δn_{eff} the peak form changes. This fact has been already discussed in section 3.4.3. The final grating which will be used in the space application must sustain a high total dose of cosmic radiation, so a type I (UV written)or a type II grating (fs-IR written) can be used. The interrogation system and hence the peak finder must comply with both types of gratings. The Bragg wavelength estimated by the peak finder algorithms is compared for different values of the induced refractive index change δn_{eff}. So possible limitations due to peak shape were identified.

First nine different peaks with an induced refractive index change δn_{eff} between $2 \cdot 10^{-5}$ and $20 \cdot 10^{-5}$ were generated by the coupled-mode model according (3.29). As can be seen in figure 4.6 on the left hand side the maximum reflectivity increases and the peaks shape

changes when δn_{eff} increases.

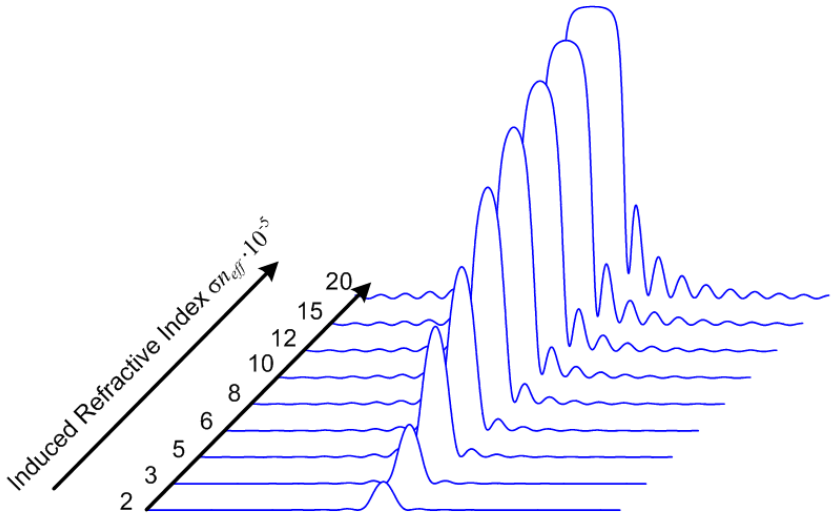

Figure 4.6: *FBG spectra with different induced refractive index changes* δn_{eff}.

Afterwards the different algorithms were applied to the spectral responses and the RMS error is analyzed. The sampling was done with a non-uniform sampling with a distance of 10 pm with a sampling variation of $\sigma = 2$ pm.

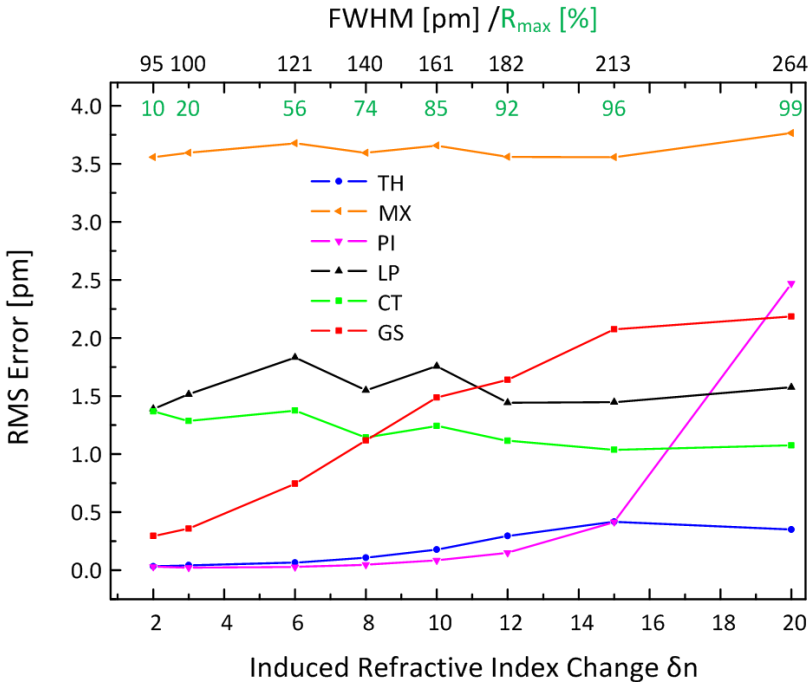

Figure 4.7: *RMS error for different peak find algorithms as function of* $\delta n_{eff} \cdot 10^{-5}$.

It can be seen in figure 4.7 that the polynomial fit and the Gaussian fit converge badly for higher refractive index changes due to the flat-top form of the spectrum. This is mathematically clear because the fit functions does not correspond anymore with the spectral form. The Trip-Hop algorithms performance keeps nearly constant over the entire range of δn_{eff} and stays far below the RMS error boundary of 1.66 pm. The slightly increase in

error is caused by the fact that the edges of high reflective spectra are sampled sparsely due their strong slope and limited sampling of 10 pm.

The centroid's wavelength error decreases for gratings with rectangular like shape, because the centroid algorithm is performing best for an ideal rectangular. It has to be noted, that the side-lobes have an impact on the performance due to the additional area spanned by them. If this area is non-symmetrical around the main peak as it is the case for apodized gratings, the estimated Bragg wavelength is shifted towards the side-lobes direction.

Trade-Off Table and Algorithm Selection

The previous presented simulation results let to a conclusion which algorithm is implemented in the measurement system. A table summarizing the simulation results is shown in table 4.7. The ratings are in the range between +2 (very good) and -2 (very poor), zero is rated as neutral.

Parameter	**GS**	**CT**	**LP5**	**DoG5**	**DoC7**	**TH**	**MX**	**PI**
Robustness - SNR	+2	+2	-2	-2	-2	+2	-2	-2
Non-uniform sampling	+2	+2	-2	-2	-2	+2	-1	+2
Wavelength spacing	+1	+1	-1	-1	-1	+1	-2	+2
Usable for low $R_{\max}$	+1	0	0	0	0	+1	0	+1
Usable for medium $R_{\max}$	0	0	0	0	0	+1	0	0
Usable for high $R_{\max}$	-2	1	0	0	0	+1	-1	-1
FPGA resources	-2	0	1	0	0	+1	+2	-1
Σ	+3	+6	-4	-5	-5	+9	-4	+1

Table 4.7: *Trade-Off table for the peak detection algorithm. GS: Gaussian fit, CT: centroid, LP5: linear phase operator, DoG: derivative of Gaussian, DoC: derivative of coupled-mode, TH: Trip-Hop, MX: maximum search, PI: parabolic interpolation*

The convolution based algorithms (LP5, DoG5, DoC7) have an low total weighting due to the malfunction for non-uniform sampled gratings and the possible instability for lower SNR values. The FPGA resources are rated neutral due to the positive effect of digital filter implementation and the negative influence of the necessary multiplication. The fitting algorithms (Gaussian fit, GS and Polynomial interpolation, PI) have a better total weight due to the better behavior for SNR (GS) and non-uniform sampling. But both algorithm suffer from a more complex FPGA implementation.

The special algorithms like the centroid and Trip-Hop algorithm showed the best performance. The implementation effort is quite low and the peak find performance is very good also when the gratings are sampled non-uniform or the SNR value of the reflected spectrum is low.

4.3.5 Trade-Off Summary

A summary of the previous presented trade-offs is given in table 4.8 for the baseline design and one alternative in the case if problems arise during the design phase.

Parameter	Baseline Selection	Alternative Selection
Scanning Laser	MG-Y laser diode	ECDL laser
Writing of FBGs	fs-IR in PSC fiber	fs-IR in F-dopded fiber
Polarization Mitigation	Pol. Switching	Scrambling
Peak-Finder	Trip-Hop	Centroid

Table 4.8: *Trade-Off summary table for the baseline design and one alternative.*

4.4 Fiber-Optical Interrogation Module Design

A detailed trade-off between the different technologies for the planned usage in space systems is presented in section 4.3.1. The trade-off has identified a semiconductor MG-Y laser diode as the preferred solution. This type of laser diode can be tuned in wavelength from 1528 nm to 1568 nm with the help of three input currents [4]. Other types of tunable laser sources are presented in section 3.1. For stable operation the MGY laser diodes internal thermo-electric cooler is controlled by a bipolar temperature controller circuit.

The resulting design of the fiber-optical interrogator unit is depicted in figure 4.8. Inside the interrogator controller module (ICM) which can be seen as the digital control system of the module, a look-up table is stored. Herein the relation between laser wavelengths and the three laser control currents is implemented. During a measurement cycle, the tunable laser scans through the optical spectrum spanning from 1528 nm to 1568 nm. The reflected light from the FBG sensor is fed over a coupler to a photodiode to measure the FBG's spectral response. The reflected signal is afterwards assigned to the laser's output wavelength in terms of a look-up table (LUT). The setup wavelength and the reflected signal are evaluated inside the FPGA by dedicated algorithms (see section 3.4.8). As best suited peak find algorithm the optimized Trip-Hop algorithm was selected, see also table 4.7.

First, a peak is detected and the sample points which are relevant for the further processing of the data are buffered. Then a second algorithm computes the Bragg wavelength of the detected peak. When the shift in Bragg wavelength in relation to a reference value is determined by the FPGA, the assignment to a physical temperature can be performed.

For the mitigation of polarization induced measurement errors due to the inherent birefringence of the FBGs the polarization switching technology has been pointed out as the most suitable candidate. The results of the trade-off are given in table 4.5.

The optical front-end is simple, only passive coupler are implemented to separate transmission path (laser's output) and reception path (photodiode input). When a coupler is used special attention must be given to unwanted back reflections into the MGY laser's output which can cause stability problems. To counteract this effect an optical isolator is placed at the output of the laser diode. The path between laser and isolator's input and the path between isolator's output and polarization switch's input must be

carried out with polarization maintaining fibers to ensure a correct functionality of the polarization switch.

The used FBG sensors will be based on fs-IR written gratings in a pure silica core fiber, this has been identified by the trade-offs as the most promising candidate, see table 4.6.

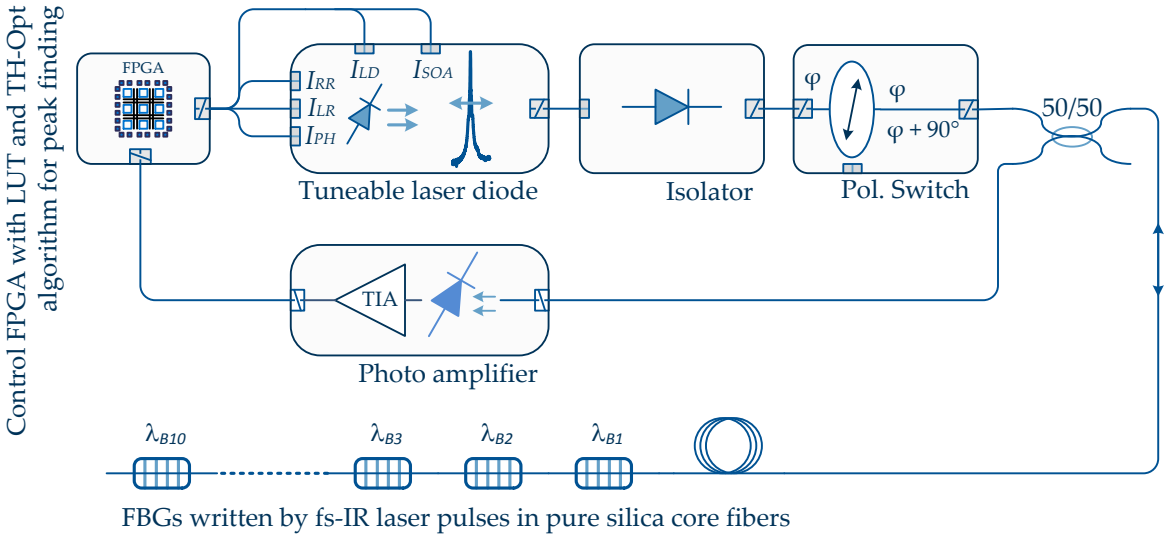

Figure 4.8: *Fiber-optical interrogator based on a tunable laser with control FPGA, optical coupler, fiber-Bragg grating sensor string and transimpedance amplifier (TIA).*

4.4.1 Querying Multiple Parallel FBG channels

The design presented in figure 4.8 can be easily adapted to multiple channels by adding passive couplers (one coupler per additional channel) and photodiodes with separate transimpedance amplifiers. Such a setup is illustrated by figure 4.9. The light coming from the MG-Y laser diode is split up in multiple branches depending on the number of FBG channels, in the here illustrated case four additional channels are defined. This fraction of light is fed over a passive 50/50 coupler to the FBG sensor string. The by the sensor string reflected light is afterwards fed to the corresponding photodiode and transimpedance amplifier which converts the reflected power to an analog voltage which is in turn measured by the ADC. This approach is possible as long as the optical power on the photodiode stays above the required SNR value. Simulations (see figure 5.15) have pointed out that four to six additional channels would be possible.

4.4.2 Redundancy Concept

The HSB system foresees a redundancy concept, for which the module is doubled, the redundant module is kept in cold redundancy meaning that it is only switched on if necessary. So the previous presented system in section 2.3 with four modules contains in a full redundant configuration eight modules for each type a *main* and a *redundant* module.

A possible implementation of redundancy is shown in figure 4.10 for a main and redundant FIM. Both ends of the sensor string are measured with the main (left end) and

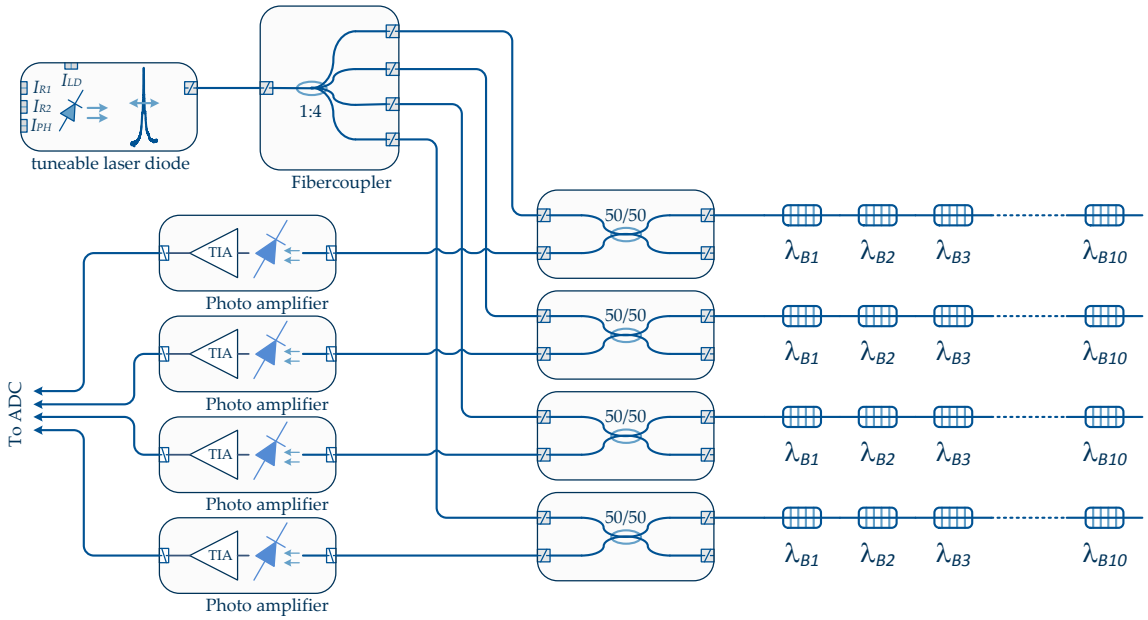

Figure 4.9: *Fiber-optical interrogator module capable to read out up to four FBG channels with a single MG-Y laser diode.*

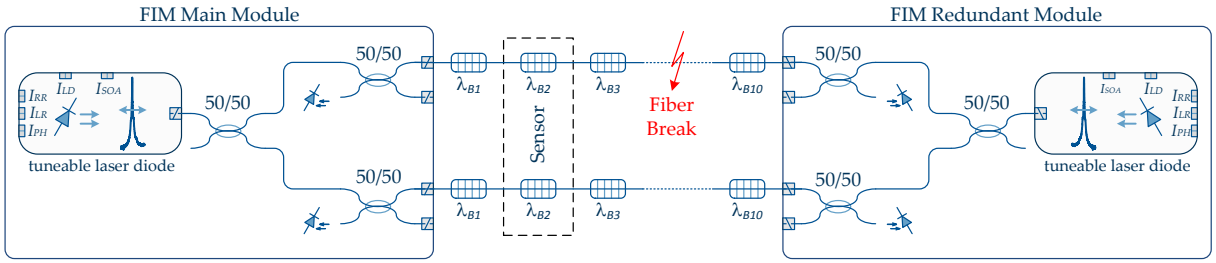

Figure 4.10: *Redundancy concept of the fiber-optical sensing system shown for two channels with a main and redundant module*

redundant (right end) FIM respectively. Next, it is assumed that in one transducer two FBGs are implemented very close to each other which can be read out from each FIM. This unit can be seen as one temperature sensor point, because both FBGs will see the same temperature. The first sensor (top sensor string) is considered as the main sensor, and the bottom sensor as the redundant one. Each sensor can be queried by either the main or the redundant FIM. If, for example, a fiber-break occurs in the main sensor line, the sensors in front of the defect can be read out by the main unit and the rest of the sensor string with the redundant unit.

4.4.3 Fiber-Optical Sensor Multiplexer

To increase the number of sensors to be interrogated by the HSB system and to enhance the bus network capabilities, the fiber-optical sensor multiplexer is introduced. The fundamental architecture of the fiber-sensor multiplexer module (FSM) is shown in figure 4.11 The multiplexer is an HSB-independent data concentrator for sensor network extension, e.g. in exposed parts of the satellite. The laser light generated by the analog

front-end is guided to the multiplexer wherein it is split to multiple fiber channels, each allowing up to ten FBG sensors. In the multiplexer, a mixed signal ASIC digitizes the FBG peak reflections measured by the photodiodes of each channel. The digital spectrum is then read back over the I²C protocol by the Interrogator Controller Module. Also the calculation of the temperature and the packaging of the data into the telemetry frames is done onboard the ICM. Assuming that the FBG sensors are mounted on a satellite panel, the FSM acts as a data acquisition unit for these sensors. The laser light is generated by the FIM-AFE. With the FSM, an additional 4×10 FBG sensors can be measured, which opens up new possibilities for the sensing system.

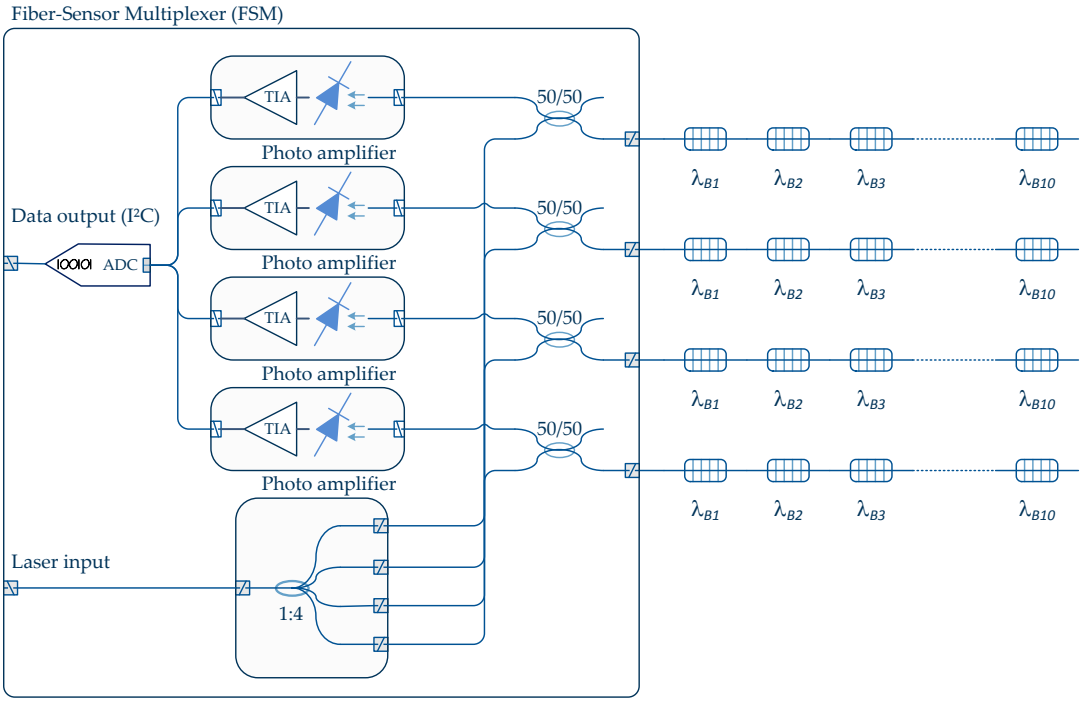

Figure 4.11: *Fiber Sensor Multiplexer (FSM) block diagram.*

4.4.4 Wavelength Referencing System

To ensure a stable operation of the interrogation system a wavelength referencing system is implemented in the system. This unit is used to detect a possible shift in output wavelength of the laser due to aging, environmental conditions or radiation. As can be seen in section 6.3.4 the MG-Y laser has a shift in wavelength between the setup wavelength and the measured wavelength of approx. 50 pm due to total dose and displacement damage effects. To counteract this shift and to ensure a long-term stability of the system the wavelength referencing system is implemented together with the coupler cascade in the optical front-end (OFE). Without the referencing system, the obtained temperatures would rely on wrong data yielding to a measurement error which is higher than the required ±0.5°C defined by the requirements in section 4.1.1. A detailed description of the OFE can be found in section 5.1.4.

Chapter 5

Fiber-Optical Interrogator Development

5.1 Hardware Architecture

In this chapter the hardware architecture (see also figure 5.1) of the fiber-optical interrogator module is described. The hardware architecture is divided into four different groups, such as laser transmitter (including internal monitoring for wavelength referencing), receiver circuit for the FBG channels, controller logic and optical front-end. These blocks are described in the next sections in more detail.

The tunable laser is controlled in wavelength by three separate DACs which control voltages are derived by the FPGA from the stored LUT. This control voltage is converted by a special designed converter circuit (see section 5.1.1) into a control current, flowing into the MG-Y's laser terminals. The generated laser light is fed over the optical front-end (see section 5.1.4) to two FBG sensing channels and two additional outputs for the connection of fiber-optical sensor multiplexers (see section 4.4.3). The, by the FBGs reflected laser light, is detected by two photodiodes with following transimpedance amplifiers (see section 5.1.2). The reflected signals are converted into digital values by a multi-channel ADC and are further processed within the FPGA. The detection of the FBG's central wavelength and the reallocation from Bragg wavelength shift to temperature is also done within the FPGA. At the end the complete dataset is packaged into a telemetry frame and send to the HSB controller module (see section 2.3).

5.1.1 Laser Transmitter

The laser transmitter is the most important part of the fiber-optical interrogator module. The transmitter is controlled by the FPGA over a serial peripheral interface (SPI), setting the nominal operating point of the temperature controller, laser and SOA section and in addition the control values of the right-, left reflector and phase inputs. A block diagram of the laser transmitter is given in figure 5.2. The DAC is a single channel, 12 Bit voltage output converter with a settling time of less than 12.5µs. This type has been selected due to the serial interface and the availability as a space qualified component [133].

The laser and SOA voltage/current converters require a moderate bandwidth due to their constant operation, whereas the converters for the laser's wavelength control sig-

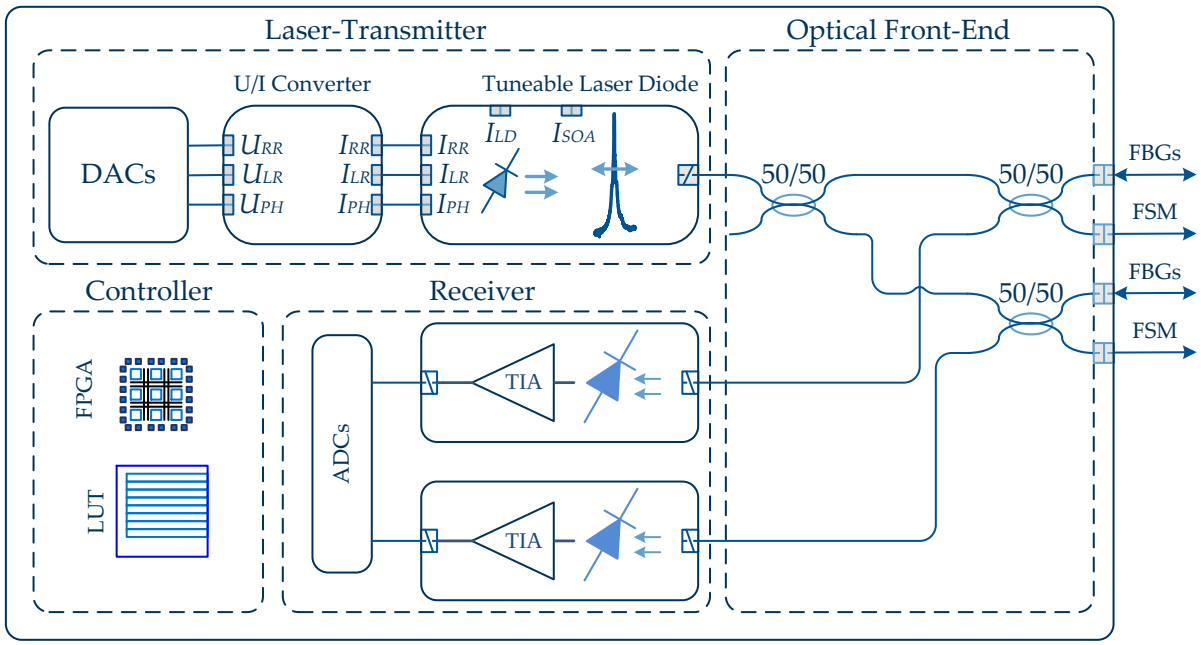

Figure 5.1: *Architecture of the designed fiber-optical interrogator module with laser transmitter unit (top left), optical front-end (right), receiver circuit (bottom) and controller including FPGA and memory for LUT storage.*

nals shall have a high bandwidth to allow a fast wavelength tuning. The tuning speed of the laser's wavelength directly affects the measurement rate of the system, as faster the FBGs can be scanned, as faster the temperature information can be obtained by the measurement system. The voltage/current converter circuit is described in section 5.1.1. The internal photodiodes, namely the etalon and reference photodiode, are connected to separate transimpedance amplifiers which output signal is sampled by an ADC. The output data is afterwards send over the SPI bus to the FPGA for processing.

To keep the temperature of the MG-Y laser at its nominal operating point, a temperature controller with bipolar output stage, allowing heating and cooling of the laser, is implemented. The internal temperature sensor is used as feedback value for the PI controller. The setpoint is also adjustable over a DAC. The temperature controller circuit is described in section 5.1.1.

Controlled Current Sources

In this section the voltage/current converter circuit is presented which is used to converter the DAC control voltage into a current for the MG-Y laser diode. In total five of this converters are necessary, supplying laser, SOA, right-, left-reflector and phase terminals of the laser. As already explained in section 3.2.1, the change in wavelength is based on changes in refractive index of the semiconductor materials which is a function of injection current instead of applied voltage.

Functional Requirements The voltage/current converter must fulfill special requirements which are identified during the first testing of the MG-Y laser. The laser behavior in special cases was not clear at the beginning so the circuit design can be seen as a continuous development which ended with the herein presented circuit. The functional

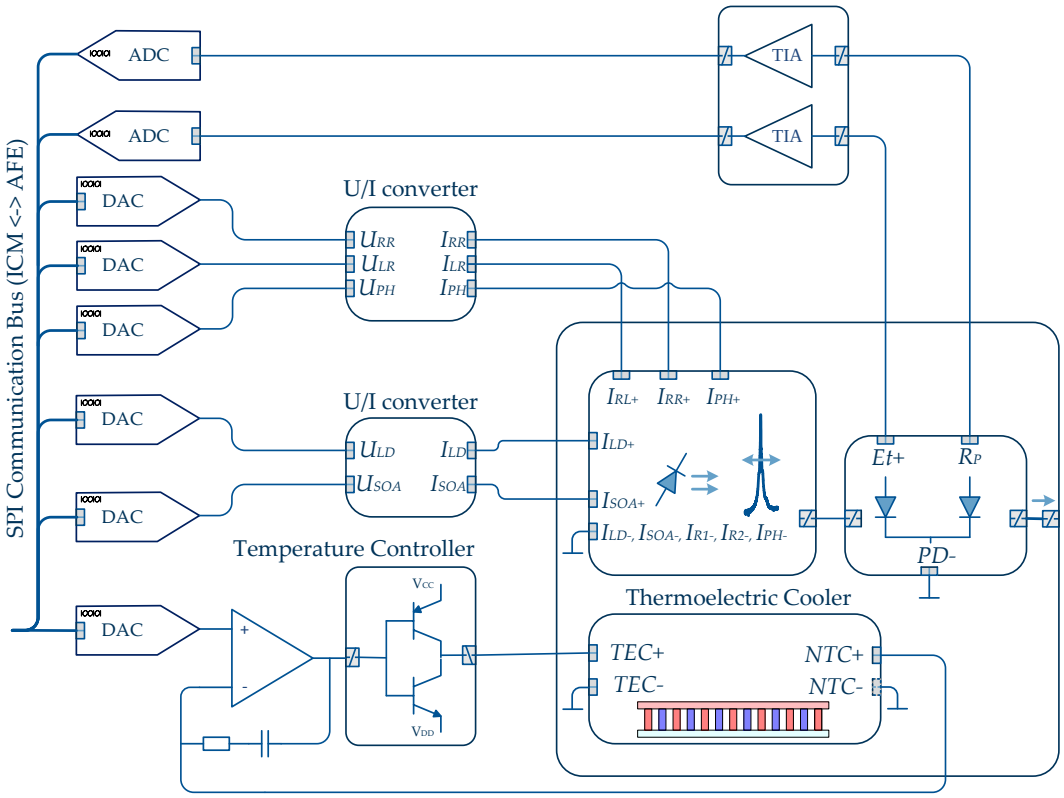

Figure 5.2: *Block diagram of the laser transmitter system including temperature controller, voltage/current converter and transimpedance amplifiers for internal photodiodes.*

requirements to the converter circuit are derived in this work and are presented here in short:

- Bipolar architecture allowing a sourcing and a sinking of current. It has been shown in tests, that the left- and right reflector sections have high leakages. When setting one reflector to zero and the other reflector to maximum, current up to 250µA flow out of the terminal which is set to zero. This directly affects the laser wavelength, so the designed circuit must be able to compensate this effect by sinking current.
- The maximum current is defined to 35 mA for the left and right reflector which shall be generated at an input control voltage of 3 V. For the phase section the maximum current is 8 mA, for laser and SOA 100 mA. These values are taken from the datasheet as the nominal condition parameters [4].
- The rise time (measured from 10% to 90%) of the output current shall be $\leq$ 10µs to achieve a nominal measurement rate of 1 Hz as required.
- The RMS current noise shall be lower than 450 nA within a bandwidth between 1Hz and 20MHz to limit the laser's wavelength noise, see also the results in table 5.1.

Taking into account the non-linear tuning characteristic of the laser which exponential fit is derived by (3.9), the sensitivity of the output wavelength to current change can be estimated.

$$\lambda_{NL} = A_1 \cdot e^{\frac{-I_{RL}}{t_1}} + A_2 \cdot e^{\frac{-I_{RL}}{t_2}} + y_0 \tag{5.1}$$

The sensitivity can be calculated to

$$\frac{\delta\lambda_{\mathrm{NL}}}{\delta I_{RL}} = \frac{-A_1}{t_1} \cdot e^{\frac{-I_{RL}}{t_1}} + \frac{-A_2}{t_2} \cdot e^{\frac{-I_{RL}}{t_2}} \tag{5.2}$$

with $A_1 = 7.54$ nm, $t_1 = 19.96$ mA, $A_2 = 2.86$ nm, $t_2 = 1.756$ mA and $y_0 = 1555.77$ nm taken from the non-linear tuning characteristic in (3.9).

As can be seen in section 3.3.3 by figure 3.15, the laser's output wavelength is more sensitive to lower control voltages or currents respectively. So the sensitivity is calculated for three operating currents, namely 2 mA, 15 mA and 30 mA. The results are taken to calculate the maximum allowed RMS current noise to obtain an RMS wavelength noise of less than 1.66 pm. The results are given in table 5.1. So, for low currents the RMS current noise in the here defined bandwidth (1 Hz and 20 MHz) shall be lower than 454 nA.

Reflector Current I_{RL} [mA]	$\delta\lambda_{NL}/\delta I_{RL}$	**RMS Current Noise [µA]**
2	-0.862	0.454
15	-0.178	0.094
30	-0.084	0.044

Table 5.1: *RMS current noise and wavelength sensitivity of the MG-Y laser at different operating currents.*

Circuit Design The voltage/current converter circuit designed according to the requirements presented in the previous section is shown in figure 5.3. The circuit consists out of a current sense amplifier (CSA) with a shunt resistor for current measurement, two feedback networks, one around the CSA and one around the bipolar output stage, the bipolar output stage itself, an error amplifier and an input lowpass filter. The current flowing into the laser's control terminal is measured by the shunt resistor R_{Shunt} and subsequently amplified by the CSA to the necessary level. This voltage is fed back to the error amplifier which generates the difference between the setpoint voltage from the DAC and the CSA signal. The error signal is used to drive the base terminals of the bipolar output stage readjusting the output current. This output stage is necessary because there are no space qualified amplifiers available delivering up to 35 mA at its outputs taken into account also the derating restrictions for space designs.

The transconductance gain (voltage to current conversion ratio) for all five currents are defined according their maximum output current given in the laser's datasheet [4] at maximum control voltage of 3.3 V:

The transconductance gain is mainly defined by the CSA feedback and shunt resistor. The output voltage of the CSA as function of the current through the shunt resistor R_{Shunt} follows the equation

$$U_{\mathrm{CSA}} = I \cdot R_{\mathrm{Shunt}} \cdot \frac{R_{\mathrm{CSA-Rf}}}{R_{\mathrm{CSA-Rg}}} \tag{5.3}$$

The CSA gain can be free selected and is here defined to 10V/V by setting $R_{\mathrm{CSA-Rf}}$ to 1kΩ and $R_{\mathrm{CSA-Rg}}$ to 100Ω. A lower input resistor will decrease the overall noise performance

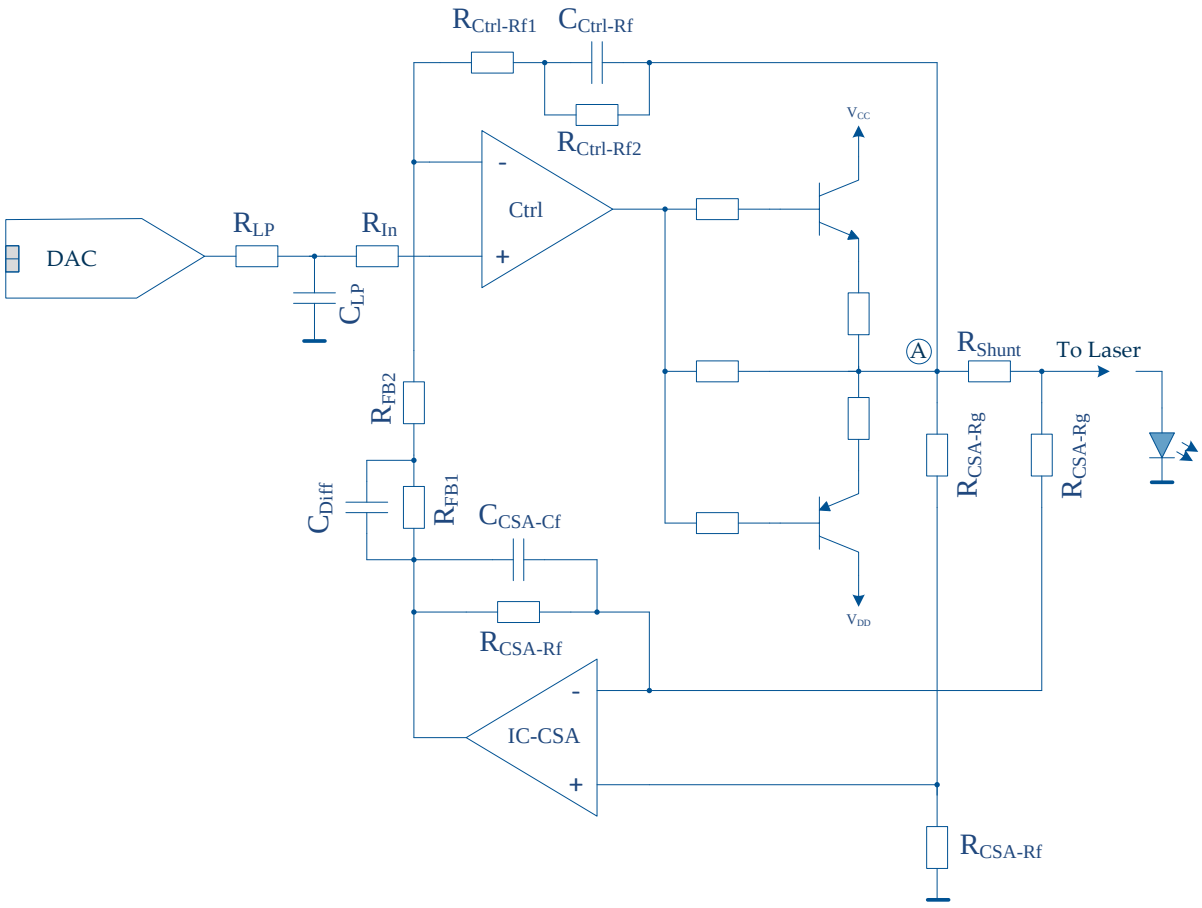

Figure 5.3: *Circuit of the MG-Y laser's voltage/current converter with current sense amplifier (CSA), feedback network and bipolar amplifier stage.*

as it is shown in the next section. So by taking into consideration the gain factor of 10V/V and the inverse transconductance values g_{mx}, derived in table 5.2, the shunt resistor can be calculated to

$$R_{\mathrm{Shunt_x}} = \frac{1}{10 \cdot 1/g_{mx}} \tag{5.4}$$

The resulting shunt resistor values are also given in table 5.2 in the right column.

The CSA has in addition an RC lowpass implemented in the feedback path to limit the contribution of the high frequency noise. Limiting the bandwidth too much increases the rise time of the converter circuit which is not desired. The risetime shall be lower than 10 µs as given above. The 3 dB corner frequency of the RC lowpass filter is calculated to

$$f_{\mathrm{CSA}} = \frac{1}{2\pi \cdot R_{\mathrm{CSA-Rf}} \cdot C_{\mathrm{CSA-Cf}}} \simeq 1.3\mathrm{MHz} \tag{5.5}$$

The amplifier stage builds up on a simple non-inverting amplifier with a push-pull stage at the output to enhance the output current. The output voltage at point A (see figure 5.3) is used as voltage feedback for the amplifier. The proportional gain of the circuit is set by [134]

$$g_{\mathrm{Amp}} = \frac{R_{\mathrm{Ctrl-Rf1}} + R_{\mathrm{Ctrl-Rf1}}}{R_{\mathrm{In}}} \tag{5.6}$$

Parameter g_{mx}	$I_{\max}$@3V	$g_m = I/U$[**A/V**]	$1/g_m$[**V/A**]	$R_{Shunt}[\Omega]$
g_{mRR}	35	0.0116	85.71	8.57
g_{mLR}	35	0.0116	85.71	8.57
g_{mPH}	8	0.0026	384.61	38.46
g_{mLD}	100	0.033	30	3.0
g_{mSOA}	100	0.033	30	3.0

Table 5.2: *Transconductance and shunt resistor values for the five different channels of the voltage/current converter (RR right reflector, LR left reflector, PH phase, LD laser, SOA semiconductor optical amplifier).*

For the circuit design here,$R_{\mathrm{Ctrl-Rf1}} + R_{\mathrm{Ctrl-Rf1}}$ is set to 1kΩ as well as R_{In}. By the help of $C_{Ctrl-Rf}$ a lowpass filter is implemented to reduce high frequency noise. To reduce the steady-state error, the feedback resistor $R_{\mathrm{Ctrl-Rf2}}$ in parallel to the capacitor can be left unpopulated.

For the DC performance of the circuit the resistors R_{FB1} and R_{FB2} as well as the capacitor C_{Diff} do not matter, so the setpoint of the DAC is set directly in relation to the CSA voltage. The error amplifier tries to bring the difference voltage across its inputs to zero, leading to

$$U_{\mathrm{DACx}} = U_{\mathrm{CSA}} = I \cdot R_{\mathrm{Shunt}} \cdot 10 \tag{5.7}$$

The current generated by the conversion circuit as function of the DAC control voltage is finally calculated to

$$I = \frac{U_{\mathrm{DAC}}}{10 \cdot R_{\mathrm{Shunt}}} \tag{5.8}$$

Simulation Results and Output Noise Optimization As can be seen in table 5.1, the current controller's output noise must be lower than 450 nA RMS. So, the point affecting the output noise must be identified. Considering the circuit given by figure 5.3, the CSA's input resistor's thermal noise and the overall voltage noise of the CSA amplifier have a direct impact to the circuit's noise performance. To proof the performance of the circuit, a noise simulation for two different types of amplifiers were carried out. A general purpose amplifier (RHF484) and a low noise amplifier (RH1128), both parts are space qualified, are taken into account for this analysis. In addition the CSA's input resistors were changed by keeping the CSA's overall gain at a constant value of 10V/V.

The noise simulation results for the converter circuit using a standard space qualified operational amplifier (RHF484) are given in bottom of figure 5.4.
For the RHF484 general purpose amplifier, no difference in amplitude transfer function for different input resistors can be observed, see top of figure 5.4. The output voltage noise is strongly dependent on the CSA's input resistance, see bottom of figure 5.4. Considering these results, an input resistance of 100Ω is preferred. It has to be noted, that a too small input resistance increases the current flow into the amplifier's inputs, resulting in a change in offset voltage. In an experiment it has been pointed out that with 100Ω input resistance always a small current flow is present. This causes problems due to limitations in the operational wavelength range of the laser, so an input resistance of 470Ω is chosen. A noise gain peaking at approximately 3 MHz can be observed and increases in

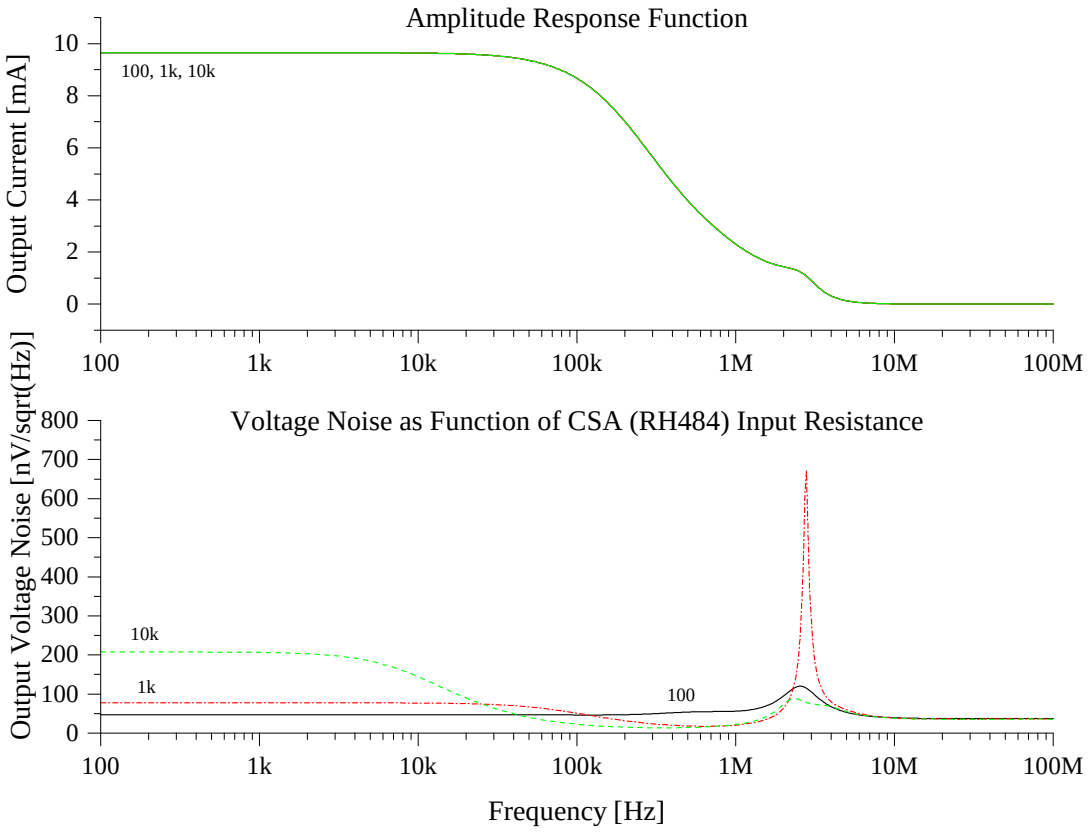

Figure 5.4: *Amplitude response function (top) and output voltage noise (bottom) for the current controller using a standard amplifier (RHF484) as function of frequency. The CSA input resistors used for the simulation were 100Ω, 1kΩ and 10kΩ.*

amplitude with higher input resistors. This peaking can be avoided by adequate filtering in the feedback path of the amplifier.

For the RH1128, see figure 5.5, the amplitude transfer function shows a different dependency on frequency for different input resistances. For the 10kΩ input resistor, the corner frequency is smaller and lies at around 100kHz, which would be still sufficient for the target application here. For the output voltage noise the same dependency as for the RHF484 is observed, but the overall voltage noise is smaller for lower source impedances. So, for the design here, the RH1128 is the preferred part which is later on implemented as the CSA amplifier.

As discussed before by the data given in table 5.1, the required noise value is given as an RMS current value, whereas the values obtained by the simulation in figure 5.4 and in figure 5.5 are given in volts per square root of the frequency. To obtain the RMS value in a certain frequency bandwidth (here defined between 100 Hz ... 100 kHz) the following formula must be applied [134]

$$U_{RMS} = \sqrt{\int_{100Hz}^{100kHz} E_n(f)^2 df} \tag{5.9}$$

where $E_n(f)$ is the voltage noise obtained by the simulation.

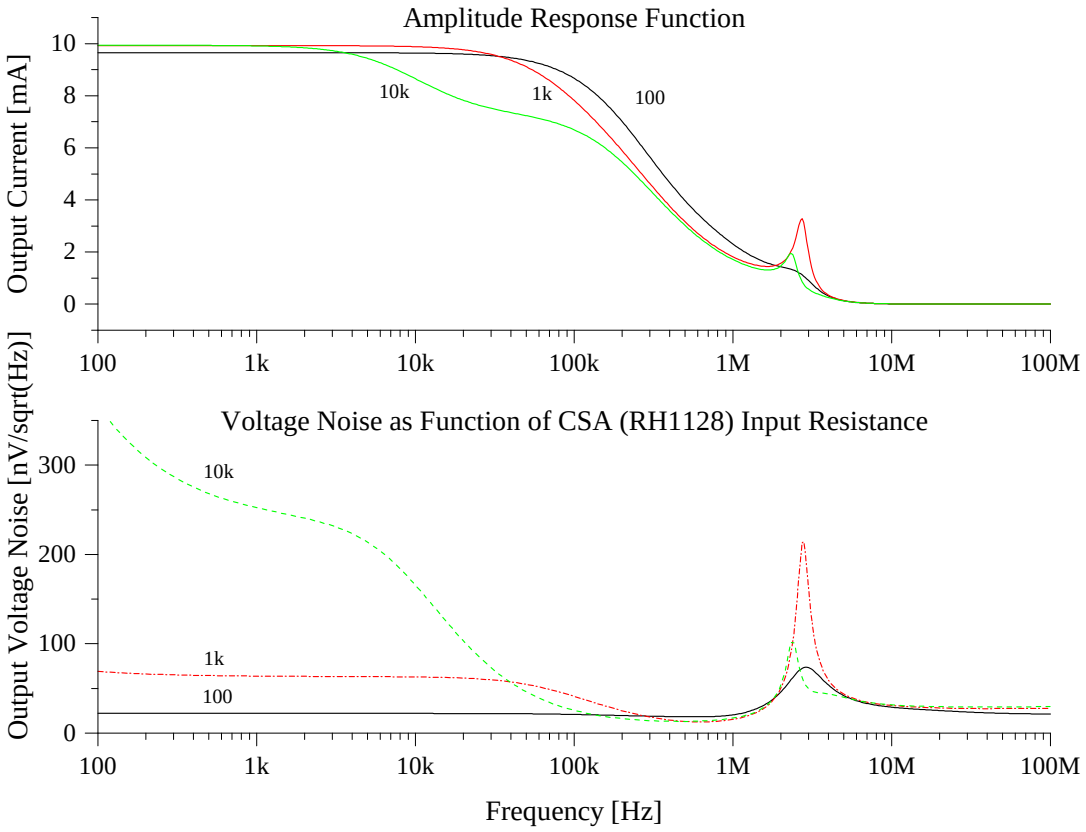

Figure 5.5: *Amplitude response function (top) and output voltage noise (bottom) for the current controller using a low voltage noise amplifier (RH1128) as function of frequency. The CSA input resistors used for the simulation were 100Ω, 1kΩ and 10kΩ.*

By applying (5.9) to the before given simulation results (see figure 5.4 and figure 5.5), the RMS noise voltages of the current controller with different types of amplifier and different values of input resistances are obtained. The integration curves within a frequency of 100 Hz and 100 kHz are given in figure 5.6 for the RHF484 and in figure 5.7 for the RH1128 amplifier respectively.

It can be seen, that the output voltage noise is smaller for the low noise amplifier (RH1128) for low values of source resistances as for the standard general purpose amplifier (RHF484). The correct selection of the input resistor plays an important role for the noise performance of the circuit. The noise simulation results are summarized in table 5.3. The voltage noise is taken from the integrated voltage noise spectral densities given by the figures 5.6 and 5.7 whereas the current noise is calculated by dividing the voltage noise value by the, in the simulation used, used load resistance of 120Ω.

There are two notable points arising from the noise analysis. First, the CSA's input resistance has a direct effect to the noise performance, increasing the resistance increases also the output noise of the circuit. Second, the use of a low-noise operational amplifier with a low input noise voltage density (E_N) reduces the noise by a factor of approximately two compared to a general purpose amplifier.

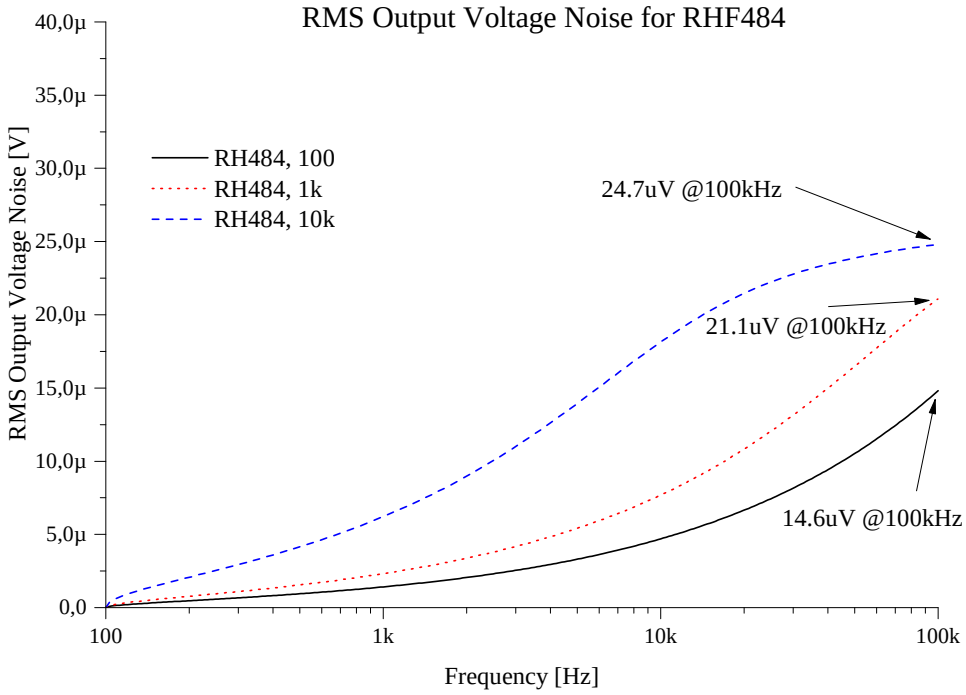

Figure 5.6: *Integration curve to obtain the RMS voltage noise in a frequency bandwidth between 100 Hz and 100 kHz for different values of input resistance for the general purpose amplifier RHF484.*

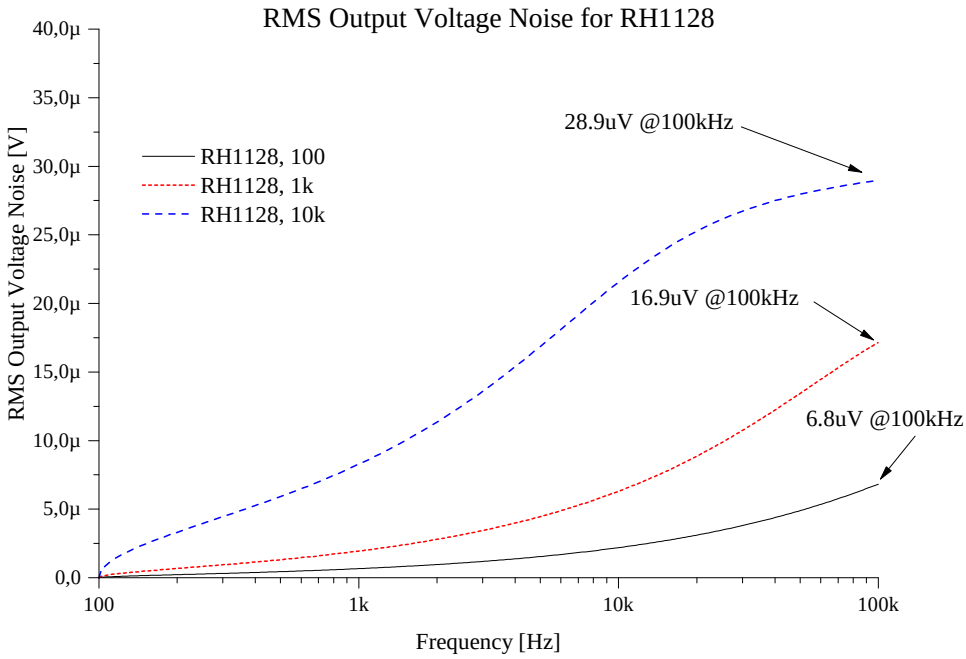

Figure 5.7: *Integration curve to obtain the RMS voltage noise in a frequency bandwidth between 100Hz and 100kHz for different values of input resistance for the general purpose amplifier RH1128.*

Test Results The test results of the voltage/current converter circuit are given in figure 5.8. The converter circuit shows a linear behavior of the generated output current to the input control voltage, only a negligible offset is present. The DC transfer function and a

Circuit Type	U_{RMS} **[µV]**	I_{RMS} **[nA]** $= U_{RMS}$**/120 Ω**
RHF484 - 100Ω	14.6	121.6
RHF484 - 1kΩ	21.1	175.8
RHF484 - 10kΩ	24.7	205.8
RH1128 - 100Ω	6.8	56.6
RH1128 - 1kΩ	16.9	140.8
RH1128 - 10kΩ	28.9	240.8

Table 5.3: *RMS voltage and current noise of the different circuit configurations with different CSA input resistances.*

linear fit describing the output current as function of the input voltage is given in figure 5.8 on the left side.

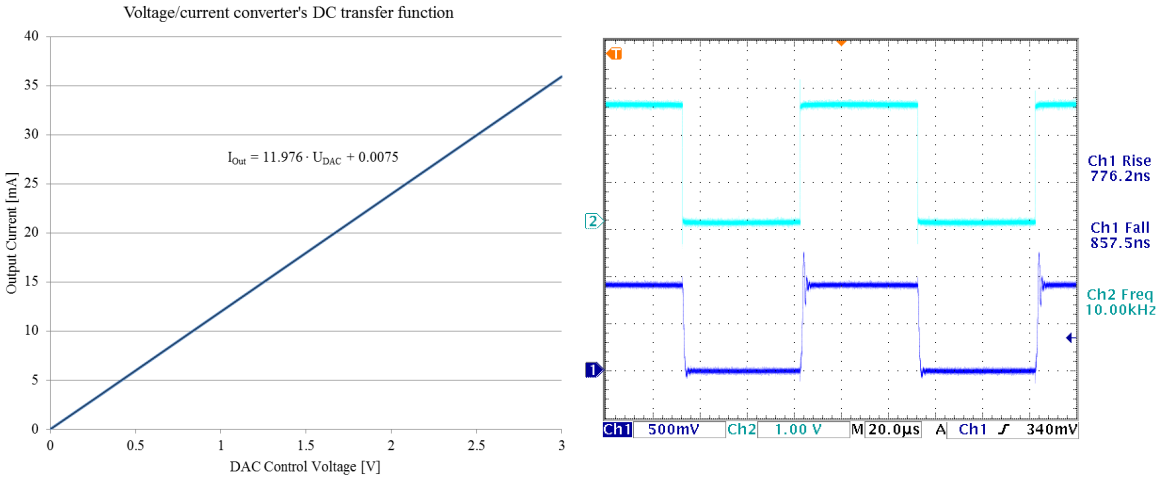

Figure 5.8: *Left: DC transfer function of the designed voltage/current converter circuit showing linear behavior. Right: Transient response curve for a 120Ω load connected to the converter circuit with rectangular input signal with a frequency of 10 kHz and with an amplitude of 3 V (top curve).*

The transient response function of the circuit obtained by applying a 10 kHz rectangular signal with an amplitude of 3 V is shown in figure 5.8 on the right. This signal was selected because it is conform with the later-on applied signals to the circuit during operation of the interrogator. The rise time of the current (measured as the voltage on a 120Ω load resistor connected to the converter's output) is smaller than 1 µs, meeting the requirements given before. The small overshot does not cause any problems, the data acquisition logic introduces a waiting-time of 100 μs until the laser's output wavelength is stable.

Noise Measurements For the current noise measurement a specialized test has been carried out. A low noise amplifier with a 3.3Ω shunt resistor was used to measure the current noise of the SOA and laser driver. For the left and right reflector the shunt resistor was 15 Ω and 50 Ω for the phase, respectively. The shunt resistor values have been selected in that way because they match with the small signal resistance of the laser diode inputs

according measurement results. A low noise oscilloscope (RTO1014 [135]) was used to measure the noise signal in time domain. Afterwards the current noise spectral densities are calculated according to the Welch method in Matlab [120]. The amplifier's gain factor and the shunt resistor are taken into account to calculate the current noise data from the, by the oscilloscope, measured voltage.

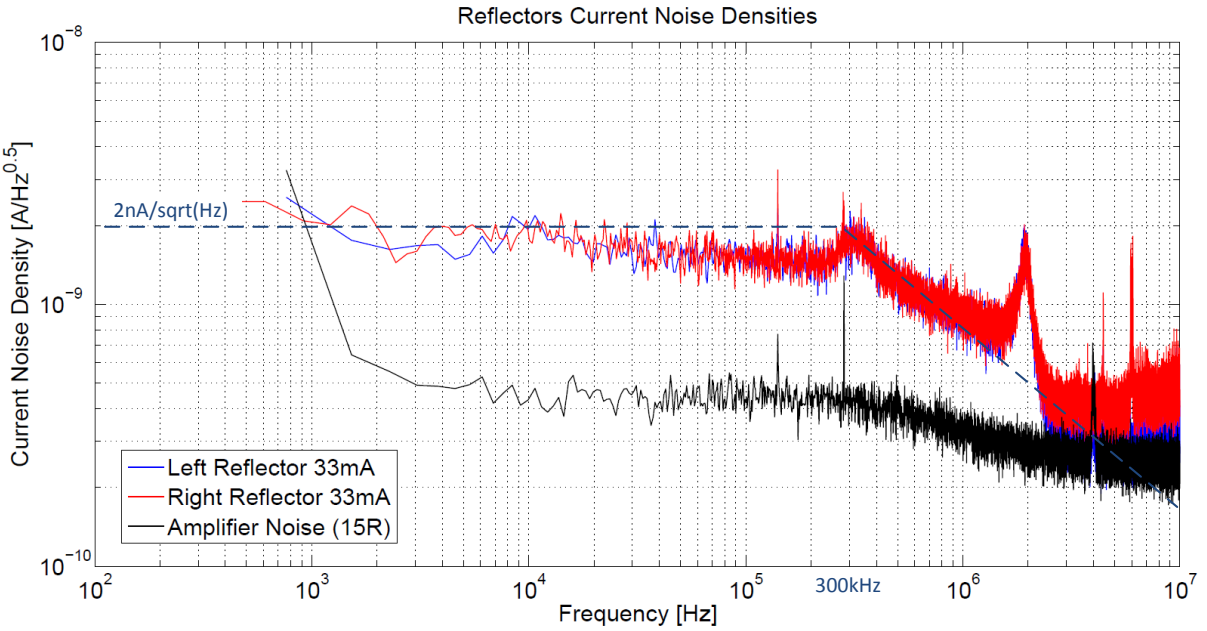

Figure 5.9: *Current noise densities of the left- and right reflector current sources measured with a 15Ω shunt resistor.*

The noise measurement results for the left (blue) and right (red) reflector current driver circuits is given in figure 5.9. In addition also the amplifier's noise contribution is illustrated with the black curve. The curve lies well below the measured data from the driver circuits, hence the results are not distorted by the amplifier. By assuming a low pass characteristic (blue dotted line) with a corner frequency of 300 kHz and a noise spectral density of 2 nA/$\sqrt{\text{Hz}}$ between 0 Hz and 300 kHz the RMS noise in this area is given to [134]

$$I_{SOA-LD} = 2\frac{\text{nA}}{\sqrt{\text{Hz}}} \cdot \sqrt{300\text{kHz}} = 1.1\mu A(\text{RMS}) \tag{5.10}$$

The results for the SOA and laser converter circuit are given in figure 5.10 for the amplifier (black), the SOA current driver operating at 115 mA (orange) and the laser current driver operating at 109 mA (blue). By assuming a low pass characteristic (see blue dotted line) with a corner frequency of 1 MHz and a noise spectral density of 30 nA/$\sqrt{\text{Hz}}$ taken from the curves between 0 Hz and 1 MHz, the RMS noise in this area of the SOA and laser current driver is given to [134]

$$I_{SOA-LD} = 30\frac{\text{nA}}{\sqrt{\text{Hz}}} \cdot \sqrt{1\text{MHz}} = 30\mu A(\text{RMS}) \tag{5.11}$$

Temperature Controller

As already mentioned in section 3.2.2, the laser's output wavelength is strongly depending on laser's temperature, hence an active temperature stabilization mechanism has

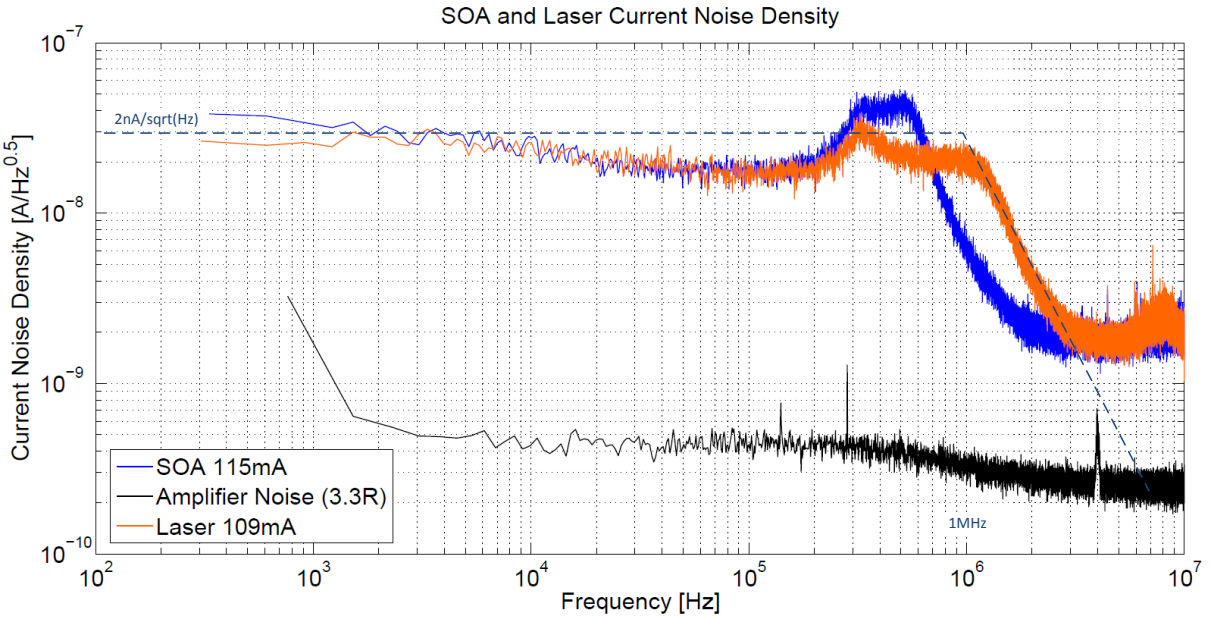

Figure 5.10: *Current noise densities of the SOA and laser current sources measured with a 3.3Ω shunt resistor.*

to be implemented to ensure stable output wavelengths. According to the temperature sensitivity in section 3.2.2, the temperature controller must have a stability better than <10 mK, resulting in a wavelength stability of less than 1.33 pm. The stability here must be seen as a drift on long time scales in seconds rather than in micro-seconds, high frequency fluctuations and noise will not be transferred to the laser crystal due to the low thermal response time. The laser diode's package has an internal thermo-electric cooler and an NTC temperature sensor implemented. So the transmitter subsystem must be able to read out the internal temperature sensor and control the thermo-electric cooler to maintain the operational temperature.

The block diagram of the here in this work designed temperature controller circuit is given in figure 5.11. The temperature of the laser diode is measured by the internal NTC temperature sensor. This temperature is converted to a voltage with the Temperature Sense Amplifier (TSA) which is afterwards subtracted from the DAC setpoint value by the error amplifier. The error signal is fed to a proportional/integral (PI) controller which in turns controls the amplifier stage for the thermo-electric cooling element.

Functional Requirements For the temperature controller first a couple of functional requirements are derived from the subsystem requirements (see section 4.1.1) and from the MG-Y laser's datasheet [4].

- The temperature controller must be able to cope with positive and negative temperature differences, this results in a bipolar design which has the ability to heat or to cool the laser diode. In the case of a minimum start-up temperature of -40°C, the thermo-electric cooling element must heat the laser crystal whereas for a temperature of +65°C the controller must cool down the laser.
- For the MG-Y laser diode a thermal test with a case temperature up to +75°C was carried out. The thermo-electric cooler was able to keep the NTC setpoint resistance

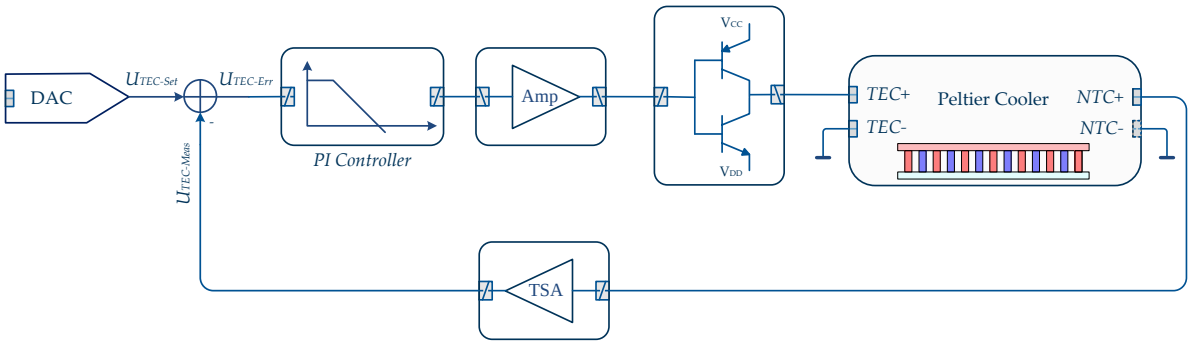

Figure 5.11: *Block diagram of the designed temperature controller circuit. The internal NTC is buffered by the temperature sense amplifier (TSA), which output voltage is used as feedback signal for the entire control loop.*

of 10kΩ with a maximum current drawn of 0.95 A. So the maximum output current in both directions is defined to ±1 A.

- The thermo-electric cooler is a current controlled device, so the temperature controller's output must be a constant current rather than a constant voltage.
- The controller can be designed with pure analog elements, this decreases the complexity and generated noise but decreases also the efficiency. For a digital temperature stabilization additional high speed ADC and FPGA resources would be necessary which are not available.
- The internal NTC shall be used to monitor the temperature direct at the laser crystal. The NTC has a resistance of 10kΩ at a temperature of 25°C, the thermistor sensitivity index β is given to 3930K according to the datasheet [4].

Circuit Design The circuit design of the temperature controller is given in figure 5.12. Beginning on the left, the temperature sense amplifier (TSA) with internal NTC sensor, the error amplifier, the PI controller circuit and the current controlled output stage are illustrated.

The NTC sensor is connected by a reference resistor to the reference voltage. The voltage at the positive input of *IC1*, acting as buffer to the followed circuit stages, follows the simple voltage divider equation. The voltage generated by the TSA at point Ⓐ in the circuit drawing is calculated according to

$$U_{\mathrm{TSA}} = U_{\mathrm{Ref}} \cdot \frac{R_{\mathrm{NTC}}}{R_{\mathrm{NTC}} + R_{\mathrm{Ref}}} + U_{\mathrm{Ofs-IC1}} \tag{5.12}$$

Where R_{Ref} is the reference resistor of 10kΩ, U_{Ref} is the reference voltage of 2.5V and R_{NTC} is the internal temperature sensor's resistance. The used amplifier adds a small offset voltage $U_{\mathrm{Ofs-IC1}}$ which can be neglected for further calculations.

The internal temperature sensor is an NTC type [4] and follows the condition [134]

$$R_{\mathrm{NTC}} = R_{\mathrm{N}} \cdot e^{\beta \cdot \left(\frac{1}{T} - \frac{1}{T_N}\right)} \tag{5.13}$$

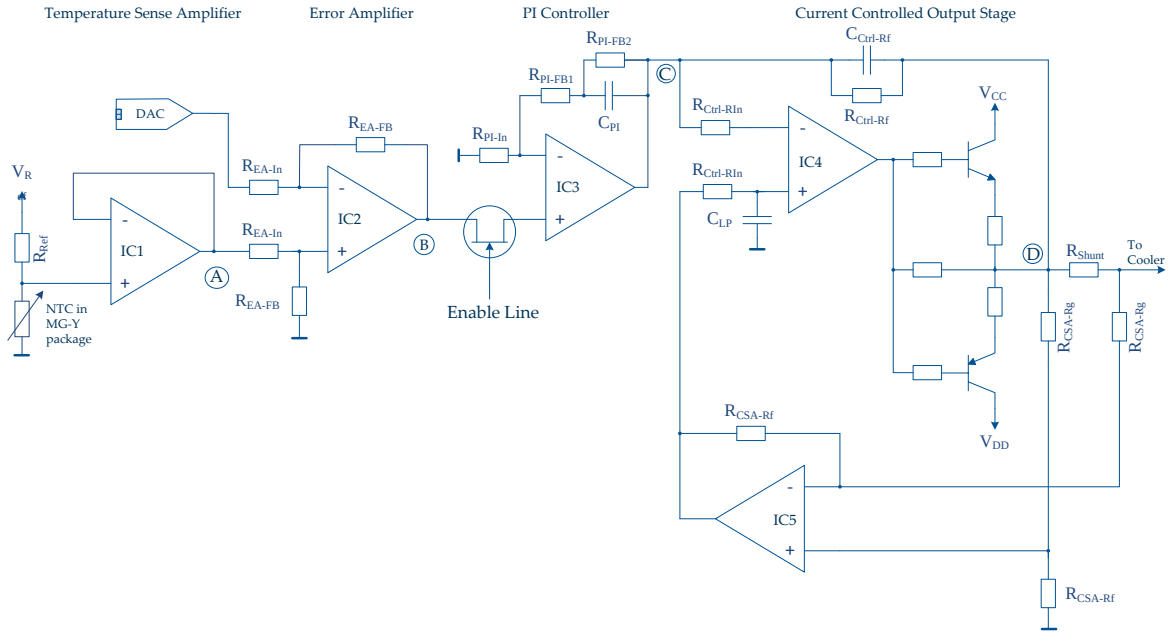

Figure 5.12: *Circuit diagram of the temperature controller circuit with temperature sense amplifier (first left), error amplifier (second left), PI controller circuit (third left) and current controlled bipolar output stage (right).*

with R_N as the sensors nominal resistance at nominal temperature T_N and β as the thermistor sensitivity index of 3930K [4].

The error amplifier built around IC2 with the input resistors R_{EA-In} and the feedback resistors R_{EA-FB} generates an output voltage at point Ⓑ which corresponds to [136]

$$U_{EA-Out} = \frac{R_{EA-FB}}{R_{EA-In}} \cdot (U_{TSA} - U_{DAC-Set}) \tag{5.14}$$

Setting the feedback and input resistors to the same value of 10kΩ, the error amplifiers output voltage is simply

$$U_{EA-Out} = U_{TSA} - U_{DAC-Set} \tag{5.15}$$

The FET between error amplifier and PI controller circuit is a JFET with specialized control circuit to enable or disable the temperature controller circuit. Afterwards the PI controller is connected, the control characteristic is given in the Laplace form to [136]

$$G_{PI}(s) = K_R \cdot \frac{1 + s \cdot T_N}{s \cdot T_N} \tag{5.16}$$

The proportional gain K_R and the reset time T_N of the PI controller are given by [136]

$$K_R = 1 + \frac{R_{PI-FB1} + R_{PI-FB2}}{R_{PI-In}} \tag{5.17}$$

$$T_N = (R_{PI-FB1} + R_{PI-FB2} + R_{PI-In}) \cdot C_{PI} \tag{5.18}$$

The parameters $C_{PI}, R_{PI-FB1}, R_{PI-FB2}$ are estimated by simulation but are afterwards trimmed within the real design.

The temperature controller circuit includes a current controlled output stage with a current sense amplifier (CSA) for current measurement and control. This is necessary because the thermo-electric cooler is a current controlled device. The output voltage of the CSA (IC5 in figure 5.12) is a function of the current through the shunt resistor, following the equation [134]

$$U_{\mathrm{CSA}} = I \cdot R_{\mathrm{Shunt}} \cdot \frac{R_{\mathrm{CSA-Rf}}}{R_{\mathrm{CSA-Rg}}} = I \cdot G_{\mathrm{CSA}} \tag{5.19}$$

The values of the above given resistors can be selected freely, here in this case the shunt resistor is set to 0.1Ω to limit the power dissipation in the shunt resistor, the feedback resistor $R_{\mathrm{CSA-Rf}}$ is set to 8.25kΩ and the input resistor $R_{\mathrm{CSA-Rg}}$ is set to 1kΩ. So the CSA gain factor G_{CSA} is 0.825 V/A, when a voltage of 0.825 V is applied to the output stage by the PI controller a current of 1 A flows. These values have pointed out a good performance during simulations and also for the later hardware implementation.

Etalon and Reference Photodiode Monitoring

For the MG-Y's internal etalon and reference photodiodes a transimpedance amplifier circuit, depicted in figure 5.13 is established. The photodiode's cathodes are connected to a single ground pin of the MG-Y laser [4]. Hence, the current generated by the diodes is positive and flows out from the anode as indicted by the red arrows. Because the transimpedance amplifier (TIA) formed by IC1 and IC2 have an inverting behavior, an additional inverting amplifier is subsequently added for each signal. So, the overall output signal is positive and can be queried by the ADC for later processing inside the FPGA.

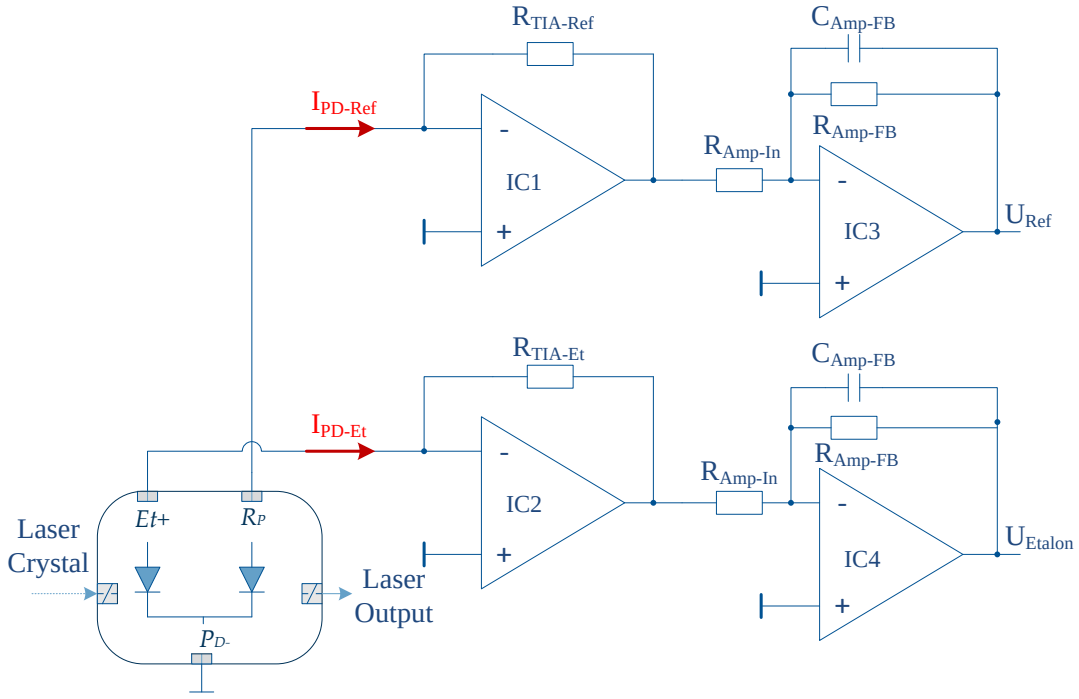

Figure 5.13: *Transimpedance amplifiers for MG-Y's internal etalon and reference photodiodes with subsequent inverting amplifier.*

The output voltages of the two TIA circuits follows the simple equation [134]

$$U_{\mathrm{TIA-Ref}} = -I_{\mathrm{PD-Ref}} \cdot R_{\mathrm{PD-Ref}} \tag{5.20}$$

$$U_{\mathrm{TIA-Et}} = -I_{\mathrm{PD-Et}} \cdot R_{\mathrm{PD-Et}} \tag{5.21}$$

The maximum output current of the reference photodiode is given in the datasheet to 500 µA for 20 mW output power [4]. Using a feedback resistor $R_{\mathrm{PD-Ref/Et}}$ of 4.3kΩ a maximum output voltage of -2.15 V results. The additional amplifier has a gain of -1 V/V so the voltage of -2.15 V is simply inverted, yielding to an overall output signal level of 2.15 V. A feedback capacitor of 330 pF in parallel to the feedback resistor $R_{\mathrm{Amp-FB}}$ limits the bandwidth to approximately 480 kHz.

5.1.2 Receiver

The receiver section consists out of a single photodiode and a single transimpedance amplifier for each FBG channel. In the here developed design two individual FBG channels are implemented, so the circuit given in figure 5.14 can be used to generate a voltage signal out from the reflected light from the FBG sensor. For both photodiodes no pre-connected configuration exist, so the anodes are connected to ground resulting in a negative output current (technically seen as a current flowing into the cathode terminal via ground). The transimpedance amplifier has an inverting behavior but here the current is also negative resulting in a positive output voltage after the first amplifier. The additional inverting amplifier as shown in figure 5.13 is not necessary for the FBG photodiodes here.

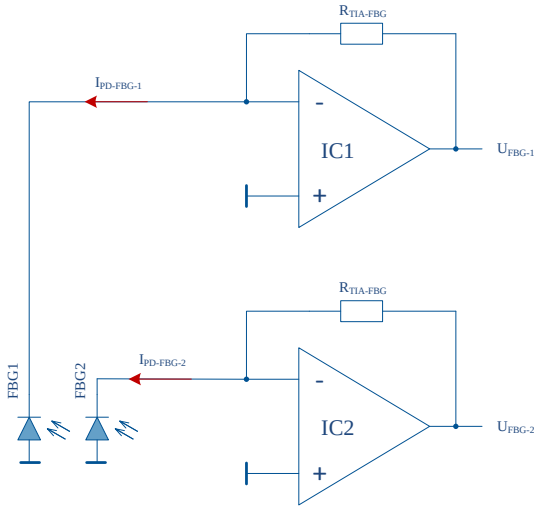

Figure 5.14: *Transimpedance amplifier for the two FBG channels with a single inverting amplifier and generated negative photocurrent resulting in a positive output voltage.*

The FBG sensors are illuminated by the light generated by the MG-Y laser diode, the reflected signal, if the wavelength of the laser and the sensor's Bragg wavelength agree, is coupled out by a passive coupler and fed to the photodiode. For the circuit design an assumption to the reflected optical power for each sensor string according to the architecture presented in figure 5.1 was made. The output power of each single string is assumed to be equal at the nominal output power of the MG-Y laser diode divided by factor four due to four outputs (two for sensing and two for the connection of FSM units)

$$P_{\mathrm{FBG-out}} = P_{\mathrm{MG-Y}} \cdot 1/4 = 20\mathrm{mW}/4 = 5\mathrm{mW} \tag{5.22}$$

For the calculation here the reflectivity of the used sensors $G_{\mathrm{FBG-Ref}}$ must be assumed. At this point a value of 50% is selected because it fits inbetween the values from UV written gratings [71] of 30% and fs-IR written gratings measured in this work to be up to 70%. The reflected power at the Bragg wavelength of a single FBG sensor string can be calculated

$$P_{\mathrm{FBG-Ref}} = P_{\mathrm{FBG-out}} \cdot G_{\mathrm{FBG-Ref}} = 5\mathrm{mW} \cdot 0.5 = 2.5\mathrm{mW} \tag{5.23}$$

The generated photo-current by the photodiode is obtained by [137]

$$I_{\mathrm{PD-FBG-1/2}} = P_{\mathrm{FBG-Ref}} \cdot r(\lambda) \tag{5.24}$$

where $r(\lambda)$ is the responsitivity of the used detector, here a value of $r(\lambda) = 1\mathrm{A/W}$ at a central wavelength of 1550 nm is taken from the datasheet [138].
The output voltage of the transimpedance amplifier is then given to

$$U_{\mathrm{FBG-1/2}} = I_{\mathrm{PD-FBG-1/2}} \cdot R_{\mathrm{TIA-FBG}} = P_{\mathrm{FBG-Ref}} \cdot r(\lambda) \cdot R_{\mathrm{TIA-FBG}} \tag{5.25}$$

For a reflected power of 2.5 mW, detected by the photodetector, and a desired output voltage of 2.5 V, a feedback resistance of

$$R_{\mathrm{TIA-FBG}} = \frac{U_{\mathrm{FBG-1/2}}}{R(\lambda) \cdot P_{\mathrm{FBG-Ref}}} = \frac{2.5V}{1 \cdot 2.5mW} = 1k\Omega \tag{5.26}$$

results.

Detection Noise and Signal-to-Noise Ratio For the transimpedance amplifier circuit, given in figure 5.14, two main noise sources are present, the current noise generated in the photodiode itself and the noise contribution from the transimpedance amplifier. For the photodiode the shot noise due to the flow of photo-generated current and dark current is the main contribution, derived by [137]

$$\overline{I_S} = \sqrt{2 \cdot q \cdot (I_P + I_D)} \ \text{ in } \ \mathrm{A}/\sqrt{\mathrm{Hz}} \tag{5.27}$$

The generated current defining the signal level is simply the photodetector's input power multiplied with the responsivity $r(\lambda)$:

$$\overline{I_P} = r(\lambda) \cdot \overline{P_{\mathrm{Opt-In}}} \ \text{ in } \ \mathrm{A} \tag{5.28}$$

For the transimpedance amplifier circuit the output current noise follows the more complex form of [139]

$$\overline{I_{N-TIA}} = \sqrt{I_N^2 + \frac{4kT}{R_{\mathrm{TIA-FBG}}} + \left(\frac{E_N}{R_{\mathrm{TIA-FBG}}}\right)^2 + \frac{2\pi \cdot E_N \cdot C_{PD} \cdot B}{3}} \tag{5.29}$$

Where I_N and E_N are the current and voltage noise densities of the operational amplifier, $R_{\mathrm{TIA-FBG}}$ is the feedback resistor, T is the temperature in Kelvin, C_{PD} is the photodiode's capacitance and B is the bandwidth of the circuit. The values E_N and I_N can be

found in the datasheet of the used amplifier type, whereas the feedback resistor's value is calculated in the section before by (5.26).

The overall current noise can be combined by taking the geometrical sum of I_{N-TIA} and I_S [137], [139]

$$\overline{I_{N-Tot}} = \sqrt{\overline{I_S}^2 + \overline{I_{N-TIA}}^2} \tag{5.30}$$

Finally the signal-to-noise ratio (SNR) can be calculated to

$$SNR = \frac{|\overline{I_P}^2|}{|\overline{I_{N-Tot}}^2|} \tag{5.31}$$

To allow a fast and convenient way to calculate the noise contribution of the photodiode and the amplifier a small software was developed. Taking the characteristic data from the photodiode (see area ①), the data from the used amplifier IC (see area ②) and the desired transimpedance output voltage and bandwidth (see area ③), the noise parameter can be calculated. The program takes the input power in milli-Watts (next to the *Calculate* button) derived by the main program which takes the complete architecture with all optical losses into account. The output values of the photodetector are shown in the area ⑤, whereas the calculated noise values of the transimpedance amplifier are shown in the area ④. The signal-to-noise ratio and the overall current noise are shown within the area ⑥.

Bandwidth Calculation To achieve the necessary measurement rate of 1 Hz all wavelength control subsystems must be designed in an adequate way. To keep a clear overview of the measurement rate when the bandwidth of subsystems is changed a small software was developed. A screenshot of the software is provided in figure 5.16.

For setting the DAC value, two possible techniques can be used, sequential writing or parallel writing. A timing diagram which illustrates the differences is shown in figure 5.17. When the DACs are loaded sequentially with their data, the I/O delay time of the DAC adds for each sequence. The time for sequential loading can be calculated to:

$$t_{DAC-seq} = \sum_{1}^{3} t_{I/O}(n) + \max(t_{\mathrm{DAC-Settling}}) + \max(t_{\mathrm{U-I}}) \tag{5.32}$$

Whereas the time for parallel writing is given by:

$$t_{DAC-par} = \max(t_{I/O}) + \max(t_{\mathrm{DAC-Settling}}) + \max(t_{\mathrm{U-I}}) \tag{5.33}$$

The I/O delay time of the DAC, the DAC settling time and the voltage-to-current converter settling time are entered in the area ①. For the designed system, the sequential writing is used, so only one SPI logic core within the FPGA is necessary instead of three cores for the parallel writing. Which sequence is used can be selected in the software (see area ② in figure 5.16. Also the number of the MG-Y's look-up table entries are defined here. The number of FBG channels and hence the number of used transimpedance amplifiers and their characteristic can be entered in area ③. The final results like ADC and DAC delay times and the LUT scan rate are depicted in area ④.

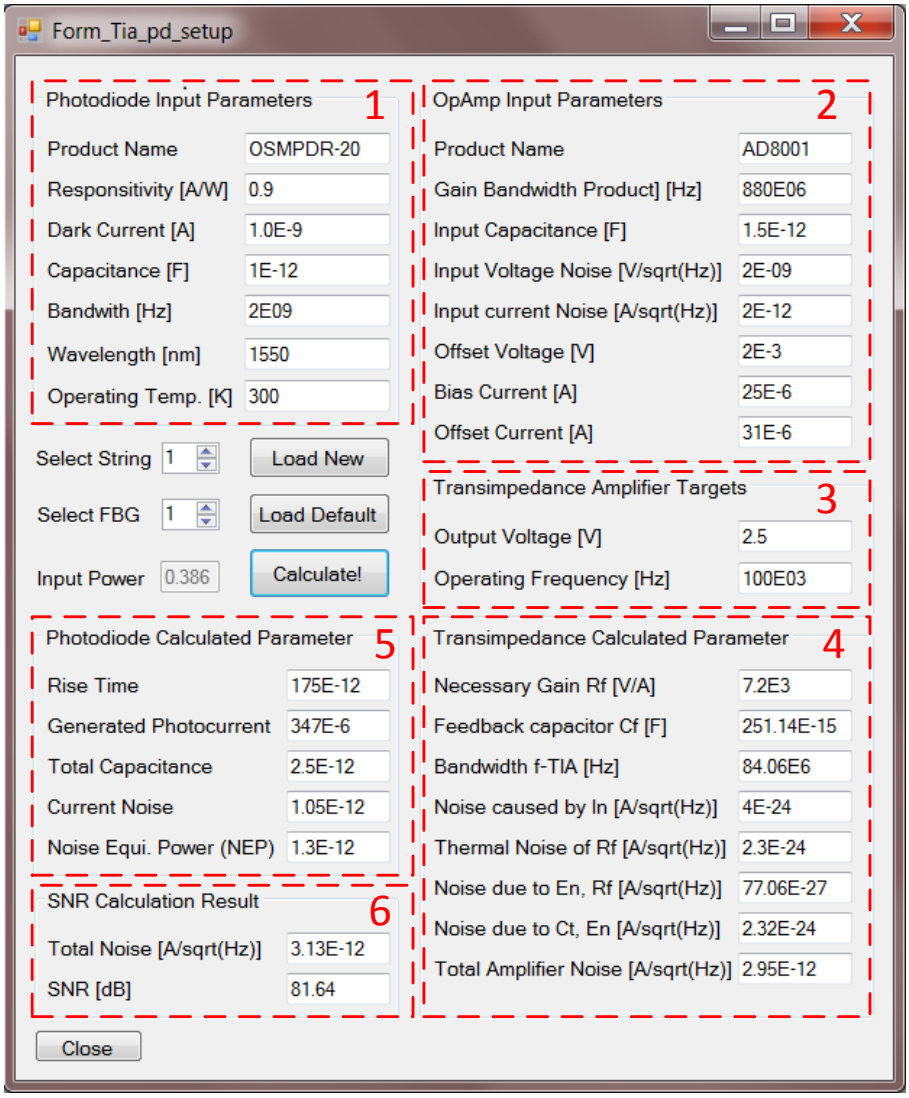

Figure 5.15: *Screenshot of the developed software program for transimpedance noise calculation.*

5.1.3 Controller Module

The block diagram of the controller module for the fiber-optical interrogator module is depicted in figure 5.18. The FPGA is located on the ICM board to which the AFE board (holding the laser transmitter and receiver) is connected. The FPGA handles also the I²C communication of the electrical interrogator module. By combining both functionalities within a single FPGA the development and verification effort decreases [37].

The data transmission from the fiber-optical interrogator module to the HSB Controller Module is done over a full redundant half-duplex serial bus based on the RS485 physical layer. The RS485 bus allows the connection of up to 32 bus transceivers to the same differential data line. The datarate for the HSB system is defined to 1Mbit/s. The communication is based on a single master concept with the ICM and other future modules as slaves and the HCM as master. Data is only transmitted by the module after the master has sent the appropriate command. [37].

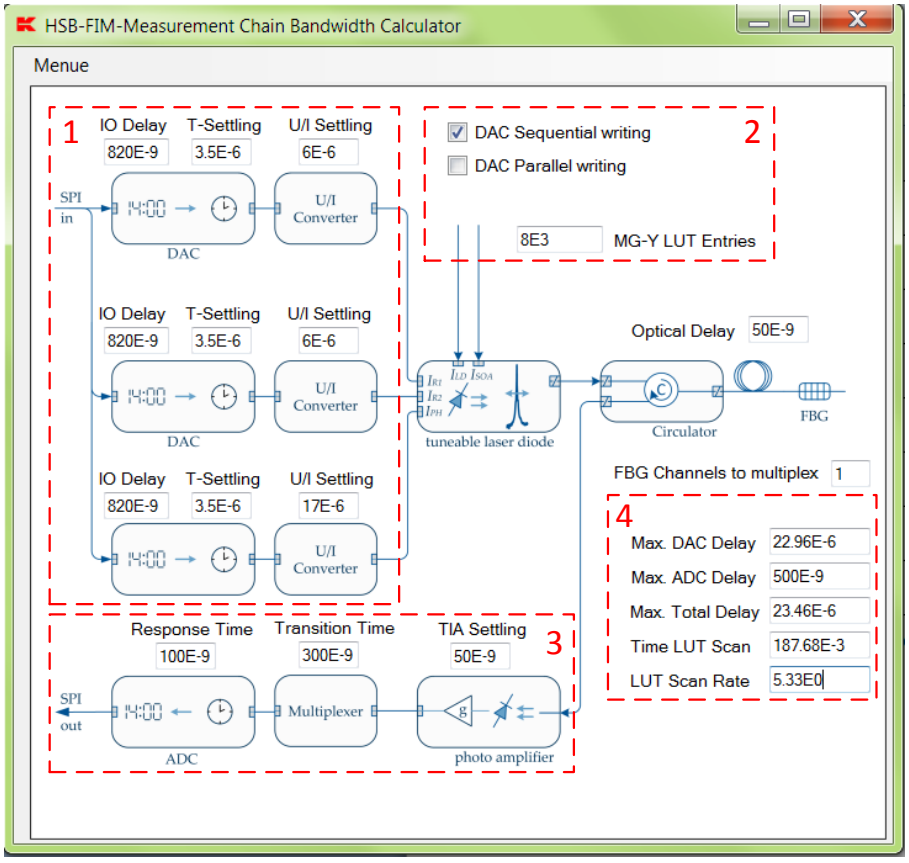

Figure 5.16: *Screenshot of the bandwidth calculation program developed for fast and easy calculations.*

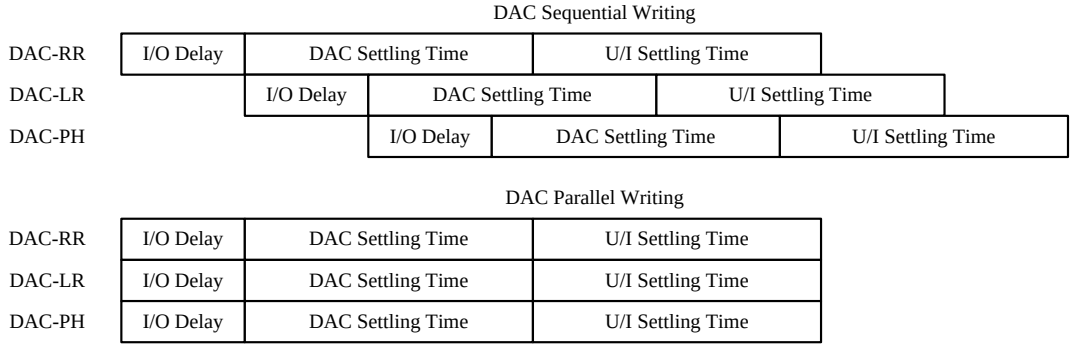

Figure 5.17: *Illustration of the sequential (top) and parallel (bottom) writing of the DACs.*

For the internal memory and LUT storage an MRAM based on ferromagnetic memory technology is used. This type of memory is quite new for the usage in space systems [140]. The access times are nearly the same as for an SRAM, but the data is held also during power off-mode. So the LUT for the implemented laser diode can be stored locally on the module. Because the information is stored by a magnetic field rather than by an electric field (FLASH cells) the memory cells itself are mostly SEU free. Nevertheless a 7Bit EDAC (error detection and correction) logic is implemented within the FPGA. This feature needs additional 7 Bits of every addressable memory word resulting in a total field bitwidth of 32Bit data + 7Bit EDAC = 39Bit. The usable memory is therefore limited to the 8 Mbit memory chip (see middle of figure 5.18), whereas the memory needed for

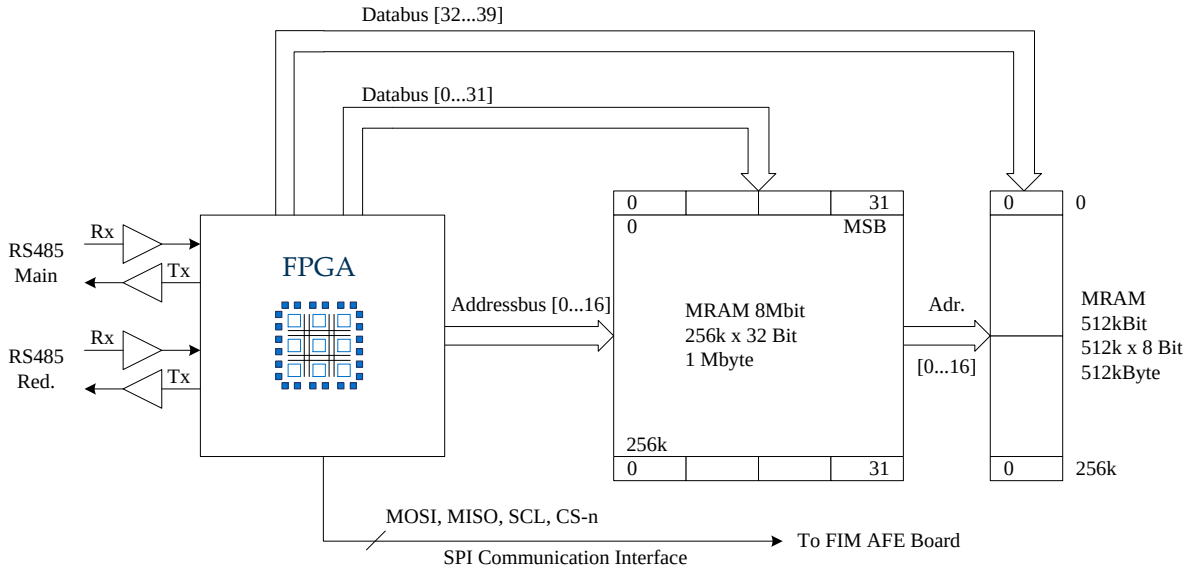

Figure 5.18: *Block diagram showing the important functional blocks for the FIM controller implemented inside the ICM FPGA. The AFE board is controlled by the SPI interface, data transfer is done over the RS485 communication bus and the data for LUT is stored in the shared MRAM memory.*

EDAC function is shown on the right. [37].

5.1.4 Optical Front-End

The referencing system is used to calibrate the MG-Y laser's wavelength during operation. As observed during the radiation test series (see section 6.3.4), the laser shows a drift in wavelength of approximately 50 pm after gamma radiation and neutron displacement damage test (100 krad TID test respectively $1 \cdot 10^{12} n_0/cm^2$ neutron displacement damage test). In addition also a slope filter is implemented in the design allowing an in-orbit re-calibration of the system [37]. The OFE holds also the passive fiber couplers for the FBG sensing subsystem used to split up the laser light and directing it to the FBG measurement channels. The OFE components are mounted on a dedicated support structure which is included onboard the AFE board. The different photodiodes are also part of the OFE, the connection between OFE's photodiodes and the transimpedance amplifiers on the AFE board is done by wires. The MG-Y laser, the optical isolator and the polarization switch are mounted on the AFE PCB and are shown in figure 5.19. The OFE is optically connected to the AFE by one single-mode fiber. From the laser's output light 10% of the optical power are coupled out and are used for the referencing system (top path in figure 5.19, the remaining 90% are used for the FBG measurement system (bottom path of figure 5.19).

Referencing System

The optical referencing system of the AFE is shown in 5.20 [37]. From the output of the MG-Y laser 10% are used for the referencing system. This laser light is split up into four branches, so each arm has 2.5% of the laser's output power. The MG-Y laser has an output power of 20 mW, so each arm receives approximately 0.5 mW (the splice losses and the losses in the isolator are not taken into account at this point). All parts are fiber

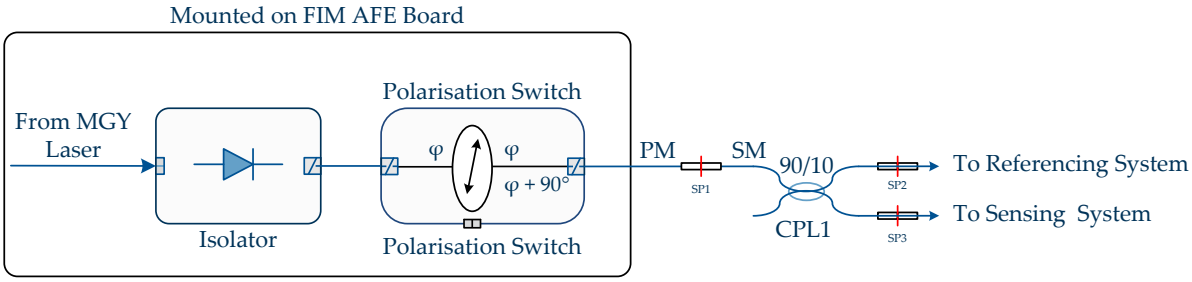

Figure 5.19: *Optical front-end illustrating the two paths of the laser's output light. Referencing channel on top with 10% and measurement channel on bottom with 90% of laser's output power respectively.*

coupled and are connected to photodiodes. The generated photo-current is amplified with transimpedance amplifiers on board the AFE module.

The fiber-optical elements used within the referencing system are given here in short:

- Etalon 25GHz [141]: This etalon has a low finesse of about 7 and a free spectral range (FSR) of 25 GHz. The etalon is completely fiber coupled and is based internally on a free space etalon. Free space etalons are better suited for space usage due to the lower impact of radiation induced effects such as compacting or changes in refraction index. According a radiation test for this etalon no change in optical properties for a TID up to 100 krad were observed. [37]

- Etalon (Spare): This etalon is not implemented in the OFE but a spare channel and additional mounting space is foreseen.

- HCN gas cell: The gas cell is used for absolute referencing of the laser's wavelength. The hydrogen cyanide (HCN), exactly speaking $H^{13}C^{14}N$ gas shows absorption lines which are ultra-stable over temperature and radiation. For the system, the strongest absorption lines are taken for absolute referencing of the laser. The pressure of the HCN inside is given to 100 Tor and the length of the cell is 5.5 cm. A detailed spectral information including the exact wavelength can be found in [142].

- Slope Filter: This unit is used for on-ground calibration of the laser and is not used online during measurement cycles.

Measurement System

The main goal of the OFE is the direction of the laser light for sensing applications to the FBG sensing channels and back to the photodiodes.
For this 90% of the output power of the MG-Y laser are fed to a coupler cascade. First the light is split into two branches with equal power (CPL3) in figure 5.21. These two ports are connected to another 50/50 splitter (CPL4 and CPL5 respectively). Sensing channel 1 is formed by CPL4 whereas sensing channel 2 is formed by CPL5. At each coupler (CPL4 and CPL5) 50% of the input light are available. For the FBG channels the reflected light is important, so this light is coupled back to the bottom left port of the coupler on which a photodetector is connected. The same holds true for the channel 2. In addition the two not used ports are made available at the outside of the HSB system.

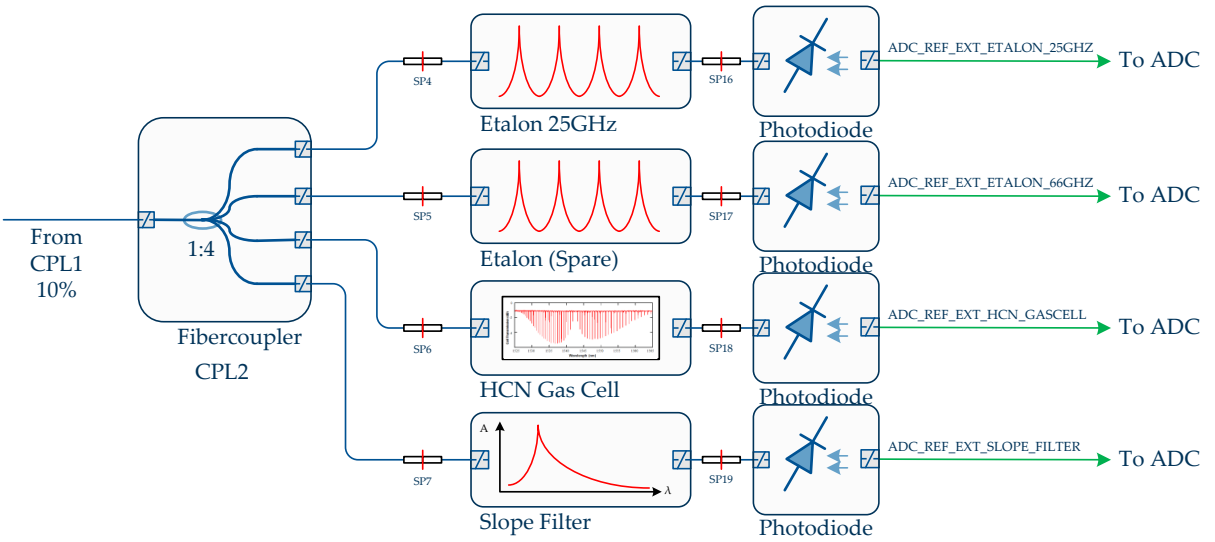

Figure 5.20: *Referencing system of the optical front-end used in the fiber-optical interrogator module for laser stabilization [37].*

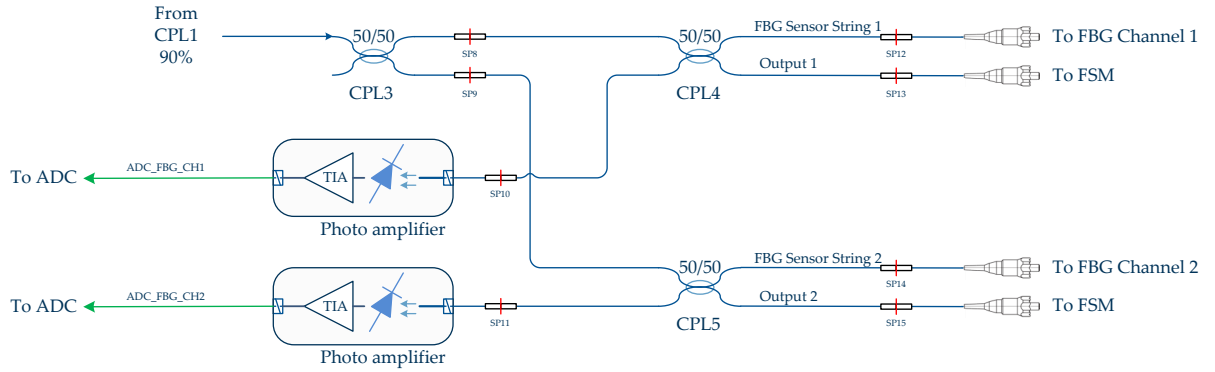

Figure 5.21: *Schematic drawing of the measurement subsystem of the optical front-end. The unit is designed for two measurement channels holding FBG sensors. In addition two pure outputs are available for the connection of FSM modules increasing the number of channels up to eight.*

These two ports allow the connection of the fiber-sensor multiplexer (FSM) to increase the number of measurement channels. An illustration of this unit is shown in figure 5.21.

5.2 Software Architecture

5.2.1 FPGA Requirements

The complete control logic of the fiber-optical interrogator shall be implemented inside the FPGA located on the ICM board. The used FPGA is an *RTAX2000* anti-fuse radiation hard FPGA special developed for the usage in space applications [143].

The functional requirements derived in this work for the control logic are as following:

- The control logic shall be able to detect the Bragg peaks inside the spectral data and determine the FBG's central wavelength by the use of certain algorithms.

- The Bragg wavelength shift shall be converted to a temperature by using the internal stored calibration values.
- The logic shall be able to handle a datastream of 10 kSamples/s.
- The logic design shall be implemented manually without the usage of Matlab/VHDL compilers due to the inefficiency of this solution
- The implementation shall be resource-sharing, saving resources by reusing the same functionality.
- All computation shall be carried out with a fixed point arithmetic with a resolution of 0.1 pm to avoid measurement inaccuracies due to numerical rounding errors.

5.2.2 Interrogation Cycle

The interrogation cycle of the fiber-optical module is presented in figure 5.22. The module is in the *idle*-state during startup mode and in-between two measurement cycles. By the configurable clock module the measurement rate of the interrogation module can be set, the module is also responsible for timestamp generation. [37]

When the clock module triggers a measurement, the data for setting the control DACs are taken from the Look-up table (LUT) memory. After setting the control values, the laser onboard the AFE changes its output wavelength according to the DAC values. In the next step, the, by the FBG reflected signal, is queried by the controller and stored into the memory. This sequence continues until all LUT entries are passed. After querying a full spectrum, the configuration data from the instruction list memory is taken to calculate the sensors response. These data can be seen as sensor calibration data allowing the conclusion from Bragg wavelength to temperature.

For monitoring and test purposes it is also possible to download the full measured spectrum. So the memory must be large enough to hold these data. For the nominal interrogation cycle it is also possible to start the peak finding algorithms as soon a peak is detected in the spectral data. This increases the measurement rate strongly. Because the control logic is implemented inside an FPGA parallel instructions are easily possible.

5.2.3 FBG Peak Detection

Before the algorithm for the Bragg wavelength detection can be applied to the measurement data, the dataset containing the peak information must be identified. For this a so called 'Hill'-detection filter was designed, shown schematically in figure 5.23. By knowing the range in which the FBG reflection peak is expected (every 4 nm an FBG peak is located) all FBGs can be identified in parallel (higher memory effort due to the saving of the full spectrum) or sequential (lower performance but also lower memory consumption). The sampled values are compared with a threshold value and in addition with their neighbor data, to check for the peak form and for centering the data within the shift register.

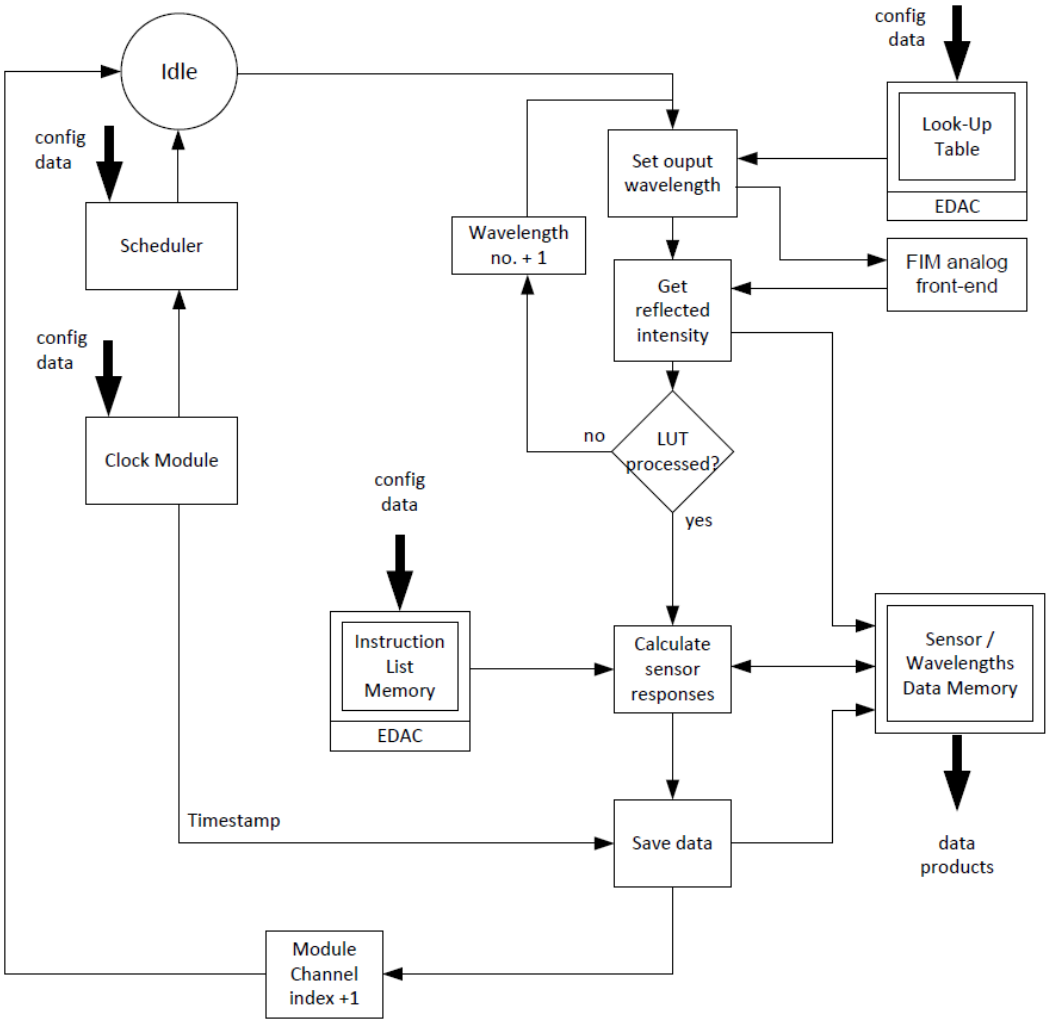

Figure 5.22: *Interrogation cycle of the fiber-optical measurement module.*

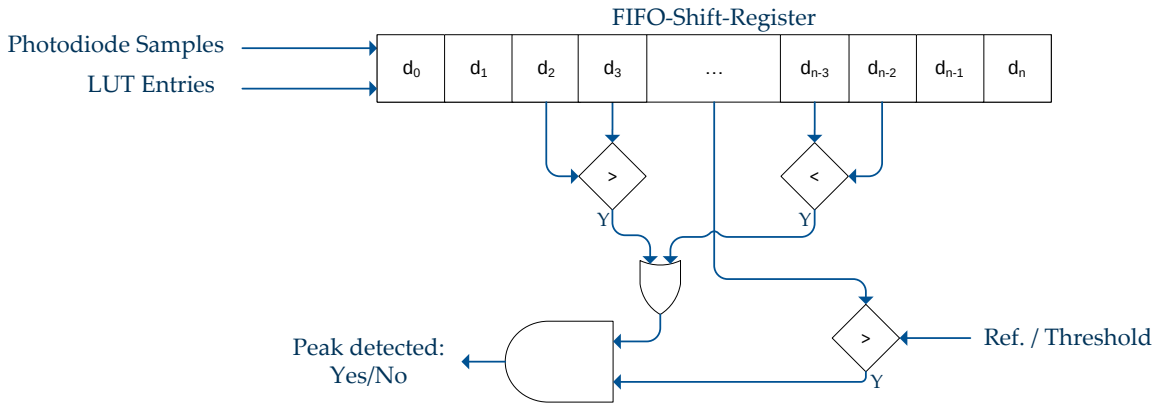

Figure 5.23: *Schematic illustration of the 'Hill'- detection logic used for FBG detection in the sampled datastream.*

Chapter 6

Fiber-Optical Interrogator Test and Verification

6.1 Functional Tests

In this section the functional test results of the developed measurement system are presented. The system showed the expected behavior when querying an FBG sensor string as can be seen in section 6.1.1. In addition for the UV-written gratings a strong polarization dependent shift in Bragg wavelength was observed. This is explained in more detail in section 6.1.3. Furthermore test results are presented showing the mitigation of the polarization dependent Bragg wavelength shift of the FBG sensors. In addition thermal cycling test results of FBG sensors in combination with the herein developed interrogation system are presented.

6.1.1 FBG Measurements

For the designed interrogator module a functional test with an FBG string containing twelve gratings was carried out. The whole spectrum was measured and the reflected light intensities, acquired by the interrogation system, was analyzed afterwards. For the measurement UV-written gratings with a reflectivity of 30% have been used [71]. In addition the fiber containing the FBG sensors was thermally stabilized at two temperatures (28°C and 46°C). Within this temperature range a linear dependency of the wavelength shift to temperature was assumed.

The results are depicted in figure 6.1 on the left for the complete string and on the right for the 7-th FBG peak located at 1545.2 nm. The data plotted in blue indicate the reflected spectrum occurring at the 'cold' temperature of 28 °C whereas the red data shows the spectrum for the 'hot' temperature of 46°C. A shift to higher wavelengths was observed with higher temperatures and, by taking into account the data of the peak number seven, the sensitivity of the FBGs was computed to 11.2 pm/°C. The decrement in signal-amplitude for the peaks No. 6, 8, and 12 has its origin in the bending induced loss of the fiber, which affects the reflectivity in a reciprocal way.

The advantage of the interrogator design is that the absolute value of the reflected power is not important as long as the SNR is sufficiently high. The measurement information is enclosed in the wavelength and not in the amplitude. Also the side-lobes

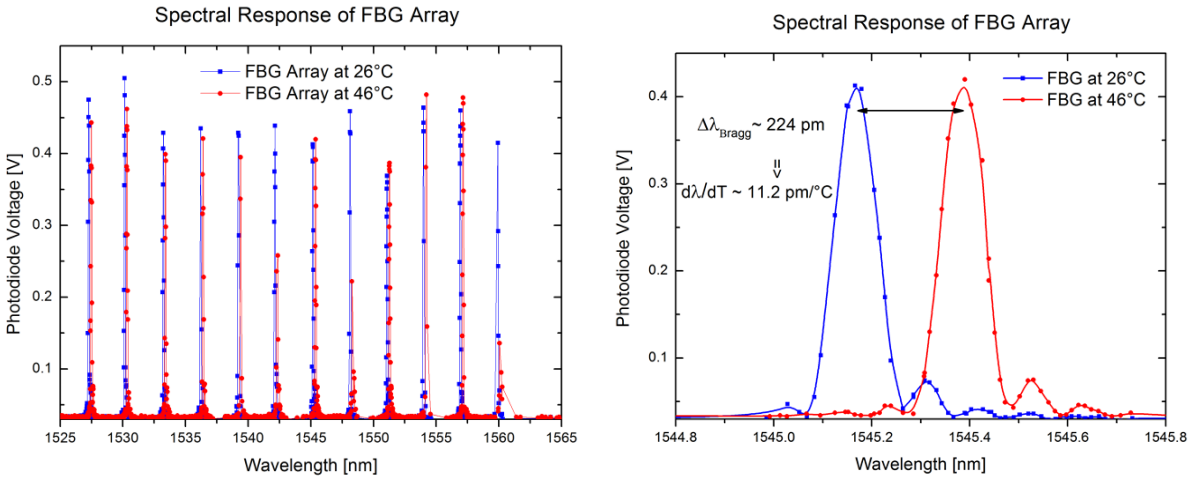

Figure 6.1: *Left: Reflected spectrum of a sensor string containing twelve FBG sensors for 28°C (blue line) and 46 °C (red line). Right: Zoom into the peak number seven, the sensitivity of the pure FBG was determined to 11.2 pm/°C.*

adjacent to the main peak are well observable which is not possible with a spectrometer based interrogator system due to the limited resolution of such systems.

6.1.2 FBG Thermal Test Results

To prove the functional performance of the designed interrogator, two strings with eight FBGs are connected to the two channels of the interrogator. The FBGs were drawn-tower gratings with an average reflectivity of 30% and an FWHM of approximately 300 pm [71]. The setup for this test is illustrated in figure 6.2.

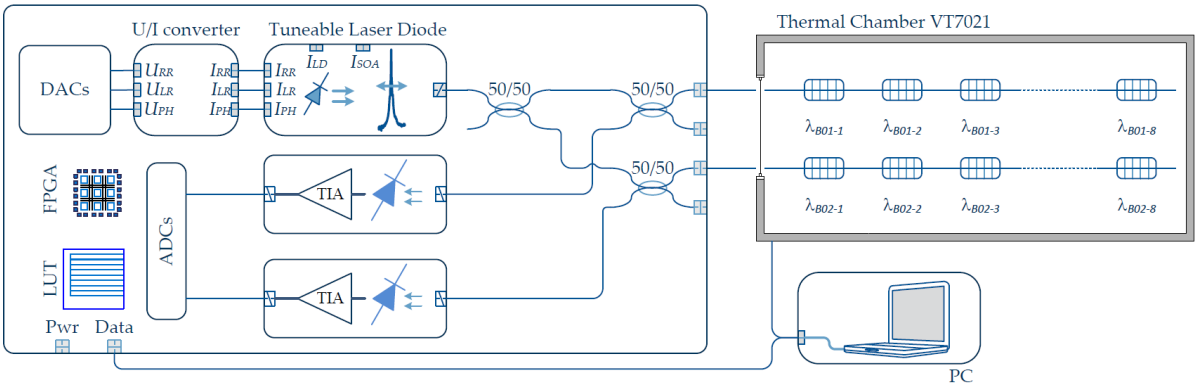

Figure 6.2: *Thermal test setup for measuring two FBG strings with the designed interrogator module.*

The temperature profile has a minimum temperature of -20°C increasing in steps of 5°C to a maximum temperature of +65°C. The measurement period was set to one minute at which the complete reflection spectrum of both strings was queried. After the test, the measurement data-set was reassigned to the single FBG wavelengths. The measurement result of the FBG no. 1 of channel 1 with a central wavelength of 1528.159 nm is illustrated in figure 6.3. Three different types of fit-algorithms were applied to the

data, namely the coupled-mode fit (CM), the Gaussian fit (GS) and the Trip-Hop (TH) algorithm to find the FBG's central wavelength. Taking into account the sensitivity of the Bragg wavelength shift, estimated in section 6.1.1 to 11.2 pm/°C, a conclusion to the sensor's temperature can be made. In the inlet on top right of figure 6.3 the temperature computed with the three different algorithms is shown. It can be seen that the Trip-Hop algorithm shows a higher deviation for this data set around a testing time of 9 hours and 30 minutes for a setpoint temperature of 20°C. For the temperature setpoints of 25°C and 15°C all three algorithms came to the same results within an error boundary of 0.2°C.

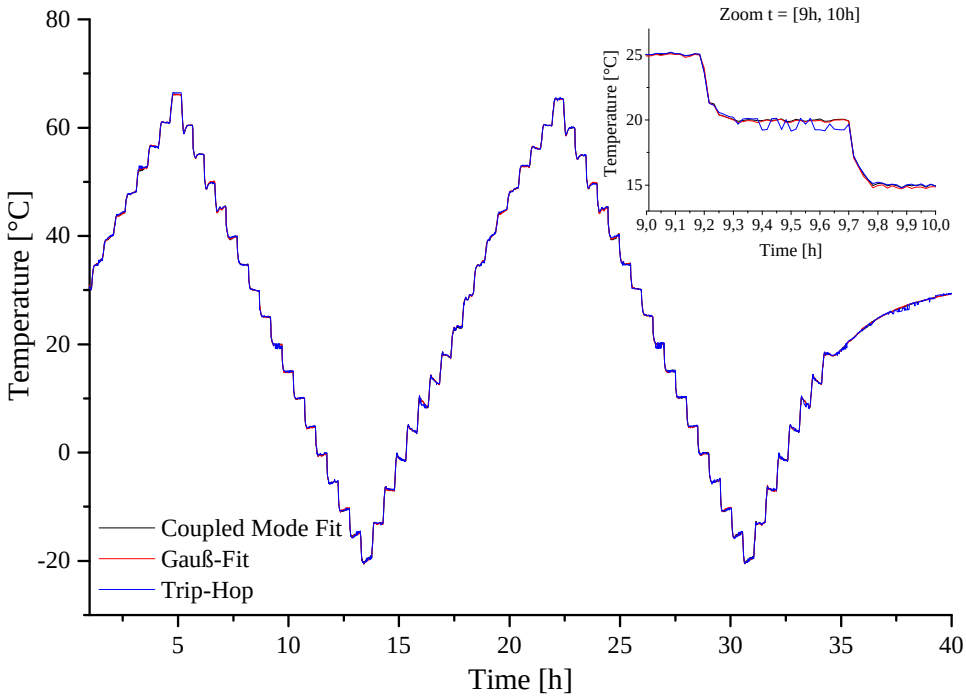

Figure 6.3: *Temperature measured with the FBG sensor and the designed interrogator during the thermal test. Three different fits are applied to the spectral data. Inlet: Zoom into timeframe between 9h:00s and 9h:30s, the Trip-Hop shows deviations.*

For further investigation, the error of the Gaussian fit and the Trip-Hot algorithm with respect to the coupled-mode fit is plotted in figure 6.4 at the bottom. The red line illustrated the error of the trip-hop algorithm whereas the black line shows the error for the Gaussian fit. The data of the temperature profile correlates well with the larger error of the trip-hop algorithm, reaching nearly ±1°C. For the Gaussian fit no excessive errors were observed, the maximum error stayed within a boundary of ±0.4°C.

To investigate the origin of the higher deviation for the trip-hop algorithm, a more detailed look into the spectral data was taken. The reflection spectrum for a temperature of 25°C at a runtime of 9 hours is depicted in figure 6.5 on the left, whereas the spectrum for 20°C and a runtime of 9 hours and 30 minutes is shown on the right. Here a small dip within the right slope of the spectrum can be seen. As described in figure 3.48 the trip-hop algorithm uses the data on the left and right slope of the spectrum, so corrupt data will led to a non-ideal central wavelength estimation. The spectral impurity comes from a discrepancy between the laser set-point wavelength and the real output wavelength. Note,

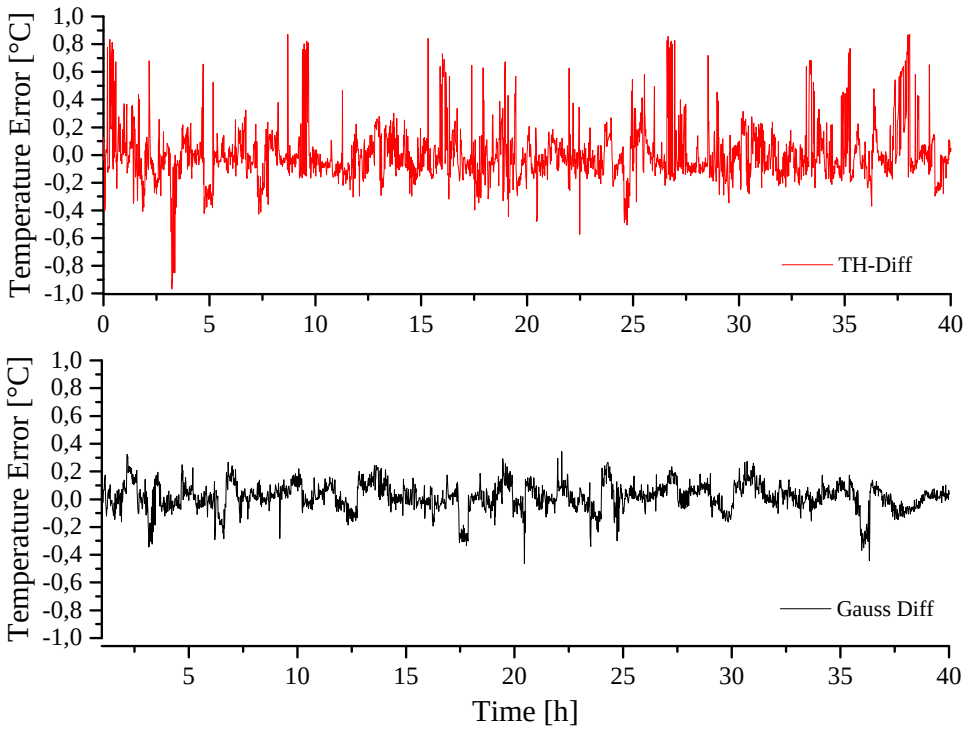

Figure 6.4: *Temperature error with respect to the coupled-mode fit for the trip-hop algorithm (red line) and Gaussian fit (black line) respectively.*

up to this test no wavelength referencing system was introduced within the measurement system. Laser instabilities (a deviation ±10pm is enough) at a certain wavelength leads to a result like shown in figure 6.5 on the right.

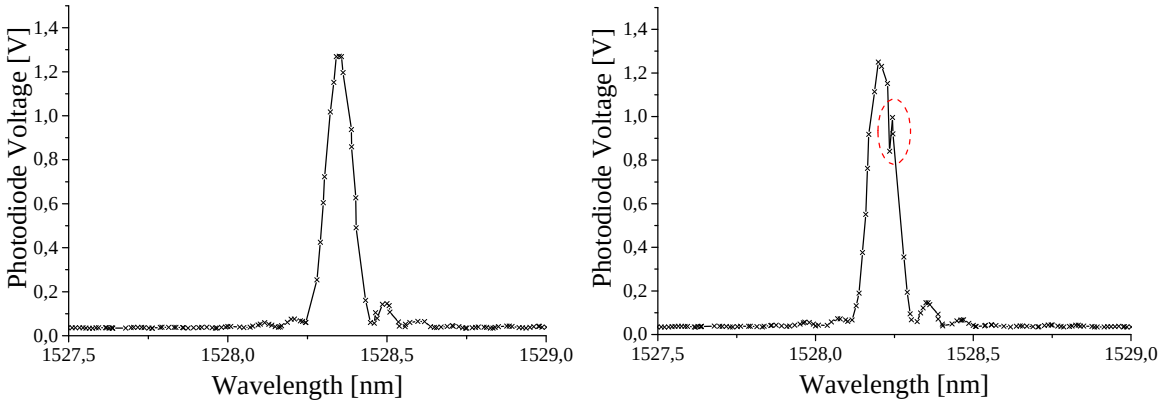

Figure 6.5: *Left: Spectral data for stable wavelength of the laser. Right: Laser instability for lower control voltages generates impurities in the spectrum.*

Having a further look into the used LUT for the wavelengths around 1528 nm, the control parameters can be found to be 0.98 V/0.17 V/2.48 V for right-, left- reflector and phase control values. It has been proved that for lower control voltages, as it is the case for the left reflector with 0.17 V, the current noise of the used voltage-to-current converter circuit influences the stability of the laser's wavelength dramatically. To overcome this problem, a detailed investigation addressed to current noise was carried out leading to an improved design of the converter circuit. The previous current controller was replaced by

a low noise circuit design as illustrated in section 5.1.1. Afterwards a new thermal test of an FBG sensor was carried out, obtaining the results given by figure 6.6. The estimated Bragg wavelength is plotted in blue color, following the temperature profile measured by a PT1000 temperature sensor. The small overshoots have their origin in the non-optimum settings of the used temperature controller during the test. A zoomed view into three cycles in figure 6.6 is given in figure 6.7. It can be clearly seen that the estimated Bragg wavelength even follows the overshoots in temperature.

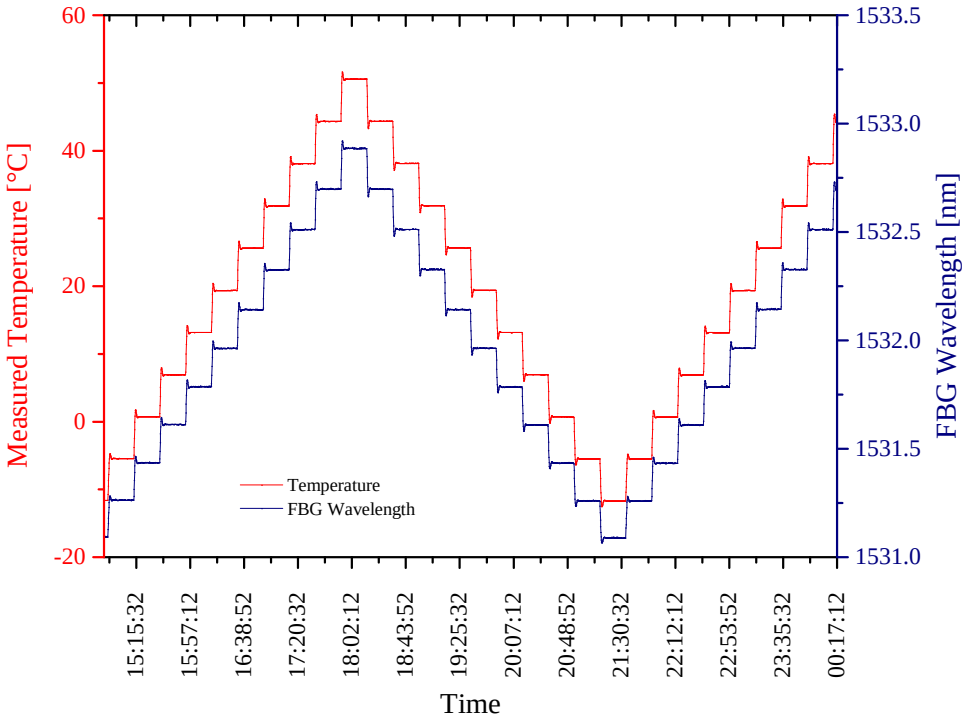

Figure 6.6: *Thermal cycle of a single FBG sensor illustrating the temperature (red) and the estimated FBG peak wavelength (blue).*

Zooming into the estimated Bragg wavelength for one temperature step, a peak to peak wavelength error of 6.5 pm can be obtained. This corresponds to a temperature error of approximately 0.58 °C for the above given sensitivity of 11.2 pm/°C. This is illustrated in figure 6.8 in more detail.

For the measurements here, the polarization effects, as discussed in section 3.4.4, are not taken into account. This was mainly because the working mitigation strategy as discussed in section 4.3.2 was implemented later in the interrogator design. For the used UV written gratings [71] the Bragg wavelength error was estimated to be in the range of 10 pm and it was assumed that the test of the functional performance will not be limited by this effect. As long as the full setup is static, meaning that the fibers are not moved or additional fiber lengths between sensors are introduced, as long the error introduced by birefringence stays constant.

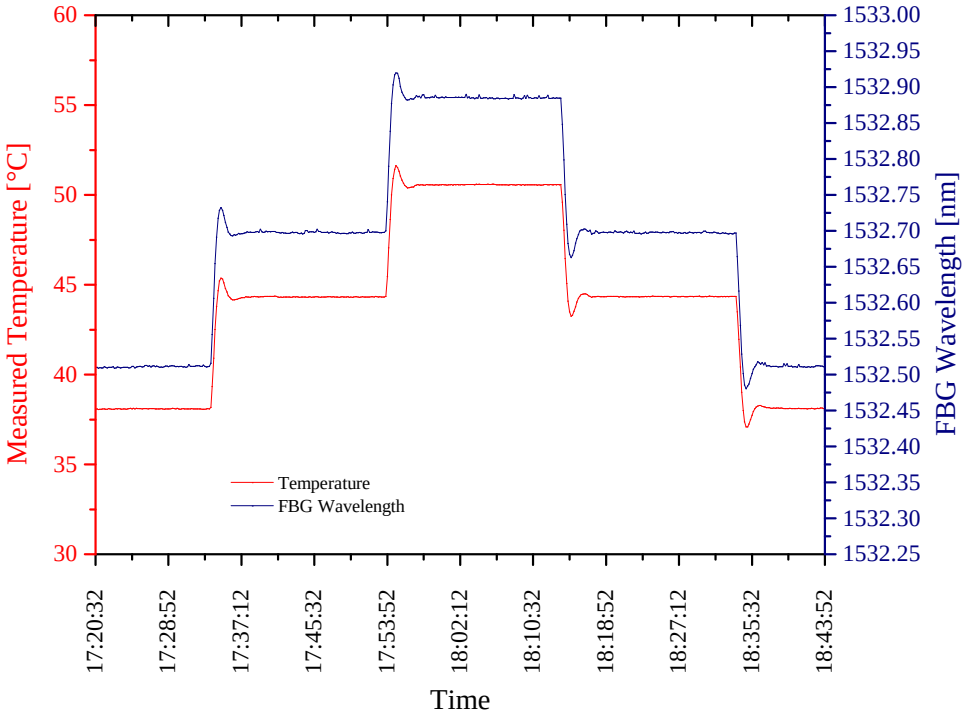

Figure 6.7: *Zoom into three temperature steps from the diagram in figure 6.6.*

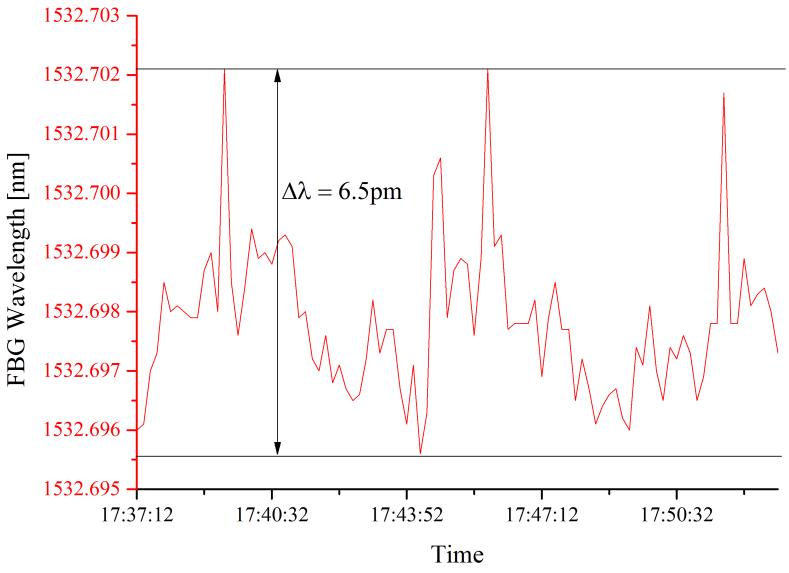

Figure 6.8: *Zoom into estimated Bragg wavelength for one temperature step showing a peak to peak wavelength deviation of 6.5pm.*

6.1.3 Polarization Induced Measurement Error

A simple setup was established to measure the effect of birefringence of the used fiber and sensor combination and the performance with the developed measurement system. The setup is given in figure 6.9. The interrogator module is connected to a polarization controller which is in turn connected to a 25 m long single mode fiber. The polarization controller consists out of a single-mode fiber which is wound around a movable paddle, by turning the paddle, the fiber is twisted and the light polarization is changed. The

FBG sensor is kept at a constant temperature while measurements with different paddle positions were carried out. In the ideal case without birefringence effects in the fiber, each spectral response would look similar, and no change due to paddle position would be observed.

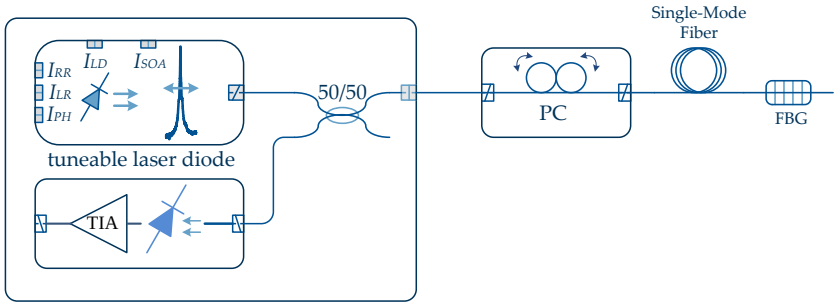

Figure 6.9: *Setup for birefringence error measurement with the scanning laser based measurement system using a manual polarization controller to change the light polarization in the 25 m long single mode fiber. PC polarization controller.*

In the real case the result looks different as can be seen by figure 6.10. This measurement was carried out with a standard UV-written grating. At a certain time interval, different spectra were measured, after some minutes the paddle position was changed and the next measurement was taken. The setup was not changed during the measurement, no disconnections of fibers or electrical components were made. The maximum error caused by polarization effects was measured to $\Delta\lambda_{\mathrm{Biref-Error}}$ =20 pm. By taking into account equation 3.16 where a theoretical temperature sensitivity of 10.338 pm was estimated, the measurement error expressed in temperature is

$$\Delta T_{\mathrm{Biref-Error}} = \frac{\lambda_{\mathrm{Biref-Error}}}{\delta\lambda_B/\delta T} = \frac{20\mathrm{pm}}{10.338\mathrm{pm/K}} = 1.93^{\circ}\mathrm{C}. \tag{6.1}$$

For the fs-IR written gratings in the tested pure silica fibers the same measurement was carried out. The results are depicted in figure 6.11 on the left for the sample fiber *INT20130417A* and on the right for the sample fiber *INT20130418A* [37]. To the measured spectra (15 spectra in total with different paddle position) the Gaussian fit, the Coupled-Mode fit and the Trip-Hop algorithm were applied afterwards. For the *INT20130417A* fiber, the difference between coupled mode fit and Gaussian/Trip-Hop fit is quite high but this resulted from a poor spectral quality of the grating (high side lobes due to misalignment during writing process). For the grating written in the fiber *INT20130418A*, the shift is in the range of 10pm, which corresponds to a measurement error of approximately 1°C.

As already shown in detail in section 3.4.4, the polarization dependent shift has the origin in the birefringence of the used fiber in which the grating is written. So depending on the fiber type (polarization maintaining, low-bend loss, standard fiber or pure silica core fiber) the induced shift is higher. For the thesis here, during the irradiation test series, the pure silica fiber has been identified as the most suitable candidate. But nevertheless to make the system work with any sensor network, a special polarization

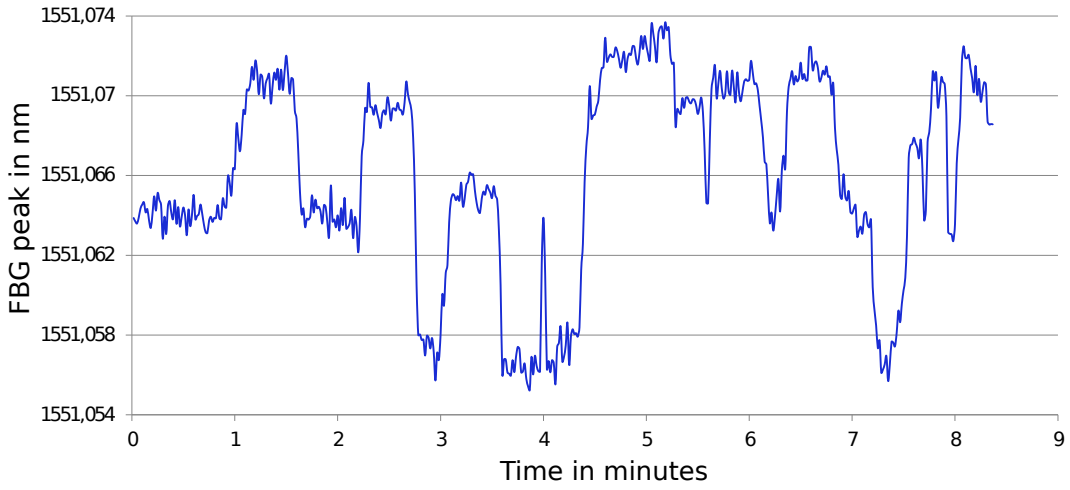

Figure 6.10: *Determined FBG Bragg wavelength with different paddle position and different polarization state in the fiber. The FBG was a commercial grating written by UV-laser light.*

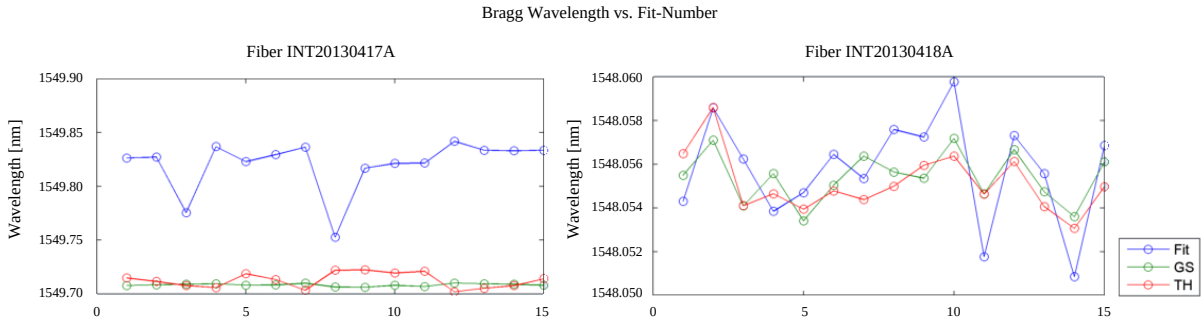

Figure 6.11: *Polarization induced shift of the Bragg wavelength for different measurements (X-axis) carried out with different paddle positions. The gratings were written in pure silica fibers by the use of the fs-IR writing technique. 'Fit' corresponds to the coupled mode fit, GS Gaussian, TH Trip-Hop algorithm.*

mitigation technique must be implemented.

As given in section 4.3.2, the polarization switching with spectral averaging has been pointed out to be the most promising solution for the target application. To check the functionality of this technique, the same measurement as described before was carried out, the only difference was that for each paddle position and polarization state in the fiber two spectral measurements were made. The mean value of both spectra is afterwards computed and finally plotted in figure 6.12. As can be seen the initial error due to birefringence effect of 33.6 pm is reduced to 6.3 pm by the selected mitigation technique.

6.2 Environmental Tests

As described already in the introduction of this thesis talking about the space environment (see section 2.2.2), special attention must be paid when designing systems for space usage. Especially for opto-electronic components, for which no space qualified parts

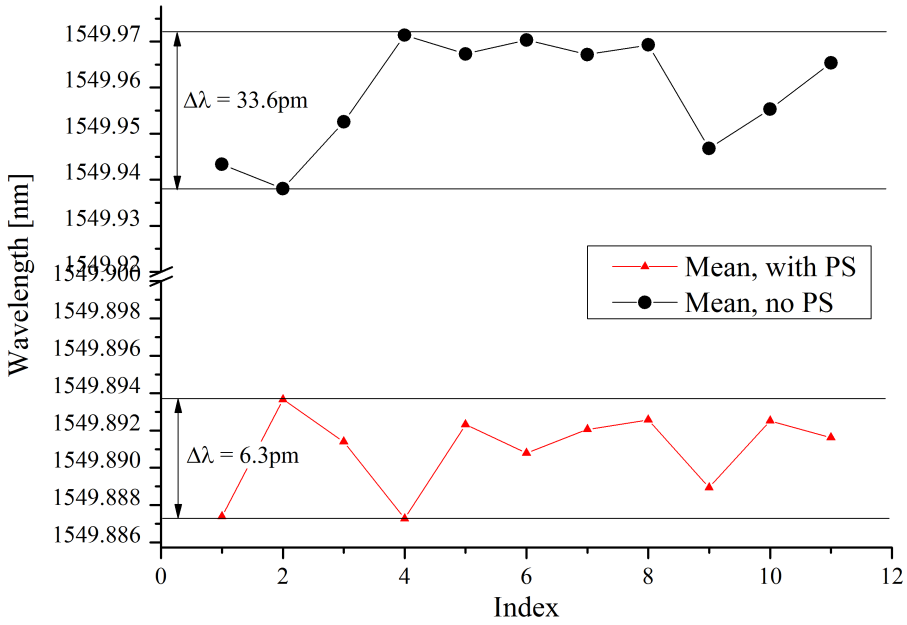

Figure 6.12: *Bragg wavelength error at different polarization states in the fiber with polarization switching and spectral averaging (red) and without (blue).*

are available, additional tests must be considered to prove the full functional behavior for the target environment. According to the different effects caused by cosmic radiation as defined by table 2.3, different tests were carried out for the different key-components of the system. The test setups are described in the next section in more detail.

6.2.1 InGaAs Photodetector Displacement Damage Test

For the selected InGaAs photodiodes a neutron test setup according to figure 6.13 was established. Taking into account the information of table 2.3, displacement damage (TNID) effects affect the performance of the photodetector. This is the reason why a more expensive neutron test was carried out and not a total ionizing dose (TID) test with gamma-rays. The displacement damage test with neutrons was carried out at the *Fraunhofer INT Institute* in Euskirchen, Germany.

The test setup is given in figure 6.13. Three samples of the photodetector were irradiated up to $1 \cdot 10^{12} n_0/cm^2$ within a time of approximately seven hours and 30 minutes. The parameters which are affected due to irradiation are:

- Increase in dark current due to radiation: It is well known that radiation increases the dark current of photodetectors [21, 11, 23]. To measure this effect the light source is periodically switched on and off whereby the dark current measurement is performed in the off-state by the sourcemeter. During the on-state the change in responsivity is measured.

- Change in dark current behavior due to reverse bias voltage: The sourcemeter is also able to reverse bias the photodetector with different voltages. So the reverse current as function of the bias voltage can be measured and a change in the characteristic would be observable if present.

- Change in responsivity: The most important factor is a possible change in the generated photocurrent due to radiation effects. For this a small portion of laser light (approx. 2mW) is fed to the photodetector and the generated current is measured with the sourcemeter. For this measurement the reverse bias voltage was set to zero.

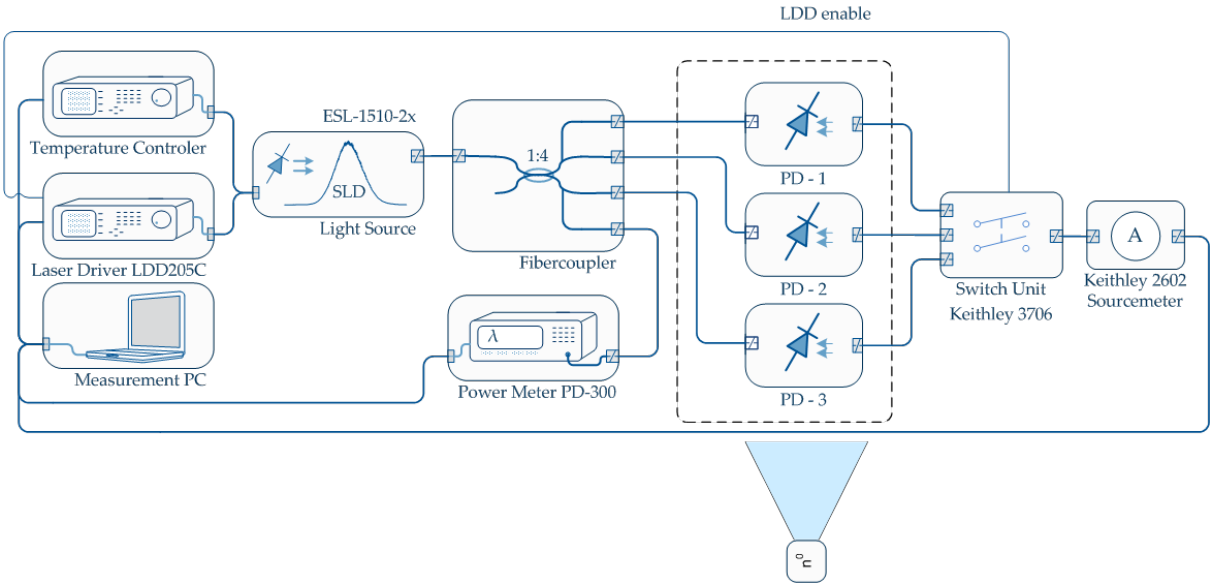

Figure 6.13: *InGaAs photodetector radiation test setup to measure the change in dark current and responsivity.*

6.2.2 Fiber-Bragg Grating Total Dose Test

In the early phase of the thesis, the idea came up to test commercial UV-written FBG sensors for the use in the target satellite application. To prove this possibility, radiation tests according the setup given in figure 6.14 were carried out. The gratings were illuminated by a broadband light source (SLD, 1550 nm, 8 mW, non PM) and the reflected spectra were measured with a spectrometer. Afterwards a fit was applied to the pixel array to calculate the Bragg wavelength. The focus lied on the shift of Bragg wavelength as function of total ionizing dose (TID). To correlate the Bragg wavelength shift to temperature also the temperature inside the test chamber was measured by a resistive PT1000 temperature sensor, so a later correction of temperature induced shift is possible.

It was also necessary to test different mechanical protections of the sensors to check whether they have an influence to the radiation behavior. So for this three FBG sensors with no mechanical protection, three FBG sensors with small protection tube and three FBG sensors with large protection tube were irradiated. For this test a small conflict raised due to the high necessary TID of 25 Mrad which would be necessary if the sensor would be placed outside in the solar panels. It is possible to achieve such high doses within some days, but the test will not cope with the real space environment where such high doses are accumulated over 15 years. A low dose rate (LDR) test would meet the real space environment closer than the high dose rate test. To check if a dose rate dependency in Bragg wavelength shift is present, a high dose rate test and a low dose rate test have

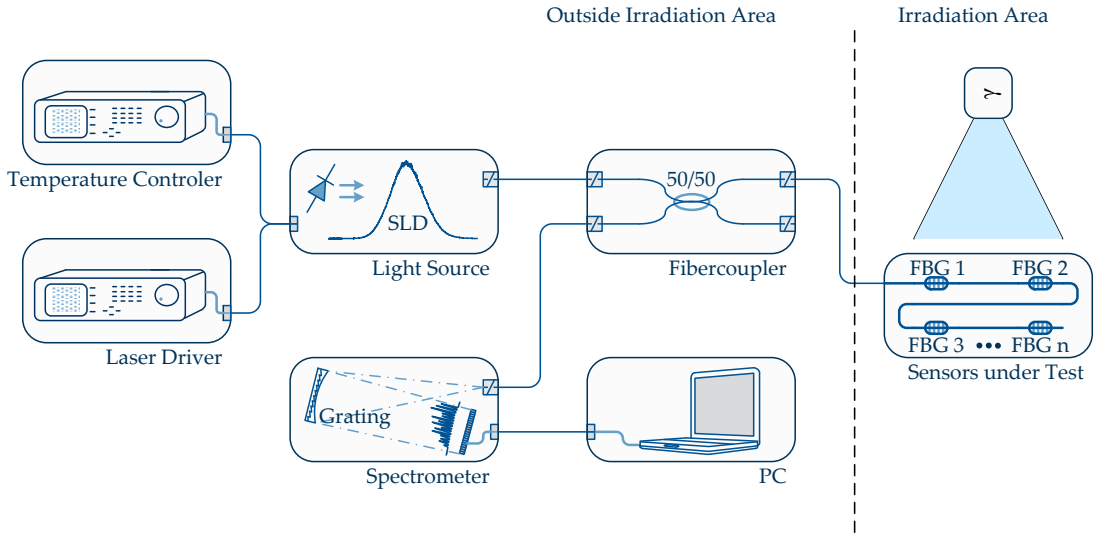

Figure 6.14: *FBG radiation test setup with SLD used as light source and spectrometer to measure the reflected Bragg wavelengths.*

been carried out. The high dose rate (HDR) test had a TID of 25 Mrad with a dose rate of 420 krad/h whereas the low dose rate (LDR) test reached a TID of 250 krad with a dose rate of 4.1 krad/h. Both test were carried out in parallel. The test setup was the same for the LDR and HDR test, only the distance between the gratings under test and the Co60 source were changed.

For the radiation test of the fs-IR written gratings (see also section 3.4.7) a more specific test configuration was necessary as indicated in figure 6.15. The tested FBG sensors where fs-IR written gratings in pure core silica (PCS) fibers. The FBGs were placed in three different areas, two areas with different dose rates and one area which was completely shielded from radiation. In the high dose area with a TID of 25 Mrad four FBG sensors protected by an acrylate coating and glued to the transducer, were placed. Each single transducer was equipped with a PT1000 temperature sensor to allow a later reassignment of the wavelength to temperature. In the low dose area with a TID of 250 krad two single FBG sensors were placed. The acrylate protective coating was removed before the gratings were glued to the transducer. For referencing, a single grating is placed far away from the radiation source in a lead (Pb) shielded box. All samples were placed in the same test chamber.

6.2.3 Single-Mode Optical Fiber Total Dose Test

As discussed in section 3.4.9, standard fibers suffer from a high radiation induced loss and are not suitable for the usage in space applications. In the worst case, the fiber darkens after some krad of total dose, leading in a malfunction of the system. As it was presented in section 3.4.9, F-doped radiation hard fibers are commercially available but writing FBG sensors into such fibers has shown some long-term stability problems. For the system here another type of radiation tolerant fiber in which FBG sensors can be written is necessary. For that reason, a pure silica core fiber has been selected which appli-

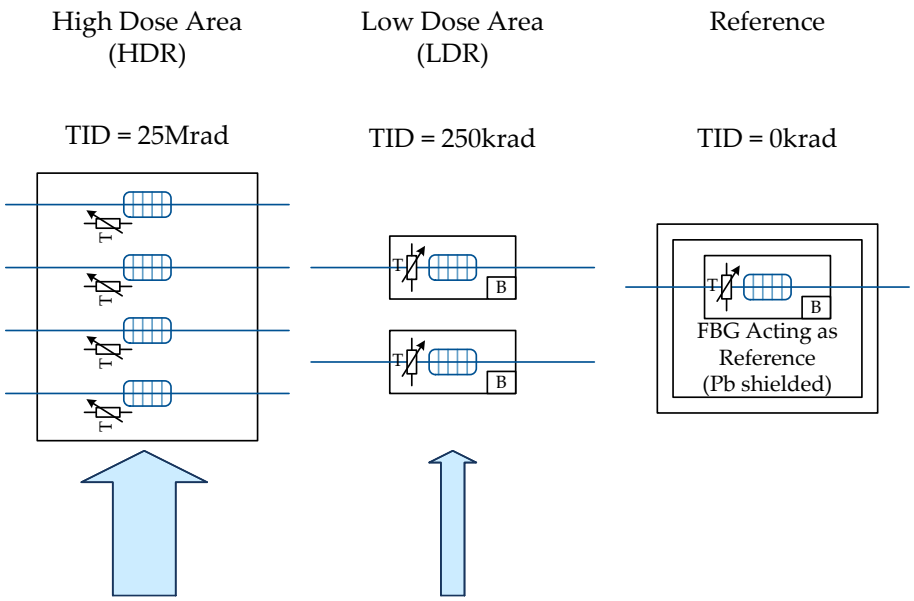

Figure 6.15: *Gamma radiation test setup for the fs-IR written gratings in the PSC fiber. The large blue arrow indicates high dose rate, whereas the small arrow indicates lower dose rate.*

cability if further tested by a gamma radiation test. For this test four fibers from different manufacturers were tested up to 25 Mrad with a dose rate of 80 rad/s (288 krad/h). The output power was measured online during the irradiation process from which the relative attenuation was calculated. The length of the fiber under test was 100m for each fiber type.

A highly stable light source with two selectable output wavelengths, namely 1310 nm and 1550 nm, controlled by a laser diode driver and a temperature controller was used. The output power of the 100 m long fiber coil was measured with a power meter. The test setup is given in figure 6.16.

6.2.4 MG-Y Laser Diode Radiation Test

The MG-Y laser diode is identified as the most critical component inside the developed fiber-optical interrogator module. For this a detailed radiation test series was carried out including a total dose test with gamma rays up to 100 krad and a neutron displacement damage test up to $1 \cdot 10^{12} n_0/cm^2$. The test setup for both tests is described here in detail. In addition a detailed characterization of the laser diode in its nominal operation condition was done including thermal-vacuum testing to prove the performance of the thermoelectric cooler at maximum environmental conditions.

The interesting parameters for the MG-Y laser diode as affected by effects generated due to TID and displacement damage are defined to:

- Optical output power and it's degeneration over radiation (TID and neutrons)
- Change in output wavelength
- Variations in the characteristics of the internal monitor diodes

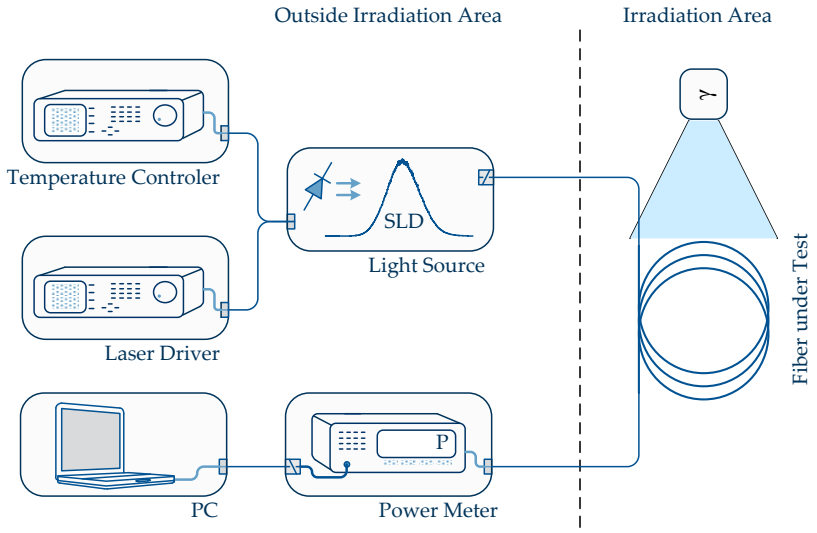

Figure 6.16: *Pure-Silica fiber radiation test setup shown for one single fiber type.*

- Change in lasers slope efficiency.

Test Setup

The test setup for the MG-Y laser diode is more complex than for the previous presented components. An illustration can be found in figure 6.17. The MG-Y laser diode (shown as light blue box in the bottom right of the figure) is irradiated, whereas the rest of the setup is located in a radiation protected area.

The radiation test setup is controlled by a computer which is responsible for the generation of the analog control signals the reflector sections and the laser and SOA currents. Also the measured parameters are read back over the GPIB bus for online visualization during the radiation test. The laser temperature is controlled with a benchtop temperature controller set to 10 kΩ for the complete test. The laser and SOA currents were kept at 100 mA for the wavelength dependency test but are changed for the slope efficiency measurement. The slope efficiency measurement was done manually at certain points at which the dose rate was changed according table 6.1. The output of the laser is split into two branches, one for power monitoring and one for wavelength measurement. The used wavelength meter (HP 86120B) has a relative accuracy of ± 1pm, which is sufficient for the measurement here.

Gamma Radiation Test Dose Rates

For the gamma radiation test different dose rates were used to identify if a dose rate dependent behavior is present. The dose rates applicable for the test are given in table 6.1 starting with a lower dose rate of 5 krad/h at the beginning and ending with 25 krad/h for a total dose of 100 krad within eight hours.

For the neutron test the total neutrons per area were in the range of $1 \cdot 10^{12} n_0/cm^2$ and the laser diode was placed in such a distance to reach the end value within a time

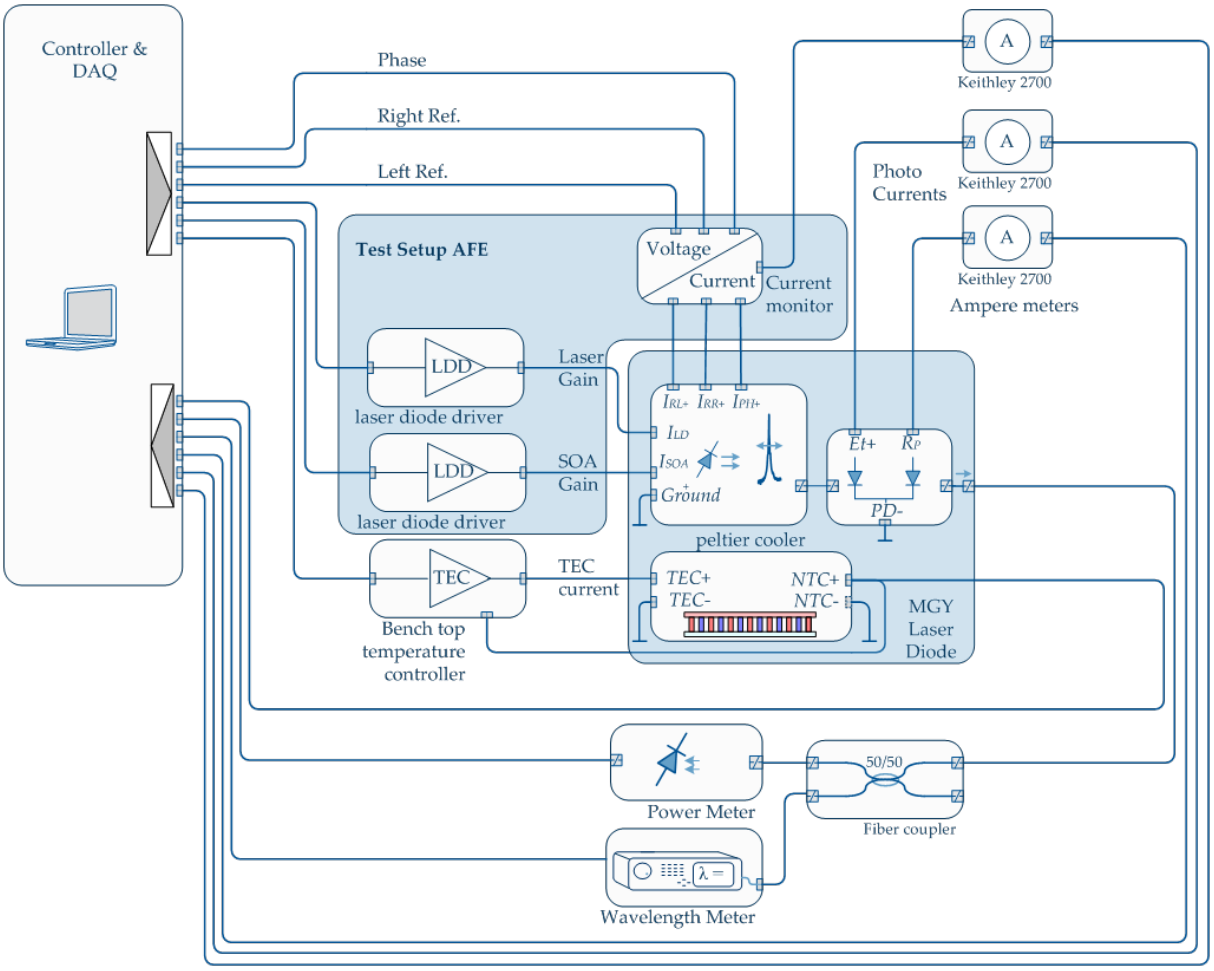

Figure 6.17: *MG-Y radiation test setup used for total dose testing with gamma rays and displacement damage testing with neutrons.*

of seven hours and 30 minutes. So the flux can be calculated to $39 \cdot 10^6 n_0/(cm^2 \cdot s)$. The neutrons in the test facility have a kinetic energy of 14 MeV. According to the NIEL diagram given in section 2.12, the resulting damage for 14 MeV neutrons is nearly the same as for protons with the same energy.

Step	Dose Rate[krad/h]	Duration[h]	TID [krad]
1	5	2	10
2	10	4	50
3	25	2	100

Table 6.1: *Dose rates applied for the gamma radiation test of the MG-Y laser diode.*

Test Flow

A special wavelength tuning procedure was elaborated to check if all wavelengths are shifted due to radiation in the same direction and by the same amount. First a special LUT was generated containing 37 stable wavelengths and their corresponding control voltage triplet. Between each wavelength a so called *Mid-Wavelength* with a wavelength

of 1552.777 nm was inserted. So the laser is not tuned from one wavelength to the next but is rather starting to the next wavelength always from the same mid-wavelength. By using the wavelength variation of the mid-wavelength, a reference point is introduced which allows conclusions about the direction of the wavelength shift. This special tuning characteristic is illustrated in figure 6.18.

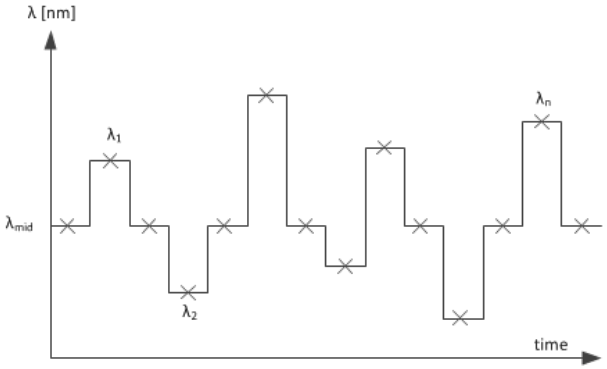

Figure 6.18: *Illustration of the wavelength tuning process during the radiation test. Each of the 37 measurement wavelengths are setup from the mid-wavelength.*

The overall test flow of the gamma radiation test is given in the flowchart of figure 6.19. Also here the setting of the mid-wavelength is illustrated. The measurement was continued until a total dose of 100 krad was reached, afterwards the gamma source was stopped and the annealing measurements were started. The annealing measurement was introduced to check if the performance of the laser recovers. All annealing measurements were carried out at TEC setpoint temperature of 10 kΩ. After the test a complete wavelength map was acquired to check if the wavelength islands have been moved.

The gamma radiation test was carried out for a biased laser diode and an unbiased laser diode. The online measurement was stopped at dose intervals of 10krad at which the unbiased laser diode was connected to the measurement setup. Then, only one measurement sequence (see flowchart in figure 6.19) was carried out for the unbiased laser diode, limiting annealing effects due to high current injection. Afterwards the online measurement continued for the biased laser diode.

6.3 Measurement Results and Evaluation

In the following sections, the measurement results of the previous presented tests are given. Starting with the irradiation test results of the photodiode and the MG-Y laser diode, covering the gamma radiation test results of the selected PCS fiber and FBG sensor tests and ending with the thermal test results of the FBG strings.

6.3.1 InGaAs Photodiode Radiation Test Results

In this section, the test results of the displacement damage test carried out for the InGaAs photodiodes are given. The focus lies on the increase in dark current and in the photodiode's responsivity.

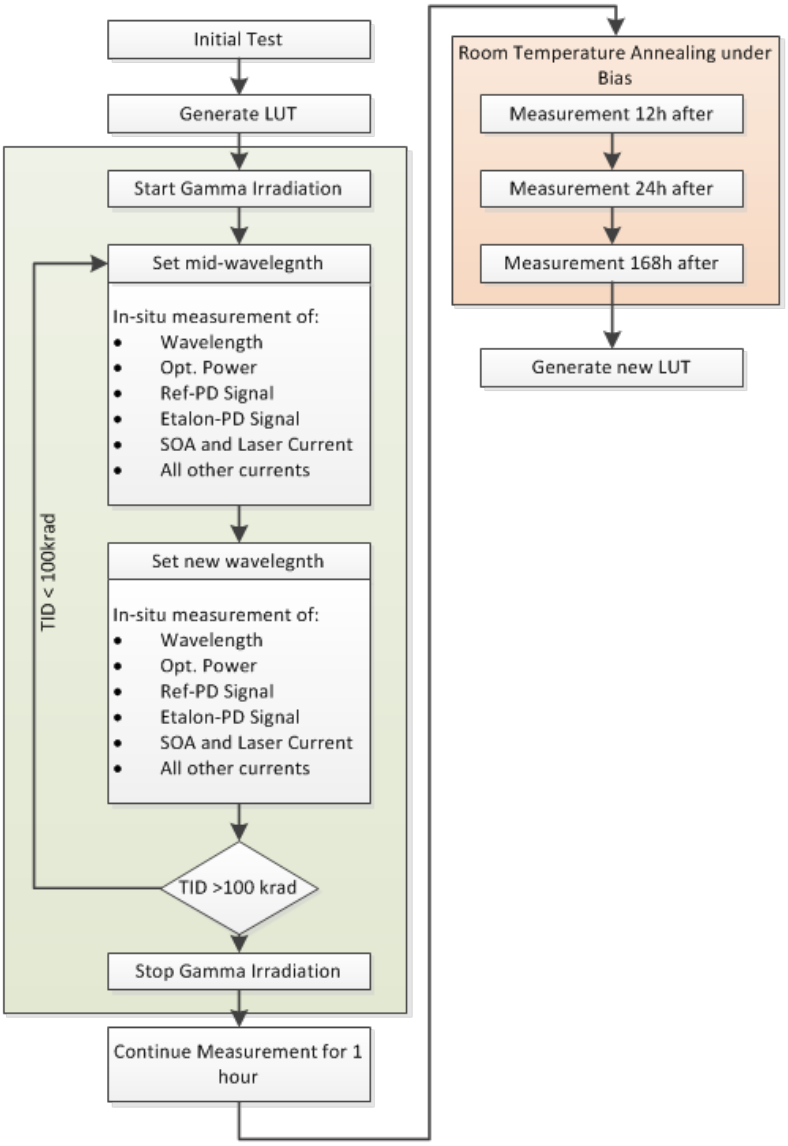

Figure 6.19: *Flowchart of the radiation test of the MG-Y laser diode, shown for the total dose test.*

Increase in Dark Current The dark current in a photodetector has its origin in the generation of electron-hole pairs due to thermal effects. This effect is always present and can be reduced by cooling down the detector to very low temperatures, at absolute zero also the dark current disappears. By applying a reverse bias voltage to the photodiode, the dark current increases with temperature and applied reverse bias voltage following the formula [137]

$$I_{Dark} = I_{Sat} \cdot \left(e^{\frac{q \cdot V_a}{k_B \cdot T}} - 1 \right) \tag{6.2}$$

Where q is the electron charge, V_a is the applied reverse bias voltage, k_B is the Boltzmann constant and T is the absolute temperature in Kelvin. It is usual to reverse bias a photodetector to reduce its capacitance and increasing its bandwidth, the drawback is then the increased dark current. The overall increment due to radiation effects is not taken into account by 6.2 and must be measured for the used photodetector, as it was done here in this work.

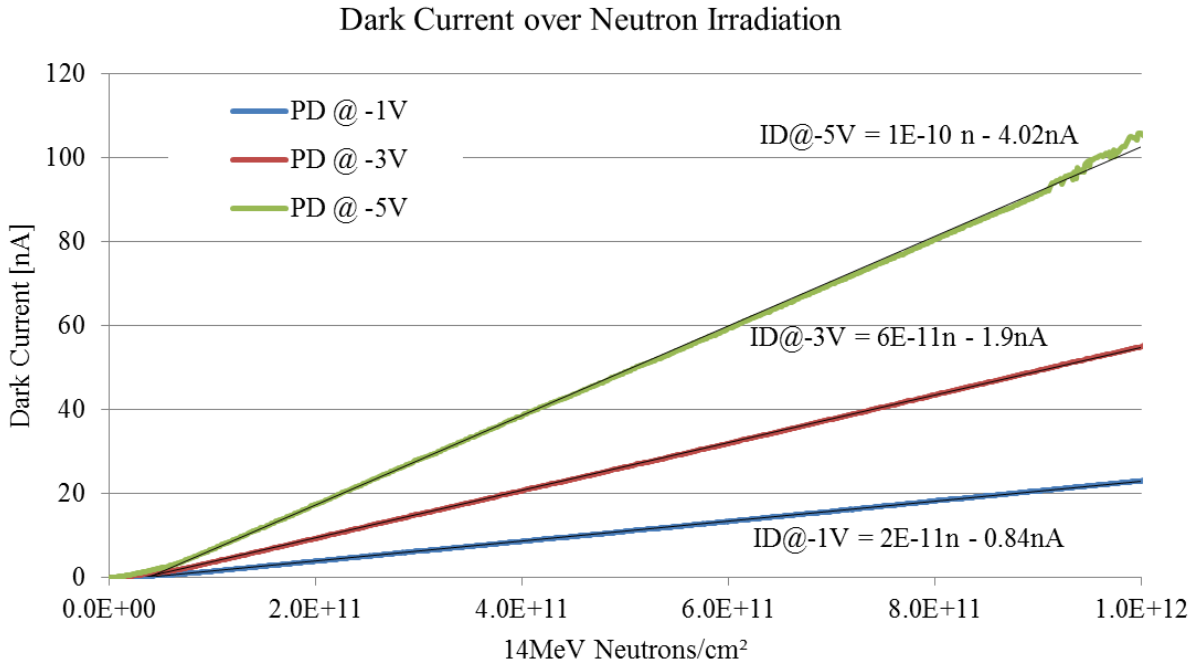

Figure 6.20: *Increase in dark current of the InGaAs photodiode as function of accumulated neutrons per area.*

The increase in dark current as function of accumulated neutrons per area is given in figure 6.20 for three different reverse bias voltages (1 V, 3 V and 5 V). This are results obtained from the radiation test series carried out in this work. In the designed interrogation system the photodiodes are biased with -5 V so after $1 \cdot 10^{12} \mathrm{n_0/cm^2}$ the dark current increased from an initial value of approximately 100 pA to 112.2 nA. The SNR value of the photodiodes before and after the test by assuming a generated photocurrent of 1.027 mA can be computed to:

$$SNR_{Initial} = 20 \cdot \log\left(\frac{\overline{|I_{PD}^2|}}{\overline{|I_{Dark0}^2|}}\right) = 20 \cdot \log\left(\frac{1.027\mathrm{mA}}{100\mathrm{pA}}\right) = 140\mathrm{dB} \tag{6.3}$$

$$SNR_{DD-Test} = 20 \cdot \log\left(\frac{\overline{|I_{PD}^2|}}{\overline{|I_{Dark-DD}^2|}}\right) = 20 \cdot \log\left(\frac{1.027\mathrm{mA}}{112.2\mathrm{nA}}\right) = 79.23\mathrm{dB} \tag{6.4}$$

The SNR value decreases with higher neutron fluence but for the overall system performance this has only minor influence because the information of the temperature is encoded in the spectral position of the Bragg reflections and not in the absolute value of the reflected light. As long as the SNR stays above a certain value which can be detected by the ADC, the algorithms are able to determine the Bragg peak and the corresponding temperature. Simulations of the peak find algorithms presented in figure 4.4 have shown that the algorithms require an SNR of at least 30 dB which is fulfilled.

Change in Photodiodes Responsivity The second important parameter is the responsivity, which indicates the amount of current generated by the incident light. If this parameter would show a decrease, the SNR would also be decreased. The test has shown that the responsivity is not affected by the displacement damage, the result is a straight line at a value of 1.028 A/W for all three tested samples.

6.3.2 Fiber-Bragg Grating Radiation Test Results

In this section the results of the FBG radiation test are presented. As discussed in section 6.2.2 two different types of FBG sensors were tested, UV written gratings in Ge doped fibers and fs-IR written gratings in PSC fibers.

UV-Written FBG

A total dose radiation test with gamma radiation was carried out for commercially available UV-written FBG sensors. For those gratings, the standard writing process with hydrogen loading is applied. The commercial gratings which were used for testing had different packages. Sensor #101 and sensor #103 had an SS304 stainless steel tube with an outer diameter of 4.7 mm and 3.1 mm respectively, sensor #107 had no mechanical package. For each type of grating three samples were tested. All tests were carried out with a Co-60 source at the *Fraunhofer INT* institute in Euskirchen, Germany.

The radiation test results given in figure 6.21 on the left indicate a high shift in Bragg wavelength for the high dose rate test. The observed shift is too high to use the sensors for the planned activity for which a shift of ±5 pm, corresponding to approximately ±0.5 °C, is allowed. The assumed TID of 25 Mrad behind the satellite's panels would result in a Bragg wavelength shift of approximately 200 pm, corresponding to a temperature error of 20°C. It was also observed that the packaging of the sensor (bare fiber, 3 mm thick stainless steel tube and 5 mm thick stainless steel tube) has only a minor effect on the induced wavelength shift. It is interesting that the FBGs irradiated with a lower dose rate (4.1 krad/h) showed a shift of app. 10 pm after 250 krad whereas the tested FBGs with a higher dose rate (420 krad/h) showed a shift of approximately 20 pm for the same total dose. So a dose rate dependent effect was observed and it can be assumed that the effect in the real environment due to lower dose rates is quite smaller as in the test here. Nevertheless, the risk that a shift higher than ±5 pm (corresponding to ±0.5 °C) will be observed during mission life time is seen as to high so the sensors and the writing technology were rejected.

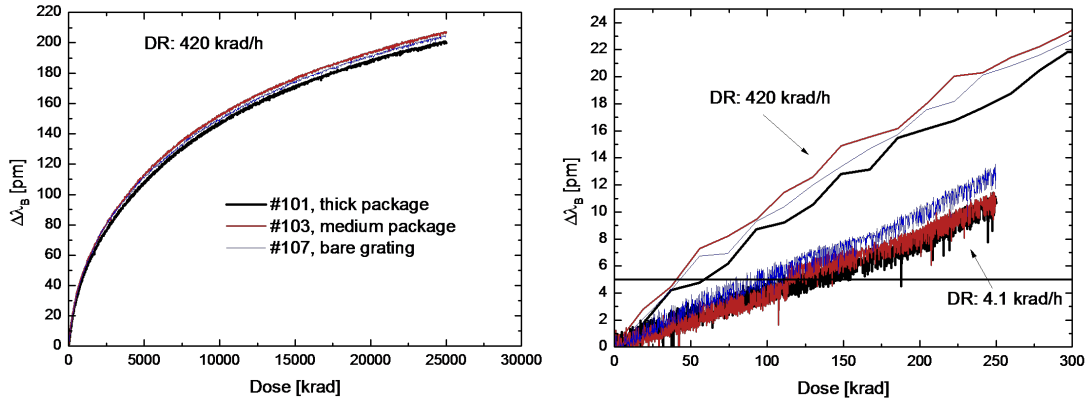

Figure 6.21: *Left: Wavelength shift at high dose rate gamma radiation test of UV-written FBGs protected with different packages. Right: Comparison between high dose rate and low dose rate test, a dose rate dependent effect is observable.*

Femto-Second Infrared (fs-IR) Written FBG

The radiation test setup for the fs-IR written FBGs in pure silica core fiber is presented in figure 6.15. A reference grating is placed in a shielded and temperature stabilized location within the test facility. The acrylate protection coating of the reference grating was removed and the bare FBG was glued with a stiff adhesive to the aluminum transducer. The grating is queried in parallel to the FBGs under test with the same interrogation system.

The temperature variation of the reference grating was measured to approximately 0.7°C during the full test. The temperature sensitivity of the gratings which were glued to the transducer made out of aluminum was estimated to be approximately 40 pm/°C. Hence the overall temperature induced wavelength shift for the reference grating is 28 pm. The wavelength variation of the reference grating over time is shown in the bottom left diagram of figure 6.22 by the red line. As can be seen, the shift is in the range of 37 pm, larger than the shift calculated before caused by temperature effects. But by considering the temperature profile, a correlation between temperature at the reference sensor and Bragg wavelength shift can be found.
Highly interesting is that the two sensors placed in the low dose rate (LDR) test area follow the trend of the reference sensor. This can be seen by the blue and green curves in the bottom left diagram of figure 6.22. The shift in wavelength of the four sensors placed in the high dose rate (HDR) show identical behavior but with a higher total shift in wavelength. Most of the induced shift in wavelength occurs in the first 24 h of the irradiation time. This effect cannot be caused by radiation effects because also the reference sensor which was completely shielded shows the same effect.

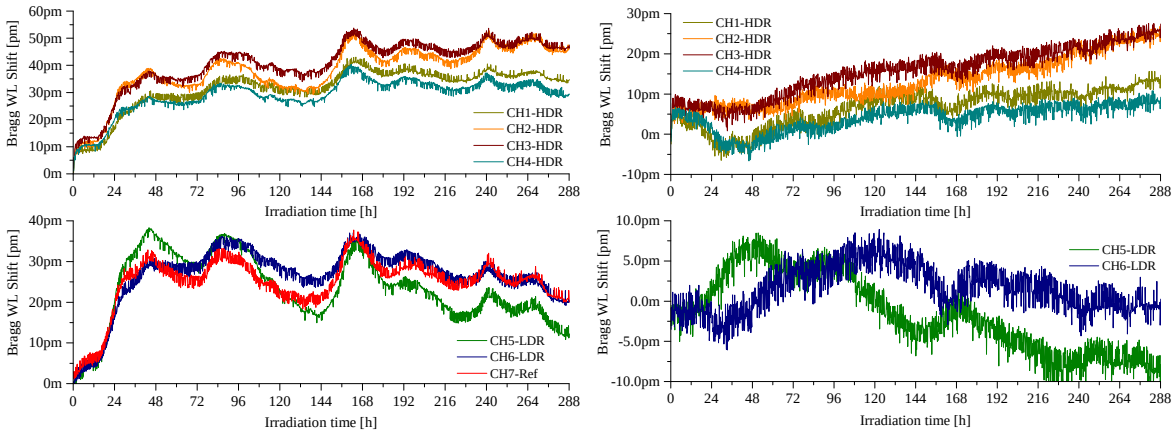

Figure 6.22: *Left: Bragg wavelength shift of sensors located in HDR area (top) and sensors in LDR area (bottom) respectively. Right: Wavelength shift of HDR sensors (top) and LDR sensors (bottom) respectively with subtracted shift of reference sensor.*

By subtracting the wavelength shift of the reference sensor from the other sensor channels the diagrams on the right side of figure 6.22 are obtained. The top diagram illustrates the deviation of the HDR FBGs, the bottom diagram the deviation of the LDR FBGs respectively. For the LDR FBGs the two curves show no correlation even if the sensors are manufactured identical and are placed in vicinity.

This might conclude that the effect measured here is not a radiation induced effect rather than a mechanical effect changing the birefringence in the fiber at the sensor position. This small shift in Bragg wavelength was expected, because the used measurement system based on an SLD and a spectrometer, does not include a depolarizer. It was assumed that a Bragg wavelength shift due to TID, if present, would be much larger than the observed shift due to birefringence effects. By taking into account the theoretical discussion about birefringence in section 3.4.4, changes in the electrical permittivity tensor will affect the refractive index which consequently changes the Bragg wavelength. Mechanical stress originating from the combination of stiff adhesive, bare fiber and aluminum transducer can have strong impact to the permittivity tensor. Due to radiolytic effects in the adhesive the effect can be enhanced.

When plotting the wavelength deviation as function of the total ionizing dose the diagram given in figure 6.23 is obtained. The blue and green curves indicate the shift of the LDR FBGs which were irradiated up to a TID level of 221.9 krad. For these two gratings the overall shift, including radiation and supposed mechanical effects, an overall value of ± 10pm results. The sensors placed in the HDR zone are irradiated up to a TID value of 25 Mrad.

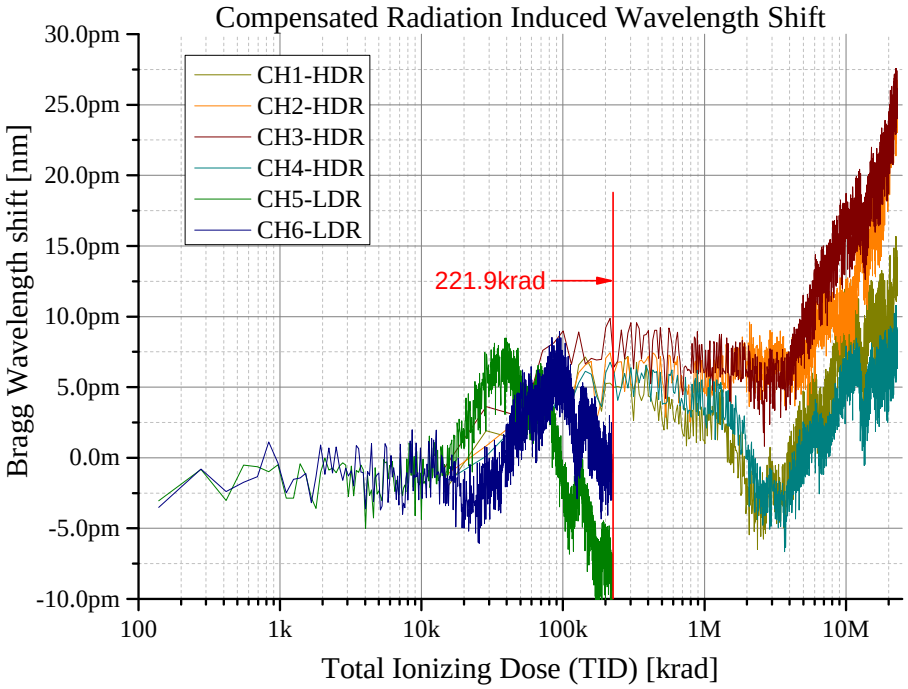

Figure 6.23: *Bragg wavelength shift, compensated by reference sensor's shift for FBGs in LDR and HDR zones respectively.*

To proove that the fs-IR writing technique itself is suited for the target application a single FBG without any transducer and adhesive was tested up to a TID of 100 krad. The tested grating was made within the same process lot and showed the same characteristic parameters than the other tested fs-IR gratings, so a representative result is supposed. This additional test was possible during a gamma radiation test series for the passive optical components and resulted in a maximum shift of 3.6 pm. So, it has been pointed out that the fs-IR written FBGs in the pure silica core fiber can be used for the target

application. Nevertheless, more investigations for the FBGs in the glued condition must be undertaken to identify the resulted high shift in Bragg wavelength. A further step would be to investigate different type if glue, a silicone based glue would eliminate the unknown coupling between structure and FBG sensor due its elasticity.

6.3.3 Pure Silica Core Fiber Gamma Radiation Test Results

Pure silica core fibers are the candidate of choice for writing FBGs with the fs-IR techniques. So first of all, the radiation performance of the fiber must be evaluated. To evaluate the radiation performance of the fiber, four samples from four different manufacturers were tested up to 20 Mrad (200 kGy, dose rate 0. 8Gy/s) [37]. The results are depicted in figure 6.24, the fibers were tested with a 1312 nm and 1570 nm laser light source. The attenuation showed a higher value for 1570nm as for 1312 nm. Only one sample from one manufacturer showed a discrepancy from the other sample fibers, which leaded to an exclusion from the subsequent grating inscription sequence.

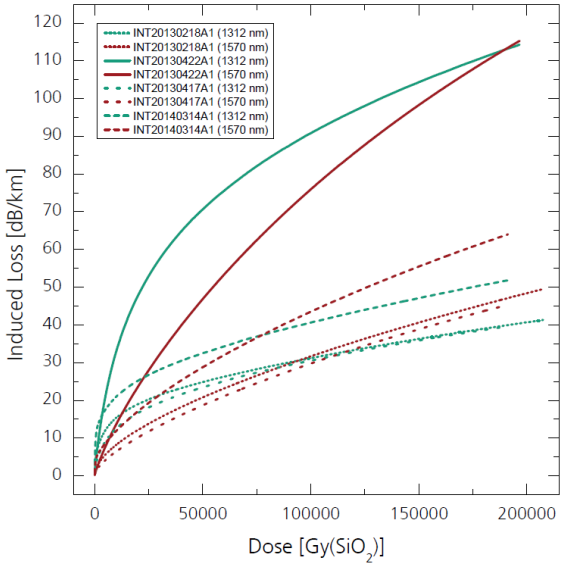

Figure 6.24: *Radiation induced attenuation as function of the total dose of pure silica core (PSC) fibers from four different manufacturer.*

For the fibers radiation induced attenuation values from 40 dB/km to nearly 60 dB/km are observed for a total dose of approximately 20 Mrad. Such values seem very high but here in this case for the target space application two facts must be considered. Firstly, the used length in the planned application is in the range of less than 20 meters which would result in an attenuation lower than 1 dB. And secondly, the test carried out was a high dose rate test due to the limitation of testing time. It is assumed that the induced loss would be lower for lower dose rates.

Based on the results here two fibers were selected into which the FBG sensors were written by the fs-IR writing technology. This technology showed a much smaller radiation induced Bragg wavelength shift (see figure 6.23) than the UV writing technology in high photosensitive fibers (see figure 6.21). These two fibers are labeled *INT20130417A* and *INT20130418A*, see also the functional test results given in figure 6.11.

6.3.4 MG-Y Laser Diode

The radiation induced performance degradation, namely the output power degradation and the change in wavelength of the MG-Y laser are described in this section. The first section described the total ionizing dose (TID) induced effects, whereas the second section focuses on the effects caused by displaced damage due to neutron irradiation.

Gamma Radiation Test Results

Within this section the test results of the TID radiation test series, carried out with a Co-60 source, are presented. The radiation test were carried out in the *Fraunhofer INT* radiation test facility. The focus of this test lies in the identification of the laser's slope efficiency change, change in optical output power and change in laser's output wavelength. These parameters highly influence the design of the necessary referencing system and overall transmitter subsystem.

Laser Diode Slope Efficiency At different total ionizing doses, the laser diode's slope efficiency and threshold current was measured. For this, the laser current was varied from 0 mA to 100 mA in 10 mA steps while the SOA current was kept at 100 mA. The optical power was measured with a power meter at the fiber coupled output of the laser diode. To measure the SOA slope efficiency, the current of the laser was kept at a constant value of 100 mA and the SOA current was changed in the same way.

The optical output power of the biased laser was measured to 6.76 mW after the 50/50 coupler at the beginning of the test and to 6.44 mW after a total dose of 100 krad. This leads to a decrease in output power of -4.7% for the biased laser diode. The laser threshold was not changed significantly during the full test, it has been proven that only the slope efficiency is sensitive to gamma radiation. The results can be seen in figure 6.25 on the left.

The biased laser diode was also tested for annealing effects to check if any recovering of the parameters is present when the radiation source is switched off. For this measurement, the measurement system continued its operation for the next 12 hours, even when a TID of 100 krad was reached and the Co60-source was stopped. The measurement of the slope efficiency and laser threshold was carried out 24 hours after the stopping of the radiation source. It can be seen that for the biased laser diode the slope efficiency nearly reaches the initial value.

For the unbiased laser diode the results are depicted in figure 6.25 on the right. The initial output power was measured to 6.44 mW and to 5.84 mW after 100 krad of total dose. This yields to a decrement of -10.3% for the unbiased laser diode which is approximately the double degradation as for the biased laser. After an annealing phase of 24 hours in unbiased condition at room temperature, the optical power increases again to 6.09 mW. So the total degradation of optical output power after annealing is given to -5.7% for the unbiased diode. For the unbiased laser diode, no complete annealing was observed as it was the case for the biased laser.

SOA Slope Efficiency The initial optical power before irradiation was measured to 6.76 mW for the biased laser diode, after 100 krad the power decreased to 6.44 mW. The same behavior as for the laser section, indicated before was seen. This is caused by the fact that if the laser power decreases due to radiation the decrease is also seen on the

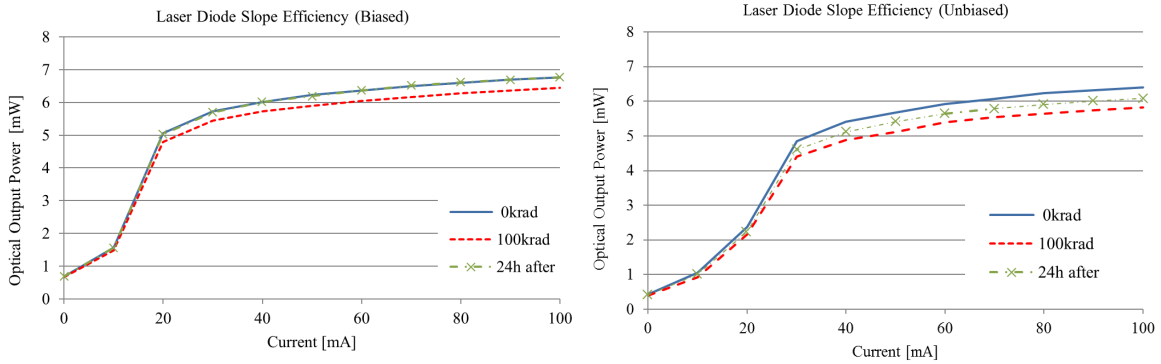

Figure 6.25: *Left: Laser (LD) slope efficiency (generated optical power as function of input current) at the beginning (blue line) and after 100 krad (red line) for biased laser including annealing phase (green line) reaching the initial performance. Right: Same plot but for unbiased laser diode, after annealing the initial performance is not reached.*

output behind the SOA. It was not possible to measure the laser without the SOA because both elements are integrated within the laser chip. It can be seen that the slope is changed by a small amount from initial 0.0676 mW/mA to 0.0644 mW/mA. The behavior of the SOA after a 24 hour annealing phase was also investigated. For this the biased laser diode was kept under operation for additional 12 hours after the irradiation was stopped. The results for the biased laser are illustrated in figure 6.26 on the left. The biased laser diode reached the same performance after annealing as at the beginning of the gamma test.

For the unbiased laser, the annealing behavior is the same as for the biased diode but the effect of optical power degradation is larger as it was observed for the laser's slope efficiency. After an annealing phase of 12 hours in biased condition the output power increased to a level of 6.09 mW from an output power of 5.84 mW after 100krad. A small difference in optical output power remained, the laser did not reach the initial performance in the unbiased condition. The SOA's slope efficiency and the annealing effect can be seen in figure 6.26 on the right.

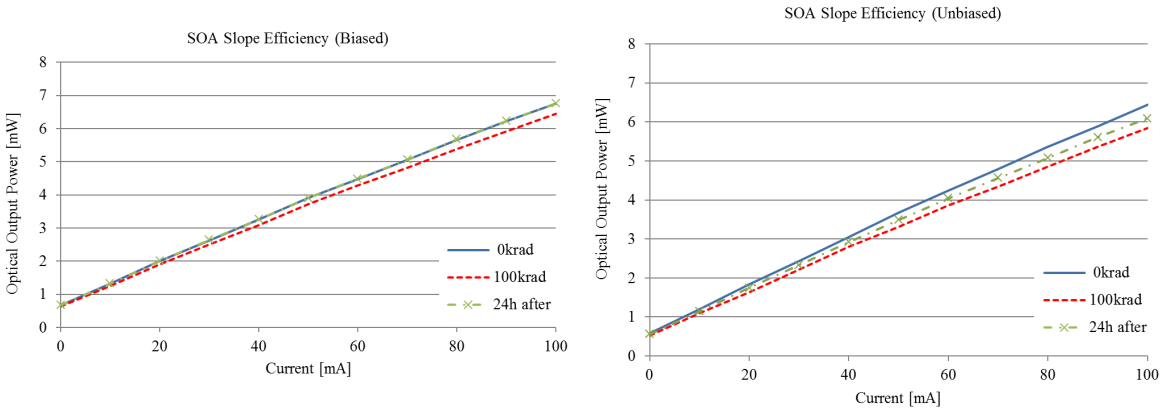

Figure 6.26: *Left: SOA slope efficiency at the beginning of the TID test (blue line) and after 100 krad (red line) for the biased laser with annealing phase (green line) reaching the initial performance. Right: Unbiased laser diode which did not reached the initial performance after annealing.*

Optical Output Power Degradation The most important parameter for the slope efficiency measurement is the overall optical output power degradation due to radiation. In figure 6.27 the optical output power as function of total dose is illustrated for the biased and unbiased laser diode respectively. Two points are notable, first, the degradation shows a saturation behavior which is advantageous for using the laser within the planned system. Second, the unbiased laser showed a higher degradation due to a non-present, current induced, thermal annealing. So one might think to use an unpowered spare laser diode within the system to increase lifetime by enhancing the power budget but taking into account the results above not the full amount of the additional output power is available from an unbiased spare laser diode. The results are also summarized in table 6.2.

Effect	Biased Diode	Unbiased Diode
Degeneration in optical power after 100krad	-4.73%	-10.27%
Degeneration after 100krad with annealing	0%	-5.74%

Table 6.2: *Summary of the output power degradation during the TID radiation test for the biased and unbiased laser diode.*

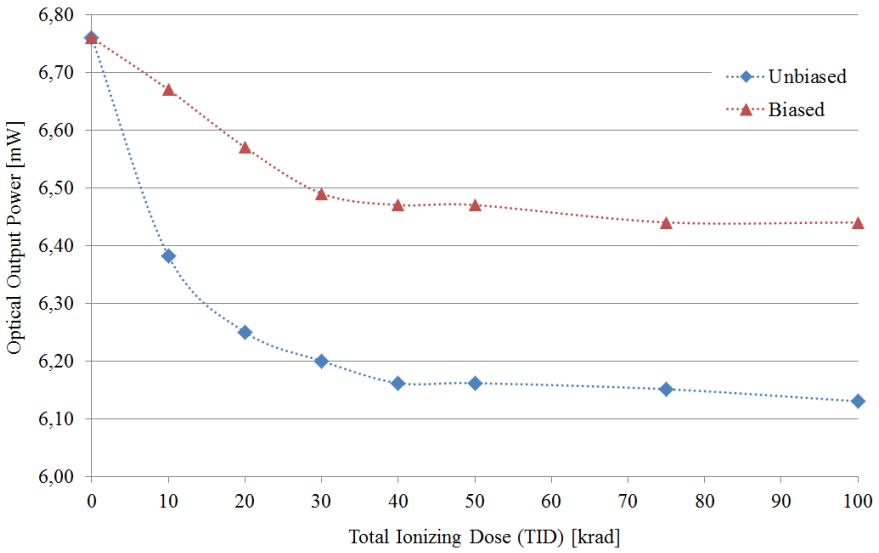

Figure 6.27: *Degradation of optical output power as function of total dose for the biased laser (red curve) and the unbiased laser (blue curve).*

Wavelength Shift and Wavelength Maps As mentioned before in the test setup description, the laser was tuned to different wavelengths, which are measured online during the gamma radiation test for the biased laser. The mid-wavelength was introduced to allow a conclusion to the overall drift of the laser. During the test the SOA and LD currents are kept at a level of 100.0 mA and the TEC at an NTC resistance of 10.0 kΩ, corresponding to the nominal values of the laser [4]. In figure 6.28 on the left side the deviation from the initial mid-wavelength of 1552.777 nm is given. The maximum drift after 100 krad of total dose is 10 pm. The spikes in the measurement arise from the measurement resolution of ±1 pm of the used wavelength meter (HP 86120B multi-wavelength

meter).

For the unbiased laser a single measurement cycle was carried out each 10 krad of total dose to obtain the actual wavelength. For this laser a mid-wavelength of 1552.096 nm was used due to different stability points of the two different lasers. A maximum deviation of 6 pm after 100 krad was observed for the unbiased laser. In comparison to the biased laser the wavelength shift due to TID is approximately by a factor of two smaller for the unbiased laser as for the biased laser.

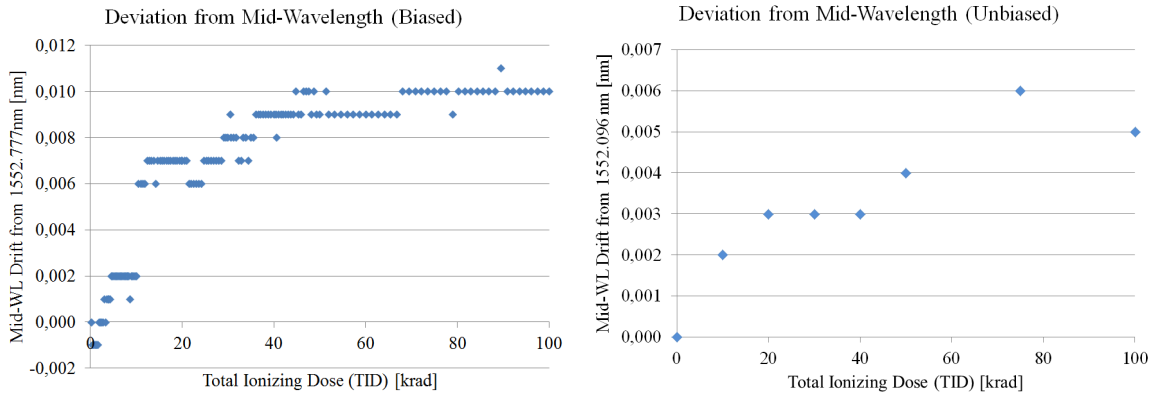

Figure 6.28: *Mid-Wavelength deviation for the biased laser (left) and for the unbiased laser (right).*

In a next step, the different wavelengths are analyzed for the biased laser and the unbiased laser, to investigate if the drift is in the same range and follows the same direction for all wavelengths. The results are given in figure 6.29 for the biased laser (left side) and for the unbiased laser (right side) respectively. The wavelength shift is higher for the biased laser and reaches a maximum value of 17 pm for a total dose of 100 krad. It can also be observed, that the shift affects all wavelengths in the same direction. For the unbiased laser the same characteristic was observed but with a smaller wavelength shift.

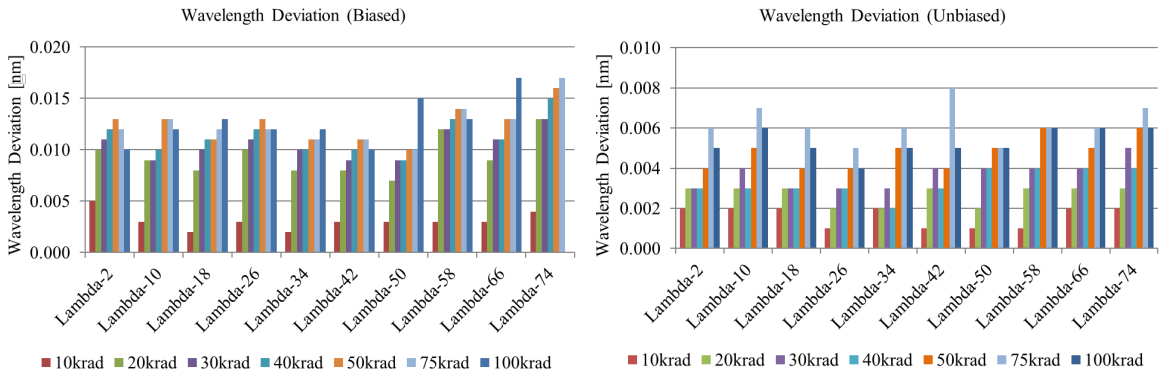

Figure 6.29: *Deviation of the different setup wavelengths due to total dose effects for the biased laser (left) and unbiased laser (right).*

In figure 6.30, the wavelength maps before and after radiation test are shown for the biased laser (left side) and for the unbiased laser (right side) respectively. The wavelength map was measured before and after the gamma test with the same conditions (0.2 V right/left reflector control voltage starting point and 20 mV step size). The 'islands'

in figure 6.30 result in a wavelength difference of 500 pm. The red lines indicate the wavelength map after the gamma test with a total dose up to 100 krad. After radiation test, the islands are shifted to the top-right corner of the wavelength map. The white areas indicate unstable wavelengths which size is not changed due radiation, only a small shift in top-right direction was observed. So the wavelength islands of the laser remain stable and are not affected by the gamma radiation.

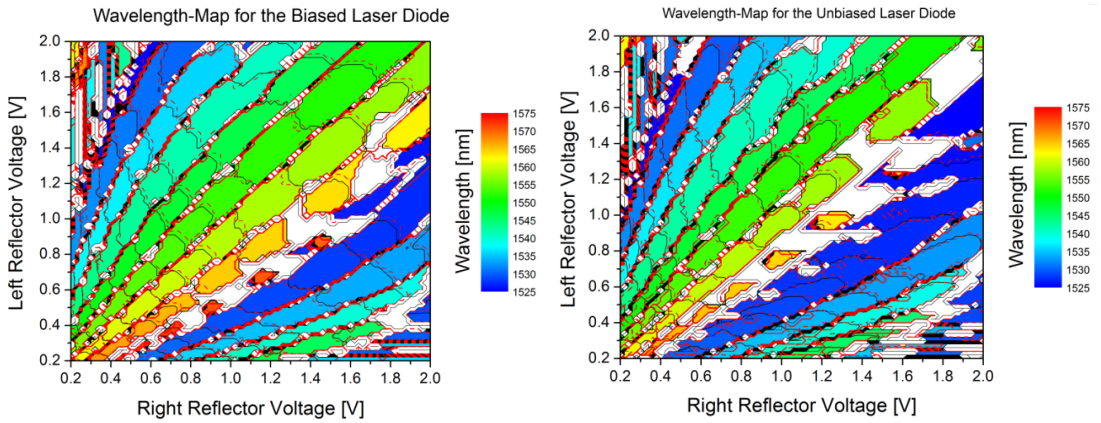

Figure 6.30: *Wavelength map of the MG-Y laser before (colored lines) and after test (red lines) for the biased (left) and unbiased (right) laser.*

Neutron Irradiation Test Results

Not only total dose effects arising from the impact of charged particles must be considered for the components inside the HSB unit but also displacement damage effects will have impact on the laser's performance. The neutron source at the test facility at Fraunhofer INT in Euskirchen provides neutrons with an energy of 14 MeV. The energy is fix and cannot be changed/accelerated due to the neutral charge of the neutrons. According to the NIEL hypothesis, described in section 2.2.2, neutrons with this energy cause nearly the same damage in the crystal as protons with 10 MeV. The main advantage here is the lower cost for a displacement damage test with neutrons instead with protons.

For neutron test also the variation in optical output power and the shift in laser's output wavelength was investigated. Afterwards a comparison with the effects seen during the TID test can be made. The measurements were carried out at different accumulated number of neutrons (n_0) of $1 \cdot 10^{10}$, $5 \cdot 10^{10}$, $1 \cdot 10^{11}$, $2.5 \cdot 10^{11}$, $5 \cdot 10^{11}$, $7.5 \cdot 10^{11}$ and $1 \cdot 10^{12} \mathrm{n_0/cm^2}$ respectively. The particle flux was approximately $2.3 \cdot 10^{9} \mathrm{n_0 \cdot cm^{-2} \cdot min^{-1}}$ which led to a total duration of 7.5 hours to reach the accumulated number of neutrons of $1 \cdot 10^{12} \mathrm{n_0/cm^2}$.

SOA and Laser's Slope Efficiency To investigate the change in optical output power, the laser current and the SOA current are changed and the optical output power is measured with an optical power meter. It was observed that the lasers output power is not influenced by the neutron impact during the full measurement cycle. So it can be concluded that the laser structure made out of Indium-Phosphide (InP) does not show any output power degradation for displacement damage effects tested with neutrons.

Wavelength Shift due to Displacement Damage The shift in mid-wavelength due to displacement damage is given in figure 6.31 on the left side. The shift shows no saturation as it was observed for the gamma radiation test. In addition the amount of wavelength change is much higher, namely 46pm after $1 \cdot 10^{12} n_0/cm^2$. This shift is too high to be used without mitigation strategy in the designed system.

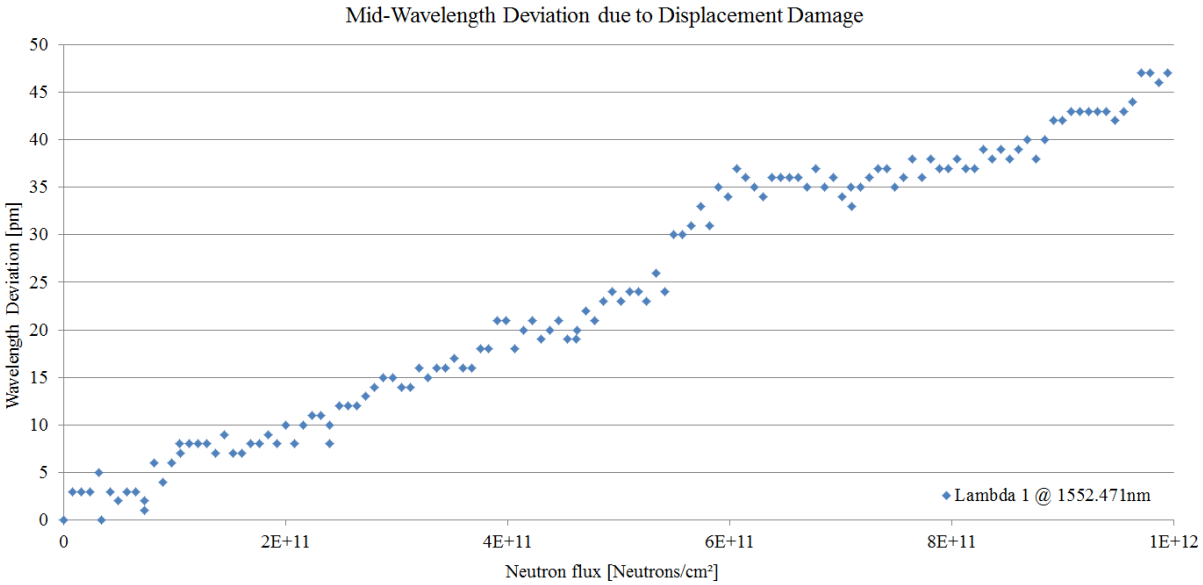

Figure 6.31: *Deviation in laser's mid-wavelength as function of neutron fluence.*

The change in wavelength for all sample wavelengths is measured to check if the shift has the same amount and the same direction. The results are plotted in figure 6.32. The maximum observed shift in wavelength lies at approximately 85 pm, the direction is the same for all wavelengths, excluding the first measurement of Lambda-74 which is possible caused by a measurement error. The used wavelength-meter (HP 86120B) had only an accuracy of 1 pm. Also after the neutron radiation test wavelength maps were obtained to see if the wavelength islands are effected. There was no change observable, only a shift in the top-right direction was identified as it was also the case for the gamma radiation test results.

Internal Reference and Etalon Signals Considering the internal etalon and photodiode signals as function of the neutron fluence, shown in figure 6.33, the change in laser's wavelength can be measured by the etalon signal. The internal photodiodes are not affected by the displacement damage because the signal of the power monitor diode stayed at a nearly constant value. So it is clear that the change in the etalon signal arises from the change in laser's wavelength which is affected by the displacement damage. For the data evaluation the etalon and reference signals for the mid-wavelength are taken.

The above noted change in etalon signal could also be caused by changes inside the internal etalon rather than a deviation in wavelength. So the characteristic etalon curve is measured before and after the test and the resulting fit-parameters are compared. By applying the Airy-Fit of equation 3.6, a change in central wavelength of 0.45 pm and a change in FSR of 0.01% was estimated. These small numbers confirm the change in laser's output wavelength as origin of the measured etalon signal. So this signal can be used to

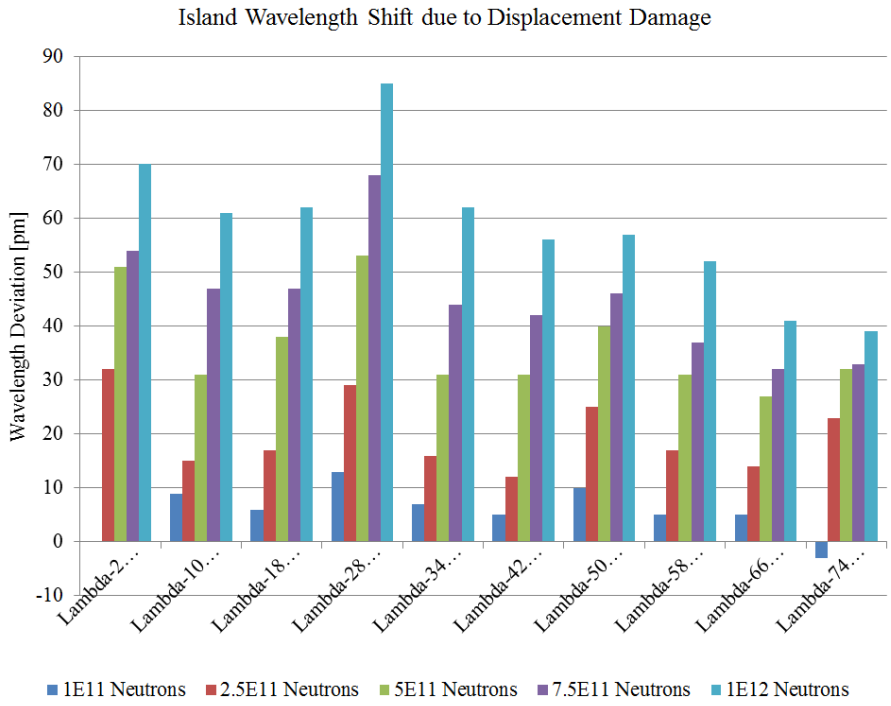

Figure 6.32: *Wavelength deviation for different wavelength setpoints for different neutron fluency.*

control the laser's output wavelength during operation ensuring a stable light source. This is highly important because the system shall operate on a satellite for 15 years without the possibility for later changes or re-adjustments.

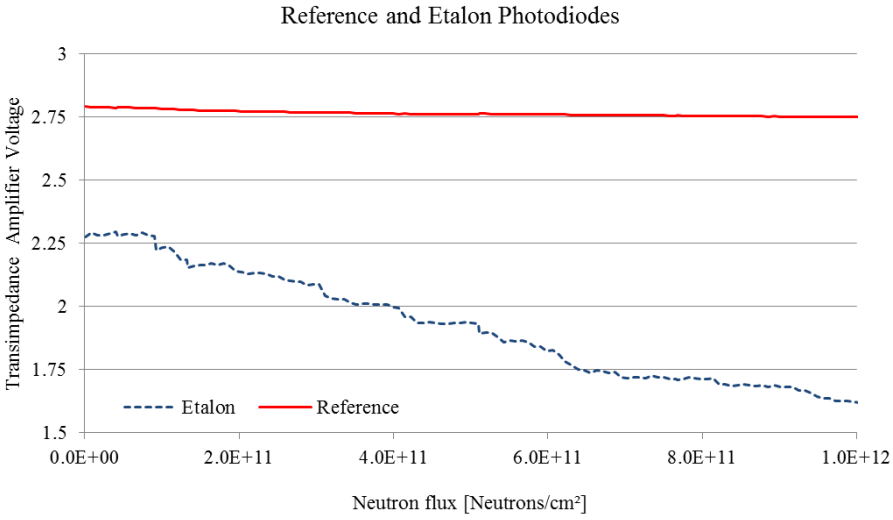

Figure 6.33: *Etalon (dashed line) and power monitor (straight line) photodiode signals.*

Chapter 7

Summary, Conclusion and Outlook

7.1 Assessments

The presented thesis focuses on the development of a fiber-optical measurement system using FBG sensors for temperature measurements. The interrogation technique is based on a tunable laser concept, more precisely on a modulated-grating Y-branch laser diode, which can be tuned in wavelength from 1528 nm to 1568 nm. A special calibration procedure is developed within this work to allow a wavelength tuning with a spacing of 10 pm.

The developed fiber-optical interrogator module (FIM) showed the expected performance as shown in section 4.1.1 for the target space environment defined in section 2.2. Different prototypes were built which have led to the engineering model of the analog front-end module (AFE) shown in figure 7.1. The interrogation module is able to read out two sensor strings, each containing up to ten single FBG sensors. In addition the module has two outputs by which extension modules can be connected increasing the total number of FBG up to 100. The FIM board can be integrated in the Hybrid Sensor Bus system developed by OHB System AG.

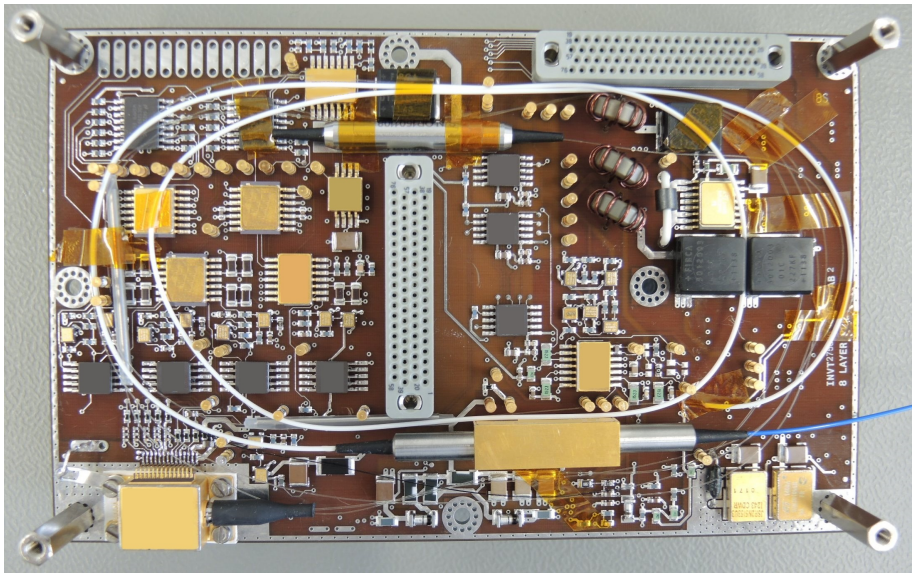

Figure 7.1: *Picture of the AFE engineering model (EM) with MG-Y laser (bottom left), polarization switch (bottom center) and optical isolator (top center) mounted onto the PCB.*

The results of the thermal test of the FBG sensors which are shown in section 6.1.2 have proven the full functionality of the developed system. The following list highlights the encountered problems, the corresponding mitigation techniques and the main achieved targets:

- **Cosmic Radiation Modeling and Simulation**
  At the beginning of the thesis detailed radiation modeling was carried out. A telecommunication satellite surrounding the Earth in the geostationary orbit with a lifetime of 15 years formed the baseline. In a first estimation an aluminum thickness of 5 mm was chosen as baseline to keep the total ionization dose (TID) inside the HSB box below 100 krad. In a second stage a radiation analysis was carried out for the HSB system based on a mechanical 3D model. The result of the radiation simulation showed a maximum TID of 59.1 krad including 20% of safety margin. For the radiation tests of the single opto-electronic components the value of 100 krad was taken as baseline. Integrated circuits, which can be used in space applications, are still available for such a TID value.

- **Selection of a Suitable Interrogator Concept**
  The fiber-optical interrogator developed in this thesis suspected to be based on a scanning, in wavelength tunable, light source. The experiment was preceded by a comprehensive theoretical research including simulations. Based on the requirements in space such as power consumption, compactness, sensitivity to environmental loads and radiation, the so called Modulated-Grating Y-branch (MG-Y) laser diode was selected. This laser diode is a commercially available device which wavelength can be controlled by three input current values. The operating wavelength range is between 1528 nm and 1568 nm, also known as the telecommunication C-band. The dependency between output wavelength and current control vector are stored in a look-up table inside a controller unit. An FPGA is responsible for loading the current triplet from the memory and sending the data to the corresponding digital-to-analog converters.

- **Characterization of MG-Y Laser Diode**
  The optical and electrical behavior of the selected laser diode was investigated very detailed to find the best suiting calibration procedure. The generation of a reliable calibration setup required much efforts due to the fact that the output wavelength of the laser showed strong nonlinear effects. To begin the nonlinear tuning characteristic of the two reflector currents was measured, afterwards a mathematical function is adapted to the corresponding data. By the use of the adapted function the tuning characteristic of the laser diode can be linearized to a certain degree. This allows a more precise sampling in sensitive areas which are identified to be located in areas with lower current values. Different wavelength maps were generated with consideration of side-mode suppression ratio, output power stability, wavelength stability and hysteresis effects. The obtained wavelength maps where cleaned by image processing filters and combined to a single master look-up table, used to control the laser diode in a calibrated way.

- **Selection of Peak-Find Algorithms**
  The developed interrogation system uses fiber Bragg gratings (FBGs) as sensor elements. The wavelength position of the light reflected by the sensor indicates the applied strain and temperature at the sensor position. In order to determine

the central wavelength of the Bragg peak, the performance of different peak finding algorithms has been simulated. Convolution based algorithms, function based algorithms and threshold/sample based algorithms have been used. Convolution based algorithms could be implemented easily into the FPGA but they suffer from high instabilities if the wavelength is not equally distributed. Equivalent spacing in wavelength is only guaranteed for spectrometer based interrogators, but not for the system here. Centroid algorithm and the trip-hop algorithm where identified as most suitable candidates. Within this thesis an algorithm, the so called trip-hop algorithm, based on threshold and slope information in the reflection spectra was developed.

- **Birefringence Effects and Mitigation**
  The birefringence effect in optical fibers and in FBGs were examined in detail. Due to the fact that the shift in Bragg wavelength of a sensor can be caused by temperature change or by applied strain to the sensor's position special mechanical decoupling is used to rely on correct data. The measurement error for temperatures without mitigation strategy caused by birefringence, shown in section 6.1.3, is in the range of $\pm$ 1.5°C, which is far too high for the required accuracy of the measurement system. Since the system is based on a highly polarized laser diode, the birefringence becomes an issue. The origin of this effect and the required degree of polarization of the output light were calculated and different mitigation techniques were found. The most suitable and later on implemented technique is based on polarization switching of the laser light by using an external device and subsequent spectral averaging of the measurement data. By this technique the error can be reduced to $\pm$ 2.2pm, corresponding to $\pm$ 0.28°C.

- **Radiation Testing of Opto-Electronic Components**
  Special attention was paid to the radiation behavior of the used optical and electro-optical elements in the system. All implemented components in the system are radiation tested, the integrated circuits were tested by the manufacturer and the non-qualified components were tested in this thesis. Special attention is given to the MG-Y laser diode and the behavior of the output wavelength under gamma-ray exposure up to 100 krad and neutron radiation (see section 6.3.4). Displacement damage effects in the crystal lattice caused by neutron radiation showed that the wavelength of the MG-Y laser has changed by more than 80 pm for certain wavelengths. Nevertheless, the change can be observed by the laser's internal etalon which can be used to work against the wavelength change. Detailed analysis of the etalon data demonstrated that the internal etalon is only marginally affected by radiation. In addition the InGaAs photodiodes were tested with neutron radiation to observe the change in dark current and the change in sensitivity. An increase in dark current was observed, decreasing the SNR of the receiver section to 80 dB which is quite large enough for the system. The sensitivity of the detector was not affected due to displacement damage generated by the neutrons.

- **Radiation Testing of Fibers and FBG Sensors**
  It is known from literature that optical fibers suffer from so called radiation induced loss when exposed to gamma rays or other types of ionizing radiation, see also section 3.4.9. In this thesis special fibers, namely pure silica core fibers, were identified as suitable candidates. Fibers from four different manufacturers were tested. The

maximum induced attenuation was found to be <1 dB for fiber lengths of 20 meters. The radiation effects for the FBGs are even worse than for fibers. The type of writing (UV laser or femto-second IR laser) and the material composition of the fiber have a high influence on the radiation induced Bragg wavelength shift. The femto-second IR writing technique was selected as the most promising writing process. In a second stage writing of fs-IR FBGs in the selected pure silica core fibers was successfully tested. A final radiation test of a pure FBG written in a pure silica core fiber successful proved this concept.

- **Hardware Design Focusing Low Noise Current Drivers**
  A specialized low noise current converter was designed for controlling the MG-Y laser. Because of the limited availability of components for space applications, a circuit was designed which showed a current noise density of 2 $\mathrm{nA}/\sqrt{\mathrm{Hz}}$. The low noise behavior was absolutely necessary for low output currents, at these operational currents the laser diode was very sensitive to current noise. Noise simulations and noise measurement results are given in section 5.1.1.

7.2 Further Applications and Outlook

7.2.1 Qualification of the HSB System

The engineering model of the developed system will be tested according to the qualification specifications mentioned in section 2.2. This test will enhance the Technology Readiness Level (TRL) and would identify any weak points of the system. The final tested model will afterwards be renamed to a so called Engineering and Qualification Model (EQM). The qualification loads are quite high and include worst case assumptions and safety margins that may result in over-stressing the components. Therefore the tested EQM cannot be reused as a proto-flight model.

It is usual for space systems to carry out various tests on different models (EM, EQM, FM) of the target equipment. Qualification tests with full loads are usually carried out for a dedicated model (EQM or QM) whereas tests for the proto-flight model are carried out for a separate model with reduced loads, the so called acceptance loads. More details about space qualification are given in section 2.2.1 and in the references herein. The planned tests for the different models are shown in table 7.1. Tests which are carried out with acceptance levels for the proto-flight model are indicated with X^{A}. Some tests are skipped due to similarity of the models such as the ESD test and the shock test. Nevertheless, these tests are considered very risky for the equipment. A performance check after each test step will be carried out to examine if the system is still in its normal operation condition and no malfunction can be observed.

7.2.2 Enhancement of Technology Readiness Level

For space systems the maturity of a technology is categorized according to the technology readiness level (TRL). The TRL system foresees nine different levels, starting with TRL1 with the lowest system performance and highest risk and ending with TRL9 for a flight proven system. TRL9 is always the target level for the development of space systems. Different TRL levels are passed during the system development. The TRL level

Test Sequence	Test Type	EM	EQM	PFM
1	Full Performance	X	X	X
2	Sine Vibration	-	X	X[A]
3	Good Health	-	X	X
4	Random Vibration	-	X	X[A]
5	Good Health	-	X	X
6	Shock	-	X	-
7	Thermal Vacuum Cycling	-	X	X
8	Full Performance	X	X	X
9	EMC	X	X	X[A]
10	ESD	X	X	-
11	Full Performance	X	X	X

Table 7.1: *Test matrix for the engineering model (EM), Engineering Qualification Model (EQM) and Proto-Flight Model (PFM) indicating different test sequences to the HSB models [35].*

is enhanced with each successful test (performance or environmental). The different levels are indicated in figure 7.2 on the left, a description of each level is also shown according to ESA's TRL description handbook. [144]

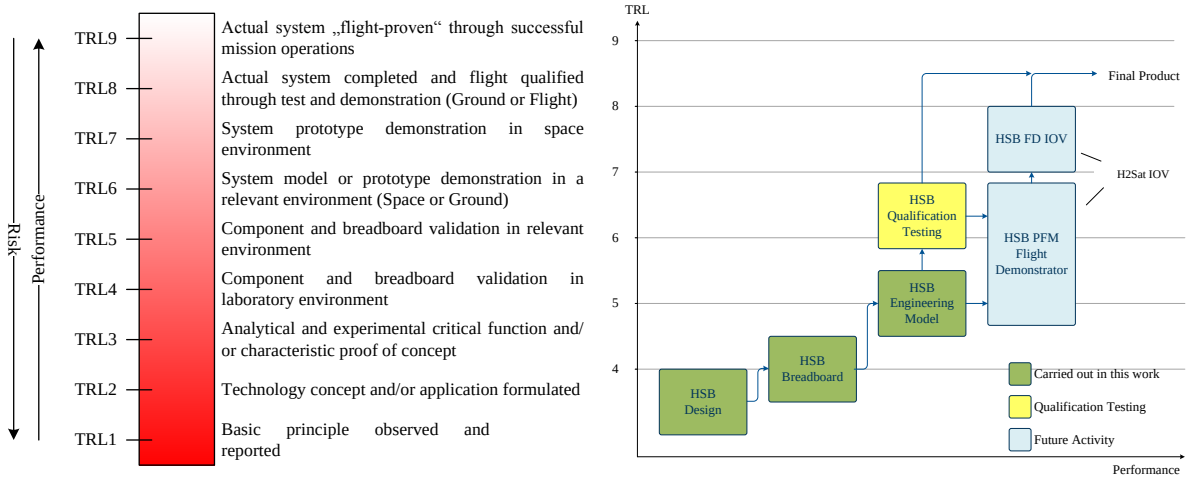

Figure 7.2: *Left: TRL levels with level description, adapted from [144]. Right: TRL levels of the HSB system including the TRL levels of the herein developed and built system (green) and planned future tests (yellow) and future missions (blue) [37].*

The TRL levels of the herein designed HSB system are described on the right of figure 7.2. The initial breadboard designed in an early phase of the project reached a TRL level of four (TRL4), whereas TRL5 is reached within the establishment of the engineering model (EM). The EM will later be used to make a full qualification of the HSB system resulting in a level of TRL6 or even TRL7.

7.2.3 In-Orbit Verification Onboard Heinrich-Hertz Satellite

The HSB system will fly onboard the German In-Orbit-Verification satellite "Heinrich-Hertz" (H2Sat) funded by the German Aerospace Agency. The H2Sat mission is a com-

munication satellite which will be orbiting in the geostationary orbit (GEO), providing an in-orbit verification (IOV) possibility for different experiments. The IOV is the last missing step in the TRL test sequence, yielding to a TRL9 after successfully testing of the experiment. The launch of the H2Sat is planned in late 2021. [145]

For this mission, the current engineering model will be rebuilt as a proto-flight model to prove the concept of sensor bus topologies and fiber-optical sensing onboard geostationary satellites. A sensor network consisting out of 16 fiber-optical sensors divided into two separate strings will be implemented in addition to the HSB system. The sensors which are read-out by the HSB system will be mounted next to the platform sensors to allow a comparison between both sensor types. So a conclusion to the difference in temperature monitoring between the HSB system and the satellite sensors can be made. Especially for the fiber-optical sensors, the radiation induced measurement error in the real environment can be monitored. The fiber-optical sensors will be mounted on specially developed transducers described more in detail in [146]. These transducers ensures the decoupling from the strain induced by the platform to the Fiber-Bragg grating sensor.

In addition, the HSB system will be able to supervise temperatures within a certain range and to trigger alarm functions when values are out of range. Averaging functions will be tested as well. This functionality is a future vision, in which the satellite management unit might be relieved from the task of housekeeping measurements, which will be carried out by decentralized units such as the HSB system.

7.2.4 Embedding Fiber-Optical Sensors in Spacecraft Panels

A future area of fibers in satellites would be the so called smart panels, a satellite panel with embedded fibers and fiber-Bragg gratings that combines thermal mapping of the panel and high speed data communication [146, 147].

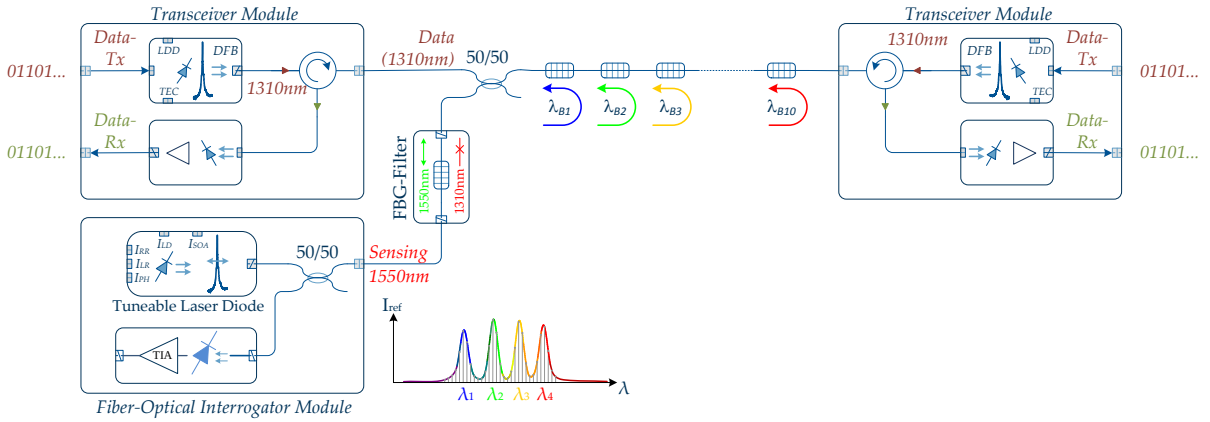

Figure 7.3: *Sketch of a possible combination between the sensor bus system (bottom left) and a data communication system for high speed data links.*

In the telecommunication area for ground based systems optical fibers are widely used for data transmission and are seen as the actual state-of-the art technology. It would be a promising option to bring this technology to the satellite market. The data rate increases dramatically specially for future scientific missions including multiple cameras and high data rate processing systems. The current used SpaceWire protocol is the transmission protocol with the highest bandwidth of 400 Mbit/s [9]. By using to fiber-optical com-

munication, datarates up to several Gbit/s are possible. The idea here is to combine the herein developed measurement system, operating at 1550 nm, with a data communication system working at different central wavelength of 1310 nm and thereby enabling sensing functionality and data transmission over the same fiber. Such a system is schematically illustrated in figure 7.3. The channel can be enabled for bidirectional data transmission by using a circulator within the transceiver module. Sensing and communication wavelengths are separated by using a slope filter from the telecommunication area.

A new project, called *Photonically Wired Spacecraft Panels* is carried out to prove the techno-economic benefit of such a system. Within this study the focus is on the economic effect by embedding the fibers into the panel. Embedding the fibers into the panel increases the productions costs but reduces the subsequent assembly efforts and enhances the overall functionality of the panel. So the embedded fibers in the satellite's wall build a neural system, which is able to sense physical parameters and can transport information as well. [147]

Appendix A

Appendix

A.1 Acknowledgment

This work has been performed in cooperation with OHB System AG and Kayser-Threde GmbH in the frame of the following ESA and DLR projects:

- *HSB - Hybrid Sensor Bus for Telecommunication Satellites - MST Subcontract*, Artes 5.2 (ESA)
- *Hybrid Sensor Bus (HSB) In-Orbit Verifikation auf H2Sat*, DLR, COMED, FKZ 50YB1310, BMBF, BMWi

Special thanks are addressed to the engineers at OHB supporting the development with their expertise in space engineering. The work was grateful enhanced by the support and discussions with the technical officers at ESA/ESTEC especially with Iain Mckenzie. For the support during the radiation test series and further discussion of the measurement results, special thanks are given to Jochen Kuhnhenn from the Fraunhofer INT institute in Euskirchen.

In the context of this work, the following publications (A.2) and student theses (A.3) were authored resp. supervised and are not cited formally.

A.2 Own Publications

- B. Eder, M. Plattner, P. Putzer, P. Eckert, A. Reutlinger, and T. Zeh *High Temperature Sensing with FBGs Using a Tunable Laser Interrogation System.* In *Optical Measurement Systems for Industrial Inspection VII, 80823M, 2011.*
- P. Putzer, A. Hurni, M. Manhart, C. Tiefenbeck, M. Plattner, and A. W. Koch. *Concept and Design of a Fiber-Optic and an I^2C Hybrid Sensor Bus System for Telecommunication Satellites* In *Proc. SPIE Vol. 8345 83453L-1, 2012.*
- P. Putzer, A. Hurni, M. Plattner, and A. W. Koch. *Design of a Fiber-Optic Interrogator Module for Telecommunication Satellites - Radiation Test Results of Optical Components* In *Proceedings of DASIA, 2012.*

- P. Putzer, A. W. Koch, A. Hurni, S. Schweyer, C. Tiefenbeck, and M. Plattner. *Fiber-Optical Temperature Sensing Onboard Geostationary Telecommunication Satellites* In *Proceedings of DASIA, 2013.*
- P. Putzer, N. Kuhenuri, A. W. Koch, S. Schweyer, A. Hurni, M. Plattner *A Space-Borne Fiber-Optic Interrogator Module based on a Narrow-Band Tunable Laser Diode for Temperature Monitoring in Telecommunication Satellites* In *Optical Measurement Systems for Industrial Inspection VIII, 878810, 2013.*
- P. Putzer, N. Kuhenuri, A. W. Koch, A. Hurni, M. Roner, J. Obermaier, and N. Lemke. *Selection of Fiber-Optical Components for Temperature Measurement for Satellite Application* In *Proceedings of ICSO, International Conference of Space Optics, 2014.*
- P. Putzer, A. Hurni, N. Lemke, M. Roner, J. Obermaier, N. Kuhenuri, and A. W. Koch. *Fiber-Optical Sensing On-Board Communication Satellites* In *Proceedings of ICSO, International Conference of Space Optics, 2014.*
- N. Kuhenuri, P. Putzer, A. W. Koch, J. Obermaier, S. Schweyer, and A. Hurni *Concept and Design of an FBG Emulator for a Scanning Laser-based Fiber-Optic Interrogator* In *Fiber Optic Sensors and Applications XI, 90980D, 2014.*
- S. Schweyer, R. Kiemberger, B. Eder, P. Putzer, A. Kölnberger, and N. Lemke *Characterization of a SESAM Mode-Locked Erbium Fiber Laser Frequency Comb with an Integrated Electro-Optic Modulator* In *Proceedings EFTF - European Frequency and Time Forum, 2014.*

A.3 Supervised Student Theses

- Florian Wißmeier: *Phasendetektion bei der Stabilisierung von Frequenzkämmen*, Bachelor Thesis, Technical University of Munich, 2012.
- Nader Kuhenuri: *Simulation and Design of an Ultra-Stable Laser Diode Controller and Implementation in a FTIR Spectroscope for the International Space Station (ISS-ANITA2)*, Master Thesis, Technical University of Munich, 2012.
- Thomas Zellner: *CAN-Bus - VHDL CAN Core and Transceiver Evaluation*, Bachelor Thesis, Technical University of Munich, 2012.
- Ahmed Shalaby: *Aufbau eines EGSE Referenz Sensor Boards*, Project Internship, Technical University of Munich, 2012.
- Alexander Jung: *Development of a Transducer for FBG-Sensors for the Application on Telecommunication Satellites*, Bachelor Thesis, Universität der Bundeswehr München, 2013.
- Johannes Obermaier: *Compensation of the Polarization Induced Measurement Error in a Fiber-Optic Temperature Sensor System for Space Applications*, Bachelor Thesis, Technical University of Munich, 2013.
- Markus Roner: *Digital Temperature Stabilization of Laser Diodes*, Bachelor Thesis, Technical University of Munich, 2013.

- Markus Roner: *Polarization Switch Driver - Design and Characterization*, Project Internship, Technical University of Munich, 2013.
- Sebastian Schweyer: *Simulation and Calibration of a Spaceborne Fiber-optical Interrogator Module*, Master Thesis, Hochschule für Angewandte Wissenschaften, 2013, (Supported)
- Markus Roner: *Auswahl und Implementierung der FBG-Evaluationslogik eines FPGA-basierten, faseroptischen Interrogators für Raumfahrtanwendungen*, Advanced Seminar, Technical University of Munich, 2014.
- Severin Kitzler: *Sicherheitssensor für absenkbares Oberschrank-Innenleben*, Master Thesis, Technical University of Munich, 2014.
- Thomas Unterholzer: *Construction and Verification of an Adaptive Frequency Counter to Measure the Frequency Stability for High-Precision Distance Measurements for Space Applications*, Bachelor Thesis, Technical University of Munich, 2015.
- Simon Bellhäuser: *Design and Construction of a Switching Low-Noise Laser Diode Controller*, Master Thesis,Technical University of Munich, 2016.
- Andreas Fischer: *Measurement Setup for Absolute and Dynamic Distance Measuring with the FDDM Method*, Master Thesis, Technical University of Munich, 2016.

List of Figures

1.1 *Graphical illustration of the content of the different sections in this work, for details refer to text.* 8

2.1 *Picture of a satellite harness [6]* 10
2.2 *Left: Current "State-of-the-art" sensor implementation for telecommunication satellites of the SGEO series [7] where all sensors are connected point-to-point to a central interrogation unit. Right: Future implementation as a sensor bus structure: The sensors can be electrical or fiber-optical.* 11
2.3 *Sketch of an integrated fiber-optical transducer inside a satellite panel.* . . . 12
2.4 *Description of a satellite orbit with Apogee (point of maximum distance), Perigee (point of minimum distance) and inclination with respect to equator.* 15
2.5 *Illustration of different satellite orbits around Earth according data obtained from [8] and [9].* 16
2.6 *Failures and mission losses due to different error mechanisms such as electrostatic discharge (ESD), single event upsets (SEU), total ionizing dose (TID) and other unknown error mechanisms [12].* 17
2.7 *Left: Proton flux forming the inner radiation belt. Right: Electron flux contributing to the inner radiation belt and forming the outer belt [15].* . . . 18
2.8 *Left: Increased proton flux above the South Atlantic. Right: Increased electron flux above South Atlantic and South- and North-Pole [15].* 20
2.9 *Radiation effects distinguished by the involved particles where displacement damage effects and ionization effects are caused by non-charged or charged particles, respectively. Diagram derived from data in [20].* 21
2.10 *Left: Conduction and valence band of a semiconductor with up-lifting of an electron from the valence band into the conductive band due to radiation. Right: Bandgap energy and necessary threshold energy for EHP generation for different semiconductor materials [11].* 23
2.11 *Left: Generation of a single Frenkel pair (vacant and interstitial lattice element) by an incident high energy particle. Right: Monte Carlo simulation of a cascaded damage structure in silicon (Si) [24].* 25
2.12 *Top: NIEL energy loss for protons, neutrons and electrons for Si as target material, bottom: NIEL energy values for GaAs as target material. [27]* . . 26
2.13 *LET diagram derived by simulation for a spacecraft shielding thickness of 2mm for a mission in the geostationary orbit. [15]* 28
2.14 *Different orbit constellations crossing the Van-Allen-Belts (not to scale). (Illustration by B. Jones, P. Fuqua, J. Barrie, The Aerospace Corporation).* 30
2.15 *Differential flux for protons (left) and electrons (right) for different satellite orbits [15].* 30
2.16 *Mean range of protons and electrons in aluminum according to [31].* 31

2.17 *Proton fluence (left) and total ionizing dose (TID, right) as function of aluminum shielding thickness for different orbits.* 32
2.18 *Left: Dose-depth curve for proton shielding for Aluminum (low-Z) and Tantalum (high-Z) acting as shielding material. Right: Dose-depth curve for electron shielding for same materials. [15]* 33
2.19 *Multi-layer shielding structure with Low-Z/High-Z/Low-Z configuration with illustrated stopping of incident particles.* 34
2.20 *Longitudinal static acceleration for the Soyuz launch vehicle taken from [34].* 36
2.21 *Left: Sinusoidal vibration spectrum for the qualification load of the HSB system. Right: Random vibration qualification spectrum of the out-of-plane (straight black line) and in-plain (dashed red line) loads [36]* 37
2.22 *Block and interface diagram of the Hybrid Sensor Bus system [5].* 39
2.23 *3D model of the Engineering Model (EM) of the HSB system [37].* 40

3.1 *Setup of a fiber based tunable laser with an Er-doped fiber as gain medium and a Fabry-Pérot filter (FPF) as wavelength selective device [43].* 45
3.2 *Tunable external cavity diode laser (ECDL) in Littrow (left) and Littman-Metcalf (right) configuration.* 46
3.3 *Schematic of the MG-Y laser diode with Y-branch reflector structure, amplifier, monitor elements and coupling lens. MMI multi-mode interferometer, SOA semiconductor optical amplifier.* 47
3.4 *Comb-like modes (theoretical model) of the left and right reflector with slightly different wavelength spacing. The different colors illustrate the different modes of each reflector (left, red and right, black). [56].* 48
3.5 *Plot of the refractive index change as function of the injection current.* . . 49
3.6 *Tuning principle of the MG-Y laser where the output wavelength is limited to the middle supermode.* 49
3.7 *Tuning principle of the MG-Y laser where the output wavelength is limited to the left supermode.* 50
3.8 *Wavelength map of the MG-Y laser at constant phase current I_P. The wavelength is given by the color of the map as function of the two reflector currents I_R and I_L. WB wavelength band, SH supermode hop, CH cavity mode hop, WI wavelength island.* 50
3.9 *Illustration of the effect of phase current injection to the MG-Y structure. The wavelength islands are illustrated as tubes which are moved in wavelength by changing the phase current.* 51
3.10 *Fitted curves to the measurement data of different stable wavelengths, minimum (red) and maximum (black) sensitivity is illustrated.* 52
3.11 *Measured data from the MG-Y's internal etalon (red points) and Airy fit (blue line) to the measurement data resulting in the etalon transmission function.* 54
3.12 *Flowchart for MG-Y calibration procedure.* 55
3.13 *Calibration setup for the MG-Y laser diode mounted onto the Analog Front-End broad (AFE).* 56
3.14 *Left: Principle of doublet generation for identifying the non-linear tuning behavior. Right: Right- and left reflector current map.* 57
3.15 *Laser's output wavelength as function of the right- and left reflector control voltages, showing a strong nonlinear behavior.* 58

3.16 *Wavelength map with smaller wavelength islands for lower right- and left reflector control currents due to constant step size of 10 mV.* 59
3.17 *Left: Laser's wavelength map obtained with the enhanced tuning vector eliminating smaller wavelength islands for lower reflector values. Right: Output wavelength as function of reflector values of uniform sampled measurement (blue curve) and scaled sampled measurement (red curve) respectively.* 59
3.18 *Left: Contour plot of the laser's output wavelength as function of the phase control voltage. Right: Nonlinear tuning characteristic of the laser as function of the right- and left-reflector control voltage for the three different phase control signals.* 60
3.19 *Flowchart for LUT generation for a single phase current of the laser. The different functions are described in the next chapter.* 61
3.20 *Left: Filter kernel with eight adjacent pixels surrounding a center pixel. Right: Applying the mode-jump filter kernel to a wavelength, schematic view.* 62
3.21 *Left: Initial wavelength map. Right: New wavelength map with removed unstable wavelengths on the border between wavelength islands.* 62
3.22 *Left: Wavelength map with repeating patterns (marked with red and black color). Right: Repeating patterns are removed.* 63
3.23 *Left: Lasers output power for different sample points with indicated threshold level of 7.5 dBm. Right: Side-Mode Suppression Ratio (SMSR) also with indicated threshold level of 25 dB.* 63
3.24 *Left: Spectral scan with high fluctuations in reflector values occur due to simple stacking of values. Right: Smooth LUT where values with a certain distance with respect to fitted values are deleted.* 64
3.25 *Left: Wavelength map before smoothing. Right: Smooth wavelength map with deleted boundary points which cause high fluctuations in reflector values.* 65
3.26 *Left: Wavelength spacing of the Master LUT as function of wavelength. Right: Histogram with regard to the wavelength spacing.* 65
3.27 *Simplified refractive index of an FBG structure along the fiber position z.* . 66
3.28 *Top: FBG structure with varying refractive index. Bottom-left: Input spectrum to the grating. Bottom-middle: Reflected spectrum at λ_B. Bottom-right: Transmitted spectrum with a dip located at λ_B due to the absence of the reflected light.* 67
3.29 *A sensor fiber with four FBGs with different Bragg wavelength $\lambda_{B1} \dots \lambda_{B4}$ is illuminated by a broadband light source. The single peaks appear in the reflected spectrum and are seen as dips in the transmitted spectrum respectively.* 69
3.30 *Sinusoidal shaped refractive index change along the fiber for an uniform grating (red) and an apodized grating (blue).* 70
3.31 *Wave in transmission $A_m(z)$ and in reflection $B_m(z)$ of the m-th mode respectively.* 70
3.32 *Comparison of the reflected spectrum between the theoretical model (blue line) and the measurement result (red points).* 74

3.33 *Simulated spectral response of an FBG as function of the grating length (L). Simulation parameters: Grating visibility* $S = 1$*, averaged induced refractive index change* $\overline{\delta n}_{eff} = 0.0001$ *and effective index of refraction* $n_{eff} = 1.45$. 75
3.34 *Simulated spectral response of an FBG as function of the averaged induced refractive index change* ($\overline{\delta n}_{eff}$)*. Simulation parameters: Grating visibility* $S = 1$*, grating length* $L = 5mm$ *and effective index of refraction* $n_{eff} = 1.45$. 75
3.35 *Reflection spectra for both polarizations in* $\vec{e_x}$ *and* $\vec{e_y}$ *direction. The blue line indicates the total reflection by adding the red and green curve. For the calculation a birefringence of* $1.8 \cdot 10^{-5}$ *and of* $5 \cdot 10^{-5}$ *for the left and right fiber was used respectively.* 79
3.36 *FBG reflection spectra for an uniform lighted FBG for different values of birefringence. For extreme values the peak breaks up into two distinct peaks.* 80
3.37 *Setup of a fiber ring depolarizer using a directional coupler (DC) with a certain coupling ratio k, for which one output is looped back to the input over a polarization controlling element (PC) [82].* 84
3.38 *Sketch of the setup of an electro-optical polarization modulator. A PM fiber is aligned with an angle of 45° to a* $LiNbO_3$ *waveguide on which a time varying electrical field is applied.* 86
3.39 *Degree of Polarization (DOP) as function of the phase shift* φ *for the three presented scrambling methods.* 87
3.40 *Setup of the amplitude splitting interferometer for FBG writing, BS beam-splitter, M mirror. Drawing according description in [92].* 90
3.41 *Illustration of the FBG writing process using a phase mask and an UV writing laser. Drawing according description in [99, 100].* 91
3.42 *Setup for writing FBGs with a femto-second infrared (fs-IR) pulsed laser and a high precision translation stage [102].* 92
3.43 *UV written grating from type I (black) and fs-IR written grating (red) with a lower spectral quality due to higher side-lobes than the UV written grating. Note the different x-axes for both FBGs.* 94
3.44 *Gaussian fit function applied to an FBG reflection spectrum, measured with the herein developed interrogator system, for all sample points (red line) and for the 14 strongest samples (blue line). A small deviation can be observed to a small fit error due to the FBGs spectral side-lobes.* 95
3.45 *Principle of the centroid fit function to an FBG reflection spectrum.* 96
3.46 *FBG spectral response (blue line) with additional noise and the first derivative of the averaged signal (red line). The black dashed line indicates the ideal theoretical model derived by the coupled mode theory.* 97
3.47 *Different filter kernels used for the convolution based algorithms. LP linear phase, DoG derivative of Gauss, DoC derivative of coupled mode fit.* 98
3.48 *Description of the Trip-Hop algorithm with the selected points* S_1 *,* S_2 *and* S_3 *on the slope of the spectrum and the calculated points* S_4 *and* $x_5 \simeq \lambda_B$. 100
3.49 *Illustration of a polynomial fit on the FBG spectral response. The vertex of the function is the estimated Bragg wavelength* λ_B. 100
3.50 *Simulation tool for algorithm evaluation.* 101
3.51 *Radiation induced loss of different fibers as function of TID, given in Gy, taken from [1].* 103

4.1 *HSB requirement data model implemented in IBM - Rational Doors.* . . . 105
4.2 *Radiation shielding approach for space systems [8], [16].* 113
4.3 *Left: 3D model of the HSB unit used to carry out the radiation analysis. Right: Detector location for the ray-tracing computation [37].* 113
4.4 *Left: Simulation results of the different peak find algorithms as function of the SNR of the reflected spectrum. Right: Simulation result of the different peak find algorithms as function of the wavelength spacing in the reflected spectra. CT centroid, GS Gaussian fit, LP linear phase convolution kernel, PI polynomial interpolation, DoG derivative of Gaussian fit (convolution based), MX maximum search, DoC derivative of Coupled-Mode fit (convolution based), TH-Opt Trip-Hop algorithm optimized, TH Trip-Hop algorithm with no optimization. Adjacent simulated points are linearly connected.* . . 119
4.5 *Simulation result of the different peak find algorithms as function of the wavelength spacing in the reflected spectra. CT centroid, GS Gaussian fit, LP linear phase convolution kernel, PI polynomial interpolation, DoG derivative of Gaussian fit (convolution based), MX, maximum search, DoC derivative of Coupled-Mode fit (convolution based), TH Trip-Hop algorithm with no optimization.* 121
4.6 *FBG spectra with different induced refractive index changes* δn_{eff}. 122
4.7 *RMS error for different peak find algorithms as function of* $\delta n_{eff} \cdot 10^{-5}$. . . 122
4.8 *Fiber-optical interrogator based on a tunable laser with control FPGA, optical coupler, fiber-Bragg grating sensor string and transimpedance amplifier (TIA).* 125
4.9 *Fiber-optical interrogator module capable to read out up to four FBG channels with a single MG-Y laser diode.* 126
4.10 *Redundancy concept of the fiber-optical sensing system shown for two channels with a main and redundant module* 126
4.11 *Fiber Sensor Multiplexer (FSM) block diagram.* 127

5.1 *Architecture of the designed fiber-optical interrogator module with laser transmitter unit (top left), optical front-end (right), receiver circuit (bottom) and controller including FPGA and memory for LUT storage.* 129
5.2 *Block diagram of the laser transmitter system including temperature controller, voltage/current converter and transimpedance amplifiers for internal photodiodes.* 130
5.3 *Circuit of the MG-Y laser's voltage/current converter with current sense amplifier (CSA), feedback network and bipolar amplifier stage.* 132
5.4 *Amplitude response function (top) and output voltage noise (bottom) for the current controller using a standard amplifier (RHF484) as function of frequency. The CSA input resistors used for the simulation were 100Ω, 1kΩ and 10kΩ.* 134
5.5 *Amplitude response function (top) and output voltage noise (bottom) for the current controller using a low voltage noise amplifier (RH1128) as function of frequency. The CSA input resistors used for the simulation were 100Ω, 1kΩ and 10kΩ.* 136
5.6 *Integration curve to obtain the RMS voltage noise in a frequency bandwidth between 100 Hz and 100 kHz for different values of input resistance for the general purpose amplifier RHF484.* 137

5.7 *Integration curve to obtain the RMS voltage noise in a frequency bandwidth between 100Hz and 100kHz for different values of input resistance for the general purpose amplifier RH1128.* 137
5.8 *Left: DC transfer function of the designed voltage/current converter circuit showing linear behavior. Right: Transient response curve for a 120Ω load connected to the converter circuit with rectangular input signal with a frequency of 10 kHz and with an amplitude of 3 V (top curve).* 138
5.9 *Current noise densities of the left- and right reflector current sources measured with a 15Ω shunt resistor.* 139
5.10 *Current noise densities of the SOA and laser current sources measured with a 3.3Ω shunt resistor.* 140
5.11 *Block diagram of the designed temperature controller circuit. The internal NTC is buffered by the temperature sense amplifier (TSA), which output voltage is used as feedback signal for the entire control loop.* 141
5.12 *Circuit diagram of the temperature controller circuit with temperature sense amplifier (first left), error amplifier (second left), PI controller circuit (third left) and current controlled bipolar output stage (right).* 142
5.13 *Transimpedance amplifiers for MG-Y's internal etalon and reference photodiodes with subsequent inverting amplifier.* 144
5.14 *Transimpedance amplifier for the two FBG channels with a single inverting amplifier and generated negative photocurrent resulting in a positive output voltage.* 145
5.15 *Screenshot of the developed software program for transimpedance noise calculation.* 147
5.16 *Screenshot of the bandwidth calculation program developed for fast and easy calculations.* 148
5.17 *Illustration of the sequential (top) and parallel (bottom) writing of the DACs.* 148
5.18 *Block diagram showing the important functional blocks for the FIM controller implemented inside the ICM FPGA. The AFE board is controlled by the SPI interface, data transfer is done over the RS485 communication bus and the data for LUT is stored in the shared MRAM memory.* 149
5.19 *Optical front-end illustrating the two paths of the laser's output light. Referencing channel on top with 10% and measurement channel on bottom with 90% of laser's output power respectively.* 150
5.20 *Referencing system of the optical front-end used in the fiber-optical interrogator module for laser stabilization [37].* 151
5.21 *Schematic drawing of the measurement subsystem of the optical front-end. The unit is designed for two measurement channels holding FBG sensors. In addition two pure outputs are available for the connection of FSM modules increasing the number of channels up to eight.* 152
5.22 *Interrogation cycle of the fiber-optical measurement module.* 154
5.23 *Schematic illustration of the 'Hill'- detection logic used for FBG detection in the sampled datastream.* 154

6.1 *Left: Reflected spectrum of a sensor string containing twelve FBG sensors for 28°C (blue line) and 46 °C (red line). Right: Zoom into the peak number seven, the sensitivity of the pure FBG was determined to 11.2 pm/°C.* . . . 156

6.2 *Thermal test setup for measuring two FBG strings with the designed interrogator module.* . . . 157
6.3 *Temperature measured with the FBG sensor and the designed interrogator during the thermal test. Three different fits are applied to the spectral data. Inlet: Zoom into timeframe between 9h:00s and 9h:30s, the Trip-Hop shows deviations.* . . . 157
6.4 *Temperature error with respect to the coupled-mode fit for the trip-hop algorithm (red line) and Gaussian fit (black line) respectively.* . . . 158
6.5 *Left: Spectral data for stable wavelength of the laser. Right: Laser instability for lower control voltages generates impurities in the spectrum.* . . . 159
6.6 *Thermal cycle of a single FBG sensor illustrating the temperature (red) and the estimated FBG peak wavelength (blue).* . . . 159
6.7 *Zoom into three temperature steps from the diagram in figure 6.6.* . . . 160
6.8 *Zoom into estimated Bragg wavelength for one temperature step showing a peak to peak wavelength deviation of 6.5pm.* . . . 160
6.9 *Setup for birefringence error measurement with the scanning laser based measurement system using a manual polarization controller to change the light polarization in the 25 m long single mode fiber. PC polarization controller.* . . . 161
6.10 *Determined FBG Bragg wavelength with different paddle position and different polarization state in the fiber. The FBG was a commercial grating written by UV-laser light.* . . . 162
6.11 *Polarization induced shift of the Bragg wavelength for different measurements (X-axis) carried out with different paddle positions. The gratings were written in pure silica fibers by the use of the fs-IR writing technique. 'Fit' corresponds to the coupled mode fit, GS Gaussian, TH Trip-Hop algorithm.* . . . 162
6.12 *Bragg wavelength error at different polarization states in the fiber with polarization switching and spectral averaging (red) and without (blue).* . . . 163
6.13 *InGaAs photodetector radiation test setup to measure the change in dark current and responsivity.* . . . 165
6.14 *FBG radiation test setup with SLD used as light source and spectrometer to measure the reflected Bragg wavelengths.* . . . 165
6.15 *Gamma radiation test setup for the fs-IR written gratings in the PSC fiber. The large blue arrow indicates high dose rate, whereas the small arrow indicates lower dose rate.* . . . 166
6.16 *Pure-Silica fiber radiation test setup shown for one single fiber type.* . . . 167
6.17 *MG-Y radiation test setup used for total dose testing with gamma rays and displacement damage testing with neutrons.* . . . 169
6.18 *Illustration of the wavelength tuning process during the radiation test. Each of the 37 measurement wavelengths are setup from the mid-wavelength.* . . . 170
6.19 *Flowchart of the radiation test of the MG-Y laser diode, shown for the total dose test.* . . . 171
6.20 *Increase in dark current of the InGaAs photodiode as function of accumulated neutrons per area.* . . . 172
6.21 *Left: Wavelength shift at high dose rate gamma radiation test of UV-written FBGs protected with different packages. Right: Comparison between high dose rate and low dose rate test, a dose rate dependent effect is observable.* 174

6.22 *Left: Bragg wavelength shift of sensors located in HDR area (top) and sensors in LDR area (bottom) respectively. Right: Wavelength shift of HDR sensors (top) and LDR sensors (bottom) respectively with subtracted shift of reference sensor.* 175
6.23 *Bragg wavelength shift, compensated by reference sensor's shift for FBGs in LDR and HDR zones respectively.* 176
6.24 *Radiation induced attenuation as function of the total dose of pure silica core (PSC) fibers from four different manufacturer.* 177
6.25 *Left: Laser (LD) slope efficiency (generated optical power as function of input current) at the beginning (blue line) and after 100 krad (red line) for biased laser including annealing phase (green line) reaching the initial performance. Right: Same plot but for unbiased laser diode, after annealing the initial performance is not reached.* 179
6.26 *Left: SOA slope efficiency at the beginning of the TID test (blue line) and after 100 krad (red line) for the biased laser with annealing phase (green line) reaching the initial performance. Right: Unbiased laser diode which did not reached the initial performance after annealing.* 179
6.27 *Degradation of optical output power as function of total dose for the biased laser (red curve) and the unbiased laser (blue curve).* 180
6.28 *Mid-Wavelength deviation for the biased laser (left) and for the unbiased laser (right).* 181
6.29 *Deviation of the different setup wavelengths due to total dose effects for the biased laser (left) and unbiased laser (right).* 182
6.30 *Wavelength map of the MG-Y laser before (colored lines) and after test (red lines) for the biased (left) and unbiased (right) laser.* 182
6.31 *Deviation in laser's mid-wavelength as function of neutron fluence.* 183
6.32 *Wavelength deviation for different wavelength setpoints for different neutron fluency.* 184
6.33 *Etalon (dashed line) and power monitor (straight line) photodiode signals.* . 185

7.1 *Picture of the AFE engineering model (EM) with MG-Y laser (bottom left), polarization switch (bottom center) and optical isolator (top center) mounted onto the PCB.* 187
7.2 *Left: TRL levels with level description, adapted from [144]. Right: TRL levels of the HSB system including the TRL levels of the herein developed and built system (green) and planned future tests (yellow) and future missions (blue) [37].* 191
7.3 *Sketch of a possible combination between the sensor bus system (bottom left) and a data communication system for high speed data links.* 192

List of Tables

2.1 *Summary of satellite orbits with height values, possible inclination and orbit usage. LEO Low Earth Orbit, MEO Medium Earth Orbit, HEO Highly Elliptical Orbit, GEO Geostationary Orbit [8].* . . . 16
2.2 *Ionization and displacement damage effects for different particles [10].* . . . 21
2.3 *Overview of damage effects for integrated circuits and opto-electronic devices according [20].* . . . 22
2.4 *Displacement threshold energy for different semiconductor materials [11].* . . 25
2.5 *Temperature requirements for the interrogation system.* . . . 35
2.6 *Random vibration loads for the out-of-plane and in-plane qualification loads of the HSB system [35].* . . . 37
2.7 *Shock qualification loads for the HSB system, values are the same for out-of-plane and in-plane loads [35].* . . . 38
2.8 *Electrical and mechanical specifications of the HSB system.* . . . 39

3.1 *Derived requirements for the laser source for the developed fiber-optical interrogator.* . . . 44
3.2 *Airy fit parameters for the MG-Y laser's internal etalon.* . . . 54
3.3 *Excerpt of a LUT for a constant phase value of 0.72V.* . . . 64
3.4 *FBG parameters used for model verification [71].* . . . 73
3.5 *Polynomial coefficients for the computation of the wavelength error induced by birefringence of the fiber.* . . . 81
3.6 *Filter kernels for the used convolution algorithms.* . . . 99

4.1 *Derived requirements for the fiber-optical interrogator module (FIM) developed within this work.* . . . 109
4.2 *Requirements for the fiber-optical sensor used for temperature sensing onboard satellites.* . . . 111
4.3 *Analysis results for the HSB box for the different detector locations.* . . . 114
4.4 *Scanning laser trade-off table.* . . . 115
4.5 *Trade-Off table summarizing the advantages and disadvantages of different polarization scrambling techniques.* . . . 116
4.6 *Trade-Off table summarizing the different FBG writing techniques, NG no-go.* 117
4.7 *Trade-Off table for the peak detection algorithm. GS: Gaussian fit, CT: centroid, LP5: linear phase operator, DoG: derivative of Gaussian, DoC: derivative of coupled-mode, TH: Trip-Hop, MX: maximum search, PI: parabolic interpolation* . . . 123
4.8 *Trade-Off summary table for the baseline design and one alternative.* . . . 123

5.1 *RMS current noise and wavelength sensitivity of the MG-Y laser at different operating currents.* . . . 131

5.2 *Transconductance and shunt resistor values for the five different channels of the voltage/current converter (RR right reflector, LR left reflector, PH phase, LD laser, SOA semiconductor optical amplifier).* 133
5.3 *RMS voltage and current noise of the different circuit configurations with different CSA input resistances.* 136

6.1 *Dose rates applied for the gamma radiation test of the MG-Y laser diode.* 169
6.2 *Summary of the output power degradation during the TID radiation test for the biased and unbiased laser diode.* 180

7.1 *Test matrix for the engineering model (EM), Engineering Qualification Model (EQM) and Proto-Flight Model (PFM) indicating different test sequences to the HSB models [35].* 190

Acronyms and Abbreviations

ADC Analog to Digital Converter
AIT Assembly, Integration and Test
BSM Binary Status Monitoring
BWS Bragg Wavelength Shift
CRC Canadian Research Center
CSA Current Sense Amplifier
CT Centroid
DAC Digital to Analog Converter
DD Displacement Damage
DoC Derivative of Centroid
DoG Derivative of Gauß
DOP Degree of Polarization
ECDL External Cavity Diode Laser
EDAC Error Detection and Correction
EHP Electron-Hole Pair
EM Engineering Model
EMC Electro-Magnetic Compatibility
EMI Electro-Magnetic Interference
EQM Engineering and Qualification Model
ESD Electro Static Discharge
FBG Fiber Bragg Grating
FBGS Fiber-Bragg Grating Sensors, company
FET Field-Effect Transistor
FIM Fiber-Optical Interrogator Module
FIM-AFE Fiber-Optical Interrogator Module - Analog Front-End
FIM-CM Fiber-Optical Interrogator Module - Controller Module
FOS Fiber-Optical Sensing
FPF Fabry-Perot Filter
FPGA Field Programmable Gate Array
fs-IR femtosecond Infra-Red
FSM Fiber-Sensor Multiplexer
FSR Free Spectral Range
FWHM Full Width at Half Maximum
GCSR Grating-assisted Co-directional Coupler with Sampled Reflector
GEO Geostationary Orbit
GPIB General Purpose Interface Bus
GPS Global Positioning System
GS Gauß
GTO Geo-Transfer Orbit

HCM HSB Controller Module
HDR High Dose Rate
HPC High-Power Command
HSB Hybrid Sensor Bus
ICM Interrogator Controller Module
IOV In-Orbit Verification
ISM I²C Sensor Multiplexer
ISS International Space Station
ITU International Telecommunication Union
JAXA Japan Aerospace Exploration Agency
LD Laser Diode
LDR Low Dose Rate
LEO Low Earth Orbit
LET Linear Energy Transfer
LHP Loop-Heat Pipe
LiNbO3 Lithium Niobate
LPx Linear Polarized
LPx Linear Phase
LR Left Reflector
LUT Look-Up Table
MEMS Microelectronic and Microelectromechanical Systems
MEO Mid Earth Orbit
MGY Modulated Grating Y-branch Laser
MISO Master-In, Slave-Out
MMI Multi-Mode Interferometer
MOSI Master-Out, Slave-In
MRAM Magnetic Random Access Memory
MX Maximum
NASA National Aeronautics and Space Administration
NG No-Go
NIEL Non-Ionizing Energy Loss
NTC Negative Temperature Coefficient
OFE Optical Front-End
OSNR Optical Signal-to-Noise Ratio
PCB Printed Circuit Board
PDFS Polarization Dependent Frequency Shift
PDL Polarization Dependent Loss
PER Polarization Extinction Ratio
PH Phase
PI Polynomial Interpolation
PM Polarization Maintaining
PSC Pure Silica Core Fiber
PSD Power Spectral Density
PSU Power Supply Unit
PT Platinum Temperature Sensor
PXI PCI eXtensions for Instrumentation
QM Qualification Model
RIA Radiation Induced Attenuation

RMS Root Mean Square
RR Right Reflector
SAA South Atlantic Anomaly
SCL Shift Clock
SEB Single Event Burn-Out
SEE Single Event Effect
SEGR Single Event Gate Rupture
SEL Single Event Latch-Up
SET Single Event Transient
SEU Single Event Upset
SGEO Small GEO
SLD Superluminescent Diode
SLSR Side-Lobe Suppression Ratio
SM Single Mode
SMF Single Mode Fiber
SMSR Side-Mode Suppression Ration
SMU Satellite Management Unit
SNR Signal-to-Noise Ratio
SOA State-of-the-Art, Semiconductor Optical Amplifier
SPENVIS Space Environment, Effects, and Education System
SPI Serial Peripheral Interface
SRAM Static Random Access Memory
SSG-DBR Super Structure Grating Distributed Bragg Reflector
TEC Thermo-Electric Cooler
TEM Transversal Electro-Magnetic
TH Trip-Hop
TID Total Ionizing Dose
TM/TC Telemetry/Tele command Data
TNID Total Non-Ionizing Dose
TRL Technology Readiness Level
TSA Temperature Sense Amplifier
TTG Sampled Grating Tunable Twin Guide
UV Ultra-Violet
VHDL Very High Speed Integrated Circuit Hardware Description Language
WDM Wavelength Division Multiplexing
WI Wavelength Island

Bibliography

[1] T. Wijnands, L. K. De Jonge, S. K. Hoeffgen, and U. Weinand. Optical absorption in commercial single mode optical fibers in a high energy physics radiation field. *IEEE Transactions on Nuclear Science*, 55, No. 4:2216, 2008.

[2] D. Grobnic, H. Henschel, S. K. Hoeffgen, J. Kuhnhenn, S. J. Mihailov, and U. Weinland. Radiation sensitivity of bragg gratings written with femtosecond ir lasers. *SPIE-Fiber Optic Sensors and Applications VI*, 7316, 2009.

[3] J. O. Wesstroem, G. Sarletm, S. Hammerfeldt, L. Lundquist, P. Szabo, and P. Rigole. State-of-the-art performance of widely tunable modulated grating y-branch lasers. In *Optical Fiber Communication Conference*, 2004.

[4] Finisar. Product Specification CW Tunable Laser S7500. Datasheet, December 2011.

[5] OHB System. A hybrid sensor bus - ESA proposal, 2012.

[6] OHB System. Harness of a galileo IOV satellite, 2010.

[7] OHB System. Small GEO (SGEO) - internal design documents.

[8] W. Ley, K. Wittmann, and W. Hallmann. *Handbuch der Raumfahrttechnik*. Number 978-3446424067. Hanser Verlag, 4th edition, 2011.

[9] P. Forthescue, G. Swinerd, and J. Stark. *Spacecraft Systems Engineering*. Wiley, 2011.

[10] V. Bothmer and I. A. Daglis. *Space Weather: Physics and Effects*. Number 978-3642062896. Springer, 1st edition, 2010.

[11] Allan Johnston. *Reliability and Radiation Effects in Compound Semiconductors*. World Scientific Publishing, 2010.

[12] H. C. Koons, J. E. Mazur, R. S. Selesnick, J. B. Blake, J. F. Fenell, J. L Roeder, and P. C Anderson. The impact of the space environment on space systems. In *6th Spacecraft Charging Technology Conference*, number AFRL-VS-TR-20001578, 2000.

[13] J. L. Barth, C. S. Dyer, and E. G. Stassinopoulos. Space atmosphere, and terrestrial radiation environments. *IEEE Transactions on Nuclear Science*, 50(3):466, 2003.

[14] European Coorporation for Space Standardization (ECSS). ECSS-E-ST-10-04C - space engineering - space environment, 2008.

[15] P. Putzer. Radiation environment simulation with SPENVIS, 2014.

[16] European Coorporation for Space Standardization (ECSS). ESA PSS-01-609 - radiation design handbook, 1993.

[17] J. R. Solin. Bremsstrahlung dose enhancement factors for satellites in 12-, 14.4- and 24-hr circular earth orbits. In *Proceedings of RADECS 2003: Radiation and its Effects on Components and Systems*, number ESA SP-536, 2003.

[18] D. R. Alexander. Transient ionizing radiation effects in devices and circuits. *IEEE Transactions on Nuclear Science*, 50(3), 2003.

[19] M. Al-Sheikhly and A. Christou. How radiation affects polymeric materials. *IEEE Transactions on Reliability*, 43(4), 1993.

[20] European Coorporation for Space Standardization (ECSS). Calculation of radiation and its effects and margin policy handbook, December 2010.

[21] C. Claeys and E. Simoen. *Radiation Effects in Advanced Semiconductor Materials and Devices*. Springer, 2002.

[22] European Coorporation for Space Standardization (ECSS). ESCC basic specification no. 22900, "total dose steady-state irradiation test method".

[23] A. Holmes-Siedle and A. Len. *Handbook of Radiation Effects*. 2002.

[24] V. A. J. van Lint, R. E. Leadon, and J. F. Colwell. Energy dependence of displacement effects in semiconductors. *IEEE Transactions on Nuclear Science*, 19(6), 1972.

[25] S. R. Messenger, E. A. Burke, G. P. Summers, M. A. Xapsos, R. J. Walters, E. M. Jackson, and B. D. Weaver. Nonionizing energy loss (NIEL) for heavy ions. 1999.

[26] G. P. Summers. Damage correlations in semiconductors exposed to gamma, electron and proton radiations. *IEEE Transactions on Nuclear Science*, 40(6), 1993.

[27] C. Poivey and G. Hopkins. Displacement damage mechanism and effects. In *EPFL Space Center 9th June*, 2009.

[28] W. R Leo. *Techniques for Nuclear and Particle Physics Experiments: A How-to Approach*. Springer, 1987.

[29] F Sturesson and S. Duzellier. Single event effects (see) mechanism and effects. In *Space Radiation and its Effects on EEE Components,*. EPFL Space Center, 2009.

[30] European Space Agency (ESA). SPENVIS - space environment, effects, and education system.

[31] Drolshagen G. Hilgers A. & Evans H. D. R Daly, E. J. Space environment analysis: Experience and trends. *Environment Modelling for Space-based Applications*, Symposium Proceedings ESA SP-392:15, 1996.

[32] J. Stefan. Über die beziehung zwischen der wärmestrahlung und der temperatur. *Sitzungsberichte der mathematisch-naturwissenschaftlichen Classe der kaiserlichen Akademie der Wissenschaften*, 79:391–428, 1879.

[33] L. Boltzmann. Ableitung des stefan'schen gesetzes, betreffend die abhängigkeit der wärmestrahlung von der temperatur aus der elektromagnetischen lichttheorie. *Annalen der Physik*, 258(6):291–294, 1884.

[34] Arianespace. *Soyuz User's Manual*, issue 2 edition, March 2012.

[35] OHB System. General equipment requirements document (GERD) version 2.0a.

[36] OHB System. Hybrid sensor bus to P/F interface requirement document (IRD), H2SAT-PF-OHB-IRD-0004. Issue 5 11.06.2014.

[37] OHB System. HSB, internal design documents and drawings, 2015.

[38] MIL-STD-1553B, digital time division command/response multiplex data bus. Technical report, Department of Defense, 1978.

[39] Gaisler AB. GR712RC dual-core LEON3FT SPARC V8 processor datasheet v. 2.3, 2016.

[40] International Telecommunication Union (ITU). Spectral grids for WDM applications: DWDM frequency grid.

[41] H. G. Bukkems. *New Approaches to Widely Tunable Semiconductor Lasers*. PhD thesis, Technical University of Eindhooven, 2006.

[42] B.E.A. Saleh and M.C. Teich. *Fundamentals of Photonics*. Wiley Series in Pure and Applied Optics. Wiley, 2007.

[43] N Park, J. W. Dawson, and K. J. Vahala. All fiber, low threshold, widely tunable single-frequency, erbium-doped fiber ring laser with a tandem fiber fabry-perot filter. *Applied Physics Letters*, 59(19):2369, 1991.

[44] J. L. Zyskind, J. W. Sulhoff, J. Stone, D. J. Digiovanni, L. W. Stulz, H. M. Presby, A. Piccirilli, and P. E. Pramayon. Electrically tunable, diode-pumped erbium-doped fibre ring laser with fibre fabry-perot etalon. 27(21):1950–1951, 1991.

[45] F. F. Zhong, Y. Xu, Y. J Zhang, and L. Ju. Widely ultra-narrow linewidth 104nm tunable all-fiber compact erbium-doped ring laser. *Laser Physics*, 21(1):219, 2011.

[46] M. Van Uffelen, S. Girard, A. Goutaland, A. Gusarov, B. Brichard, and F. Berghmans. Gamma radiation effects in er-doped silica fibers. *IEEE Transactions on Nuclear Science*, 51(5):2763, 2004.

[47] M. Plattner. *Laser based Measurement Systems for Space Applications*. PhD thesis, Institute for Measurement Systems and Sensor Technology, TU Munich, 2012.

[48] B. Brichard, A. F. Fernandez, H. Ooms, and F. Berghmans. Space radiation effects on erbium doped fibers. In *Conference on Photonics for Space Environments IV*, volume SPIE Vol.2811, 1996.

[49] J. Ma, M. Li, L. Y Tan, Y. P. Zhou, and C. Che. Space radiation effect on edfa for inter-satellite optical communication. *International Journal for Light and Electron Optics*, 121(6):535, 2008.

[50] A. Q. Liu, X. M. Zhang, J. Li, and C. Lu. Single-multi mode tunable laser using mems mirror and grating. *Sensors and Actuators, A: Physical*, 108:49, 2003.

[51] K. Liu and M. G. Littman. Novel geometry for single-mode scanning of tunable lasers. *Optics Letters*, 6(3):117, 1981.

[52] A. Q. Liu and X. M. Zhang. A review of mems external-cavity tunable lasers. *Journal of Micromechanics and Microengineering*, 17:R01, 2007.

[53] R. Laroy, G. Morthier, R. Baets, G. Sarlet, and J. O. Wesstroem. Characteristics of the new modulated grating y laser (mg-y) for future wdm networks. In *Proceedings Symposium IEEE/LEOS Benelux Chapter*, 2003.

[54] J.-O. Wesstrom, S. Hammerfeldt, J. Buus, R. Siljan, R. Laroy, and H. de Vries. Design of a widely tunable modulated grating y-branch laser using the additive vernier effect for improved super-mode selection. In *Semiconductor Laser Conference, 2002. IEEE 18th International*, pages 99–100, 2002.

[55] R. Todt and C. Amman. Influence of facet reflections on monolithic widely tunable laser diodes. *IEEE Photonic Technology Letters*, 17(12), 2005.

[56] J. O. Wesstroem, S. Hammerfeldt, J. Burus, R. Siljan, R. Laroy, and H. Vries. Design of a widely tunable modulated grating y-branch laser using the additive vernier effect for improved super-mode selection. In *Semiconductor Laser Conference*, 2001.

[57] Finisar. Controlling the s7500 cw tunable laser. Technical Report AN-2095, Finisar Corp.

[58] D. Demtröder. *Laser Spectroscopy*. Springer, 2008.

[59] K. O. Hill, Y. Fuji, D. C. Johnson, and B. S. Kawasaki. Photosensitivity in optical fiber waveguides: Application to reflection filter fabrication. *Applied Physics Letters*, 32(647):1263, 1978.

[60] G. Meltz, WW. Morey, and WH. Glenn. Formation of bragg gratings in optical fibers by a transverse holographic method. 15(14):823–5, 1989.

[61] K. O. Hill and G. Meltz. Fiber bragg grating technology fundamentals and overview. *Journal of Lightwave Technology*, 15, No. 8:1263, 1997.

[62] Hyuk-Jin Yoon and Chun-Gon Kim. The mechanical strength of fiber bragg gratings under controlled uv laser conditions. *Smart Materials and Structures*, 16(4):1315, 2007.

[63] Turan Erdogan. Fiber grating spectra. *Lightwave Technology, Journal of*, 15(8):1277–1294, 1997.

[64] A. D. Kersea, A. Davis, H. J. Patrick, M. LeBlanc, K. P. Koo, C. G. Askins, M. A. Putnam, and E. J. Fiebele. Fiber grating sensors. *Journal of Lightwave Technology*, 15, No. 8:1442, 1997.

[65] J. Komma, C. Schwarz, G. Hofmann, D. Heinert, and R. Nawrodt. Thermo-optic coefficient of silicon at 1550nm and cryogenic temperatures. *Applied Physics Letters*, 101, 2012.

[66] K.G. Lyon, G. L. Salinger, C. A. Swenson, and G. K. White. Linear thermal expansion measurements on silicon from 6 to 340 k. *Journal of Applied Physics*, 48, 1977.

[67] A. Othonos and Kalli K. *Fiber Bragg Gratings*. Artech House, 1999.

[68] S. Yin, P. B. Ruffin, and F. T. S. Yu. *Fiber Optic Sensors*. CRC Press, 2008.

[69] S. Ugale and V. Mishra. Fiber bragg grating modeling, characterization and optimization with different index profiles. *International Journal of Engineering Science and Technology*, 2(9):4463, 2010.

[70] H. Kogelnik. *Theory of Optical Waveguides*. Number 354052780X. Springer-Verlag Berlin Heidelberg, 1990.

[71] FBGS International. *Draw Tower Gratings (DTGs) in Low Bend Loss fiber LBL-1550-125, Datasheet*, 2016.

[72] F. Heismann. Compact electro-optic polarization scramblers for optically amplified lightwave systems. *Journal of Lightwave Technology*, 14(8):1801–1814, 1996.

[73] R. Gafsi and M. A. El-Sherif. Analysis of Induced-Birefringence Effects on Fiber Bragg Gratings. *Optical Fiber Technology*, 6:299–323, July 2000.

[74] J-lchi Sakai, SUSUMU Machida, and TATSUYA Kimura. Degree of polarization in anisotropic single-mode optical fibers: Theory. *Microwave Theory and Techniques, IEEE Transactions on*, 30(4):334–341, 1982.

[75] M. Fernandez-Guasti, H. Palafox, and C. Roychoudhuri. Coherence and frequency spectrum of a nd:yag laser: generation and observation devices. *The Nature of Light: What are Photons*, 8121:81211E–81211E–10, 2011.

[76] C. Seidel. *Optimierungsstrategien für faseroptische Rotationssensoren: Einfluss der spektralen Eigenschaften der Lichtquelle*. PhD thesis, Universität Fridericiana Karlsruhe, 2004.

[77] B. H. Billings. A monochromatic depolarizer. *Journal of the Optical Society of America*, 41(12):966, 1951.

[78] K. Böhm, K. Petermann, and E. Weidel. Performance of lyot depolarizers with birefringent single-mode fibers. *Journal of Lightwave Technology*, 1(1):71, 1983.

[79] P. D. Richter. The lyot depolarizer in quasimonochromatic light. *Journal of the Optical Society of America*, 69(3):460, 1979.

[80] B. Lyot. Annales de l'observatoire d'astronomie de paris. *Mendon VIII*, 1929.

[81] D. R. Lutz. A passive fiber-optic depolarizer. *IEEE Photonic Technology Letters*, 4(4):463, 1993.

[82] M. Martinelli and J. C. Palais. Theory of a tunable fiber ring depolarizer theory. *Applied Optics*, 40(18):3014, 2001.

[83] P. Shen and J. C. Palais. Passive single-mode fiber depolarizer. *Applied Optics*, 38(9):1686, 1999.

[84] V. Kopp and A. Genack. Adding twist. *Technology Focus*, 5:470–472, 2011.

[85] Chiral Photonics. *Datasheet, LERCP-ASSY-1550-FC/APC*, 2013.

[86] D. V. I. Kopp, V. I. Churikov, J. Singer, N. Chao, D. Neugrosch, and A. Genack. Chiral fiber gratings. *Science*, 305(5680):74, 2004.

[87] Dr. Victor I. Kopp, Dr. Azriel Z. Genack, Dr. Victor M. Churikov, Jonathan Singer, and Norman Chao. Chiral Fiber Gratings Polarize Light. *Photonics Spectra*, September:78, 79, 2004.

[88] Victor I. Kopp, Victor M. Churikov, and Azriel Z. Genack. Synchronization of optical polarization conversion and scattering in chiral fibers. *Optics Letters*, 31(5):571–573, Mar 2006.

[89] *Photline Technologies, PS-LN series Polarization Switches.*

[90] Hiroyuki Fujiwara. *Spectroscopic Ellipsometry: Principles and Applications.* ISBN: 9780470016084. Wiley, 2007.

[91] R. Kashyap. *Fiber Bragg Gratings.* Academic Press, 1999.

[92] K.T.V. Grattan and B.T. Meggitt. *Optical Fiber Sensor Technology: Advanced Applications - Bragg Gratings and Distributed Sensors.* Optical fiber sensor technology. Springer, 2000.

[93] S. J Mihailov, C. W. Semsler, P Lu, R. B. Walker, D. Grobnic, H. Ding, and G. Henderson. Fiber bragg gratings made with a phase mask and 800-nm femtosecond radiation. *Optics Letters*, 28, No. 12:995, 2003.

[94] D.P. Hand, L.J. Poyntz-Wright, and P.St.J. Russell. Enhanced photorefractivity in germanosilicate fibres: Effects of bleaching with 488nm light. In *Integrated Photonics Research*, 1990.

[95] B. Poumellec, P. Niay, P. Douay, and J. F. Bayon. The uv-induced refractive index grating in ge:sio2 preforms: Additional cw experiments and the macroscopic origin of the change in index. *Journal of Applied Physics D*, 29:1842, 1996.

[96] P.J. Lemaire, R.M. Atkins, V. Mizrahi, and W.A.; Reed. High pressure h2 loading as a technique for achieving ultrahigh uv photosensitivity and thermal sensitivity in geo2 doped optical fibres. *Electronic Letters*, 29, No. 13:1191, 1993.

[97] T-E. Tsai, G. M. Williams, and E. J. Friebele. Index structure of fiber bragg gratings in $ge - sio_2$ fibers. *Optics Letters*, 22(4):224, 1997.

[98] S. A. Slattery, D. N. Nikogosyan, and G. Brambilla. Fiber bragg grating inscription by high-intensity femtosecond uv laser light: Comparison with other existing methods of fabrication. *Journal of the Optical Society of Amerika B*, 22, No. 2:354, 2005.

[99] P. E. Dyer and R. Farley, R. J. Giedl. Analysis of grating formation with excimer laser irradiated phase mask. *Optical Communciations*, 115:327, 1995.

[100] A. Othonos and X. Lee. Novel and improved methods of writing bragg gratings with phase masks. *IEEE Photonic Technology Letters*, 7, No. 10:1183, 1995.

[101] C. W. Semsler, S. J. Mihailov, and D. Grobnic. Formation of type I-IR and type II-IR gratings with an ultrafast IR laser and a phase mask. *Optics Express*, 13, No. 14:5377, 2005.

[102] T. Geernaert, Kalli K., C. Koutsides, M. Komodromos, T. Nasilowski, W. Urbanczyk, J. Wojcik, F. Berghmans, and H. Thienpont. Point-by-point fiber bragg grating inscription in free-standing step-index and photonic crystal fibers using near-ir femtosecond laser. *Optics Letter*, 35(10):1647, 2010.

[103] J. Thomas, E. Wiksak, T. Clausnitzer, U. Fuch, U. Zeitner, S. Nolte, and A. Tünnermann. Inscription of fiber bragg gratings with femtosecond pulses using a phase mask scanning technique. *Applied Physics A*, 86:153–157, 2007.

[104] C. Voigtländer, D. Richter, J. Thomas, A. Tünnermann, and S. Nolte. Inscription of high contrast volume bragg gratings in fused silica with femtosecond laser pulses. *Applied Physics A*, 102:35–38, 2011.

[105] S. J Mihailov, C. W. Semsler, D. Grobnic, R. B. Walker, P Lu, H. Ding, and J Unruh. Bragg gratings written in all-SiO2 and Ge-doped core fibers with 800-nm femtosecond radiation and a phase mask. *Journal of Lightwave Technology*, 22, No. 1:94, 2004.

[106] S. J Mihailov, D. Grobnic, and C. W. Semsler. Efficient grating writing through fibre coating with femtosecond IR radiation and phase mask. *Electronics Letters*, 43, No. 8:–, 2007.

[107] S. J Mihailov. Fiber bragg grating sensors for harsh environment. *Sensors 2012*, 12:1898, 2012.

[108] G. D. Goodno, G. Dadusc, and R. J. D. Miller. Ultrafast heterodyne-detected transient-grating spectroscopy using diffractive optics. *Journal of the Optical Society of America B*, 15:1791, 1998.

[109] C. W. Semsler, S. J Mihailov, and D. Grobnic. Hydrogen loading for fiber grating writing with a femtosecond laser and a phase mask. *Optics Letters*, 29(18):2127, 2004.

[110] D. Grobnic, C. W. Semsler, S. J Mihailov, R. B. Walker, and P Lu. Fiber bragg gratings with suppressed cladding modes made in smf-28 with a femtosecond ir laser and a phase mask. *IEEE Photonic Technology Letters*, 16(8):1864, 2004.

[111] C. Voigtländer, J. Thomas, E. Wiksak, P. Dannberg, S. Nolte, and A. Tünnermann. Chirped fiber bragg gratings written with ultrashort pulses and a tunable phase mask. *Optics Letters*, 34, No. 12:1888–1890, 2009.

[112] E. Wiksak, J. Thomas, S. Nolte, and A. Tünnermann. Inscribing fiber bragg gratings using ir-fs pulses and a phase.mask scanning technique: Potential and applications. In *Commercial and Biomedical Applications of Ultrafast Lasers VII, Proc. SPIE 64600Z*, 2007.

[113] M. Becker, S. Bröckner, Lindner E., M. Rothhardt, S. Unger, J. Kobelke, K. Schuster, and H. Bartelt. Fiber bragg grating inscription with uv femtosecond exposure and two beam interference for fiber laser applications. In *Photonics North, Proc. SPIE Vol. 775015*, 2010.

[114] M. Becker, J. Bergmann, S. Bröckner, E. Lindner, M. Rothhardt, K. Schuster, J. Kobelke, S. Unger, H. Bartelt, L. A. Fernandes, and Marques P. V. S. Fiber bragg grating inscription with duv femtosecond exposure and two beam interference. In *Photonics North 2009, Proc. SPIE Vol. 73862Y*, 2009.

[115] M. Becker, L. A. Fernandes, Rothhardt M., S. Bröckner, K. Schuster, J. Kobelke, O. Franzao, H. Bartelt, and Marques P. V. S. Inscription of fiber bragg grating array in pure silica suspended core fibers. *IEEE Photonic Technology Letters*, 21, No. 19:1453–1455, 2009.

[116] M. Becker, J. Bergmann, S. Bröckner, M. Franke, Lindner E., Rothhardt M., and H. Bartelt. Fiber bragg grating inscription combining duv sub-picosecond laser pulses and two beam interferometry. *Optics Express*, 16, No. 23:19169–19178, 2008.

[117] T. Elsmann, A. Hartung, E. Lindner, M. Rothhardt, and H. Bartelt. Interferometric inscription of volume bragg gratings in a commercial high-refractive index glass (S-TIH53) by 400nm femtosecond (fs) laser pulses. In *Micro-Optics 2012, Proc. SPIE Vol. 84280H*, 2012.

[118] G. D. Marshall, R. J. Williams, N. Jovanovis, M. J. Steel, and M. J. Withford. Point-by-point written fiber-bragg gratings and their application in complex grating designs. *Optics Express*, 18(19):19844, 2010.

[119] R. J. Williams, C. Voigtländer, Marshall G. D., A. Tünnermann, S. Nolte, M. J. Steel, and M. J. Withford. Point-by-point inscription of apodized fiber bragg gratings. *Optics Letters*, 36, No. 15:2988–2990, 2011.

[120] V. Ingle and J. Proakis. *Digital Signal Processing Using MATLAB*. CENGAGE Learning Custom Publishing, 2011.

[121] L. Negri, A. Nied, H. Kalinowski, and A. Paterno. Benchmark for peak detection algorithms in fiber bragg grating interrogation and a new neural network for its performance improvement. *Sensors*, 11:3466–3482, 2011.

[122] T. Bodendorfer, M. S. Müller, F. Hirth, and A. W. Koch. Comparision of different peak detection algorithms with regards to spectrometric fiber bragg grating interrogation systems. *International Symposium on Optomechatronic Technologies*, pages 122–126, 2009.

[123] T. Zeh. *Optical Fiber Bragg Sensors - Measurement Systems and Signal Processing*. PhD thesis, Institute for Measurement Systems and Sensor Technology, TU Munich, 2004.

[124] H. Henschel, D. Grobnic, S. K. Hoeffgen, J. Kuhnhenn, S. J Mihailov, and U. Weinand. Development of highly radiation resistant fiber bragg gratings. *IEEE Transactions on Nuclear Science*, 58, No. 4:2103, 2011.

[125] K. Aikawa, K. Izoe, N. Shamoto, M. Kudoh, and T. Tsumanuma. Radiation-resistant single-mode optical fiber. *Fujikura Technical Review*, 37:9, 2008.

[126] K. V. Zotov, M. E. Likhachev, A. L. Tomashuk, M. M. Bubnov, M. V. Yashkov, A. N. Guryanov, and S. N. Klyamkin. Radiation-resistant erbium-doped fiber for spacecraft applications. 2007.

[127] A. F. Fernandez, B. Brichard, and F. Berghmans. Long-term radiation effects on fiber bragg grating temperature sensors in mixed gamma neutron fields. In *RADECS*, 2003.

[128] H. Henschel, S.K. Hoeffgen, K. Krebber, J. Kuhnhenn, and U. Weinand. Comparision of the radiation sensitivity of fiber bragg gratings made by four different manufacturer. *IEEE Transactions on Nuclear Science*, 58, No. 3:906, 2011.

[129] H. Henschel, S. K. Hoeffgen, J. Kuhnhenn, and U. Weinand. Influence of manufacturing parameters and temperature on the radiation sensitivity of fiber bragg gratings. *IEEE Transactions on Nuclear Science*, 57, No.4:2029, 2010.

[130] A. I. Gusarov, F. Berghmans, A. F. Fernandez, O. Deparis, Y. Defosse, D. Starodubov, M. Decreton, P. Megret, and M. Blondel. Behavior of fiber bragg gratings under high total dose gamma radiation. *IEEE Transactions on Nuclear Science*, 47, No. 3:688, 2000.

[131] A. I. Gusarov, C. Chojetzki, I. McKenzie, H. Thienpont, and F. Berghmans. Effect of the fiber coating on the radiation sensitivity of type I fbgs. *IEEE Photonics Technology Letters*, 20, No. 21:1802, 2008.

[132] C. Gierl, T. Gruendl, P. Debernardi, K. Zogal, C. Grasse, H. A. Davani, G. Böhm, S. Jatta, F. Küppers, P. Meissner, and M.-C. Amann. Surface micromachined tunable 1.55 um-vcsel with 102 nm continuous single-mode tuning,. 19(18):17336, 2011.

[133] Texas Instruments. *DAC121S101QML, Datasheet (SNAS410E)*, 2013.

[134] P. Horowitz and W. Hill. *The Art of Electronics*. Cambridge University Press, 2015.

[135] Rohde und Schwarz. *RTO1014 Datasheet*, 2010.

[136] H Lutz and W. Wendt. *Taschenbuch der Regelungstechnik*. Harri Deutsch, 6th edition, 2005.

[137] S. Donati. *Photodetectors: Devices, Circuits and Applications*. Prentice Hall, 1999.

[138] Kyosemi. *KPDE030SLTU InGaAs photodiode Datasheet (0905/KPDE030)*, 2009.

[139] Texas Instruments. *Datasheet OP656*, 2008.

[140] J. Heidecker. MRAM technology status. Technical report, Jet Propulsion Laboratory, 2013.

[141] Primanex. *Athermal Wavelength Reference Filter (PETL1-111T41100, 25GHz) datasheet*, 2014.

[142] S. Gilbert, W. C. Swann, and C.-M. Wang. Hydrogen cyanide $H^{13}C^{14}N$ absorption reference for 1530 nm to 1565 nm wavelength calibration – SRM 2519a. Technical report, National Institute of Standards and Technology (NIST), 2005.

[143] Microsemi. *RTAX-S/SL and RTAX-DSP Radiation-Tolerant FPGAs datasheet*, 17 edition, 2015.

[144] European Coorporation for Space Standardization (ECSS). Technology readiness levels handbook for space application, TEC-SHS/5551/MG/ap, 2008.

[145] OHB System. H2-Sat mission description (https://www.ohb-system.de/heinrich-hertz.html), 2016.

[146] P. Putzer, N. Kuhenuri, A. W. Koch, A. Hurni, M. Roner, J. Obermaier, and N. Lemke. Selection of fiber-optical components for temperature measurement for satellite application. In *Proceedings of ICSO, International Conference of Space Optics*, 2014.

[147] A. Hurni. Photonically wired spacecraft panels. In *Intra-satellite Fibre Optic Links Workshop*, 2015.